Perturbations of protein synthesis: from antibiotics to genetics and physiology

by

Bor Kavčič

October, 2020

A thesis presented to the
Graduate School
of the
Institute of Science and Technology Austria, Klosterneuburg, Austria
in partial fulfillment of the requirements
for the degree of
Doctor of Philosophy

The thesis of Bor Kavčič, titled *Perturbations of protein synthesis: from antibiotics to genetics and physiology*, is approved by:

Supervisor: Prof. Gašper Tkačik, IST Austria, Klosterneuburg, Austria

Signature: _____

Supervisor: Prof. Tobias Bollenbach, University of Cologne, Cologne, Germany

Signature: _____

Committee Member: Prof. Martin Loose, IST Austria, Klosterneuburg, Austria

Signature: _____

Committee Member: Prof. Stefan Klumpp, University of Göttingen, Göttingen, Germany

Signature: _____

Defense Chair: Prof. Mikhail Lemeshko, IST Austria, Klosterneuburg, Austria

Signature: _____

signed page is on file

IST Austria Thesis, ISSN: 2663-337X
ISBN: 978-3-99078-011-4

I hereby declare that this thesis is my own work and that it does not contain other people's work without this being so stated; this thesis does not contain my previous work without this being stated, and the bibliography contains all the literature that I used in writing the dissertation.

I declare that this is a true copy of my thesis, including any final revisions, as approved by my thesis committee, and that this thesis has not been submitted for a higher degree to any other university or institution.

I certify that any republication of materials presented in this thesis has been approved by the relevant publishers and co–authors.

Sequences of HiBit-tag are proprietary (Promega). Usage for research has been approved in the license agreement between the author and company Promega. The use of sequences without Promega approval is not allowed.

Signature: _____

Bor Kavčič
October, 2020
signed page is on file

Abstract

Synthesis of proteins – translation – is a fundamental process of life. Quantitative studies anchor translation into the context of bacterial physiology and reveal several mathematical relationships, called "growth laws," which capture physiological feedbacks between protein synthesis and cell growth. Growth laws describe the dependency of the ribosome abundance as a function of growth rate, which can change depending on the growth conditions. Perturbations of translation reveal that bacteria employ a compensatory strategy in which the reduced translation capability results in increased expression of the translation machinery.

Perturbations of translation are achieved in various ways; clinically interesting is the application of translation-targeting antibiotics – translation inhibitors. The antibiotic effects on bacterial physiology are often poorly understood. Bacterial responses to two or more simultaneously applied antibiotics are even more puzzling. The combined antibiotic effect determines the type of drug interaction, which ranges from synergy (the effect is stronger than expected) to antagonism (the effect is weaker) and suppression (one of the drugs loses its potency).

In the first part of this work, we systematically measure the pairwise interaction network for translation inhibitors that interfere with different steps in translation. We find that the interactions are surprisingly diverse and tend to be more antagonistic. To explore the underlying mechanisms, we begin with a minimal biophysical model of combined antibiotic action. We base this model on the kinetics of antibiotic uptake and binding together with the physiological response described by the growth laws. The biophysical model explains some drug interactions, but not all; it specifically fails to predict suppression.

In the second part of this work, we hypothesize that elusive suppressive drug interactions result from the interplay between ribosomes halted in different stages of translation. To elucidate this putative mechanism of drug interactions between translation inhibitors, we generate translation bottlenecks genetically using inducible control of translation factors that regulate well-defined translation cycle steps. These perturbations accurately mimic antibiotic action and drug interactions, supporting that the interplay of different translation bottlenecks partially causes these interactions.

We extend this approach by varying two translation bottlenecks simultaneously. This approach reveals the suppression of translocation inhibition by inhibited translation. We rationalize this effect by modeling dense traffic of ribosomes that move on transcripts in a translation factor-mediated manner. This model predicts a dissolution of traffic jams caused by inhibited translocation when the density of ribosome traffic is reduced by lowered initiation. We base this model on the growth laws and quantitative relationships between different translation and growth parameters.

In the final part of this work, we describe a set of tools aimed at quantification of physiological and translation parameters. We further develop a simple model that directly connects the abundance of a translation factor with the growth rate, which allows us to extract physiological parameters describing initiation. We demonstrate the development of tools for measuring translation rate.

This thesis showcases how a combination of high-throughput growth rate measurements, genetics, and modeling can reveal mechanisms of drug interactions. Furthermore, by a gradual transition from combinations of antibiotics to precise genetic interventions, we demonstrated the equivalency between genetic and chemical perturbations of translation. These findings tile the path for quantitative studies of antibiotic combinations and illustrate future approaches towards the quantitative description of translation.

Acknowledgments

Foremost, I would like to express my sincere gratitude to my supervisors – Gašper and Tobias – for continuous support during my PhD studies. Their reliability, scientific and editorial support [thank you for spotting the missing (in)definite articles and correcting my overly baroque language!], patience, and trust were essential. I am grateful for all the opportunities throughout my studies as well as the freedom in my research. Even though sometimes things moved with a speed of a particularly lazy glacier, they believed that we would figure things out. Furthermore, I am grateful to Călin, who took me in and became my third – albeit unofficial – supervisor. Thank you for all the help and encouragement, lunches at Redlinger, and scientific wisdom. Together with Gašper and Tobias, he offered valuable advice: about science but also other things. I am grateful to all of them: it was a privilege.

Many people helped me throughout the year – too many to list them all, unfortunately. I thank (in no particular order): Georg, for showing me the useful tricks of the lab work, hosting me in the US, and all the motorcycle rides. Karin and Andreas, for teaching me with patience and wisdom and for being such good friends. Wiktor and Mike, for the continuous stream of horrible dad jokes and camaraderie. Tomi, for not allowing me to starve – online on various biomes or offline by menus of pulled-pork and risottos. Vlad, for all the fun debates and widening of my culinary horizon in Vienna and beyond. Maroš, for hosting me in the US and being a wise friend. Louisa, Marta, Martin, Marcin, Qi Qin, and Veronika: for being great colleagues. My office mates Bella, Kathrin, Mike, Kirti, Bryan, Nathalie, Anna, (and all the interns who passed through Guet group) for all the lunch discussions (at 11.30 sharp!), support in everyday work, help with my

writing, and for the opportunity to learn from them. Exeter team, Manchester's Mato, Stockholm's Rok, Urban, and Valanx: for showing how to do things afterward. Primož Ziherl, for his support and help, even after I left University of Ljubljana. FriSBi team, for organizing a vibrant series of seminars. Organizing teams of Young Scientist Symposium 2016 and Science-Industry Day 2017, for allowing me to help with organization.

I thank Stefan Klumpp and Martin Loose for serving on my PhD committee and their interest in my work. Likewise, I thank Mikhail Lemeshko for chairing my qualifying exam and the thesis defense, thus both starting and concluding my PhD studies. I am grateful to the Knafelj foundation for granting me a doctoral stipend of the Tuma family. I thank Life Science Facilities for their continuous support with providing top-notch laboratory materials, keeping the devices humming, and coordinating the repairs and building of custom-designed laboratory equipment with the MIBA Machine shop.

Last but not least, I would like to thank my family for their support and encouragement. Finally, I am forever grateful to Kaja: for her patience, encouragement, sacrifices, and all the joy you brought to my life. I love you very much!

About the Author

Bor Kavčič completed a BSc (2012) and MSc (2014) in physics and biophysics, respectively, at University of Ljubljana, Slovenia. During his master studies, he worked with Prof. Primož Ziherl on the mechanics of confined lipid vesicles. He joined IST Austria graduate school in 2014. There, he switched from pen-and-paper biophysics to pipette-and-centrifuge systems biology. His work was partially supported by Tuma Scholarship from the Lukas Knaffelsche Privatstiftung.

List of Publications

The main part of this thesis is or will be published in the following articles

1. B. Kavčič, G. Tkačik, and T. Bollenbach, "Mechanisms of drug interactions between translation-inhibiting antibiotics," Nat. Commun. 11, 4013 (2020),

2. B. Kavčič, G. Tkačik, and T. Bollenbach, "Minimal biophysical model of combined antibiotic action," bioRxiv DOI: 10.1101/2020.04.18.047886v2.

Table of Contents

List of Tables

List of Figures

List of Abbreviations

Abbreviation	Meaning
aa	amino acid
aTc	anhydrotetracycline
ATP	adenosine triphosphate
bp	base pair
BD	bottleneck dependency (score)
cAMP	cyclic adenosine monophosphate
CAT	chloramphenicol acetyltransferase
CDF	cumulative distribution function
CERG	constitutively expressed resistance genes
CRY	capreomycin
CHL	chloramphenicol
DMSO	dimethyl sulfoxide
DNA	deoxyribonucleic acid
DOG	2-deoxy-galactose
E. coli	*Escherichia coli*
EF	elongation factor
ERM	erythromycin
FLP	recombinase flippase
FRT	FLP recognition target
FUS	fusidic acid
GFP	green fluorescent protein
GTP	guanosine 5′-(tetrahydrogen triphosphate)

Continued on next page

List of Abbreviations – continued from previous page

Abbreviation	Meaning
IF	initiation factor
IPTG	isopropyl β-D-1-thiogalactopyranoside
KSG	kasugamycin
KAN	kanamycin
LAM	lamotrigine
LB	lysogeny broth
LI	Loewe interaction (score)
LCY	lincomycin
MIC	minimal inhibitory concentration
mRNA	messenger RNA
MUP	mupirocin
NIT	nitrofurantoin
nt	nucleotide
OD	optical density
ODE	ordinary differential equation
ORF	open reading frame
PCA	principal component analysis
PCR	polymerase chain reaction
PDF	probability distribution function
(p)ppGpp	guanosine (penta)tetra phosphate
PTC	peptidyl-transferase centre (PTC)
RF	release factor
RI	Rand index
RNA	ribonucleic acid
rRNA	ribosomal RNA
RBS	ribosome binding site
RNAP	RNA polymerase
S. cerevisiae	*Saccharomyces cerevisiae*

Continued on next page

List of Abbreviations – continued from previous page

Abbreviation	Meaning
SD	Shine-Dalgarno (sequence)
SMA	starvation-mimicking antibiotic
STR	streptomycin
TASEP	totally asymmetric simple exclusion process
tRNA	transfer RNA
UTR	untranslated region
WT	wild type

1 General introduction

Escherichia coli is the most widely studied prokaryotic organism [Blount, 2015]. Yet, for about two-thirds of its genes no regulatory mechanisms are known [Santos-Zavaleta *et al.*, 2019] and one third of the genes are without a functional annotation [Gao *et al.*, 2018]. This lack of understanding slashes the likelihood of the bottom-up prediction of the system behavior in response to stimuli. Alternatively, rather than trying to describe all steps in the process of response, one can try to focus on the higher-level of the organization or a macroscopic observable – such as the rate of population growth – that shows a distinct response to the environmental change.

One of the most fundamental properties of bacteria is their ability of autocatalytic growth. As F. Neidhardt fascination (*. . . the liquid in the flask progressed* [. . .] *to a milky whiteness thick with the stuff of life.* [Neidhardt, 1999]) shows, the ability to rapidly manufacture copies of themselves directly results in the perfect manifestation of the equation $\mathrm{d}N/\mathrm{d}t = \lambda N$, leading to an exponential increase in the number of bacterial cells $N = N_0 \exp(\lambda t)$, where N_0, t, and λ are the initial number of cells, time, and growth rate, respectively.

The growth rate imposes a remarkable requirement: every cell constituent has to (on average) double every doubling. While this might seem as an obvious consequence and at danger of circular reasoning, it instills a notion of coupling between the growth rate and regulation of cellular components. Essential non-structural components of the cell either support the supply of building blocks (*e.g.*, amino acids, nucleotides) or synthesize new cell components from the supplied building blocks. Thus, a plethora of supply-and-demand relationships exists within the bacterial metabolism. Even more, these relationships and pertaining components are all put into the context of biophysical (*e.g.*, diffusion rates, enzyme kinetics, *etc.*)

and physiological constraints.

These constraints also underlie a still under-appreciated issue of synthetic biology: the latter holds the promise of predicting the behavior of synthetically-engineered genetic circuits, but sometimes fails to faithfully describe the behavior of the system [Arkin and Fletcher, 2006]. The often-mentioned reason for discrepancies is the failure of the insulation of synthetic circuitry from the host physiology [Kwok, 2010]. This context-dependence arises from sharing expression machinery (*e.g.*, ribosomes, polymerases, *etc.*) and other resources [Andrianantoandro *et al.*, 2006]. Without a comprehensive mechanistic understanding of these impacts, the rational design of genetic circuitry will remain difficult to achieve. Yet, these constraints also offer an opportunity to facilitate understanding of global effects on gene expression [Klumpp *et al.*, 2009].

It is illustrative to consider gene expression in the scope of Francis Crick's central dogma of molecular biology [Crick, 1970], which describes the flow of information between basic "units" of molecular biology (Fig. 1.1). DNA can serve as a template

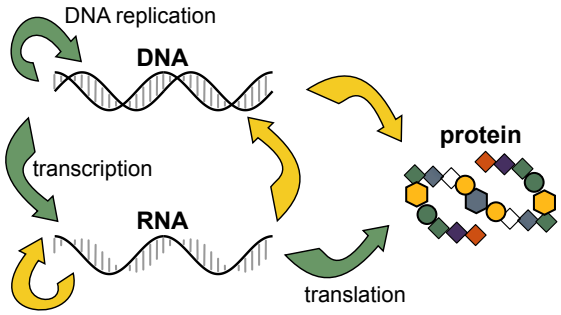

Figure 1.1: **The central dogma of molecular biology.** It describes the direction of information transfer between DNA, RNA, and protein. The information cannot be recovered from protein back to the DNA or RNA. Green and yellow arrows indicate general and special information transfers, respectively [Crick, 1970].

to make an identical copy of it or the DNA-encoded information can be transferred into RNA in the process of transcription. From there, information is translated into a protein. Information "stored" in protein cannot be recovered back into RNA or DNA anymore. This is a consequence of different information encoding through sequences of nucleotides or amino acids in nucleic acids (DNA, RNA) or proteins, respectively. There are special information transfers (achieved *in vitro* or in specific organisms) in which RNA can serve as a template for RNA replication (occurs in certain viruses), or can be reverse-transcribed to DNA. There were even successful attempts to

translate single-stranded DNA directly to protein [McCarthy and Holland, 1965; Uzawa *et al.*, 2002]. Central dogma only describes the direction of information transfer (Fig. 1.1). Rate of information transfer from DNA over RNA into protein, however, will directly depend on the abundance of the template and transfer machinery, as well as the efficacy of the latter [Hausser *et al.*, 2019; Klumpp *et al.*, 2009]. When these vary, global changes in gene expression are inevitable, leading to a profound alteration of the macroscopic biochemical composition of the bacterial cell.

1.1 Growth rate-dependent effect on gene expression

Global changes in cellular composition were actively investigated in the context of the growth rate. Copenhagen school of bacterial physiology, led by Ole Maaløe and inspired by Jacques Monod's work, was spearheading the research of the interplay between macroscopic composition of bacterial cells and the growth rate. Studies at the Institute of Microbiology (founded by Maaløe) spurred not only the observations we discuss below but also a school of researchers asking *"How fast?"*, *"How many?"*, and *"How long?"* which led to the quantitative investigations of bacteria as integrated systems [Andersen *et al.*, 2006]. A remarkable number of experiments showed that many cellular parameters largely depend on the growth rate, rather than the exact composition of the growth medium.

Examples of these growth-rate dependent parameters are the cell size and gross chemical compositions (protein, RNA, DNA, carbohydrates, and lipid) [Bremer and Dennis, 1996; Neidhardt, 1999]. Additionally, more specific parameters (*e.g.*, a fraction of active RNA polymerase synthesizing ribosomal and transfer RNA or fraction of the proteome corresponding to ribosomal proteins) vary with the growth rate in a monotonic manner. Yet, some parameters seem to reach saturation above a certain growth rate and remain constant over a range of growth rates (*e.g.*, time to replicate the chromosome). Finally, some parameters are a direct physical consequence of growth – such as an apparent increase in "degradation" due to dilution by growth.

Many dependencies are necessities of rapid growth; for example, *E. coli* can

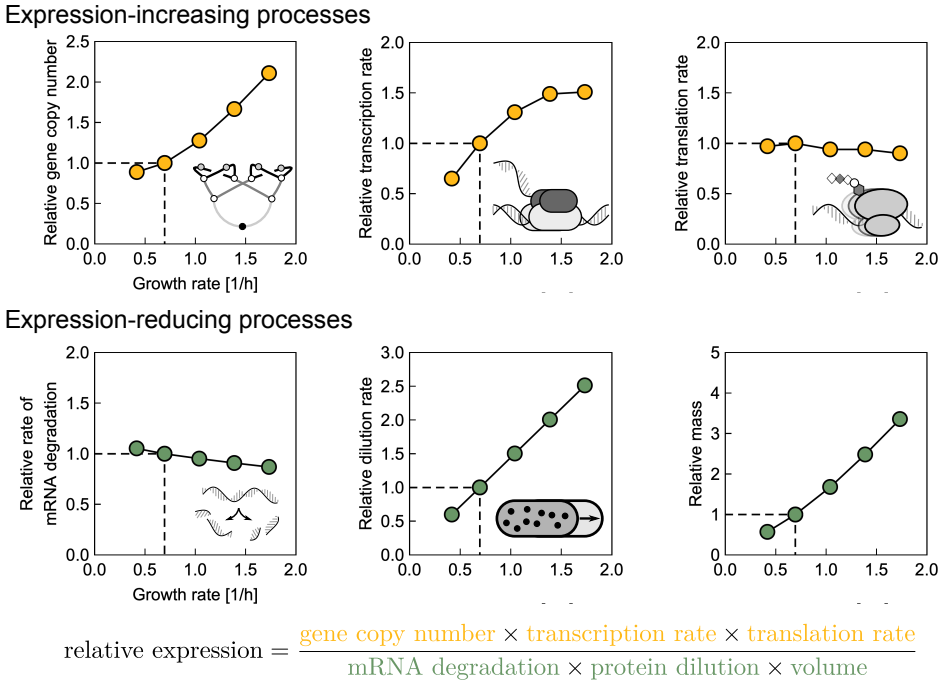

Figure 1.2: **Growth rate dependencies of global cell parameters.** Determinants of gene expression are globally altered and affect the expression of all genes, regulated or constitutively expressed, grouped relative to their effect on the expression. All dependencies were normalized to their value at one doubling per hour. Data from [Klumpp *et al.*, 2009; Bremer and Dennis, 1996]. Bottom: Equation that connects relative gene expression to global parameters.

double every ≈20 minutes, yet the minimal time required for replication of a chromosome is around 40 minutes. In *E. coli*, this apparent problem is resolved by multiple replication rounds that are initiated from the chromosome that is still being replicated [Cooper and Helmstetter, 1968]. In turn, this directly leads to an increase in the DNA content per cell and an additional difference in the gene copy number based on the chromosomal location [Schmid and Roth, 1987]. Moreover, the synthesis of proteins directly correlates with how quickly bacteria can grow. At growth rates above $\approx 1\,\mathrm{h}^{-1}$ translation rate per ribosome saturates at 16-17 aa/s [Dai *et al.*, 2016]; therefore, bacteria can increase protein synthesis only by increasing the number of ribosomes and the fraction of those that actively synthesize proteins.

A basic unit that illustrates the remarkable impact of global changes in physiological parameters on gene expression is a constitutively expressed gene: as it lacks dedicated regulation, the differences in its expression can only arise due to

the global changes [Wanner *et al.*, 1977]. A model that takes into account growth rate-dependencies of the gene copy number, transcription and translation rates, and rates of transcript and protein removal, shows an approximately linear decrease in proteome fraction corresponding to the constitutively expressed gene [Klumpp *et al.*, 2009]. Experimental confirmation of these observations shows the challenge of attributing the dependence to any parameter alone – while some parameters might increase, decrease, or remain constant, but it is the combination of all contributions that matters.

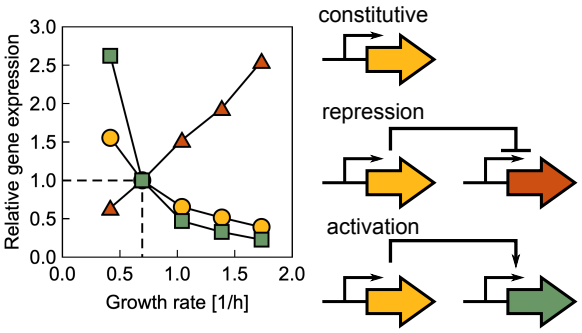

Figure 1.3: **Interdependence of growth rate and gene expression.** As the global physiological parameters change with the growth rate, the expression of the gene is changed. The expression of a gene changes even in the absence of specific regulation. In the case of repression and activation, the dependence is further altered. Shown plots are recalculated from Ref. [Klumpp *et al.*, 2009].

For regulated genes, these effects become even more apparent. Even though there is a regulation (*e.g.*, a repressor that inhibits the expression), the expressions of both genes are under the influence of global effects (Fig. 1.3). Constitutively expressed activator leads to an increasingly nonlinear decrease of expression of the activator-regulated gene (Fig. 1.2). On the other hand, the expression of the repressor-regulated gene intricately depends on the specifics of the regulatory function that describes the repression and can result in a decrease or increase of expression with the growth rate (Fig. 1.2). As homeostasis is often required, a growth rate-independent expression is sought. Including negative autoregulation in the circuit (in which repressor inhibits own expression) decouples the expression from the growth rate [Klumpp *et al.*, 2009; Savageau, 1974]. Growth rate-dependent effects also shift the bistable regions of bistable circuits (*e.g.*, autoactivator or toggle-switch). This illustrates that unexpected behavior of a circuit (*e.g.*, absence of the bistability) might simply result from global feedbacks overriding the "hardwired" topology of

the circuit [Tan *et al.*, 2009; Klumpp *et al.*, 2009].

A gene can, when expressed, either stimulate or hinder growth (*e.g.*, as toxins [Keren *et al.*, 2004]). For example, if a toxin (*e.g.*, metabolic inhibitor) is constitutively expressed (*i.e.*, its expression decreases with the growth rate), this could lead to growth bistability (Fig. 1.4): slower growth results in more toxin expressed which in turn leads to stronger inhibition. Such feedback creates a possibility for the existence of heterogenous population containing a mixture of growing and non-growing cells [Klumpp *et al.*, 2009]. Feedbacks that spur from the interdependence of gene expression and growth might underlie persistence [Keren *et al.*, 2004], for example, and could shape the answers to many ecological, evolutionary, and physiological puzzles.

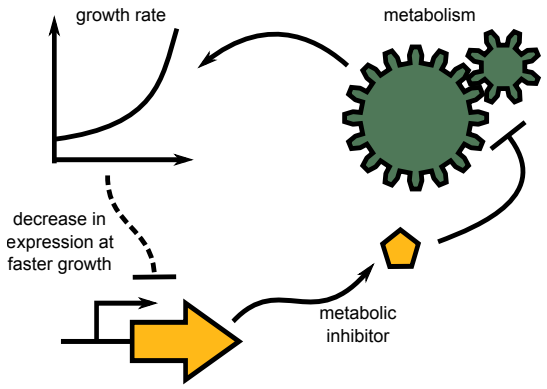

Figure 1.4: **Interdependence of gene expression can lead to growth bistability.** Positive feedback forms as the expression of metabolic inhibitor decreases with the growth rate. When the latter decreases, the inhibitor's expression increases and the growth rate decreases further, completing the feedback.

This leads to an important consequence: the rate of bacterial growth results from the combined efficacy of all growth-required types of machinery replicating bacterial components. This in turn determines the utilization of both intra- and extracellular resources (*e.g.*, nutrients). Bacteria have evolved various mechanisms that keep the physiology running smoothly, ranging from intricate feedbacks to sensors that provide inputs required for the adjustments of the gene expression [Jun *et al.*, 2018]. However, not all systems that require altered response have a dedicated regulation that would optimally adjust the physiological state to match the change in the environment. Here, an optimal response is largely a matter of definition and can range from growth maximization to long-term survivability.

Non-optimality of the response is especially apparent when the regulation

is lumped into a single or a few regulatory elements (*e.g.*, transcription factors, metabolites, ...) that regulate multiple processes. Such regulatory architecture allows for a lean regulation, yet it can only respond to changes in a approximate fashion [Kochanowski *et al.*, 2017], which can be non-optimal (*i.e.*, there might exist a regulatory strategy in which the molecular machinery would be better utilized). Yet, in evolutionary terms, this "good enough" regulation is likely sufficient in the long term and thus preserved. Challenging the regulation with diverse stresses, especially the ones perturbing the essential processes, or variations in the environment allows the inference of regulatory strategies and hence offers a deep insight into the physiological and evolutionary constraints that continue to shape the biology of bacteria.

1.2 Growth laws

Systematic studies of dependencies of a particular parameter on the growth rate led to the establishment of the bacterial growth laws [Jun *et al.*, 2018; Scott and Hwa, 2011]. Growth laws are mathematical relations that formalize these dependencies. One of the first growth laws was the nutrient growth law, which describes the exponential dependency of cell size on the growth rate [Schaechter *et al.*, 1958]. Cooper and Helmstetter derived the expression for the average amount of DNA per cell [Cooper and Helmstetter, 1968]. Donachie later introduced the concept of the initiation mass, *i.e.*, a new round of replication is initiated when protein mass per replication origin exceeds a certain threshold [Donachie, 1968]. This together allowed prediction of the cellular composition even in the absence of exact knowledge of molecular details. What is particularly remarkable is the fact that the underlying molecular regulation is strikingly complex, yet these relations occur robustly and in a simple mathematical form.

1.2.1 Translation and the growth laws

A growth law that is of high importance for this thesis is describing the abundance of the translation machinery. Ribosomal protein fraction ϕ_R increases linearly with the growth rate when the latter depends on the nutrient quality [Schaechter *et al.*, 1958; Bremer and Dennis, 1996; Scott *et al.*, 2010]

$$\phi_R = \phi_{R,\min} + \frac{\lambda}{\kappa_t'}, \tag{1.1}$$

where $\phi_{R,\min}$ and κ_t' are empirical parameters describing the minimal fraction of ribosomal proteins (when $\lambda \to 0$) and κ_t' is the translational capacity, respectively (Fig. 1.5; [Scott *et al.*, 2014]). Due to the centrality of this relationship, it is insightful to derive the meaning of the parameters. To note: protein fractions can be converted into concentrations, which is useful for modeling in later chapters [Scott *et al.*, 2014; Greulich *et al.*, 2015; Klumpp *et al.*, 2013].

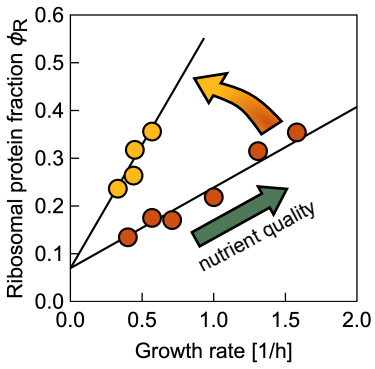

Figure 1.5: **Increase in the ribosomal protein fraction.** Red circles show an increase in ϕ_R [Eq. (1.1)], when the growth rate is varied by the nutrient quality (green arrow). However, when the experiment is repeated using a strain with genetically perturbed translation, the slope is increased. Data from Ref. [Scott *et al.*, 2010].

This growth law arises from the mass-balance of autocatalytic growth. As the abundance of every cell constituent increases exponentially, it follows that $\mathrm{d}M/\mathrm{d}t = \lambda M$, where M is total protein mass. Because proteins are made by actively-translating ribosomes, it follows that

$$\lambda M = k\,(N_R - N_{R,\min})\,, \tag{1.2}$$

where N_R and $N_{R,\min}$ are the total number of ribosomes and the number of ribosomes not actively translating. The latter are ribosomes in search of the ribosome-binding sites on mRNA and ribosomes being recycled or waiting for the charged tRNA. Because components of translation are co-regulated, we assign all these auxiliary

proteins and ribosomal proteins into ribosomal protein mass m_r. Then, because $M_r = N_R m_r$ we can rewrite Eq. (1.2) into Eq. (1.1). Translational capacity is proportional to the protein translation rate, as $\kappa_t' = k/m_R$. This also puts a bound on how quickly bacteria could grow: By setting $\phi_R = 1$ and $\phi_{R,\min} = 0$, and noting that ribosomal proteins together contain 7,336 amino acids [Scott *et al.*, 2010; Bremer and Dennis, 1996] and the maximal elongation rate is around 20 amino acids per second, this yields a doubling time of around six minutes. Additionally, this implies that if translation is perturbed (lower k) the relation Eq. (1.1) will result in a steeper slope (Fig. 1.5) [Scott *et al.*, 2010].

This consideration assumes that the supply of the building blocks matches the demand. The supply is facilitated by metabolic proteins, whose combined mass is M_p. Yet, every cell can allocate only a particular fraction of the proteome to the translation and metabolic proteins. The allocation of the proteome depends on the efficacy of individual components in support of growth. On the other hand, there exists a constant fraction of the proteome, allotted to housekeeping proteins [Scott *et al.*, 2010]. Thus, in this simplified case, we have one fixed fraction and the two variable fractions. In the limiting case, the whole growth-dependent fraction is allotted to translation machinery – we denote this limiting value as $\phi_{R,\max}$. This value is a maximal "dynamic range" of proteome allocation, *i.e.*, $\phi_{R,\max} = \phi_R + \phi_P$, where $\phi_p = M_p/M$.

We can illustrate the implication of this constraint by a short derivation [Scott *et al.*, 2014]. If we assume that growth rate is proportional to the supply of the building blocks, we note

$$\frac{\mathrm{d}M_z}{\mathrm{d}t} = J_{z,\mathrm{in}} - \Theta\frac{\mathrm{d}M}{\mathrm{d}t}. \tag{1.3}$$

Here, M_z, $J_{z,\mathrm{in}}$, and Θ are the mass of a limiting building block, supply rate, and fraction of the building block usage in the growth of biomass. Normalizing by the total mass M and considering the chain rule we arrive at

$$\frac{\mathrm{d}z}{\mathrm{d}t} = \frac{J_{z,\mathrm{in}}}{M} - \frac{1}{M}\frac{\mathrm{d}M}{\mathrm{d}t}\left(\Theta + z\right), \tag{1.4}$$

where $z = M_z/M$. Because the mass fraction of a "free" building block is much smaller than the frequency of its usage (*i.e.*, $z \ll \Theta$), this leads to $\lambda = J_{z,\mathrm{in}}/(\Theta M)$ [Scott

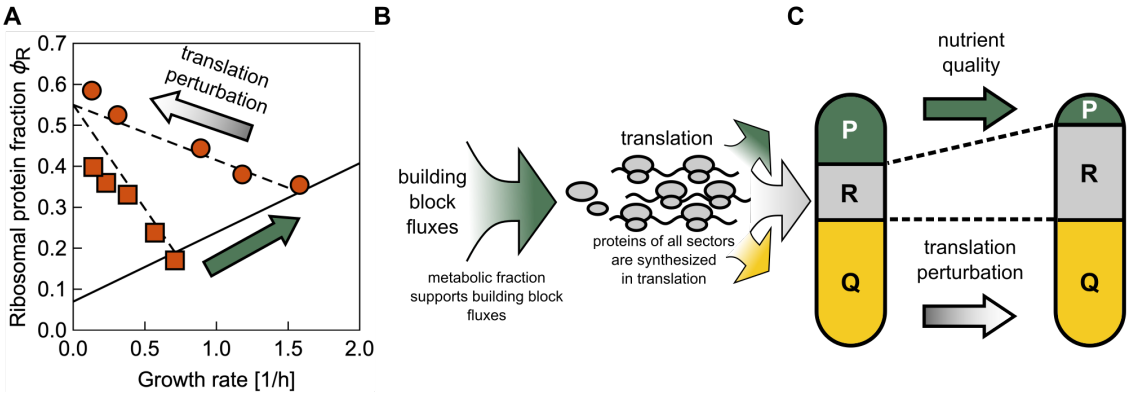

Figure 1.6: **Second ribosomal growth law. (A)** Perturbations of translation at a fixed nutrient quality result in another linear dependence of ribosomal protein fraction ϕ_R (dashed lines). Increasing the nutrient quality (green arrow), results in a decrease in the slope of the response. Data from Ref. [Scott *et al.*, 2010]. **(B)** Supply-and-demand chain: metabolic fraction processes nutrients into building blocks, which are consumed by translation. Translation synthesizes proteins from metabolic, ribosomal, and housekeeping fraction. **(C)** Partitioning of the proteome. Beside a fixed housekeeping fraction (Q), two proteome fractions, metabolic and ribosomal (P and R, respectively) are adjusted according to the efficiency of translation and quality of nutrients.

et al., 2014]. We can express $J_{z,\text{in}} = k_z \Gamma_z M_p$, where Γ_z and k_z are the fraction of metabolic proteins of the pathway that provides the building block z, and the corresponding rate, respectively. Noting the definitions above, we arrive to

$$\begin{aligned} \lambda &= \frac{k_z \Gamma_z}{\Theta} \left(\phi_{R,\max} - \phi_R\right) = \\ &= \kappa'_n \left(\phi_{R,\max} - \phi_R\right), \end{aligned} \tag{1.5}$$

which is the second ribosomal growth law. Empirical parameter κ'_n is termed nutritional capacity. This law is observed if the growth rate is varied by translation perturbations. Variations of the growth rate by translation perturbation or by the quality of the nutrients are orthogonal to one another as they reveal different parameters governing proteome allocation.

The growth laws together [Eqs. (1.1, 1.5)] give rise to a smooth, Michaelis-Menten relation for the growth rate that depends on both translational and nutritional capacities [Scott *et al.*, 2010]:

$$\lambda = \left(\phi_{R,\max} - \phi_{R,\min}\right) \times \frac{\kappa'_n \kappa'_t}{\kappa'_n + \kappa'_t}. \tag{1.6}$$

Importantly, if we fix the translation capacity κ'_t in Eq. (1.6), the function becomes identical to the Monod equation describing the growth dependence on nutrient availability. Here, however, the expression describes the nutrient quality rather than its availability and reflects the amount of resources the cell has to allocate towards metabolism. Namely, low κ'_n corresponds to poor quality of nutrients and extensive proteome allocation towards metabolic pathways.

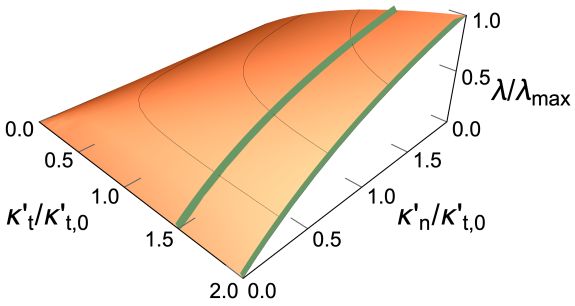

Figure 1.7: **Dependency of the growth rate on translation and nutritional capacities.** Growth rate changes smoothly as the capacities are varied. Here, we normalized the capacities with respect to wild-type translational capacity $\kappa'_{t,0}$. Shown are two examples (green) change in the growth rate as we vary the nutritional capacity, resulting in a Monod-like dependency.

1.3 Growth-variations reveal trade-offs in physiology

Identification of orthogonal (distinct) modes of growth variation by perturbation of individual growth-supporting modules is crucial in the identification of regulatory schemes. As these can be challenging to identify purely by genetics, chemical means can be of use. Similarly, as the variation of a nutrient quality revealed the linear upregulation of translation machinery, orthogonal means of growth variation can validate the proteome allocation postulate at and beyond a two sector model.

Proteome partitioning offers a direct prediction for growth decrease due to protein overexpression. Overexpressed protein causes the dynamic range $\phi_{R,\max} - \phi_{R,\min}$ to shrink as if a fixed fraction would increase [Scott *et al.*, 2010]. The theory from above [Eq. (1.6)] would suggest that the growth rate would linearly decrease with shrinking amount of the proteome available for allocation towards the metabolic and translation sector. This reasoning also offers a testable hypothesis about the growth under a protein overexpression, since the latter does exactly that [Scott *et al.*, 2010]. Indeed, this hypothesis has been experimentally confirmed; importantly, the

prediction required no free parameters.

The metabolic sector can be further refined by imposing different orthogonal perturbations of growth. Limiting catabolism or anabolism by genetic or chemical means [You *et al.*, 2013; Hui *et al.*, 2015] reveals a similarly constrained subpartitioning within the metabolic sector. This observation led to the putative coarse-grained metabolic regulation scheme in which pools of α-ketoacids and amino acids act as the "gauge" of the cell state and serve as inputs that govern the proteome allocation [You *et al.*, 2013; Hui *et al.*, 2015].

1.4 Molecular details of translation

Protein synthesis – translation – is the basis of gene expression. Translation as a central part of cellular machinery is both component- and resource-demanding [Scott *et al.*, 2010; Li *et al.*, 2014]. Yet, bacterial translation is also a very efficient system as it can incorporate close to twenty amino acids every second into a nascent peptide chain. With its plethora of components and constraints, translation presents a remarkable evolutionary achievement that is shaped by different evolutionary pressures as is, for example, a eukaryotic translation, which is four-times slower [Olofsson *et al.*, 1987]. Even more strikingly, bacterial translation is remarkably precise as it incorporates a wrong amino acid between 5×10^{-5}-3×10^{-3} per correct one (BioNumbers 107702), which depends on specific codon context and is comparable to the errors in transcription [Traverse and Ochman, 2016]. Below we briefly describe the main components of translation, constraints under which it operates, and underlying regulation that together allow translation to achieve these remarkable features.

1.4.1 The ribosome

The main macromolecular machine of translation is the ribosome. It is composed of two subunits (small and large, denoted as the 30S and 70S, respectively, where "S" stands for Svedberg sedimentation unit). Both subunits are composed of RNAs and proteins, thus making the ribosome a ribonucleoprotein complex [Rodnina

et al., 2011]. In *E. coli*, smaller subunit contains 1,542 nt long 16S rRNA (ribosomal RNA), whereas the 50S contains 2,904 nt 23S and 120 nt 5S rRNA. Ribosomal RNAs contain catalytic centers for peptide bond synthesis, mRNA hybridization, and provide a structural scaffold for the binding of ribosomal proteins [Rodnina *et al.*, 2011]. Ribosomal proteins (in *E. coli*, 22 and 34 in a small and large subunit, respectively [Arnold and Reilly, 1999]) stabilize the structure of the ribosome and aid the catalysis of processes. Evolutionary speaking, this together suggests that the ribosome ancestor has emerged first as a ribozyme: a complex of RNAs that catalyzed reactions of primitive protein synthesis [Noller, 2014; Petrov *et al.*, 2015].

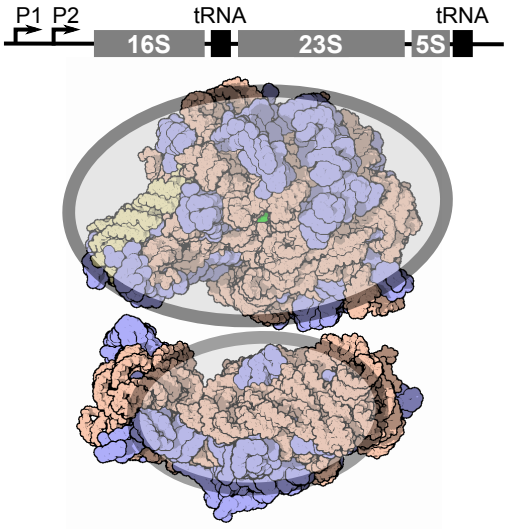

Figure 1.8: **Ribosomal RNA operon and the ribosome.** Top: Schematic structure of the *rrn* operon. Indicated are the position of tRNAs (for general operons, exceptions are described in the text), organization of promoters (P1 and P2), and order of rRNA genes. Bottom: Molecular details of ribosomal subunit arrangements of r-proteins (blue) and rRNA (orange and yellow). Peptidyl transferase center is highlighted in green. Structure from Protein Data Bank, https://pdb101.rcsb.org/motm/10.

The ribosome is a bulky molecular complex with a mass of ≈2.7 MDa [Yamamoto *et al.*, 2006] and volume between $3-4\times10^3$ nm^3 [Zhu *et al.*, 1997]. In turn, this means that while at rapid growth around 5% of the cell volume is occupied by ribosomes, they represent nearly one-third of the dry mass. The composition of a ribosome is additionally considered to be optimized for autocatalytic production and fast growth [Reuveni *et al.*, 2017; Kostinski and Reuveni, 2020]. A mathematical model explains why it is beneficial for autocatalytic growth to partition protein fraction of a ribosome into many short peptides while keeping two-thirds of the mass in only three long rRNAs [Reuveni *et al.*, 2017]. Additionally, mathematical analysis demonstrates that the proportion of ribosomes making other ribosomes is simply equivalent to the fraction of the proteome allotted to ribosomes [Scott *et al.*, 2014]. We briefly discuss the regulation that underlies such properties later.

Since ribosomes are two-thirds RNA by mass, the regulation of expression of rRNA is of crucial importance. *Escherichia coli* K-12 has seven rRNA operons *rrnA*, *B*, *C*, *D*, *E*, *G*, and *H*. The *rrn* operon copy number in various bacterial geneomes ranges from a single to fifteen copies [Acinas *et al.*, 2004; Gyorfy *et al.*, 2015]. These operons are one of the most highly transcribed regions (accounting for more than half of total RNA synthesis at rapid growth [Kaczanowska and Rydén-Aulin, 2007]) because the production of rRNA is at the core of ribosome biogenesis required for rapid growth. Operons have very similar sequences and overall organization. Ribosomal RNAs are transcribed as a single RNA and processed afterward: they are ordered as 16S, 23S, and 5S. The region between 16S and 23S contains one or two tRNAs, while two operons (*rrnC* and *rrnH*) contain additional tRNAs downstream of 5S. The *rrnD* operon has two 5S genes with tRNA in-between [Kaczanowska and Rydén-Aulin, 2007].

1.4.2 Translation cycle and translation factors

Broadly considered, translation consists of four phases: initiation, elongation, termination, and recycling (Fig. 1.9) [Rodnina, 2018]. Each of these phases is composed of several steps and requires multiple dedicated translation factors. Translation factors catalyze the progression of the ribosome throughout the translation cycle and deliver building blocks required for translation. In principle, we can consider any step that is factor-mediated as regulated and directed. Below we coarsely summarize the main steps in translation.

When translation machinery encounters a pool of mRNAs as templates for protein synthesis, the first step is the "locking" of the mRNA into the small subunit, finding of the start codon, locking of the large subunit into the assembled ribosome, and initiating the elongation. In the process of initiation, two initiation factors (IF1 and IF2) bind to the small subunit, followed by recruitment of another initiation factor (IF3) [Milon and Rodnina, 2012; Rodnina, 2018] and initiator fMet-tRNA^{fMet}, yielding a pre-initiation complex [Milon *et al.*, 2012]. Here, IF2 aids the binding of the initiator fMet-tRNA^{fMet}, whereas IF3 aids with the fidelity of the start-

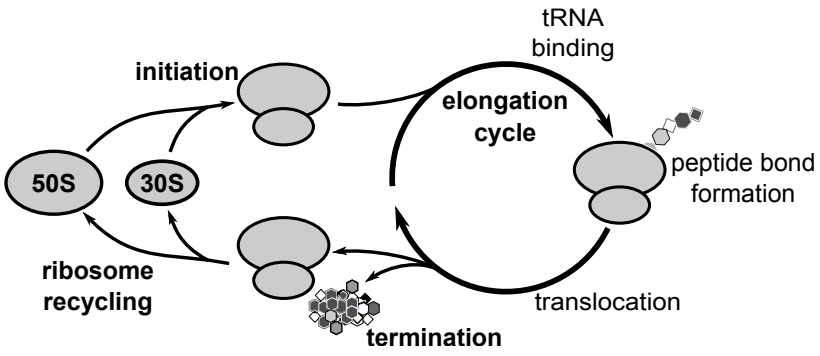

Figure 1.9: **Main phases in translation.** Ribosomes transit through different phases and steps during translation. Main phases (in bold) are composed from a multitude of orchestrated steps (see text).

site selection. Recruitment of mRNA is mediated by the hybridization between Shine-Dalgarno (SD) sequence on mRNA and anti-SD (aSD) on 16S [Duval *et al.*, 2015]. Upon locking the start codon and mRNA, the 30S pre-initiation complex becomes stable 30S initiation complex (Fig. 1.10) and the arrival of the large subunit completes the assembly of the 70S ribosome, which in turn enters into the elongation phase [Rodnina, 2018].

Elongation starts as the second codon becomes available for "reading" by the elongator aa-tRNAs [Rodnina, 2018]. During elongation, the ribosome progresses along the mRNA one codon at the time and sequentially adds corresponding amino

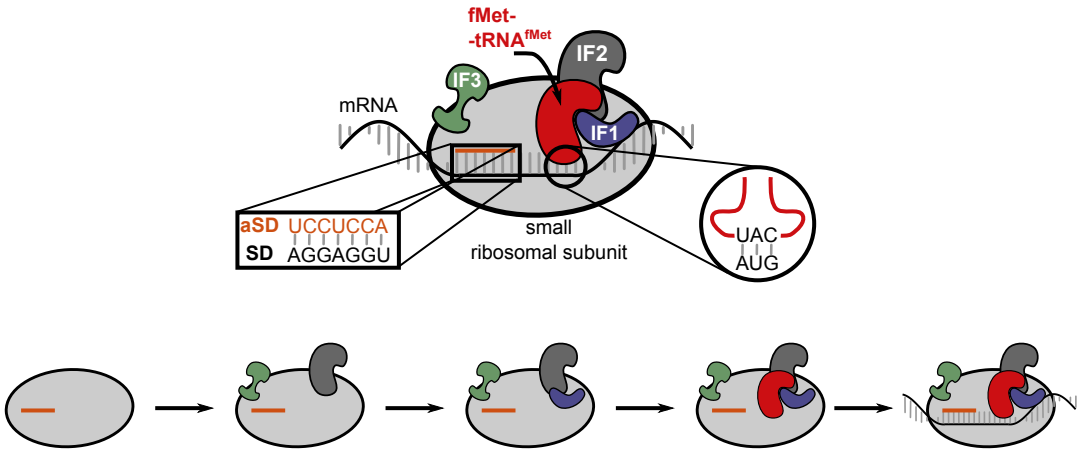

Figure 1.10: **Formation of the 30S initiation complex.** Top: Assembled initiation complex with translation factors and mRNA. The rectangle and the circle highlight the crucial RNA-RNA hybridizations between aSD-SD and start codon-anticodon, respectively. Bottom: Sequence of steps, as per Ref. [Rodnina, 2018]. See text for details.

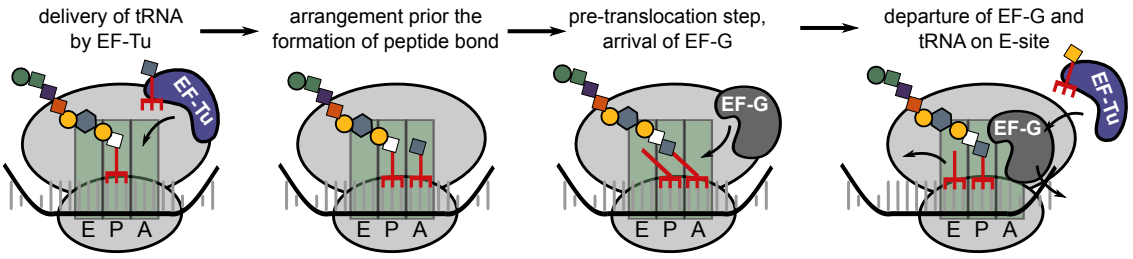

Figure 1.11: **Key steps in elongation.** Schematic shows a typical sequence of events during elongation. Nascent chain (colored chain) is extended by one amino acid. For this to happen, (i) EF-Tu delivers a new amino acid on a cognate tRNA, (ii) peptide bond is formed, (iii) ribosome and all auxiliary parts arrange into the pre-translocation step, (iv) which is followed by translocation and departure of EF-G and tRNA on E-site.

acids to the nascent peptide chain (Fig. 1.11). This process consists of decoding, peptide bond formation, and translocation. Decoding refers to the association of the codon with a correct amino acid. The process is based on Watson-Crick base-pairing of an exposed codon in the A-site and the anticodon of the arriving aa-tRNA (charged tRNA). Charged tRNA is delivered to the ribosome by the elongation factor Tu (EF-Tu) [Nierhaus and Wilson, 2004]. Successful codon-anticodon pairing triggers a complex cascade of conformational and chemical changes in the ribosome and EF-Tu. Notably, the hydrolysis of GTP on EF-Tu after the initial pairing of codon-anticodon represents the irreversible step required for kinetic proofreading initially proposed by Hopfield [Hopfield, 1974]. Kinetic proofreading is an error-correcting mechanism that at the energy expense allows higher accuracy than expected solely on the energy difference between correct or incorrect base pairing of codon-anticodon.

After the hydrolysis of GTP on EF-Tu, the correct amino acid on tRNA on A-site and peptidyl-tRNA on P-site are close together in the vicinity of the peptidyl transferase center (PTC). The active site that catalyzes the reaction is a part of the rRNA of the 50S; the PTC increases the rate of peptide bond formation by 10^7 [Rodnina, 2018; Sievers *et al.*, 2004]. In the process, the nascent polypeptide chain is transferred from P- to A-site tRNA (Fig. 1.11). The ribosome requires no additional translation factor for the formation of the peptide bond; however, long stretches of proline residues or doublets of prolines flanked by specific amino acids cause stalling that is alleviated by non-essential elongation factor P [Ude *et al.*, 2013; Peil *et al.*, 2013].

After a successful formation of a peptide bond, translocation follows during which the ribosome moves (translocates) along the mRNA by one codon further, thus freeing the A-site [Rodnina and Wintermeyer, 2011; Wilson, 2014; Nierhaus and Wilson, 2004]. Likewise, the tRNA on P-site moves onto the E-site (Fig. 1.11). During this process, both tRNAs spontaneously move relative to the large subunit (thus forming a so-called hybrid state). Vacating of P and A sites relative to the small subunit requires an intricate movement of the small subunit that is catalyzed by GTPase elongation factor G (EF-G) [Rodnina and Wintermeyer, 2011]. During the process, small subunit rotates and some of its parts swivel, during which GTP on EF-G is hydrolyzed. After the movement, EF-G is partially inserted into the A-site from which it eventually departs, thus leaving the ribosome ready for a new elongation step (Fig. 1.11).

In the process of elongation, the nascent polypeptide chain extends through the exit tunnel (which is ≈30 amino acids long) and starts to fold partially inside but predominantly outside the tunnel [Rodnina, 2018]. When the ribosome reaches the stop codon, release factors (RF) 1 and 2 recognize it and release the newly made peptide by hydrolyzing the peptidyl-tRNA bond [Rodnina, 2018; Nierhaus and Wilson, 2004]. Another release factor (RF3) catalyzes the release of RF1/2. The reuse of the ribosome requires the release of mRNA and tRNA, which are still within the assembled ribosome. The factor for ribosome recycling (Frr) and EF-G orchestrate the disassembly of the ribosome into individual subunits [Janosi *et al.*, 1994; Janosi *et al.*, 1998; Rodnina, 2018].

1.4.3 Auxiliary enzymes, factors, and tRNAs

Above we briefly discussed the core translation machinery, directly involved in the synthesis of proteins. Yet, the core translation apparatus is blanketed by another set of auxiliary machinery that is involved in the delivery and processing of building blocks, handling of the ribosomes, and processing of newly synthesized proteins. Below we discuss this auxiliary machinery only coarsely.

A crucial element of decoding are the tRNAs. *E. coli* has 79 tRNA genes, with

46 different amino acid acceptor species, coding for 61 sense codons [Dong *et al.*, 1996]. Transfer RNAs, upon delivery to the ribosome by EF-Tu [Nierhaus and Wilson, 2004], are directly involved in the decoding: they bridge the gap between the nascent protein chain and mRNA sequence through codon-anticodon pairing. Correct pairing leads to conformational changes of 30S subunit which affect the GTP hydrolysis by EF-Tu [Rodnina, 2018]. Some tRNA species – isoacceptors – are aminoacylated with the same amino acid but have a different anticodons. The rarity of the codon is also reflected in the level of charging of the respective tRNA. The abundance of charged tRNA corresponding to a specific codon will partially determine how quickly the ribosome can pass over said codon; the rate of the latter are correlated with a rarity of the codon as well [Sørensen and Pedersen, 1991]. The expression of tRNA species, especially for abundant codons, increases with the growth rate, albeit less prominently than the ribosome content [Dong *et al.*, 1996; Bremer and Dennis, 1996]. Additionally, individual amino acids (*e.g.*, serine or cysteine), when internalized, are toxic and this manifests in different charging levels: higher toxicity of the amino acid will correlate with low levels of charging [Avcilar-Kucukgoze *et al.*, 2016].

An important part of decoding starts before charged tRNAs arrive at the ribosome. Charging itself is a very specific process, in which aminoacyl-tRNA synthetases charge tRNAs [Nierhaus and Wilson, 2004]. Synthetases in *E. coli* are encoded by twenty-three genes. With the exception of three synthetases, most are encoded by a single gene [Giegé and Springer, 2016]. A single tRNA synthetase charges different tRNAs with synonymous anticodons, except for methionine and tryptophan which are encoded by only one codon. This remarkable feature is again possible due to kinetic proofreading [Hopfield, 1974]. The charging of tRNA is selective when a particular amino acid becomes limiting [Elf *et al.*, 2003]. Charging is therefore a very intricate process, as both aminoacyl-tRNA synthetases and tRNAs have a highly complex regulation and dynamics, involving multiple different molecular species.

Translation of the ORF begins with the N-Formylmethionine (fMet), which is a derivative of the amino acid methionine [Rodnina, 2018]. It is exclusively used for initiation of translation and is delivered by special initiator $tRNA^{fMet}$ [Guillon

et al., 1993]. While non-formylated methionine can be loaded onto both elongator and initiator tRNA, only when charged onto the latter a dedicated transferase Fmt (10-formyltetrahydrofolate:L-methionyl-tRNA^{fMet} *N*-formyltransferase) attaches a formyl group onto the methionine [Kahn *et al.*, 1980; Guillon *et al.*, 1992]. As the synthesized protein partially exits the ribosome through the tunnel, a peptide deformylase (encoded by *def*), cleaves the formyl group from the N-terminal methionine residue of the nascent chain [Bingel-Erlenmeyer *et al.*, 2008]. Formyl on methionine has been suggested to serve as a cotranslational degradation signal [Piatkov *et al.*, 2015]. Upon removal of the formyl group on the leading methionine, another enzyme methionine aminopeptidase (encoded by *map*) modifies the nascent chain: depending on the first three amino acids downstream of methionine, the latter can be cleaved-off [Ben-Bassat *et al.*, 1986; Frottin *et al.*, 2006; Hirel *et al.*, 1989].

Besides the delivery of the building blocks and processing of finished proteins, various assembly, maturation, stability, modulation, and hibernation-promotion factors affect the ribosome throughout its life cycle. Ribosome assembly and maturation is very complex, as it involves a high number of components that need to be positioned correctly. This issue is particularly pressing for rRNA components, as these tend to form complex and unwanted secondary and tertiary structures through base-pairing that would prevent the formation of a functional rRNA scaffold [Kaczanowska and Rydén-Aulin, 2007]. Therefore, a cohort of RNA chaperons, RNA helicases, and ribosome-dependent GTPases (such as Era [Bunner *et al.*, 2010] or Der [Hwang and Inouye, 2006]) aids the correct folding and assembly, which drives the assembly across the protein-folding landscape and prevents sinking of the folding complex into the so-called kinetic traps [Kaczanowska and Rydén-Aulin, 2007].

1.4.4 Physical constraints

We discussed above some of the molecular details somewhat out of biological context and ignored some of the biological, chemical, and physical details. Most are out of the scope of this thesis; however, some physical limitations directly affect parameters we will later use in the mathematical analysis.

As the ribosomes are loaded onto the transcript, each occupies a certain stretch of codons. Estimates of this "footprint" differ [Kang and Cantor, 1985; Mitarai *et al.*, 2008; Shaw *et al.*, 2003b; Mohammad *et al.*, 2019; Woolstenhulme *et al.*, 2015] but range somewhere between 7-16 codons. This exclusion limits the number of translation rounds that can happen simultaneously. This spatial constraint couples the dynamics of the ribosomes on the same transcript as we will show later.

Another aspect comes from the crowdedness of the intracellular environment. Diffusion of, for example, a 30 kDa protein (*e.g.*, green fluorescent protein) is around ten-times slower in the cytoplasm of *E. coli* compared to water (7.7 $\mu m^2\ s^{-1}$ versus 87 $\mu m^2\ s^{-1}$, [Elowitz *et al.*, 1997; Swaminathan *et al.*, 1997; Milo and Phillips, 2016]). Thus, bulky proteins have to "navigate" through crowded cytoplasm, which can limit the rapidity of processes they catalyze [Klumpp *et al.*, 2013]. This aspect can additionally emphasize the differences between experiments performed at more sparse *in vitro* experimental conditions compared to the observations in the *in vivo* observations.

1.4.5 Regulation

To counter various constraints, minimize the costly expression of translation machinery, and meet the requirements of rapid growth, a translation regulation has evolved. Yet, as noted earlier, gene expression is driven by both global effects and topology of genetic regulatory circuitry.

During the fast growth, copies of *rrn* in the cell will exceed native seven due to multiple simultaneous replication rounds (Fig. 1.12 [Bremer and Dennis, 1996]). This effect is even more pronounced as the *rrn* operons tend to cluster around the origin of replication. Cooper-Helmstetter relation [Cooper and Helmstetter, 1968;

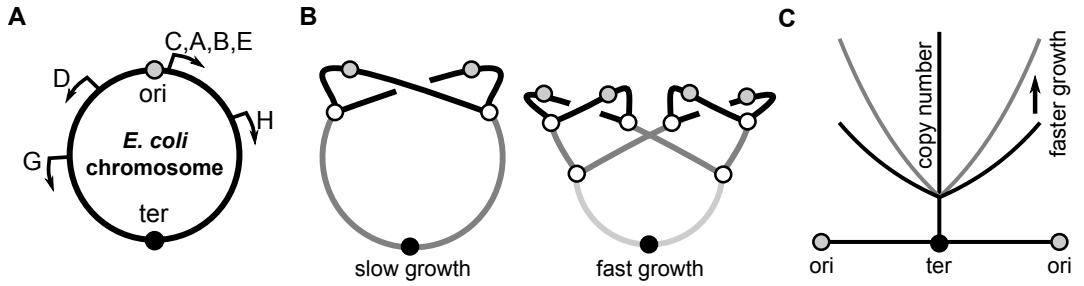

Figure 1.12: **The expression of ribosomal constituents has a physical limit. (A)** The *E. coli* chromosome contains 7 *rrn* operons, which are all oriented at the direction of replication and mostly centered in the vicinity of the *ori*. **(B,C)** Due to growth rate-dependent gene copy number, relative gene expression is increased when growth is faster and depends on the gene location on the chromosome [Cooper and Helmstetter, 1968; Schmid and Roth, 1987].

Bremer and Churchward, 1977], which mathematically describes the dependency of chromosomal gene copy number on the growth rate, allows us to estimate the increase in effective copy number to ≈35.9 [Bremer and Dennis, 1996], thus exceeding the copy number per chromosome by more than five times. This suggests a likely existence of a feedback regulation that curbs the tentative overexpression of *rrn* operons. Conversely, when operons are deleted, the expression from the remaining ones is increased [Condon *et al.*, 1993]. When the number of translating ribosomes is reduced by lowering the amount of initiation factor 2, upregulation of *rrn* operons is observed, indicating that the feedback is (at least in part) coupled to the number of translating ribosomes [Cole *et al.*, 1987]. Taken together, these considerations support the existence of feedback regulation, albeit it is less clear to what extent the regulation of *rrn* operons is active and to what extent passive.

The expression of each *rrn* operon is controlled by two promoters, P1 and P2 (Fig. 1.13) [Condon *et al.*, 1995]. Promoter P1 is most active during fast growth, while P2 tends to overtake at lower growth rates [Kaczanowska and Rydén-Aulin, 2007]. Upstream of both promoters are FIS binding sites (two of which overlap with binding sites of H-NS DNA-bending protein that counters the action of FIS), and a UP element (another is between P1 and P2) [Kaczanowska and Rydén-Aulin, 2007; Condon *et al.*, 1995]. The UP element enhances binding of RNAP by interacting with α-subunit of RNAP. Discriminator (Fig. 1.13) sequence is essential for stringent

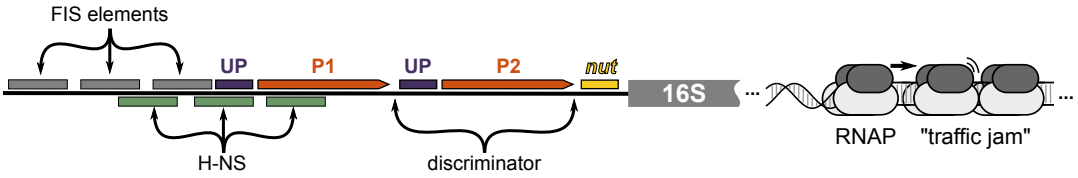

Figure 1.13: **Details of the regulatory region of ribosomal RNA operons.** Regulation of *rrn* operons involves multiple transcription and regulatory factors. Additionally, operons are regulated by two promoters of a different character. Since *rrn* operons are one of the most highly transcribed chromosomal segments, traffic jams can form.

response, which we describe below. Additionally, there is an antiterminator sequence *nut* downstream of P2 and in spacer regions between 16S and 23S: antitermination allows for enhanced transcription of the operons, reflected in a decreased probability of pausing [Vogel and Jensen, 1995]. Due to the dense traffic of polymerases, antitermination becomes even more important as it partially removes the detrimental effects of traffic jams [Klumpp and Hwa, 2008]. Active regulation is highlighted in dynamic changes in the translation requirements, *e.g.*, during the change in the growth environment from rich to poor or *vice versa*.

If bacteria grow in a nutrient-rich environment, cells do not have to synthesize all building blocks (*e.g.*, amino acids) from other compounds. Yet, if the switch to a poor environment happens, a depletion of internal amino acid pools will manifest in the reduced supply of building blocks. When a supply-demand relationship is disrupted, a quick series of events unfolds in which the expression of translation machinery is inhibited [Condon *et al.*, 1995]. This cascade is called the "stringent response." It depends on the charging levels of eight amino acids [Zhang *et al.*, 2006]. This response was directly linked to the aminoacylated-tRNA deprivation, sensed by the RelA protein [Potrykus and Cashel, 2008]. The latter recognizes a stalled ribosome that lacks a codon-specific, charged tRNA on the A-site of the ribosome [Kaczanowska and Rydén-Aulin, 2007]. RelA then uses adenosine triphosphate (ATP) as a source of pyrophosphate and catalyzes the synthesis of (p)ppGpp [guanosine (penta)tetra phosphate] [Cashel and Potrykus, 2001]. Level of alarmone (p)ppGpp is also controlled by SpoT – a bifunctional enzyme with hydrolase and synthetase activities [Cashel and Potrykus, 2001; Potrykus and Cashel,

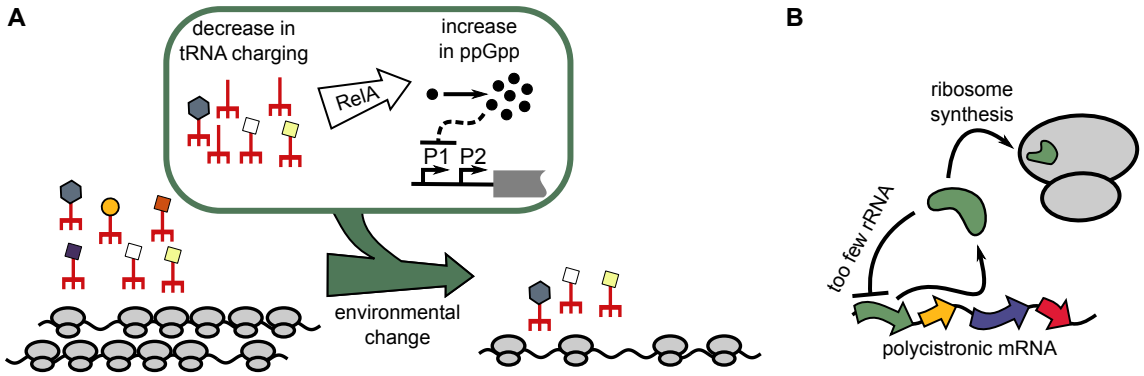

Figure 1.14: **Stringent response and post-transcriptional regulation.** Regulation of *rrn* operons involves multiple transcription and regulatory factors. **(A)** Upon change to an environment poor with nutrients, a decrease in expression of translation machinery takes place. High-level molecular details of *stringent response* are in a box. **(B)** Post-transcriptional regulation of translation-related operons by autogenous feedback regulation. A protein (dark green) binds to its mRNA if there are too few free rRNAs.

2008]. SpoT hydrolyzes (p)ppGpp, thus reducing its intracellular levels, which is important for recovery from the repressed state. During stress, the hydrolase activity is inhibited and consequently increases the levels of (p)ppGpp [Kaczanowska and Rydén-Aulin, 2007]. Increased levels of the alarmone (p)ppGpp lead to intricate changes in the expression of the translation machinery.

The intracellular concentration of (p)ppGpp can increase by more than ten-fold during a stringent response [Kaczanowska and Rydén-Aulin, 2007; Chatterji and Ojha, 2001]. Elevated levels of (p)ppGpp cause the shutdown of transcription from the P1 promoter of *rrn* operons and reduced transcription of tRNA genes [Cashel and Potrykus, 2001; Potrykus and Cashel, 2008]. Alarmone directly affects the activity of RNA polymerase [Bremer and Dennis, 1996] by binding to the vicinity of the active center [Artsimovitch *et al.*, 2004]. Furthermore, ppGpp not only lowers the initiation but also increases the rate of the pausing of RNA polymerase [Kaczanowska and Rydén-Aulin, 2007]. Additionally, ppGpp skews the synthesis rate of RNA towards mRNA rather than stable RNA (tRNA and rRNA) [Dennis *et al.*, 2004]. At very low growth rates, the majority of rRNA comes out of transcription from the P2 promoter. However, it was additionally shown that a strain without *relA* and *spoT* still exhibits growth rate-dependent control of rRNA synthesis described by the growth law [Gaal

and Gourse, 1990]. This suggested that growth rate-dependent control and stringent response use different, but potentially overlapping mechanisms for regulation of rRNA synthesis.

Regulation of the expression of ribosomal proteins further demonstrates the importance of rRNA. There are nineteen operons of ribosomal proteins (r-protein), in which other translation-related genes (EF-G, EF-Tu, EF-Ts, *etc.*) appear together with r-proteins [Kaczanowska and Rydén-Aulin, 2007]. As these genes are transcribed as a part of a polycistronic mRNA, an autogenous feedback regulation controls the expression of the whole operon [Nomura *et al.*, 1984]. Ribosomal proteins have a high affinity for binding to rRNA: when the latter is present in excess, r-proteins bind rapidly to form the ribosome. However, certain r-proteins have additionally a binding affinity to their polycistronic mRNA: when free rRNA is scarce (*i.e.*, r-proteins are overproduced), they will bind to their mRNA and halt its translation. Such autogenous feedback directly couples the expression of rRNA to the rest of translation machinery and keeps the stoichiometry between the ribosome and factors relatively constant (Table 1.1) [Bremer and Dennis, 1996].

Molecule	Number per ribosome
EF-G	0.80-0.83
EF-T	0.18
IF1	0.25
IF2	0.3
IF3	0.2
tRNA	9-13

Table 1.1: **Stoichiometric values of translation factors and tRNA relative to the ribosome.** Values are from Refs. [Bremer and Dennis, 1996; Dai *et al.*, 2016; Dong *et al.*, 1996]. Note, that number of tRNA species per ribosome varies wildly between different tRNAs [Dong *et al.*, 1996].

1.5 Translation perturbations

This compendium illustrates that translation is a highly dynamic process, during which ribosome passes through numerous states in which different factors catalyze

(or prevent) the movements of the ribosome and auxiliary components. Since the process contains numerous steps, it is unclear how perturbation of a specific step affects the kinetics of the whole process, especially in the light of constraints and regulation that intertwine translation-related processes. Many of the aspects of translation that we discussed above were deducted through targeted perturbations of translation. These perturbations can be genetical or chemical. A particular way of perturbing bacterial physiology and translation in particular is by application of antibiotics.

1.6 Antibiotics

Antibiotics are small molecules that inhibit or outright kill bacteria, classifying antibiotics as bacteriostatic or bactericidal, respectively [Walsh, 2003]. A revolution in medicine started with one of the most fruitful laboratory mishaps – Fleming's accidental discovery of penicillin [Tan and Tatsumura, 2015; Fleming, 1929]. Together with synthetic sulfonamide drugs, these early antibiotics made many of the previously deadly diseases treatable almost overnight [Aminov, 2010; Walsh, 2003]. Penicillin became one of the most important chemical compounds of the first half of the 20th century, altering a human perception of infections forever. However, it was difficult to produce – best illustrated by the fact that it was recrystallized for reuse from the urine of patients receiving penicillin [Barry, 2004]. Soon after, isolation and the whole manufacturing processes of penicillin and other antibiotics were optimized and industrial production increased quickly to meet the need for antibiotics. As an illustration, mold grown in early fermentors in the 1950s produced only about 0.5-1.0 g/L of penicillin, while nowadays modern techniques allow yields as high as 40 g/L [Elander, 2003]. Such advances made antibiotics affordable (*e.g.*, penicillin price dropped from $300 to $17 per kg in the same period [Elander, 2003]), while a whole new industry was spawned this way. The demand drove the discovery of new antibiotic compounds.

Over the years, many additional different chemicals were discovered, either as products of living organisms or of direct chemical synthesis, that exhibited antibiotic

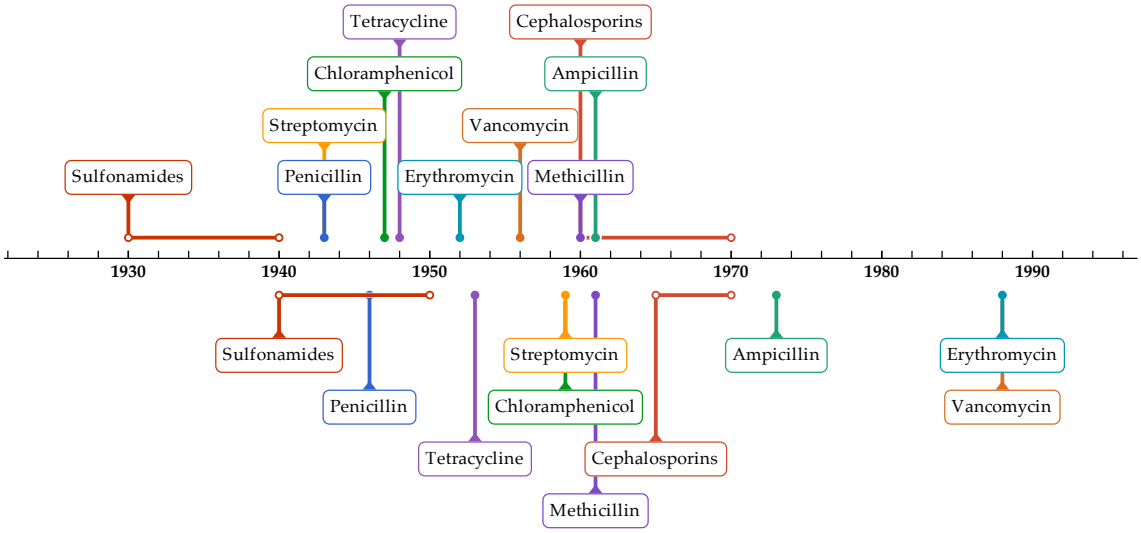

Figure 1.15: **Timeline of antibiotic deployment and the evolution of antibiotic resistance.** Snapshot of the period between 1930s and 1990s; deployment and occurrence of resistance are shown above and below the timeline, respectively. Data from Ref. [Palumbi, 2001].

activity. While certainly a breakthrough, widespread use of antibiotics instilled a high selection pressure for the occurrence of antibiotic resistance [Clatworthy *et al.*, 2007; Palumbi, 2001]. The time between the deployment and occurrence of resistance varies between antibiotics, yet the timeline in Fig. 1.15 illustrates a sobering reality – bacteria seem to exhibit the ability to evolve resistance to any antibiotic compound given sufficient time. While it is unlikely that we will obtain a silver bullet to which bacteria cannot evolve resistance, antibiotics remain a powerful tool in medicine and basic research. It is fascinating that even after a rather long period of extensive use, effects of antibiotics on bacteria remain a fruitful area of research, which uncovers intricate responses and resistance mechanisms in bacteria.

1.7 Antibiotic targets

The antibiotics inhibit crucial cellular processes. Common targets of antibiotics are the essential processes: synthesis of the cell wall, RNA and proteins, DNA replication/modification, and folate biosynthesis (Fig. 1.16). Folate synthesis is crucial for the synthesis of DNA building blocks and other metabolites such as certain amino acids [Dias *et al.*, 2018; Walsh, 2003]. Alternatively, some antibiotics (such as nitrofurantoin) cause a formation of free radicals that damage the cell. The main reason for the efficacy of antibiotics in the treatment of infections lies in the sufficient differences between the physiology of pathogenes and the host. Some of the antibiotic targets (such as the cell wall) do not exist in the host organism, while others [*e.g.*, dihydrofolate reductase (involved in folate synthesis) or a ribosome] are sufficiently different to prevent the binding of the antibiotic in the host.

Antibiotics differ in many aspects besides their mode of action. Antibiotics enter into the cell either passively or actively [Choi and Lee, 2019; Smith and Chopra, 1984; Braun *et al.*, 2001], and can be effluxed out of the cell by dedicated antibiotic

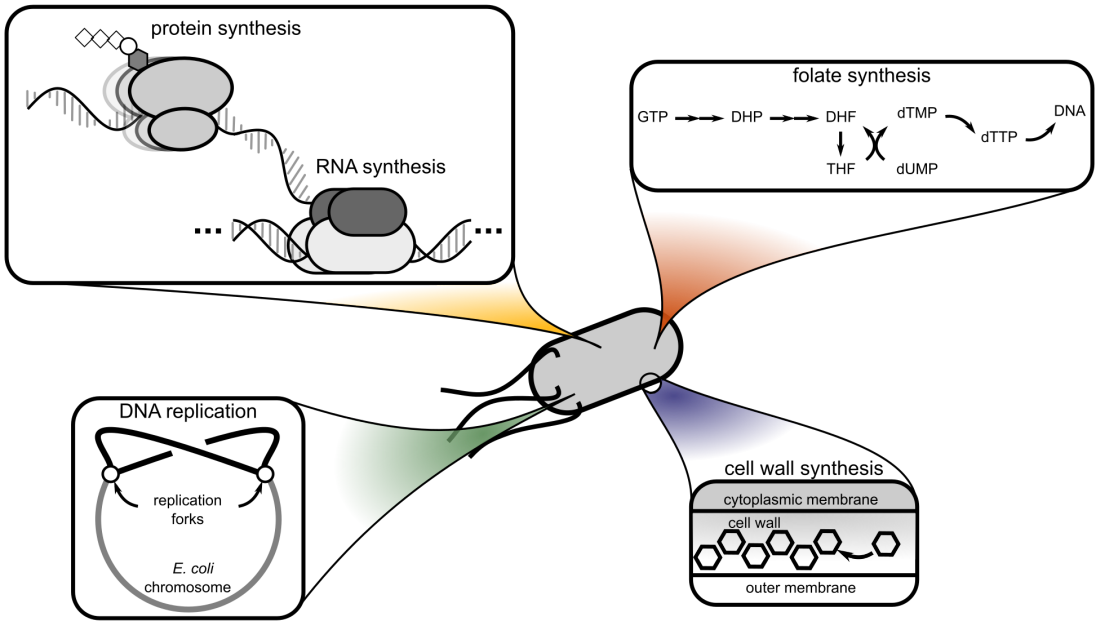

Figure 1.16: **Main antibiotic targets.** Upon entry into the cell, antibiotics inhibit essential cellular processes, pertaining to catabolism (*e.g.*, protein synthesis), metabolism (*e.g.*, folate synthesis), structural (*e.g.*, cell wall synthesis) or replication processes (*e.g.*, DNA replication).

pumps (*e.g.*, multiple efflux pump AcrAB-TolC [Bergmiller, 2017]). Abundances of antibiotic targets per cell also differ significantly, ranging from tens of thousand for ribosomes [Bremer and Dennis, 1996] to a few dozen for gyrases and reductases [Taniguchi *et al.*, 2010]. Antibiotics can act as competitive inhibitors, in which case antibiotic competes with the substrate for binding (*e.g.*, trimethoprim competes with dihydrofolate for binding to the dihydrofolate reductase [Dias *et al.*, 2018; Walsh, 2003]), or can divert metabolic flux of substrates (*e.g.*, sulphonamides covalently bind to the pteridine diphosphate, which cannot be used by the cell [Brown, 1962; Rolland *et al.*, 1979; Palmer and Kishony, 2014]) and drain the pool of essential metabolites. This diversity in details of antibiotic modes of action is further emphasized by the diverse responses to antibiotic-induced stresses.

1.8 Bacterial responses to antibiotics

Bacteria can aptly change their physiology in response to environmental changes. This remarkable flexibility allows bacteria to dynamically alter the expression of genes coding for metabolic pathways, and in turn attempt to match the supply and demand set by the rapid bacterial growth.

Growth rate λ is one of the most important macroscopic parameters that can be measured in the laboratory. Deviations of the growth rate from unperturbed one indicate the irregularities in the core metabolic processes, altered regulatory responses or point towards some genetical change. Thus, precise quantification of the growth rate in the response to antibiotics is a necessary first step towards understanding the effects of antibiotics on bacterial physiology [Neidhardt, 1999].

Measuring the growth rates at various antibiotic concentrations a_{ex} produces a dose-response curve [Chevereau and Bollenbach, 2015; Chevereau *et al.*, 2015; Mitosch and Bollenbach, 2014]. Various attributes can describe the dose-response curve: its steepness, a concentration at which the growth rate is halved (*i.e.*, IC_{50}) or completely inhibited (minimal inhibitory concentration or MIC). Dose-response curves are usually monotonically decreasing, *i.e.*, the growth rate decreases with increasing antibiotic concentration. Various mathematical functions can be used

to describe the dose-response, as long its parameters allow for sufficient flexibility in the shape of the curve. One frequently used mathematical description is a Hill function:

$$\lambda = \lambda_0 \times \frac{1}{1 + (a_{ex}/IC_{50})^n}, \tag{1.7}$$

where n is a steepness parameter. This function quantifies the response with only three parameters, which can be inferred from the measurements. While Hill function

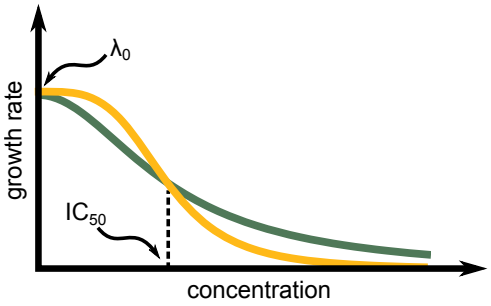

Figure 1.17: **Hill function characterizes typical dose-response curve.** Curves of growth rate-change in the response to an increasing antibiotic concentration can have different steepnesses. Here, shallow and steep response correspond to $n = 2$ and 4, respectively.

offers a very practical way of describing the effect of the antibiotic, it cannot associate the parameters (such as n or IC_{50}) with characteristics of the antibiotic or physiology. Said differently, the mechanistic origins of the specific shape of the dose-response curve are not traced back to molecular and biological details. Yet, – as we discuss later – Hill functions allow comparisons between different antibiotics invariantly of the molecular and physiological origins of the response. Importantly, they formalize the concept of the dose-response curve in a tractable manner and illustrate how antibiotics effects transpire over narrow or wide concentration window (for high or low n, respectively).

Here, antibiotics appear particularly useful as they gradually inhibit essential cellular processes and in turn allow studies of bacterial responses to such perturbations. This adds another dimension to the use of antibiotics in the laboratory – apart from their clinical relevance, antibiotics can perturb cellular functions that are otherwise difficult to probe by classical approaches from genetics (*e.g.*, gene deletions) [Falconer *et al.*, 2011]. Changes in gene expression in response to antibiotic stress are very diverse [Shaw *et al.*, 2003a; Goh *et al.*, 2002]. In some cases, bacteria might simply upregulate the antibiotic target or any auxiliary genes that in turn partially alleviate

the antibiotic effects, *e.g.*, as is the case of protein synthesis inhibitors [Scott *et al.*, 2010; Bennet and Maaløe, 1974; Harvey and Koch, 1980] or under folate synthesis inhibition [Flensburg and Sköld, 1987]. While this reasoning sounds intuitive, recent studies have shown that simple upregulation of the target is rarely sufficient to alleviate the antibiotic action [Palmer and Kishony, 2014; Palmer *et al.*, 2018]. Additionally, as the growth rate is reduced, expression of many genes and physiology of the whole-cell are altered due to global cellular feedbacks [Goh *et al.*, 2002]. The specific and global response intertwine and should thus be considered together [Bollenbach and Kishony, 2011; Lukačišin and Bollenbach, 2019]. Due to these effects, genes that are unrelated to the target or targeted pathway can attribute to the net effect of the antibiotic. Genome-wide studies in which genes are systematically deleted or overexpressed and changes in the response to antibiotics are investigated can identify such effects [Chevereau and Bollenbach, 2015; Palmer *et al.*, 2018; Palmer and Kishony, 2014].

The choice of the measurement technique critically determines the level from which we aim to discern the regulatory responses. High-dimensional, genome-wide datasets are increasingly abundant since the advent of laboratory automatization and affordable sequencing technologies. Strains libraries containing promoter-reporter [Zaslaver *et al.*, 2006] or protein-reporter fusions [Taniguchi *et al.*, 2010] are available and allow investigations of gene expression on both population and single-cell level. Multiplexed sequencing of the transcriptome, for example, allows an insight into the transcriptional intricacies [Lukačišin and Bollenbach, 2019] of responses while proteomic studies directly investigate abundances of individual proteins [Hui *et al.*, 2015]. Furthermore, single-cell studies are becoming increasingly accessible and offer unprecedented insights into bacterial responses to changes in the environment [Wang *et al.*, 2010]. These techniques complement classical and modern approaches from genetics. These approaches together allow quantitative studies of response to antibiotics that reach beyond steady-state response of the batch cultures towards understanding of dynamical responses to antibiotics, single-cell responses and population heterogeneity [Bergmiller, 2017; Deris *et al.*, 2013], and tracking the emergence of evolutionary changes [Tomanek *et al.*, 2020]. In this

regard, these techniques can reveal temporal sequences of responses [Mitosch *et al.*, 2019] and even uncover unexpected pleiotropic effects such as cross-protection to other environmental stresses [Mitosch *et al.*, 2017]. An important and more recent component of the studies of gene expression is inclusion of the mathematical modeling and evolutionary considerations.

1.9 Antibiotic resistance

Apart from changing their gene expression to alleviate the impact of antibiotics, bacteria occasionally become tolerant to antibiotics or acquire antibiotic resistance. The crucial difference between resistance and other means of tolerance is that resistance is a genetically inherited trait. Tolerance on the other hand allows bacteria to survive the transient exposure to antibiotics [Brauner *et al.*, 2016]. Many of known antibiotics are of natural origin and produced by bacteria (predominantly of the genus *Streptomyces*) [Walsh, 2003]. These antibiotic-producing bacteria have self-protection mechanisms; this in turn constitutes a pool of resistance-conveying elements that can be acquired by other organisms.

The most common resistance mechanisms are reduced drug influx, active efflux, target mutation or modification, overproduction of target mimic, factor-associated protection, and drug modification or degradation [Wilson, 2014; Lukačišinova and Bollenbach, 2019]. These mechanisms arise *de novo* from spontaneous mutations or are acquired from another species by the means of mobile genetic elements (*e.g.*, plasmids, bacteriophages,...) in the process of horizontal gene transfer [Frost *et al.*, 2005]. While genetic determinants were cataloged for many of these mechanisms [McArthur *et al.*, 2013], it is still not clear how many of these resistance mechanisms depend on the physiological state of the cell or on the environment [Lukačišinova and Bollenbach, 2019; Gilbert *et al.*, 1990; Brown *et al.*, 1990]. Tracking of resistance evolution dynamics is another area of active research. Tracking of evolutionary dynamics became possible due to recently developed technologies such as next-generation sequencing [Goodwin *et al.*, 2016] or devices for dynamical tracking of evolution, such as morbidostat [Toprak *et al.*, 2012;

Lukačišinova *et al.*, 2020], in which antibiotic concentration is constantly adjusted to keep the selection pressure constant throughout gradual increase in resistance.

Evolutionary trajectories are affected by many factors; however, it was recently shown that the shape of the dose-response curve is one of the crucial determinants [Chevereau *et al.*, 2015]. The latter has proved to be remarkably robust to the genetic perturbations, which mostly rescaled the dose-response curves [Wood *et al.*, 2014; Chevereau and Bollenbach, 2015; Chait *et al.*, 2007]. The dose-response curve relates the distribution of effective concentrations to the distribution of fitness effects arising from mutations [Chevereau *et al.*, 2015]. This in turn highlights the importance of understanding the mechanistic origins of the shape of the dose-response curve.

1.10 Modeling of antibiotic action

Providing a mathematical basis for the shape of the dose-response curve is of fundamental importance for understanding the effect of antibiotics. Connecting the known physiological constraints (*e.g.*, rate of protein synthesis, number of targets,. . .) with biochemical properties of antibiotics (*e.g.*, uptake rate, the dissociation constant of binding,. . .) to yield dose-response curve would isolate the crucial parameters that determine the response. This would consequently formalize the observations and offer predictions for altered physiological and biochemical parameters. With an increasing number of experimental observations, a rising number of unexpected and potentially unintuitive outcomes are establishing mathematical modeling as an integral part of investigations.

Antibiotics that target translation have received the most modeling attention. Antibiotics that bind to the ribosome have a mathematical advantage over certain other targets: ribosomes are relatively abundant compared to other cellular components and due to recently established physiological response to translation perturbation (discussed above). High number of ribosome makes the effects of stochasticity less prominent and can be therefore described in a continuous manner. Dose-response curves for translation inhibitors have been modeled within this

framework in Ref. [Greulich *et al.*, 2015; Elf *et al.*, 2006]. These theoretical models have well defined molecular parameters; yet, if these parameters (*e.g.,* binding constants, antibiotic transport) change due to resistance mutations, these models become useful in understanding of resistance evolution [Deris *et al.*, 2013; Pinheiro *et al.*, 2020].

While the shapes of the dose-response curves are largely unchanged by mutations [Wood *et al.*, 2014; Chevereau and Bollenbach, 2015], certain observations challenge this robustness. In particular, it was demonstrated that when the antibiotic-degrading enzyme was a part of the positive, growth rate-dependent feedback loop, the dose-response curve changed from shallow to steep [Deris *et al.*, 2013]. Moreover, the dose-response curve exhibited a bistable region in which the clonal population branched into two subpopulations with different growth rates, which was observed experimentally. This observation was further supported by a mathematical model that included the intertwining of global effects on gene expression and antibiotic action. We discuss this model further in Chapter 4.

Despite its usefulness, mathematical modeling of antibiotic action is still underutilized. Beside improving the understanding of antibiotic action, mathematical models can help us understand the constraints under which the antibiotic resistance develops and how it integrates into the overall physiological picture [Allen and Waclaw, 2016]. While modeling of antibiotic action for individual antibiotics remains challenging, it is a necessary stepping stone for understanding of combined antibiotic stresses.

1.11 Antibiotic combinations

A particularly promising strategy to increase the efficacy of treatments and curbing rampant antibiotic resistance is the use of more than one antibiotic simultaneously [Bollenbach, 2015; Yeh *et al.*, 2009]. Therapies using combinations of antibiotics sometimes arise out of necessity, *e.g.,* when multiple pathogens susceptible to different antibiotics are present. Here, however, we focus on a question: what is the combined effect of multiple antibiotics on a single strain, and what are the underlying

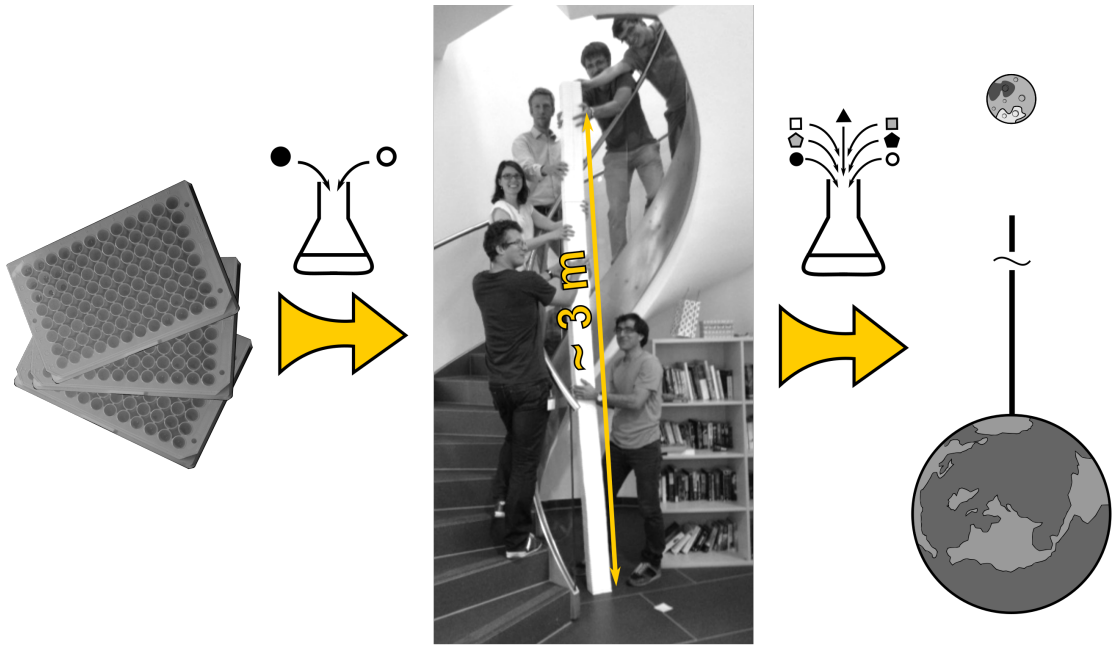

Figure 1.18: **An illustration of combinatorial explosion for twenty different antibiotics at twelve different concentrations.** We can fit all measurements for individual drugs onto three standard microtiter plates (left). Yet, if we measure all pairwise combinations, we already need around three-hundred plates (middle) that yield a nearly three-meter tower if stacked! If we consider all ultra-high combination cocktails of seven drugs, the stack of plates will span over two-thirds of the distance to the Moon with its height of 290,000 km (right, not to scale).

mechanisms? This question becomes increasingly challenging as combinations of antibiotics are burdened by the combinatorial explosion, which becomes even more problematic when more than two drugs are combined.

The number of combinations of N drugs is given as $\binom{N}{k}$, where k is a number of drugs in the combination. For example, if we consider $N = 20$, we can see that the number of distinct combinations increases as 190, 1140, and 4845 for 2-, 3-, and 4-drug combinations, respectively. Additionally, multiple different concentrations of drugs can be used, which further increases the number of required measurements as $\binom{N}{k} \times D^k$, where D is the number of concentrations per drug. This dramatic increase in the number of required measurements quickly becomes prohibitive for brute-force experimentation. The automation of experimental workflows can partially alleviate the effects of combinatorial explosion [Yeh *et al.*, 2006; Chevereau and Bollenbach, 2015; Russ and Kishony, 2018; Brochado *et al.*, 2018].

1.11.1 Antibiotic interactions

The combined effect of multiple antibiotics results in a drug interaction. Drug interactions are defined by comparing the measured to the expected effect. If the combined effect is stronger or weaker than the expected effect, a drug interaction is either antagonistic or synergistic, respectively. A special case of antagonism is suppression, in which combined response is not only weaker than the null expectation, but also weaker than at least of the drugs alone. Here, different expectations for the combined effect can be used. Loewe additivity [Loewe, 1928] and Bliss independence [Bliss, 1939] are most frequently used expectations and both use responses to individual drugs in the combination as inputs. Bliss independence is particularly suited for a low number of measurements, as it requires only four measurements (no drug, individual drugs, and combination) and expectation is simply a product of responses to individual drugs [Bliss, 1939; Mitosch and Bollenbach, 2014]. Here, responses y_i are relative growth rates, normalized by the drug-free growth rate, and Bliss independence is given as $y_{\text{Bliss}} = y_A \times y_B$ [Mitosch and Bollenbach, 2014].

The definition of Bliss independence is intuitive and simple to evaluate; yet, it generally fails to recognize that the same drug should exhibit additivity, *i.e.*, the combined effect the drug with itself should be $y(a+b) = y(c+d)$, if $a+b = c+d$. If this is the case, then for Bliss independence $y(a+b) = y(a) \times y(b)$ – this relation holds only if the dose-response curve is exponential [Mitosch and Bollenbach, 2014]. Therefore, it is not possible to recognize additive interaction using Bliss independence for drugs with non-exponential dose-response curve. Loewe additivity – as the name suggests – alleviates this issue and is defined such that the expected responses are additive in the concentrations [Loewe, 1928]. It is based on the shape of the dose-response surface, which is obtained by measuring the growth rate over the grid of concentrations (Fig. 1.19). The lines of equal growth (contours of the dose-response surface) are called the isoboles.

The shape of isoboles defines the type of interaction (Fig. 1.19). Linear isoboles define additivity; here, if combined drugs have the same shape of the dose-response

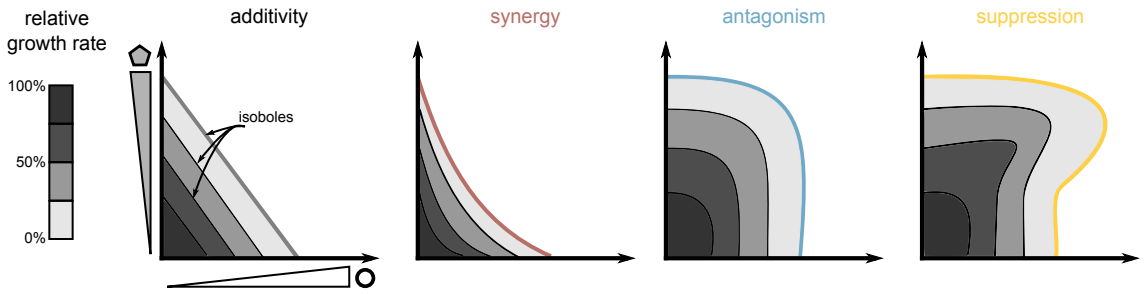

Figure 1.19: **Definition of drug interactions per Loewe.** Interactions are defined relative to the additive expectation. Synergy indicates that the combination is more potent than the additive expectation. In contrast, antagonism indicates that the combination is less potent. Suppression is an extreme case of antagonism in which at least one of the drugs has lost potency [Bollenbach, 2015; Mitosch and Bollenbach, 2014; Loewe, 1928].

curve, then additive isoboles are parallel [Loewe, 1928]. Additive surface can be calculated from individual responses by systematically connecting concentrations of each drug that leads to the same response. Curving of isoboles towards (isoboles are convex) or away (isoboles are concave) from the origin is indicative of synergy or antagonism, respectively (Fig. 1.19). Determining the type of interaction requires measuring the growth rate for multiple concentration combinations and is thus more comprehensive.

Dose-response surface resulting from such checkerboard assay has the added advantage of discerning multiple additional features of the interaction: (i) its concentration dependence, as isoboles might change the shape based on the particular pair of concentrations, and (ii) the direction of interaction. The latter is impossible to evaluate reliably for point measures required in Bliss definition and especially problematic for suppression. On the other hand, Bliss definition of interaction is based on expected independence of applied drugs, which can be a plausible assumption for particular drug combinations, and can serve as a useful expectation [Yeh *et al.*, 2006; Russ and Kishony, 2018].

Both Bliss and Loewe definitions can be generalized to higher-order drug combinations with appropriate modifications. Upon measuring drug interactions for many drug combinations, we can evaluate a drug interaction network [Yeh *et al.*, 2006; Cokol *et al.*, 2011; Cokol, 2014; Brochado *et al.*, 2018]. A network of this sort can

reveal clusters of drugs that interact similarly with drugs from other clusters but can interact diversely within the cluster [Yeh *et al.*, 2006]. When such investigation was performed for twenty-one drugs and corresponding pairwise interactions, drugs of similar mode of action ended up in the same cluster [Yeh *et al.*, 2006]. This suggests that the drug interactions are mostly determined by the mode of action, rather than exact chemical details of combined drugs.

1.11.2 Antibiotic interactions in the context of drug resistance and evolution

Antibiotic combinations offer a lucrative opportunity to counter the emergence of antibiotic resistance [Yeh *et al.*, 2009; Bollenbach, 2015]. A naïve expectation is that already the requirement to develop resistance to multiple simultaneously applied antibiotics with different modes of action will curb the emergence of resistance [Pillai *et al.*, 2005]. However, such reasoning is challenged when considered in the light of cross-resistance and collateral sensitivity between antibiotic pairs [Imamovic and Sommer, 2013], epistatic interactions between mutations, and the impact of mutations on the type of interaction [Chevereau and Bollenbach, 2015].

The impact of drug interactions on the rate of resistance evolution is still a subject of active investigation. Compelling arguments were suggested for considering the interplay of drug interactions and resistance evolution purely in a geometric manner [Chait *et al.*, 2007; Wood *et al.*, 2014]. If we assume that mutations only rescale the effective drug concentrations, interaction remains unchanged. Such rescaling and consequent invariance of interactions postulate a useful null expectation when libraries of mutants are considered; deviations from these expectations point towards mutants that change the interaction type and suggest the potential mechanisms underlying the interaction [Chevereau and Bollenbach, 2015].

This geometric framework has several important implications on the understanding of resistance and its evolution. It suggests that antagonistic interactions – while less potent – slow down the evolution of resistance; synergistic interactions on the other hand speed it up (Fig. 1.20A) [Hegreness *et al.*, 2008]. This intuitive picture

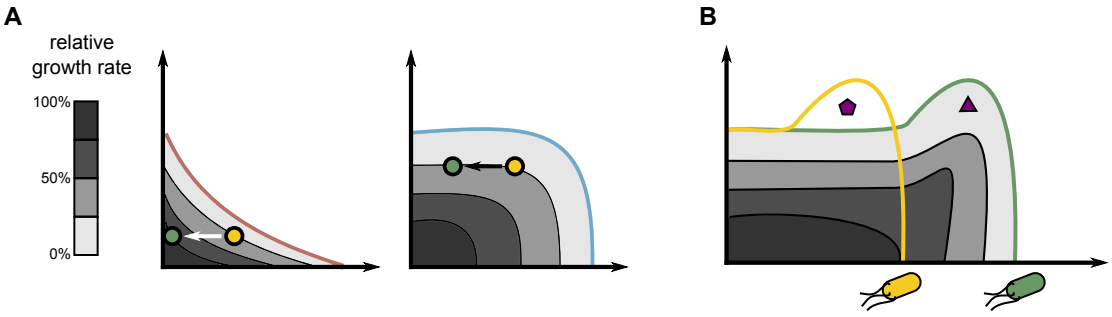

Figure 1.20: **Drug interactions affect resistance evolution. (A)** Synergy and antagonism affect the rate of resistance evolution differently. If a mutation does not change the interaction, but only rescales the effective concentration; see arrow from sensitive (yellow) to resistant (green). In the case of antagonism this does not result in the increase in fitness, while it does for synergistic interaction. This effect depends on the particular details of rescaling and strength of interaction. **(B)** Suppressive interaction selects against resistance. In the point denoted with a purple pentagon, sensitive strain can grow whereas resistant cannot. However, for higher concentrations (triangle) the situation is reversed.

has been challenged in a recent study [de Evgrafov *et al.*, 2015], in which *Staphylococcus aureus* was evolved in the presence of different antibiotic combinations; cross-resistance and collateral sensitivity were shown to be important in the degree of resistance evolution against a particular antibiotic combination.

While evolutionary determinants of drug resistance remain elusive, rescaling of effective concentrations by resistance mutations can explain the occurrence of differential selection. A particular example of the latter are drug interactions that select against resistance [Chait *et al.*, 2007]. In this study, suppressive interaction between quinolone ciprofloxacin and translation inhibitor doxycycline leads to the existence of a concentration region in which only sensitive strain grows (Fig. 1.20B). Such effects of drug interactions suggest an untapped potential that can be employed in the design of therapies, as these phenomena can potentially revert the evolutionary trajectories leading to ever-increasing drug resistance.

In sum, pairwise drug interactions and their mechanistic origins are important in the evolutionary context as they can affect the rate of resistance evolution, impose differential selection, or are themselves altered by the resistance mutations. Knowing the mechanisms of drug interactions would help us understand the role of drug

interactions in resistance evolution.

1.11.3 Gene expression in response to drug combinations

Drug combinations offer a unique opportunity to investigate changes in bacterial gene expression to the combinations of environmental signals. While changes in gene expression in response to some antibiotics might be consistent (*i.e.,* each of antibiotics leads to the same response), for others responses might be conflicting. Additionally, knowing responses to individual stresses can be difficult to consolidate to the combined stress; are responses averaged, prioritized to a particular drug, or biased? Additionally, on a single-cell level these responses might be deterministic (*i.e.,* all cells show roughly the same response to the combination of signals) or stochastic (*i.e.,* respond "randomly" to a particular signal from a combination) [Bollenbach and Kishony, 2011]. Studies of gene expression in response to combinations of antibiotics are of great interest, as these responses can reveal general strategies of gene regulation that govern the responses to mixed signals and can reveal intricate mechanisms of drug interactions [Bollenbach *et al.*, 2009].

Tacking the mechanisms of responses to mixed signals is especially challenging due to the overwhelming number of genes that can potentially lead the response. Various techniques have been employed, ranging from high-throughput microscopy and laboratory-automatization employing fluorescent reporters [Bollenbach and Kishony, 2011], to flow-cytometry and batch-sequencing of transcriptome (in fission yeast *S. cerevisiae* [Lukačišin and Bollenbach, 2019]). In analysis of these high-dimensional datasets in which number of readouts (*e.g.,* expression data for genes) far exceeds the number of conditions, various dimension-reduction methods were employed to identify combinations of genes that co-vary.

Dimension-reduction methods have the added benefit of delineating global, specific and emergent gene expression responses. Global response emerges due to the effects of antibiotics on macroscopic parameters such as the growth rate [Lukačišin and Bollenbach, 2019; Bollenbach and Kishony, 2011]. Specific responses are pertinent to individual drugs and can be conflicting or consistent between drugs in

the combination. In the combination these responses can prioritize one response over the other or can be averaged. Emergent gene expression occurs when genes are strongly up- or down-regulated in the presence of both drugs but not for any drug alone [Lukačišin and Bollenbach, 2019]. Emergent behavior in the presence of drug combination was shown to be predictive of higher-order drug interactions in which more than two antibiotics are present [Lukačišin and Bollenbach, 2019]. Here, a combination of two drugs could cause an upregulation of a particular pathway, suggesting that a drug targeting this pathway would be antagonized by this combination. Interestingly, it was demonstrated in *S. cerevisiae* that a combination of translation inhibitor and sphingolipid synthesis inhibitor, which caused upregulation of DNA replication checkpoint-machinery, antagonized DNA-damaging drug [Lukačišin and Bollenbach, 2019]. This example in which emergent response to pairs predicted the emergence of antagonism suggests that the higher-order drug interaction might arise as a "mixture" of pairwise interactions.

1.11.4 Mechanism-independent models of higher-order drug interactions

A methodological framework developed in Ref. [Wood *et al.*, 2012] showed that while experimental complexity increases with number of combined drugs beyond pairs, the prediction can actually become simpler. In their work, they considered growth rates as variable drawn from a probability distribution $P(x_1, x_2, \ldots, x_k) = P(\mathbf{x})$, where $\mathbf{x} = \{x_1, x_2, \ldots, x_k\}$ is a vector of k stochastic variables, defined such that measured response is given as $y_i = \langle x_i \rangle$. By construction, this probabilistic framework dictates that the drug interactions arise as correlations between stochastic variables x_i, or $y_{ij} = \langle x_i x_j \rangle$. The central premise of the maximum entropy models is based on: (i) probability distribution has to recover experimentally determined moments (or any expected value), and (ii) distribution with highest entropy (maximally unstructured distribution) is chosen [Jaynes, 1957]. This allows estimation of higher-order drug interactions, and – under some assumptions – results in a simple formula

for three-drug combination:

$$y_{ABC} = y_A y_{BC} + y_B y_{AC} + y_C y_{AB} - 2 y_A y_B y_C, \tag{1.8}$$

where y_i and y_{ij} are relative growth rates at the given concentration of drug i and at the combination of drugs i and j, respectively [Wood *et al.*, 2012]. This is an example of Isserlis' theorem, in which higher moments are constructed from known covariance matrix. While predictive, this framework requires knowledge of pairwise interactions y_{ij}.

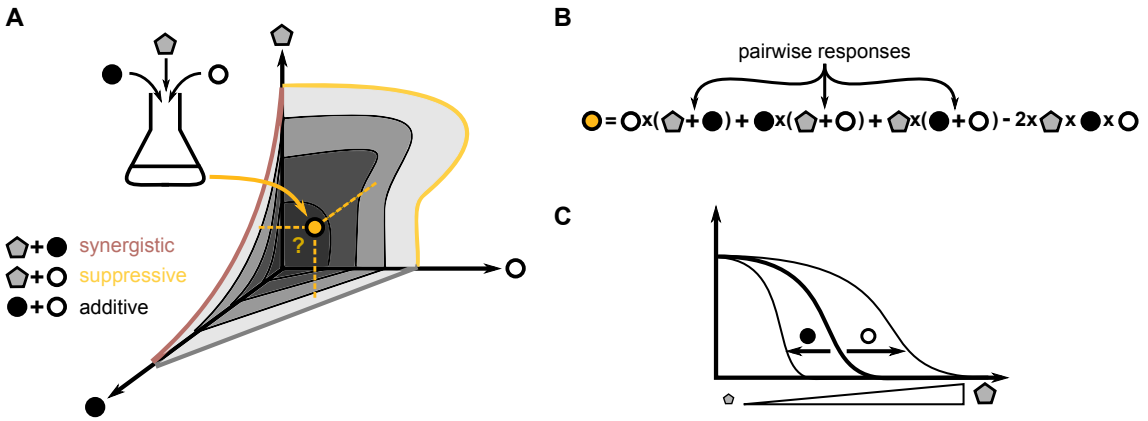

Figure 1.21: **Higher-order drug interactions mainly depend on pairwise interactions (A)** A schematic of three-antibiotic combination between drugs of known pairwise interactions. Mechanism-free models can predict the combined effect. **(B)** Schematic representation of the expression obtained for mechanism-free model as obtained by entropy-maximization. **(C)** Schematic representation of the effective-dose model. Addition of the second drug increases or decreases the effective concentration for synergistic and antagonistic/suppressive interactions, respectively.

Maximum entropy framework and its Isserlis' model [Eq. (1.8)] successfully predicted higher-order interactions; however, it is prone to errors arising from experimental inaccuracies in y_i and y_{ij} [Zimmer *et al.*, 2016]. An alternative approach for predicting the effect of combinations of chemotherapeutic drugs was suggested by Zimmer *et al.*, in which drug interaction materialize through rescaling of effective concentrations of individual drugs. Namely, combined effect is given as

$$y_{1,\ldots,k} = \prod_{i}^{k} g_i(d_{i,\text{eff}}), \tag{1.9}$$

where

$$d_{i,\text{eff}} = d_i \prod_{i \neq j} \left(1 + a_{ij} \frac{d'_{j,\text{eff}}}{1 + d'_{j,\text{eff}}}\right)^{-1} . \quad (1.10)$$

Here, $d'_{j,\text{eff}} = d_{j,\text{eff}}/d_{j,0}$ and $d_{j,0}$ is concentration leading to 50% inhibition. Since $y_i(d_i)$ is the known response to a single drug, what remains is determination of a_{ij} from pairwise interactions. This model has been generalized to predictions of ultra-high-order antibiotic combinations based on pairwise interactions [Katzir *et al.*, 2019]. Both Isserlis' and effective-dose models demonstrate that pairwise interactions are at the core of understanding higher-order drug combinations. It is hence imperative to uncover the mechanisms that govern the pairwise interactions.

2 Aims of this thesis

The work presented in this thesis aims to investigate the interplay of perturbations of cell physiology and the growth rate. Specifically, by focusing on the translation, we investigate the effects of antibiotics and antibiotics combinations that perturb the synthesis of proteins. The main body of the thesis (Chapters 3-6) consists of the work presented in two manuscripts: *"Minimal biophysical model of combined antibiotic action"* and *"Mechanisms of drug interactions between translation-inhibiting antibiotics"*. To integrate the material consistently into the thesis, we made several changes to the manuscript text and figures.

The disposition of the thesis is as follows:

Aim 1: Determination of a drug-interaction network
We selected several antibiotics that target various steps in translation and do so by binding to different sites of the translation machinery. This provides us with a diverse repertoire of chemical perturbations that allows investigation of combined perturbations of translation. Chapter 3 describes the determination of the drug interaction network and highlights the features of the diverse interactions between translation inhibitors.

Aim 2: Construction of a minimal model of drug interactions
Next, we construct a minimal model of combined antibiotic action, described in Chapter 4. We build a mathematical model of antibiotics targeting the ribosome; the model takes into account bacterial growth laws and kinetic properties of antibiotic transport and binding. It allows the prediction of drug interactions based on the re-

sponses to individual drugs alone. We systematically refine the model by including the direct physical interactions of different antibiotics on the ribosome. We elaborate on the correspondence between mechanism-free models of higher-drug interactions and limiting cases of our model. We additionally extend the model to include the effects of resistance genes and drugs that mimic a poor nutrient environment. We experimentally test the model predictions and isolate the cases in which the model did not correctly predict the experimental results.

Aim 3: Establishing the equivalence between genetic perturbations and antibiotics As we hypothesized that drug interactions might spur from the interplay of the ribosomes halted at different points in translation, we developed a synthetic system that allowed us to impose artificial bottlenecks in translation, which is described in Chapter 5. This directly leads to probing of the effects translation bottlenecks have on the efficacy of antibiotics. We integrate these effects into a series of "antibiotic fingerprints" that provide an insight into the workings of the antibiotics. We directly illustrate the equivalency of genetic and chemical perturbations by remapping. This further allows us to directly predict drug interactions from genetic interventions in translation.

Aim 4: Associating the simultaneous variation of rates of two essential processes with continuous epistasis and developing the TASEP-based model of translation Chapter 6 builds further on the idea that interactions between translation inhibitors arise from fundamental interplays between inhibited processes. By constructing a strain with two translation factors under inducible control, we showcase how the suppression emerges between the initiation and translocation inhibitors. Next, we construct the Totally Asymmetric Simple Exclusion (TASEP) model of translation. It takes into account the growth laws, and does not consider ribosomes as self-propelled particles, but rather establishes the kinetic rates on the catalysis by translation factors. As we associate the chemical and genetic perturbations, we develop the notion of continuous epistasis, which quantifies the deviations from

expected independence of two processes.

Aim 5: Construction of tools that allow quantitative characterization of translation
Motivated by these insights we develop a set of experimental tools for quantitative characterization of translation. We design the tools for measuring the translation rate and for precise quantification of intracellular abundances of translation factors. In Chapter 7 we showcase the construction of these tools and demonstrate the characterization of the physiological state of the cell. By titration of a translation factor, we quantitatively probe the state of the translation and try to infer the relationships between processes. We further develop these insights by constructing simple models of translation that allow us to infer the physiological parameters. We conclude by laying out the next steps in studies of translation.

3 Pairwise interactions between translation inhibitors

Inhibiting translation is one of the most common antibiotic modes of action, crucial for restraining pathogenic bacteria [Walsh, 2003]. Antibiotics targeting translation interfere with either the assembly or the processing of the ribosome, or with the proper utilization of charged tRNAs and translation factors (Fig. 3.1; Table 3.1) [Wilson, 2014]. Still, the exact modes of action and physiological re-

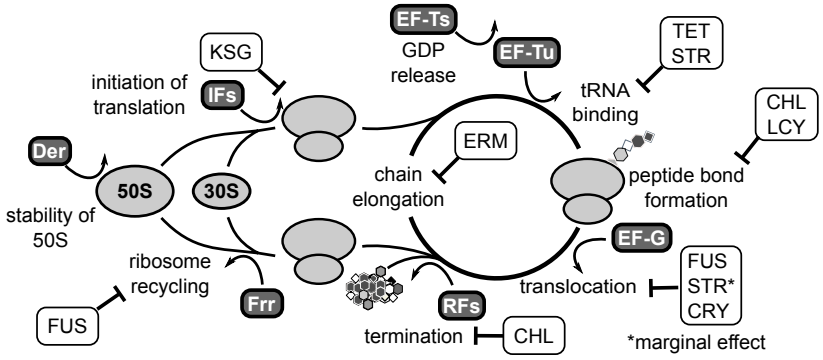

Figure 3.1: **Antibiotics targeting different translation steps.** Schematic of the translation cycle and translation inhibitors. Translation factors are shown in dark gray boxes. Stability of the large subunit is mediated by Der and initiation by initiation factors (IFs). Elongation factors Tu and G (EF-Tu, EF-G) catalyze ribosome progression. Release of GDP from EF-Tu is facilitated by EF-Ts. Release factors (RFs) facilitate the ejection of the finished peptide from the ribosome, whose recycling is mediated by the factor for ribosome recycling (Frr). Translation inhibitors are shown in white boxes (abbreviations in Table 1).

sponses to many such translation inhibitors are unclear. Responses to drug combinations, which may offer effective ways to combat antibiotic resistance [Yeh *et al.*, 2009], are even harder to understand. Apart from their clinical relevance, antibiotic combinations provide powerful quantitative and controlled means of studying perturbations of cell physiology [Falconer *et al.*, 2011] – conceptually

similar to studies of epistasis between double gene knockouts [Yeh *et al.*, 2006; Segre *et al.*, 2005]. Recently, mechanism-independent mathematical approaches to predict the responses to multi-drug combinations were proposed [Zimmer *et al.*, 2016; Wood *et al.*, 2012], yet these approaches rely on prior knowledge of pairwise drug interactions, which are diverse and have notoriously resisted prediction. One of the main reasons for this situation is that the underlying mechanisms of drug interactions are largely unknown. They include synergism (drug effect is stronger than predicted), antagonism (drug effect is weaker), and suppression (one of the drugs loses potency) [Bollenbach, 2015; Mitosch and Bollenbach, 2014] (Fig. 1.19). To design optimized treatments, the ability to predict or alter drug interactions is crucial. Such predictions would be facilitated by understanding their underlying mechanisms [Chevereau and Bollenbach, 2015].

Antibiotic	Abbreviation	IC_{50} [μg/mL]	Mode of action, notes
Chloramphenicol	CHL	1.55 ± 0.06	Binds in the vicinity of the peptidyl-transferase centre (PTC) on the 50S subunit [Wilson, 2014]; partially overlaps with the aminoacyl moiety of tRNA on the A-site [Dunkle *et al.*, 2010].
Lincomycin	LCY	280 ± 10	Lincosamide antibiotic; binds next to PTC and interferes with peptide bond formation [Wilson, 2014].
Erythromycin	ERM	25 ± 1	Macrolide antibiotic that binds further down the nascent peptide exit channel (Fig. 3.2), and physically blocks the egress of some newly synthesized peptide chains [Wilson, 2014]. Some nascent peptide chains can bypass this block, leading to proteome modification [Kannan *et al.*, 2012; Vazquez-Laslop and Mankin, 2018].
Kasugamycin	KSG	127 ± 5	Aminoglycoside; interferes with translation initiation by destabilization of the P-site initiator tRNA and mRNA [Schluenzen *et al.*, 2006].
Streptomycin	STR	2.55 ± 0.02	Aminoglycoside; interferes with the tRNA binding on the A-site and marginally lowers the rate of translocation [Wilson, 2014; Blanchard *et al.*, 2010; Peske *et al.*, 2004]. It additionally induces mistranslation [Blanchard *et al.*, 2010].
Tetracycline	TET	0.32 ± 0.01	Interferes with the binding of aminoacyl-tRNA to the A-site [Tritton, 1977].
Capreomycin	CRY	24 ± 1	Inhibits translocation by binding to the interface between subunits and stabilization of the ribosome in the pretranslocation state of the ribosome. It only binds the 70S ribosome and not the individual subunits [Stanley *et al.*, 2010].
Fusidic acid	FUS	64 ± 3	Inhibits elongation by preventing dissociation of EF-G from the ribosome and lowers the rate of ribosome recycling [Savelsbergh *et al.*, 2009].

Table 3.1: Translation-targeting antibiotics used in this study, abbreviations, IC_{50} measured for *E. coli* MG1655 grown in LB medium at 37°C, and notes on their mode of action.

Predictions of drug interactions should ideally only require information about responses to individual antibiotics. This information, together with an account of the global physiological response to drug action, could provide us with an improved null model of drug interactions. Established null models are based on mechanism-independent expectations such as Loewe additivity (Fig. 1.20) [Loewe and Muischnek, 1926], which mainly serve as a reference for classifying drug interactions. In contrast, an improved null model would capture well-understood processes such as drug uptake, target binding, and the physiological response to target inhibition, which are relevant for all drugs that share the same target. In this work, we experimentally challenge quantitative predictions of such a theoretical model of drug interactions. Any deviations from model predictions expose drug interactions that cannot be explained by established biological and physical processes alone. In this way, an improved null model could offer a plausible mechanism for some drug interactions and at the same time expose more complex situations where additional molecular or physiological details are crucial.

Here we focus on translation inhibitors and their interactions, because translation is a fundamental, yet complex multi-step process that still lacks a comprehensive quantitative description. A key step toward such a description are bacterial "growth laws," which quantitatively capture the compensatory upregulation of the translational machinery in response to perturbations of translation [Scott *et al.*, 2010]. Growth laws have enabled a model that explains the growth-rate dependent bacterial susceptibility to individual translation inhibitors [Greulich *et al.*, 2015]. These empirical relations offer a phenomenological description of the growth-dependent state of the bacterial cell and provide a solid foundation for quantitative studies of bacterial physiology. Similar to laws in physics, such as Fourier's law of heat conduction or Ohm's law, these phenomenological relations enable the construction of predictive mathematical models without free parameters even if their microscopic origins are not yet understood [Scott and Hwa, 2011]. Well-defined translation steps cannot only be perturbed chemically [Wilson, 2014; Blanchard *et al.*, 2010], but also genetically, as these steps are regulated by translation factors – specialized proteins that mediate the stability of ribosomal subunits,

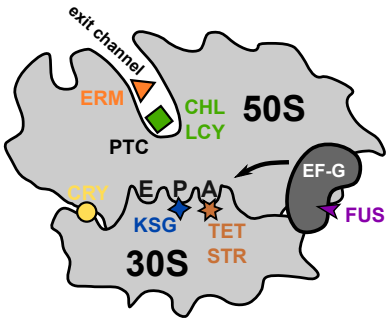

Figure 3.2: **Translation inhibitors bind to different sites of the ribosome.** Antibiotics (in color) bind to either of the subunits, the interface between both (CRY), or to the translation factor. The binding site of the translation inhibitor determines which process it inhibits.

catalyze the assembly of 70S ribosomes and initiation, deliver charged tRNAs to the ribosome, release finished peptides, and mediate ribosome recycling (Fig. 3.1). Both genetic and chemical perturbations obstruct the progression of ribosomes along the translation cycle, which generally results in a lower growth rate. Comparing the effects of antibiotics to those of precisely defined genetic perturbations offers an opportunity to elucidate the mechanisms responsible for drug interactions between translation inhibitors and could quantitatively test the equivalence of genetic and chemical perturbations of bacterial physiology.

As drug interactions are largely determined by the modes of action of the combined antibiotics [Yeh *et al.*, 2006], we hypothesized that a key determinant of interactions between pairs of translation inhibitors are the specific steps in the translation cycle where the two inhibitors halt ribosomal progression (Fig. 3.1). As a second key determinant of these drug interactions, we considered the compensatory physiological response to translation inhibition captured quantitatively by ribosomal growth laws [Scott *et al.*, 2010] together with the kinetics of antibiotic transport and ribosome binding. We show that these determinants suffice to explain most drug interactions between translation inhibitors and that these interactions can be predicted solely from known responses to the individual drugs. To establish this result, we used a combination of precise growth measurements, quantitative genetic perturbations of the translation machinery, and theoretical modeling.

To systematically map the network of drug interactions between translation inhibitors, we selected eight representative antibiotics that interfere with different stages of translation and bind to different sites on the ribosome (Fig. 3.2; Table 3.1). We determined high-resolution dose-response surfaces for all pairwise combinations of

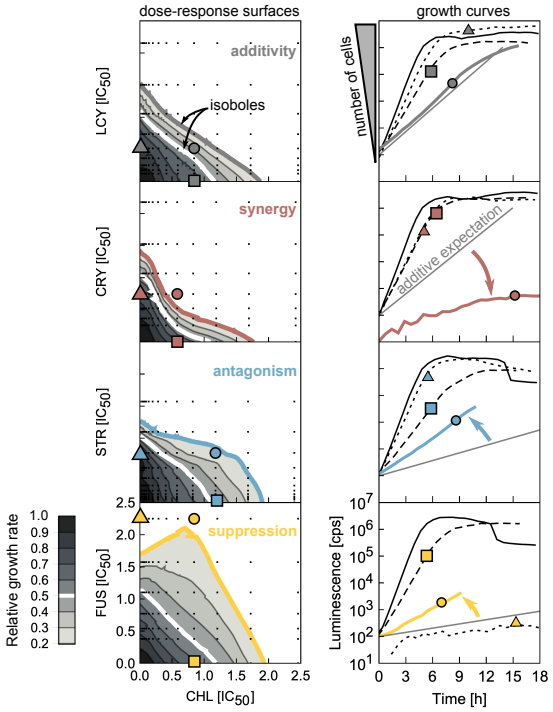

Figure 3.3: **Response surfaces and examples of growth curves.** Left: Dose-response surfaces for different drug combinations. Gray scale shows normalized growth rate as a function of concentrations of two antibiotics. Symbols show drug conditions in which growth curves shown in the right column were measured. Right: Growth curves (*i.e.*, time courses of luminescence) for four conditions (no drug, individual drugs and a combination); thin gray line shows additive expectation of the growth curve for the combined stress. Symbols on the growth curves indicate the condition used: no symbol, triangle, square and a circle correspond to no drug, CHL-only, second drug only (see y-axis), and the combination of both, respectively. The growth curves were shifted in time so as to originate from the same point at time zero.

these antibiotics by measuring growth rates in two-dimensional drug concentration matrices using a highly precise technique based on bioluminescence [Yeh *et al.*, 2006; Kishony and Leibler, 2003; Chait *et al.*, 2007] (Fig. 3.3 and Fig. E.2; see Appendices B, C). The shape of the contour lines, along which growth rate is constant in two-drug space, reveals the drug interaction type (Fig. 3.3). To quantify the drug interactions, we defined the Loewe interaction score LI, which integrates deviations from Loewe additivity (Methods). In this way, we characterized all twenty-eight pairwise interactions and constructed the interaction network between the translation inhibitors (Fig. 3.4).

The translation inhibitor interaction network (Fig. 3.4) we measured has several notable properties. First, antibiotics with similar mode of action tend to exhibit additive drug interactions: In particular, there are purely additive interactions between capreomycin (CRY) and fusidic acid (FUS), which both inhibit translocation, and streptomycin (STR), which interferes with tRNA binding and also slightly lowers the translocation rate. Chloramphenicol (CHL) and lincomycin (LCY), which both inhibit peptide bond formation, interact additively as well. This observation is

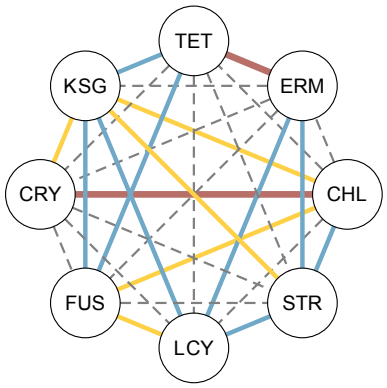

Figure 3.4: **The drug-interaction network of translation inhibitors.** Color-code is as in Fig. 3.3; dashed gray lines denote additivity. Note the prevalence of antagonism and suppression.

consistent with the view that drugs with similar mode of action can substitute for one another. Second, kasugamycin (KSG) is a prominent hub in the network: it shows almost exclusively antagonistic and suppressive interactions with other translation inhibitors. Third, we identified a previously unreported synergy between CRY and CHL. A number of other interactions confirm previous reports. For example, synergy between erythromycin (ERM) and tetracycline (TET) was observed before [Yeh *et al.*, 2006; Russ and Kishony, 2018]. Additivity between CHL and TET was also reported; moreover, this interaction proved to be highly robust to genetic perturbations [Chevereau and Bollenbach, 2015]. Finally, antagonism and suppression are more common in the translation inhibitor interaction network than synergy, consistent with a general prevalence of antagonistic interactions between antibiotics [Brochado *et al.*, 2018]. We reasoned that general trends like the prevalence of antagonism in the drug interaction network may be due to a general physiological response to translation inhibition.

4 Minimal model of antibiotic action

As a first step toward understanding the origin of the observed drug interactions, we developed a mathematical model that predicts such interactions from the effects of the individual drugs alone. We generalized a biophysical model for the effect of a single antibiotic on bacterial growth [Greulich *et al.*, 2015] to the situation where two antibiotics are present simultaneously. In the spirit of Ref. [Greulich *et al.*, 2015], our model aims to predict the response to a pair of "generic" translation inhibitors whose action leads to a physiological response that obeys established bacterial growth laws [Scott *et al.*, 2010]. Considerable experimental support from observations of the effects on translation by diverse chemical and genetic perturbations strengthens the generality of growth laws [Cole *et al.*, 1987; Olsson *et al.*, 1996; Bennet and Maaløe, 1974]. This parsimonious approach keeps the number of unknown model parameters to a minimum. Cases where the response to a drug pair deviates from the predictions of this physiologically relevant null model indicate that more complex mechanisms – specific to one or both of the drugs used – are essential for understanding the drug interaction.

Here, we present a biophysical model that predicts bacterial growth responses to combinations of translation inhibitors. Starting from responses to single antibiotics, we derive approximate analytical solutions of this model and investigate the effects of direct physical or allosteric interactions between antibiotics on the ribosome. We discuss several relevant extensions of the model, in particular (1) interactions with antibiotics that induce starvation, (2) the effects of resistance genes, (3) the correspondence to non-mechanistic models of interactions between more than two drugs, and (4) predictions for interactions of translation inhibitors with antibiotics that alter growth law parameters. We validate several non-trivial predictions made

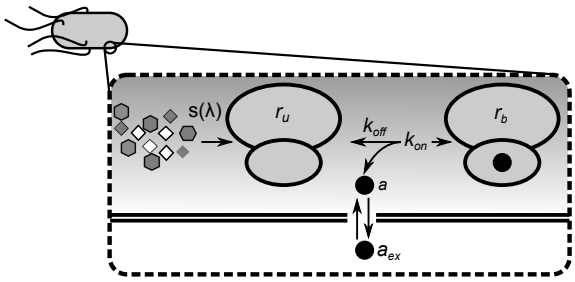

Figure 4.1: **Main components of the model for a single translation inhibitor.** Ribosomes (double ovals) are synthesized with the rate $s(\lambda)$ and are initially unbound by antibiotic (r_u). Unbound ribosomes contribute to growth. Antibiotics enter the cell ($a_{\mathrm{ex}} \rightarrow a$) and bind to and detach from ribosomes with second-order and first-order rate constants k_{on} and k_{off}, respectively. Bound ribosomes (r_b) do not contribute to growth.

by the biophysical model in experiments.

4.1 Model for a single translation inhibitor

First, we recapitulate the biophysical model for a single translation inhibitor [Greulich *et al.*, 2015]. The model captures the kinetics of antibiotic transport into the cell and binding to the ribosome (Fig. 4.1), as well as the physiological response of the cell to translation perturbation. This physiological response is described by bacterial growth laws, which summarize the interdependence of the intracellular ribosome concentration r and the growth rate λ (Fig. 4.2). Bacterial physiology and the response to antibiotic treatment strongly depend on the nutrient environment. In particular, the number of ribosomes per cell varies over approximately $5 - 75 \times 10^3$ [Bremer and Dennis, 1996]. The ribosome concentration increases linearly with the growth rate when the latter is varied by changing the quality of the growth medium:

$$r_u = r_{\mathrm{min}} + \lambda/\kappa_t, \tag{4.1}$$

where $\kappa_t = 0.06\ \mu\mathrm{M}^{-1}\mathrm{h}^{-1}$, r_u and $r_{\mathrm{min}} = 19.3\ \mu\mathrm{M}$ are the translational capacity, the concentration of unperturbed ribosomes, and a minimal ribosome concentration, respectively [Scott *et al.*, 2010; Greulich *et al.*, 2015]. This first growth law, which we introduced in the Introduction, states that unperturbed ribosomes synthesize

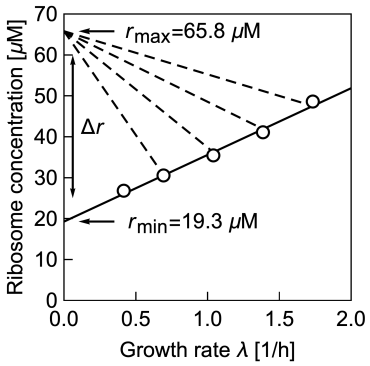

Figure 4.2: **Bacterial growth laws.** When the growth rate is varied by changing the quality of the nutrient environment, the ribosome concentration increases linearly with growth rate (solid line). If growth is inhibited by a translation inhibitor, the ribosome concentration increases with decreasing growth rate (dashed lines). The intercepts of the solid and dashed lines determine the minimal ($r_{\min}$) and maximal ribosome concentration ($r_{\max}$), respectively, which are Δr apart.

new proteins, whose overall synthesis rate is proportional to the growth rate. Here, we expressed the quantities in the units of concentrations, rather than proteome fractions [Greulich *et al.*, 2015; Klumpp *et al.*, 2013; Scott *et al.*, 2014]. This relation holds across diverse growth media and different *Escherichia coli* strains [Scott *et al.*, 2010]. Typical values for doubling times range from hours to approximately twenty minutes, corresponding to growth rates up to around 2.5 h^{-1}. However, when the growth rate is lowered by addition of a translation inhibitor in a constant nutrient environment, the total ribosome concentration r_{tot} and growth rate become negatively correlated [Scott *et al.*, 2010]. Mathematically, this dependency is given as:

$$r_{\text{tot}} = r_u + r_b = r_{\max} - \lambda\Delta r[1/\lambda_0 - 1/(\kappa_t\Delta r)], \tag{4.2}$$

where $r_{\max} = 65.8\ \mu$M is the maximal ribosome concentration, $\Delta r = r_{\max} - r_{\min} = 46.5\ \mu$M is the dynamic range of ribosome concentration, r_b is the concentration of antibiotic-bound ribosomes, and λ_0 is the maximal growth rate in the absence of antibiotics [Scott *et al.*, 2010]. Eq. (4.2) quantitatively describes the upregulation of ribosome production that occurs in response to translation inhibition: Bacteria produce more ribosomes to compensate for the ribosomes blocked by antibiotics.

When antibiotics enter the cell, they can bind to ribosomes. The net rate of forward and reverse binding of antibiotics to the ribosome is given by $f(r_u, r_b, a) = -k_{\text{on}}a(r_u - r_{\min}) + k_{\text{off}}r_b$, where k_{off} and k_{on} are first and second order rate constants, and a is the intracellular antibiotic concentration (Fig. 4.1). Here, we assumed that only ribosomes

capable of translation ($r_u - r_{\min}$) can be bound by the antibiotics [Greulich *et al.*, 2015; Greulich *et al.*, 2017].

The intracellular antibiotic concentration is affected by the kinetics of antibiotic entry into the cell, which is given by $J(a_{\text{ex}}, a) = p_{\text{in}} a_{\text{ex}} - p_{\text{out}} a$, where a_{ex} is the extracellular antibiotic concentration. Typical influx and efflux rates, p_{in} and p_{out}, for different translation inhibitors range from $1 - 1000\ \text{h}^{-1}$ and from $0.01 - 100\ \text{h}^{-1}$, respectively. Typical rates of forward and reverse binding, k_{on} and k_{off}, are around $1000\ \mu\text{M}^{-1}\text{h}^{-1}$ and between $0 - 10^5\ \text{h}^{-1}$, respectively [Greulich *et al.*, 2015; Greulich *et al.*, 2017]. Here, $k_{\text{off}} = 0$ corresponds to antibiotics with effectively irreversible binding such as streptomycin [Greulich *et al.*, 2015; Davis, 1987]. All molecular species in the cell are effectively diluted at rate λ as cells grow and divide. Since the ribosome concentration is determined by Eq. (4.2), the ribosome synthesis rate s depends on the growth rate, *i.e.*, $s = s(\lambda)$. Together, these terms constitute a closed system of ordinary differential equations:

$$\frac{\mathrm{d}a}{\mathrm{d}t} = -\lambda a + f(r_u, r_b, a) + J(a_{\text{ex}}, a), \tag{4.3a}$$

$$\frac{\mathrm{d}r_u}{\mathrm{d}t} = -\lambda r_u + f(r_u, r_b, a) + s(\lambda), \tag{4.3b}$$

$$\frac{\mathrm{d}r_b}{\mathrm{d}t} = -\lambda r_b - f(r_u, r_b, a). \tag{4.3c}$$

Here, the ribosome synthesis rate reads $s(\lambda) = \lambda r_{\text{tot}} = \lambda \{r_{\max} - \lambda \Delta r [1/\lambda_0 - 1/(\kappa_t \Delta r)]\}$. The steady-state solution of Eqs. (4.3) represents a balanced-growth state of the system – the situation that is commonly investigated in experiments. The steady-state solution reads [Greulich *et al.*, 2015]

$$\begin{aligned} 0 = \left(\frac{\lambda}{\lambda_0}\right)^3 - \left(\frac{\lambda}{\lambda_0}\right)^2 \quad + \\ + \left(\frac{\lambda}{\lambda_0}\right)\left[\frac{1}{4}\left(\frac{\lambda_0^*}{\lambda_0}\right)^2 + \frac{a_{\text{ex}}}{2\text{IC}_{50}^*}\left(\frac{\lambda_0^*}{\lambda_0}\right)\right] \quad - \quad \frac{1}{4}\left(\frac{\lambda_0^*}{\lambda_0}\right)^2, \end{aligned} \tag{4.4}$$

where $\lambda_0^* = 2\sqrt{p_{\text{out}} \kappa_t K_D}$ with $K_D = k_{\text{off}}/k_{\text{on}}$, and $\text{IC}_{50}^* = \Delta r \lambda_0^* / 2 p_{\text{in}}$. We can recast Eq. (4.4) into (Appendix A.1):

$$\frac{1}{\alpha^2 + 1}\left(\frac{\alpha^2}{y} - \alpha^2 + 4y - 4y^2\right) - c = 0 \tag{4.5}$$

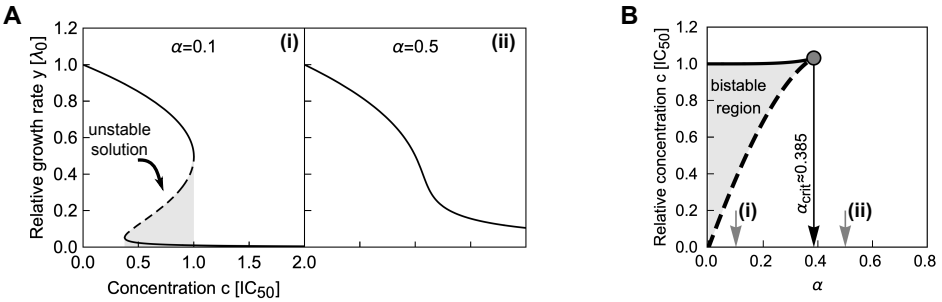

Figure 4.3: **Dose-response curves and bistability phase diagram. (A)** Examples of dose-response curves. The model can produce both (i) steep and (ii) shallow dose-response curves, depending on the parameter α (see text). The steep dose-response curve has a region of concentrations (gray shaded area) where one unstable (dashed line) and two stable (solid lines) solutions exist. **(B)** Exact phase diagram for dose-response curves. The shaded area shows the region of drug concentrations where two stable solutions exist. Gray arrows show α for the examples from (A); black arrow shows the critical value $\alpha_{\text{crit}} = 2/3\sqrt{3}$ above which no bistability can occur.

by defining $a_{\text{ex}} = c \times \text{IC}_{50}$, $\lambda = y \times \lambda_0$ and $\lambda_0^* = \alpha \times \lambda_0$, where IC_{50} is the extracellular antibiotic concentration that leads to 50% growth inhibition, a common measure of drug sensitivity. Here, we call α the response parameter, as it describes the dose-response curve shape: The higher the value taken by α, the shallower the dose-response curve (Fig. 4.3A).

Since Eq. (4.5) is cubic in the relative growth rate y, there are generally either one or three real solutions for y (Fig. 4.3A). This indicates that there is a parameter regime in which the dynamical system can exhibit bistability [Greulich *et al.*, 2015; Elf *et al.*, 2006]. Previous studies identified the bistable parameter regions numerically or in closed expression with many parameters [Greulich *et al.*, 2015; Greulich *et al.*, 2017]. Notably, the rescaling shown above enables the exact calculation of the bifurcation point (see Appendix A.1): When $\alpha < \alpha_{\text{crit}} = 2/(3\sqrt{3}) \approx 0.385$ the system can be bistable (Fig. 4.3B), *i.e.*, there is a region of concentrations with stable solutions at two different growth rates. In this region, the growth rate sharply declines when a critical concentration is exceeded. It is difficult to measure such steep dose-response curves experimentally since very low growth rates are challenging to detect and quantify. Additionally, bistability cannot be observed in population-level experiments since the high-growth-rate branch will quickly dominate the

population; single-cell experiments are needed to observe growth bistability [Deris *et al.*, 2013]. On the other hand, if the antibiotic concentration can be varied during the experiment, bistability can be tested by determining the hysteresis of the response, as observed for synthetic gene networks [Kramer and Fussenegger, 2005].

Steep dose-response curves ($\alpha < \alpha_{\text{crit}}$) occur for antibiotics with tight binding to the ribosome ($K_D \to 0$) or inefficient efflux ($p_{\text{out}} \to 0$). Alternatively, if these two quantities are growth-rate invariant, dose-response curves become steeper with increasing growth rate in the absence of drug, as $\alpha \propto 1/\lambda_0$. For typical values of the relevant parameters (discussed above), α ranges from 0 to ~ 10. We have experimentally observed values of α for different translation inhibitors in the range $0 - 2$. In the limit $\alpha \gg 1$, Eq. (4.5) simplifies into $y = 1/(1 + c)$; if $\alpha \to 0$ then this expression becomes $y = \left(1 + \sqrt{1 - c}\right)/2$ for $c \geq 1$, [Greulich *et al.*, 2015]. This biophysical model for a single translation inhibitor provides the foundation for a predictive theory of multiple drug interactions between different translation inhibitors.

4.2 Model for interaction between two translation inhibitors

When combinations of two different translation inhibitors are present, each ribosome can be bound by either of them alone or by both simultaneously. To generalize the model described in Sec. 4.1 to this situation, we need to introduce additional populations of ribosomes. Extending the mathematical model [Eqs. (4.3)] to two translation inhibitors yields:

$$\begin{aligned}
\frac{\mathrm{d}a_i}{\mathrm{d}t} &= -\lambda a_i + f_i(r_u, r_{b,i}, a_i) + J_i(a_{\mathrm{ex},i}, a_i) + \\
&\quad + \delta_{\mathrm{off},i} k_{\mathrm{off},i} r_d - \delta_{\mathrm{on},i} k_{\mathrm{on},i} a_i r_{b,\bar{i}} && \text{(4.6a)} \\
\frac{\mathrm{d}r_{b,i}}{\mathrm{d}t} &= -\lambda r_{b,i} - f_i(r_u, r_{b,i}, a_i) + \delta_{\mathrm{off},\bar{i}} k_{\mathrm{off},\bar{i}} r_d - \delta_{\mathrm{on},\bar{i}} k_{\mathrm{on},\bar{i}} a_{\bar{i}} r_{b,i}, && \text{(4.6b)} \\
\frac{\mathrm{d}r_d}{\mathrm{d}t} &= -\lambda r_d + \sum_{i=A,B} \delta_{\mathrm{on},i} k_{\mathrm{on},i} a_i r_{b,\bar{i}} - \sum_{i=A,B} \delta_{\mathrm{off},i} k_{\mathrm{off},i} r_d && \text{(4.6c)} \\
\frac{\mathrm{d}r_u}{\mathrm{d}t} &= -\lambda r_u + \sum_{i=A,B} f_i(r_u, r_{b,i}, a_i) + s(\lambda). && \text{(4.6d)}
\end{aligned}$$

The terms $f_i(r_u, r_{b,i}, a_i)$ and $J_i(a_{\mathrm{ex},i}, a_i)$ describe the first binding step and membrane transport of antibiotic i, respectively. The additional terms $\delta_{\mathrm{off},i} k_{\mathrm{off},i} r_d$ and $\delta_{\mathrm{on},i} k_{\mathrm{on},i} a_i r_{b,\bar{i}}$ describe the unbinding of antibiotic i from double-bound ribosomes r_d and the binding of antibiotic i to ribosomes already bound by the other antibiotic $\bar{i}$ (*e.g.*, for antibiotics A and B, $\bar{A} = B$), respectively. The dimensionless parameters $\delta_{\sigma,i}$ with $\sigma \in \{\mathrm{on}, \mathrm{off}\}$ denote the relative change of the rate of forward and reverse binding of antibiotic i to ribosomes already bound by the other antibiotic. When the binding kinetics for both antibiotics are independent, all $\delta_{\sigma,i} = 1$. When both antibiotics compete for the same binding site on the ribosome, $\delta_{\mathrm{on},i} = 0$. In general, the parameters $\delta_{\sigma,i}$ can vary continuously to capture any changes in ribosome binding of one antibiotic due to the binding of the second.

What is the main consequence of including the double-bound ribosomes? Below, we show that in the absence of double-bound ribosomes, drug interactions are

generally expected to be additive. If we assume that no double-bound ribosomes can form, *e.g.*, by setting $\delta_{\mathrm{on},i} = 0$, Eq. (4.6c) becomes equal to zero and all terms associated with the second binding event disappear. To show that this situation necessarily yields an additive drug interaction, we examine the system along the isobole. At the fixed growth rate, *i.e.*, along an isobole, $r_u = \lambda/\kappa_t + r_{\min}$ is constant. This implies that the total concentration of ribosomes bound by either antibiotic (*i.e.*, $r_b = r_{b,A} + r_{b,B}$) remains constant for all different concentration pairs (c_A, c_B) along the isobole. In a steady state, the concentration of ribosomes bound by the antibiotic i is $r_{b,i} = a_i \times \xi_i$, where $\xi_i = k_{\mathrm{on},i}\lambda/\left[\left(k_{\mathrm{off},i} + \lambda\right)\kappa_t\right]$. The bound ribosome concentration reads

$$r_b = r_{b,A} + r_{b,B} = r_{\mathrm{tot}} - r_u = \Delta r\,(1 - \lambda/\lambda_0) \tag{4.7}$$

where we have taken into account Eqs. (4.1) and (4.2). We express a_i as a function of $a_{\mathrm{ex},i}$ from Eq. (4.6a), which yields:

$$a_i = a_{\mathrm{ex},i} \underbrace{\frac{p_{\mathrm{in},i}}{\left[\lambda\left(k_{\mathrm{on},i}/\kappa_t + 1\right) + p_{\mathrm{out},i} - \xi_i k_{\mathrm{off},i}\right]}}_{\Upsilon_i}. \tag{4.8}$$

The proportionality constant Υ_i in this expression depends only on λ and kinetic parameters; in particular, it is invariant of the concentration of the other antibiotic. Because $r_b = r_{b,A} + r_{b,B} = \xi_A a_A + \xi_B a_B$ [Eq. (4.7)], it follows

$$\Delta r\left(1 - \frac{\lambda}{\lambda_0}\right) = a_{\mathrm{ex},A}\Upsilon_A\xi_A + a_{\mathrm{ex},B}\Upsilon_B\xi_B, \tag{4.9}$$

which is the equation of the isobole because coefficients $\Upsilon_i\xi_i$ are independent of the other antibiotic. This argument shows that additivity generally occurs when double-bound ribosomes cannot form. Additionally, this confirms that the model correctly predicts additivity when the antibiotic is combined with itself–double-bound ribosomes cannot form in this case.

In the limit where $k_{\mathrm{off}}, p_{\mathrm{out}} \gg \lambda$, *i.e.*, $\alpha \to \infty$, the Eq. (4.9) takes a simple form of $c_A + c_B = \lambda_0/\lambda - 1$, where $c_i = a_{\mathrm{ex},i}/\mathrm{IC}_{50,i}$. To derive this expression, we noted the definitions of α and $\mathrm{IC}^*_{50,i}$ used for a single antibiotic (see preceding section) as well as that $\mathrm{IC}_{50,i} \approx \mathrm{IC}^*_{50,i}\alpha/2$ for $\alpha \gg 1$ (see Appendix A.1). This simplified expression

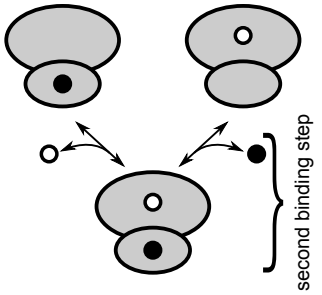

Figure 4.4: **Ribosomes already bound by a single antibiotic (black and white circles) can be bound by another one.** If the binding is independent of the presence of an already bound antibiotic, the second binding step follows the same kinetics as for a single antibiotic.

clearly shows the linear dependency between external concentrations supporting growth rate λ.

To study the effect of double-bound ribosomes (Fig. 4.4), we systematically calculated dose-response surfaces for both competitive and independent binding (Fig. 4.5A; Appendix A.3). The Loewe interaction score (LI) is a convenient way to characterize the type and strength of drug interactions by a single number, with negative values corresponding to synergy and positive values to antagonism. The LI score quantifies the interaction using the volume under the dose-response surface:

$$LI = \log\left(\frac{\int y(c_A, c_B)\mathrm{d}c_A\mathrm{d}c_B}{\int y_{\mathrm{add}}(c_A, c_B)\mathrm{d}c_A\mathrm{d}c_B}\right), \tag{4.10}$$

where y_{add} is the response surface of the additive expectation, which is calculated directly from the responses to the individual drugs (see Appendix A.2). By calculating the LI score of the dose-response surfaces for varying response parameters α_A, α_B of the two antibiotics that are combined, we determined the complete phase diagram of drug interactions (Fig. 4.5B). This procedure revealed that antagonism generally occurs for combinations of antibiotics with steep dose-response curves, and the interaction becomes additive and then synergistic with increasing response parameters (Fig. 4.5A). This transition from antagonism to synergy is smooth and partitions the phase diagram into two regions (Fig. 4.5B). However, suppressive interactions remain elusive.

The fact that combinations of antibiotics that bind the ribosome irreversibly yield antagonism can be understood intuitively. If a low concentration of an irreversibly-binding antibiotic is added to a bacterial population in the presence of a high concentration of another such antibiotic, it will mostly bind ribosomes that are already tightly bound by the other antibiotic. Such double-binding events will not

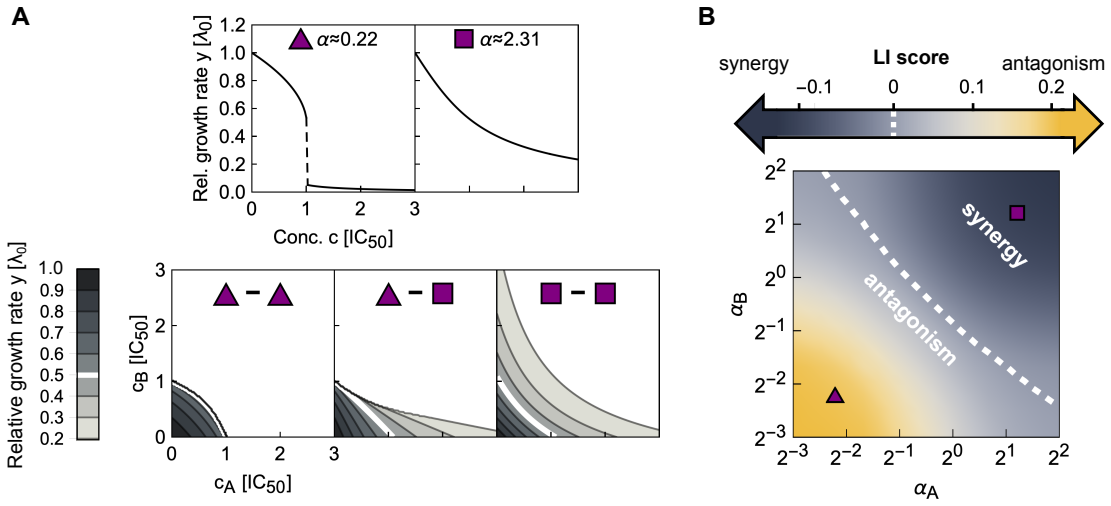

Figure 4.5: **Biophysical model of two antibiotics that can bind the ribosome simultaneously produces different types of drug interaction. (A)** Examples of dose-response curves of different steepness and corresponding dose-response surfaces calculated from the model. Top: Dose-response curves with low or high α are steep (left) or shallow (right), respectively. Bottom: Depending on the shape of the dose-response curves of the antibiotics that are combined, the calculated drug interactions range from antagonism (left, low α) to synergy (right, high α). Combining antibiotics with different α results in a dose-response surface of more complicated shape (middle). **(B)** Phase diagram of drug interactions: LI score for dose-response surfaces of antibiotic pairs with response parameters α_A, α_B; white dashed line shows additive interactions ($LI = 0$). The left- and right-hand antibiotic pairs from (b) are shown by a purple triangle and a purple square, respectively.

lower the growth rate further since the ribosomes were already inactivated by the first antibiotic that bound. Irreversibly-bound ribosomes thus effectively act as a "sponge" that soaks up antibiotics which can then no longer contribute to growth inhibition – a situation that results in antagonism.

What causes the transition from antagonism to synergy as α increases? Increasing α implies that the binding of the antibiotic becomes more and more reversible or efflux becomes high (*i.e.*, $K_D p_{\text{out}} \to \infty$). If the growth rate is low due to inhibition, then the $r_{\text{tot}} \approx r_{\text{max}}$ as the ribosome synthesis is upregulated to its maximum. In this case, the typical rate of dilution by growth is much slower than that of antibiotic-ribosome binding and we obtain $a_i \approx a_{\text{ex},i} p_{\text{in},i} / p_{\text{out},i}$. In this regime, we can derive an approximate solution that yields a synergistic dose-response surface, supporting the conclusion that qualitatively changing the binding kinetics alters

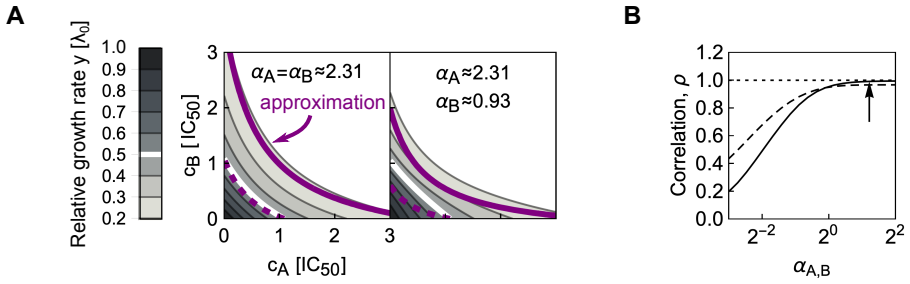

Figure 4.6: **Combining antibiotics with rapidly reversible ribosome binding yields synergistic drug interactions. (A)** Comparisons of numerically calculated dose-response surfaces and approximate solution. Purple isoboles (dashed and solid lines correspond to 50% and 20% relative growth rate, respectively) show the approximate solution on top of the dose-response surface calculated from the biophysical model (gray scale). Examples are shown for two pairs of antibiotics with identical (left) or different α (right). **(B)** Pearson correlation ρ between approximate and numerically calculated growth rate, evaluated for 121×121 equidistant concentration pairs. Solid and dashed line correspond to the cases with identical or different α, respectively. The correlation increases for antibiotics with higher α. The arrow shows α for the example on the left in A.

the drug interaction type. The system becomes linear and analytically solvable (see Appendix A.4). The growth rate is then:

$$\begin{aligned} y &\approx \frac{\lambda_{\max}/\lambda_0}{\left\{1 + c_A\left[(\alpha_A^2+1)\lambda_{\max}\right]/(\alpha_A^2\lambda_0)\right\}\left\{1 + c_B\left[(\alpha_B^2+1)\lambda_{\max}\right]/(\alpha_B^2\lambda_0)\right\}} = \\ &= \frac{\lambda_{\max}/\lambda_0}{\left(1+c'_A\right)\left(1+c'_B\right)}, \end{aligned} \tag{4.11}$$

where $c'_i = c_i \times \left[(\alpha_i^2+1)\lambda_{\max}\right]/(\alpha_i^2\lambda_0)$. This expression for y is simply a product of relative responses, which is equivalent to the definition of Bliss independence. This approximate solution agrees well with the full numerical solution at lower growth rates and for antibiotics with higher α (Fig. 4.6). Equation (4.11) becomes even simpler in the limit $\lambda_0 = \lambda_{\max}$ and $\alpha \to \infty$ as these two limits yield a product of two Langmuir-like equations with only relative concentrations c_A, c_B as arguments, *i.e.*, $y = 1/[(1+c_A)(1+c_B)]$, which is independent of λ_0 and α.

Using this model, we calculated the predicted response surfaces for all translation inhibitor pairs and compared them to the experimentally measured surfaces (Fig. 4.7). Certain drug interactions were correctly predicted by this approach (*e.g.*, ERM-KSG,

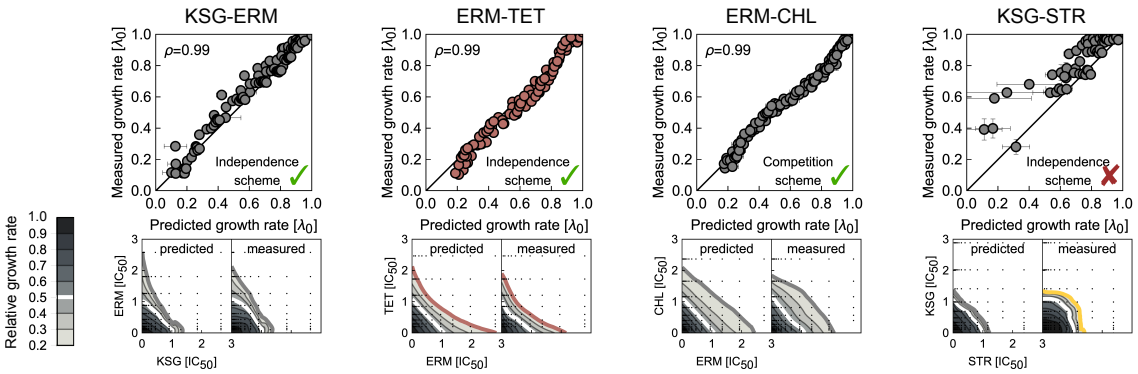

Figure 4.7: **Mathematical model of combined antibiotic action based on growth laws partially predicts drug interactions.** Examples of predicted dose-response surfaces. The scatter plot depicts the correlation between predicted and measured growth rates. Means and error bars (standard deviation) of predicted growth rates are estimated from $n = 100$ bootstrap repetitions. The binding scheme assumed is indicated on the bottom right and Pearson's ρ on the top left. Predicted and measured dose-response surface are shown below the scatter plot. Color of 20% isobole (bottom) and plot markers (top) denotes the type of predicted interaction. The model correctly predicts response surfaces for KSG-ERM, ERM-TET, and ERM-CHL, yet it fails to predict the interaction between STR and KSG.

TET-ERM in Fig. 4.7), indicating that binding kinetics and growth physiology alone suffice to explain these interactions. Correctly predicted drug interactions include additive cases which often involve antibiotics that have either similar modes of action (CRY-FUS, CHL-LCY) or partially overlapping binding sites (CHL-LCY, ERM-CHL) [Wilson, 2014]. For the latter, the assumption that the formation of the doubly-bound ribosome population is prohibited, which yields an additive response surface, offers even better agreement with the experimental data (Fig. 4.7). Occasionally, drug interactions are better explained if competitive binding is assumed (*e.g.*, CHL-TET) even though the binding sites of the antibiotics involved do not overlap.

4.2.1 Symmetric direct interactions on the ribosome amplify drug interactions

We next asked how more general binding schemes, in which two different antibiotics can directly interact on the ribosome to stabilize or destabilize their binding affect the

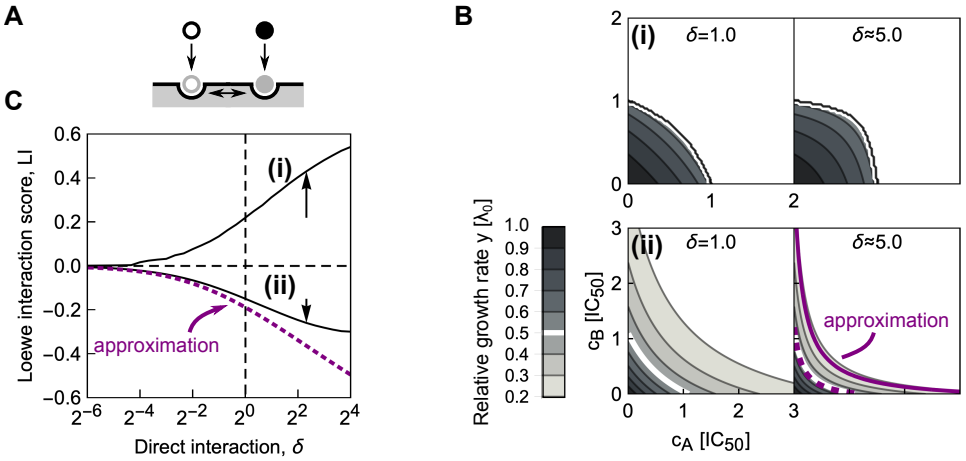

Figure 4.8: **Direct interactions between antibiotics on the ribosome can amplify drug interactions.** **(A)** Schematic of antibiotics symmetrically affecting their binding on the ribosome. **(B)** Changes in the shape of the dose-response surfaces for pairs of antibiotics with (i) identical $\alpha = 2^{-5}$ and (ii) identical $\alpha = 2^{2}$, when δ is increased from 1 (left) to ≈ 5.0 (right). Purple dashed and solid line in the bottom-right panel show the approximate solution in Eq. (4.14) for the 50% and 20% isoboles, respectively. **(C)** Increase in absolute value of the LI score as a function of δ for pairs of antibiotics with different response parameters. Solid lines (i) and (ii) correspond to the examples in B; arrows show increase in $|LI|$ at $\delta \approx 5.0$. Note, that for both antibiotic combinations, LI collapses to 0 for competitive binding, *i.e.*, $\delta = 0$. The dotted line shows the LI score calculated using the approximate solution in Eq. (4.14).

resulting drug interactions. Two antibiotics do not need to come into direct, physical contact to affect each other's binding: Allosteric effects (*i.e.*, changes in ribosome structure due to antibiotic binding) can produce the same result. In the most plausible scenario, the antibiotics affect each other's binding in a symmetric way, *i.e.*, $\delta_{\sigma,i} = \delta_{\sigma,\bar{i}}$ (Fig. 4.8A). For example, the antibiotics lankamycin and lankacidin (which interact synergistically [Auerbach *et al.*, 2010]) are near each other when bound to the ribosome; their binding is stabilized by a direct physical interaction [Wilson, 2014; Belousoff *et al.*, 2011]. Yet, it is unclear if the mutual stabilization of binding necessarily leads to synergy. In principle, stabilization of binding could also increase the sequestration of tightly binding antibiotics or "lock" an antibiotic that would rapidly unbind on its own in the bound state, thus potentially promoting prolonged inhibition of the ribosome. In contrast, the two antibiotics may also mutually

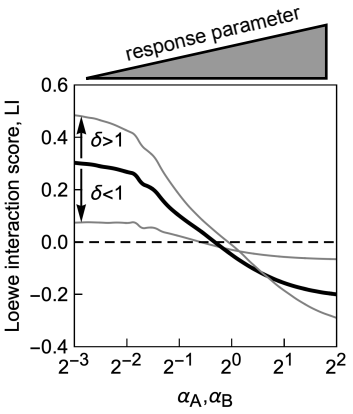

Figure 4.9: **Diagonal cross-section ($\alpha_A = \alpha_B$) through the phase diagram for different δ.** Black solid line corresponds to the case of independent binding (*cf.* Fig. 4.5B); the two gray lines show examples with either $\delta < 1$ or $\delta > 1$. Irrespective of drug interaction type, the drug interaction is amplified for $\delta > 1$ and weakened for $\delta < 1$.

destabilize their binding to the ribosome. The limiting case of this scenario is competition for the same binding site. To investigate such effects systematically, we computed dose-response surfaces for antibiotics with different response parameters α and varying kinetics for the second binding step.

We focused on pairs of antibiotics in which both drugs either have low or high α, corresponding to steep or shallow dose-response curves, respectively. Numerical solutions for continuously varying $\delta_{\mathrm{on},i} = \delta$ at fixed $\delta_{\mathrm{off},i} = 1$ (Fig. 4.8B,C) showed that a stabilizing interaction ($\delta > 1$) enhances the resulting drug interaction. If the drug interaction is antagonistic for $\delta = 1$, stabilization amplifies this antagonism; synergistic interactions are amplified analogously (Fig. 4.8B). If one antibiotic destabilizes the binding of the other, *i.e.*, $\delta < 1$, a smooth transition to additivity occurs, independent of whether the dose-response curve of the antibiotic pair is steep or shallow (Fig. 4.8C). This result is further corroborated by fixing δ and continuously varying α for the combined antibiotics (Fig. 4.9). Taken together, these numerical results indicate that direct positive interactions of translation inhibitors on the ribosome ($\delta > 1$) essentially amplify the drug interaction that occurs in the absence of such direct interactions, irrespective of drug interaction type.

To corroborate these numerical results, we investigated the limit of reversibly binding antibiotics with rapid binding kinetics at low growth rates as for Eq. (4.11).

In this limit, there is again an analytical solution for the dose-response surface:

$$y \approx \frac{\lambda_{\max}/\lambda_0 \left(\delta_{\text{off,A}} + \delta_{\text{off,B}} + c'_A \delta_{\text{on,A}} \delta_{\text{off,B}} + c'_B \delta_{\text{on,B}} \delta_{\text{off,A}}\right)}{\left(1 + c'_A + c'_B\right)\left[\delta_{\text{off,B}} \Phi_A + \delta_{\text{off,A}} \Phi_A\right] + c'_A c'_B \Phi_{AB}}, \tag{4.12}$$

where $\Phi_{AB} = \left[\delta_{\text{on,A}} + \delta_{\text{on,B}} + \delta_{\text{on,A}} \delta_{\text{on,B}} \left(c'_A + c'_B\right)\right]$, $\Phi_B = \left(1 + c'_B \delta_{\text{on,B}}\right)$, and $\Phi_A = \left(1 + c'_A \delta_{\text{on,A}}\right)$. This closed-form expression facilitates the analysis of several limiting cases. For example, if the antibiotics mutually stabilize their binding to the extreme extent that they cannot detach from the double-bound ribosomes anymore ($\delta_{\text{off},i} = 0$), Eq. (4.12) returns $y = 0$ indicating strong synergism. In contrast, prohibiting the formation of double-bound ribosomes by setting $\delta_{\text{on},i} = 0$, yields

$$y_{\text{add}} \approx \frac{\lambda_{\max}/\lambda_0}{1 + c'_A + c'_B}, \tag{4.13}$$

which corresponds to perfect additivity. This corroborates the previous result that competitively binding antibiotics interact additively. For the case $\delta_{\text{on},i} = \delta$ and $\delta_{\text{off},i} = 1$ the expression in Eq. (4.12) simplifies to:

$$y \approx \frac{\lambda_{\max}/\lambda_0}{1 + c'_A + c'_B + \delta c'_A c'_B}, \tag{4.14}$$

which becomes Eq. (4.11) if $\delta = 1$. We can further show that the effect of increasing δ on drug interaction strength depends on the concavity of the individual dose-response curves; for response parameters $\alpha > 2$, increasing δ amplifies synergy (see Appendix A.5). Overall, this analysis corroborates the general result that direct stabilizing interactions of reversibly-binding antibiotics on the ribosome amplify synergistic interactions, while destabilizing interactions weaken them up to the point where any drug interaction becomes additive.

4.2.2 Asymmetric direct interactions alter the phase diagram

More generally, direct interactions between the antibiotics on the ribosome could be asymmetric. For example, binding of only one of the antibiotics could trap the ribosome in a conformation that facilitates the binding of the other antibiotic but not *vice versa*. To investigate such effects, we fixed $\delta_{\text{off},i} = 1$ and varied $\delta_{\text{on},i}$ for

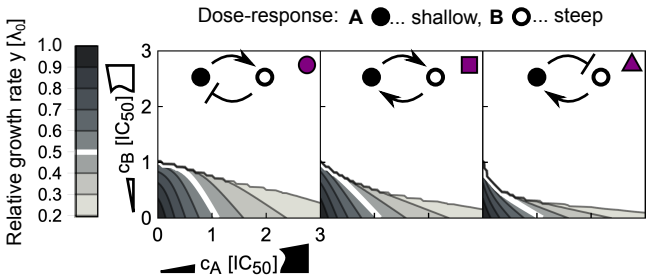

Figure 4.10: **Asymmetric direct interactions reshape the phase diagram of drug interactions.** Dose-response surfaces for different instances of asymmetric direct interaction and response parameters; insets on top show schematics of the type of direct interaction and top-right symbols correspond to those in Fig. 4.10. Antibiotics with shallow ($\alpha_A = 2^2$) and steep ($\alpha_B = 2^{-3}$) dose-response curves are shown by black and white disks, respectively. Left: Antagonism occurs when an antibiotic with a steep dose-response asymmetrically hinders the binding of another one with a shallow dose-response, which in turn promotes the binding of the former. Middle: Symmetrizing the direct interaction almost completely abolishes antagonism. Right: Inverting the scenario from the left-most panel results in mild synergy.

antibiotics with different response parameters α (Fig. 4.10). The resulting difference in kinetic parameters describes an asymmetric direct interaction on the ribosome. We systematically calculated the shape of the dose-response surface for this situation.

When antibiotics with identical response parameters α are combined, the same trend as for symmetric direct interactions occurs: Increasing δ_{on} enhances the drug interaction. For combinations of antibiotics with different dose-response curve shapes, asymmetric direct interactions on the ribosome result in a different behavior (Figs. 4.10-4.11). If an antibiotic with a steep dose-response curve asymmetrically hinders the binding of an antibiotic with a shallow dose-response, while the binding of the former is stabilized by the latter, antagonism emerges (Fig. 4.10). In contrast, synergy occurs if the roles of the antibiotics are inverted. The latter can be rationalized by interpreting the direct interaction on the ribosome as a change of the effective binding characteristics of the antibiotics. Specifically, in the case where the steep-response antibiotic promotes the binding of the shallow-response antibiotic, the latter will in turn destabilize the binding of the former – effectively, the steep-response antibiotic will thus behave as if it had a shallower response. As a result, synergy occurs – exactly as expected when two shallow-response antibiotics are

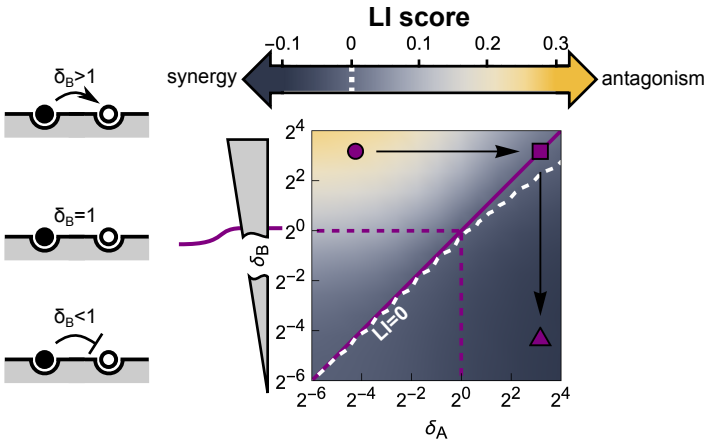

Figure 4.11: **Phase diagram of drug interactions for asymmetric direct interactions between antibiotics with different response parameters.** Different response parameters ($\alpha_A = 2^2$ and $\alpha_B = 2^{-3}$) profoundly affect the resulting drug interaction: A continuous transition from antagonism to synergy occurs (white dashed line denotes $LI = 0$). Purple symbols show the examples from Fig. 4.10 in the phase diagram.

combined (Fig. 4.5B). In the opposite situation, the binding of the shallow-response antibiotic becomes even looser and the binding of the steep-response antibiotic is stabilized. From the phase diagram in Fig. 4.5B, antagonism is the expected outcome in this case as we combine antibiotics with steep and shallow responses, respectively. Taken together, these results show how complicated direct interactions between antibiotics bound to their target can lead to unexpected emergent drug interactions.

4.2.3 Relation to mechanism-independent models of higher-order drug interactions

The biophysical model described above can predict the pairwise drug interactions that are needed to apply recently proposed mechanism-independent models for higher-order drug interactions [Wood *et al.*, 2012]. While a detailed analysis of higher-order drug interactions is beyond the scope of this work, it is instructive to demonstrate how the pairwise interactions bridge the gap between responses to individual drugs and higher-order drug combinations. In the framework of Ref. [Wood *et al.*, 2012], higher-order drug interactions can be predicted using an entropy maximization method, in which the joint drug effects are fully determined

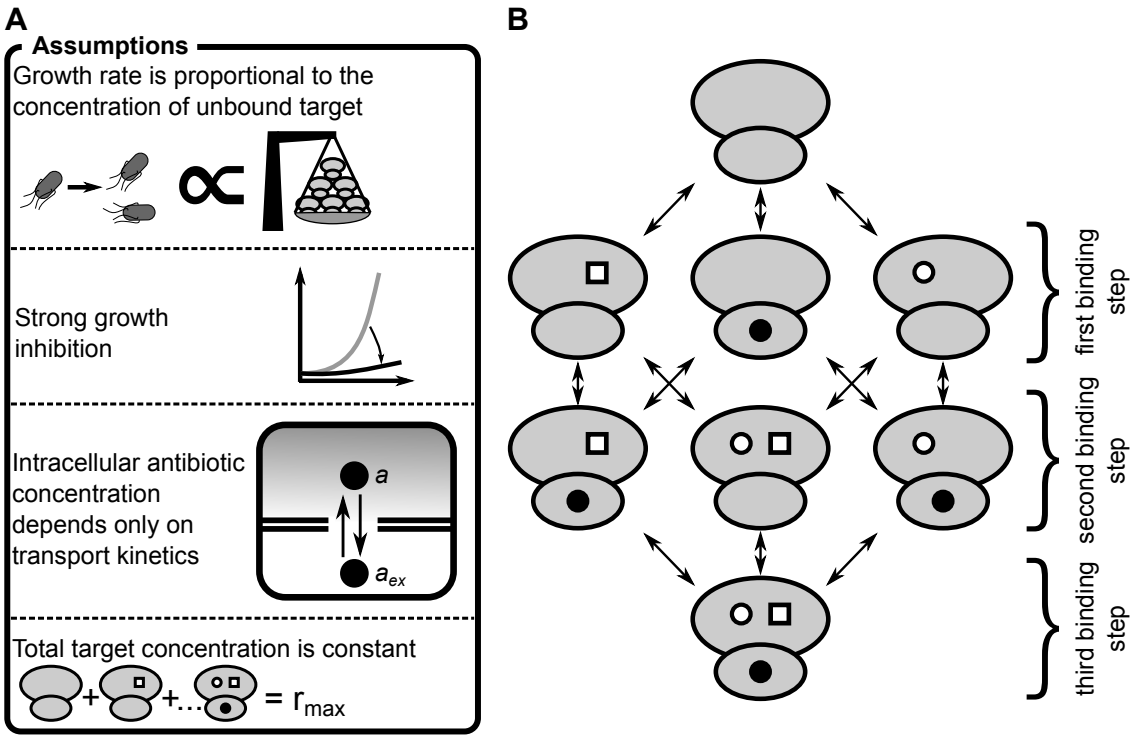

Figure 4.12: **Assumptions and binding kinetics diagram underlying the calculation of higher-order drug interactions. (A)** Assumptions that simplify the system to allow obtaining a closed solution. **(B)** Binding kinetics diagram shows allowed transitions between ribosome subpopulations. Different symbols on the ribosomes denote different antibiotics.

by the responses to the individual drugs (y_i) and their pairwise combinations (y_{ij}):

$$y_{ABC} = y_A y_{BC} + y_B y_{AC} + y_C y_{AB} - 2 y_A y_B y_C. \tag{4.15}$$

In the limit of reversibly binding antibiotics used in Secs. 4.2 and 4.2.1, it is straightforward to analyze the effects of higher-order drug combinations. The approximate results below are based on the assumptions that: (i) the growth rate is directly proportional to the concentration of unblocked ribosomes, (ii) growth rate is nearly zero, (iii) intracellular concentration depends only on transport kinetics (*i.e.*, $a \approx a_{\mathrm{ex}} p_{\mathrm{in}}/p_{\mathrm{out}}$), and (iv) the growth rate is directly proportional to the concentration of unblocked ribosomes (Fig. 4.12A). Under these assumptions, analytical solutions can be obtained. For example, we can construct a system of differential equations describing the binding of three different antibiotics (A, B, C);

the steady-state solution of this system is:

$$y \approx \frac{\lambda_{\max}/\lambda_0}{(1+c'_A)(1+c'_B)(1+c'_C)}. \tag{4.16}$$

To derive this result, we considered three different kinds of single- and double-bound ribosomes as well as triple-bound ribosomes (Fig. 4.12B); for simplicity, all binding steps were considered to be independent of already bound antibiotics. To verify the consistency of mechanism-independent model with this fully specified but approximative mechanistic model, we need to obtain responses to individual drugs y_i and pairwise combinations y_{ij}. We obtain responses $y_i = 1/(1+c'_i)$ and $y_{ij} = 1/[(1+c'_i)(1+c'_j)]$ from Eq. (4.16) by setting $c'_{j,k\neq i}$ and $c'_{k\neq i,j}$ to zero, respectively. If mechanism-independent expression is consistent with our simplified model, then plugging these responses into Eq. (4.15) should yield Eq. (4.16), which is indeed the case.

Next, we tested if the mechanism-independent formula for three drugs [Eq. (4.15)] can be reconciled with our model when there is one direct competitive interaction on the ribosome. If the antibiotics B and C cannot bind to the ribosome simultaneously, the solution of the approximate system is:

$$y_{ABC} = \frac{\lambda_{\max}/\lambda_0}{\left(1+c'_A\right)\left(1+c'_B+c'_C\right)}. \tag{4.17}$$

By following same reasoning as for the independent case above, we see that the mechanism-independent and simplified mechanistic model are consistent.

The assumptions described above can be generalized to antibiotics with other modes of action, provided that the combined antibiotics bind to the same target. For example, if growth is limited by a specific enzyme due to antibiotic inhibition, we can consider the growth rate to be proportional to the abundance of this limiting enzyme. If enzyme concentration does not change (due to lack of compensatory mechanism or due to inability of bacteria to increase its expression further), the approximative mathematical framework from this section is applicable to antibiotics targeting this enzyme. These results provide a potential mechanistic explanation for the apparent validity of the mechanism-independent model, at least for combinations of antibiotics binding the same target.

4.3 Extensions of the model

Other phenomena than those treated so far can shape drug interactions. Below, we discuss two cases in which (1,2) antibiotics perturb translation in orthogonal ways and (3) the expression of antibiotic resistance genes alters a drug interaction. While certainly not exhaustive, these two cases illustrate relevant extensions of the model.

4.3.1 Effects of antibiotic-induced starvation

Translation inhibitors target the protein synthesis machinery, which is carefully regulated in response to changes in the nutrient environment [Scott *et al.*, 2014]. Thus, if an antibiotic effectively interferes with cellular state variables that represent the nutrient environment, it should be possible to predict its effect on the action of a translation inhibitor and, in turn, its drug interaction with a translation inhibitor.

Bacterial growth strongly depends on the availability and quality of nutrients. Protein synthesis requires that amino acids are delivered to the translation machinery (ribosomes) by dedicated proteins [elongation factors (EF-Tu)] [Rodnina, 2018]. The latter bring charged tRNAs (*i.e.,* tRNAs with an attached amino acid) to the ribosome (Fig. 4.13). tRNAs are charged (*i.e.,* amino acids are attached to them) by tRNA synthetases. Usually, the supply and demand of amino acids can be considered to be nearly optimally regulated [Scott *et al.*, 2014] (see Introduction). However, under starvation, a mismatch between the supply and demand of amino acids occurs [Elf and Ehrenberg, 2005]. Bacteria respond to amino acid starvation by triggering the stringent response. This starvation response is primarily controlled by the alarmone ppGpp (guanosine tetraphosphate) which down-regulates the expression of the translation machinery (see Introduction) [Maaløe, 1979]. Amino acid starvation is reflected in reduced tRNA charging and usually occurs when the nutrient environment becomes poor. However, amino acid starvation can also be caused by a starvation-mimicking antibiotic (SMA) that blocks tRNA synthetases (Fig. 4.13) [Durfee *et al.*, 2008; Cassels *et al.*, 1995].

We can capture the effect of an SMA in our model and thus make predictions for the drug interactions between an SMA and translation inhibitors. To this end,

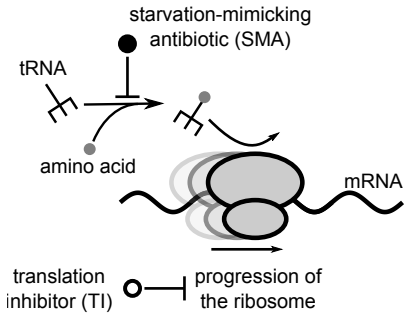

Figure 4.13: **Starvation-mimicking antibiotic.** Translation inhibitors (TI) inhibit progression of the ribosome, while a starvation-mimicking antibiotic (SMA) perturbs the amino acid supply. The ribosome progresses along the mRNA (black wavy line), if charged tRNAs (black fork with gray circle) deliver amino acids (gray circles) at a sufficient rate to support the rapid synthesis. A SMA inhibits tRNA charging and thus mimics amino acid depletion, a hallmark of starvation.

we assume that the growth rate in the absence of drug λ_0, which characterizes the quality of the nutrient environment in Eq. (4.4), depends on the concentration c_s of the SMA only. Under this assumption, the growth rate in the simultaneous presence of an SMA and a translation inhibitor can be derived directly from the previous results for a single antibiotic [Eq. (4.5)]. In the absence of translation inhibitor, the growth rate is given by the dose-response function of the SMA $g(c_s)$. Since $\mathrm{IC}_{50} \propto \left(\alpha^2+1\right)/\alpha$ and $\alpha = \alpha_F/g(c_s)$, the relative change in IC_{50} at constant SMA concentration becomes

$$\psi = \frac{\mathrm{IC}_{50}}{\mathrm{IC}_{50,F}} = \frac{\alpha_F^2 + g^2(c_s)}{\left(\alpha_F^2+1\right) g(c_s)}, \tag{4.18}$$

where α_F and $\mathrm{IC}_{50,F}$ are α and IC_{50} in the absence of the SMA, respectively. It follows that ψ increases monotonically with SMA inhibition if $\alpha_F > 1$; this condition is obtained by solving $\partial_g \psi = 0$ for $g(c_s) \leq 1$. If $\alpha_F \leq 1$, then the minimal ψ is reached at $g(c_s) = \alpha_F$. We further note that two functional limits exist: in the limits $\alpha \to 0$ and $\alpha \to \infty$, Eq. (4.18) becomes $\psi = g(c_s)$ and $\psi = 1/g(c_s)$, respectively.

The dose-response curve for a single antibiotic is given by $y = f(\alpha, c)$ [a solution of Eq. (4.5)]. Since we know how IC_{50} [Eq. (4.18)] and α change as a function of $g(c_s)$, we can evaluate the entire dose-response surface:

$$y(c, c_s) = g(c_s) \times f\left(\alpha_F/g(c_s), c/\psi\right). \tag{4.19}$$

Equation (4.19) deviates from a simple multiplicative expectation since the SMA affects the parameters of the dose-response curve of the translation inhibitor as

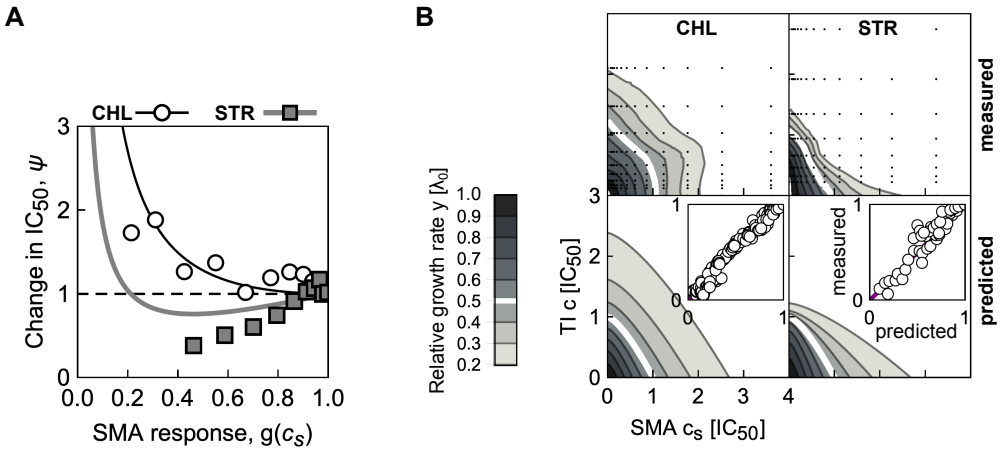

Figure 4.14: **Effects of a starvation-mimicking antibiotic on the efficacy of translation inhibitors.** **(A)** Dependence of relative change in IC_{50} on SMA inhibition $\left(\psi = IC_{50}/IC_{50,F}\right)$. Example solutions of Eq. (4.18) were calculated for chloramphenicol (CHL; black line with $\alpha_F = 1.04$, white circles show experimental data) and streptomycin (STR; gray line with $\alpha_F = 0.46$, gray squares show experimental data). In the experiments, mupirocin (MUP) was used as SMA. The horizontal dashed line indicates no change with respect to $g(c_s)$. Response parameters are from Table F.1. **(B)** Measured (top) and predicted (bottom) dose-response surfaces for CHL-MUP (left) and STR-MUP (right). Insets show scatter-plots of predicted and measured non-zero growth rates.

well. This result illustrates how deviations from Bliss independence occur when the combined drugs mutually affect their dose-response characteristics. Hence, this generalization of our model makes non-trivial quantitative predictions for drug interactions that occur between an SMA and translation inhibitors.

A specific example of an SMA is the antibiotic mupirocin (MUP), which reversibly binds to isoleucin tRNA synthetase and prevents tRNA charging [Hughes and Mellows, 1978]. MUP, which is used against clinically problematic methicillin-resistant *Staphylococcus aureus* (MRSA) infections [Rode *et al.*, 1989], induces the stringent response [Durfee *et al.*, 2008; Cassels *et al.*, 1995] and can thus be used to test our theoretical prediction. To this end, we measured the change of the IC_{50} at different levels of growth inhibition caused by MUP $g(c_s)$ for two translation inhibitors: chloramphenicol (CHL) and streptomycin (STR). CHL and STR have extremely different response parameters α, which leads to different dependencies of ψ on SMA inhibition (Fig. 4.14A), an effect that is closely related to the results for different nutrient environments in Ref. [Greulich *et al.*, 2015]. Similarly, we

measured the complete dose-response surfaces for both drug pairs. The theoretically predicted dose-response surfaces qualitatively agree with the experimentally observed ones (Fig. 4.14B). Below (Section 4.3.2) we discuss further examples of pairwise antibiotic combinations in which a translation inhibitor is combined with a drug that alters the growth law parameters. Together, these results illustrate how our theoretical model can be extended to predict the effects of drug combinations beyond antibiotics that directly target the ribosome.

4.3.2 Combinations of translation inhibitors with drugs that alter growth law parameters

We elaborated above on a specific example of a starvation mimicking antibiotic, which invokes a response that is similar to shifting bacteria to poorer media (*i.e.*, change in λ_0). As growth laws capture this change, a response could be analytically predicted and was experimentally tested. Below we show two more hypothetical examples of antibiotic combinations in which translation inhibitor is combined with a drug that alters growth law parameters. We consider the case in which this hypothetical drug alters either $r_{\min}$ alone or in concert with $r_{\max}$; in either case a shift in growth laws happens, which affects both dynamic range Δr as well as the apparent response parameter α. Here, we note that there is some experimental data illustrating that such shift could be achieved by antibiotics inhibiting *transcription*, *e.g.*, rifampicin (Fig. 4.15 and Supplementary Information of Ref. [Scott *et al.*, 2010]). However, the combined effect of transcription and translation inhibition of translation machinery has not be experimentally assessed.

If we consider an antibiotic that affects the $r_{\min}$, yet it does not affect the κ_t (Fig. 4.15), then the following modification to the growth law arises:

$$\begin{aligned} \lambda_0' = \lambda_0 g_{\min}(x) &= \kappa_t \left(\frac{\lambda_0}{\kappa_t} + r_{\min} - r_{\min}' \right) \\ \implies r_{\min}' &= r_{\min} + \frac{\lambda_0 \left[1 - g_{\min}(x) \right]}{\kappa_t}. \end{aligned} \tag{4.20}$$

Here, we denoted by $g_{\min}(x)$ a dose-response function of a $r_{\min}$-varying antibiotic and x its concentration; $r_{\min}'$ denotes an apparent new $r_{\min}$ as a function of $g_{\min}(x)$. Thus,

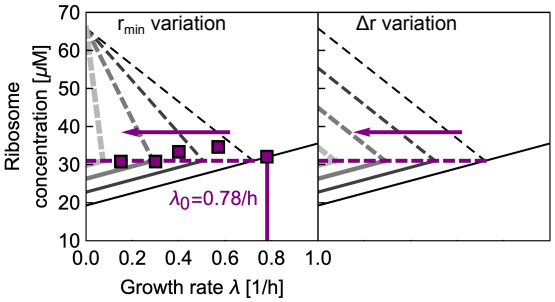

Figure 4.15: Changes in growth laws as a function of variation in $r_{\min}$ (left) and Δr (right). Purple arrow denotes the effect of growth law-varying drug, which alter the "origin" of the translation inhibition growth law line (dashed gray lines). Slope of dashed lines is altered when $r_{\min}$ is varied; when $r_{\max}$ is varied simultaneously with $r_{\min}$ the slope is invariant of the "origin." Purple squares is data describing the ribosome abundance in response to rifampicin from Ref. [Scott *et al.*, 2010]; we converted reported RNA/protein measurements to ribosome concentrations by fixing the drug-free data point to the concentration predicted by the Eq. (4.1) at $\lambda_0 = 0.78\ \mathrm{h}^{-1}$. Note, that the data points lie approximately on the horizontal dashed line.

the reduced dynamic range reads $\Delta r' = r_{\max} - r'_{\min} = \Delta r - \left[1 - g_{\min}(x)\right] \lambda_0/\kappa_t = \Delta r \left\{1 - \left[1 - g_{\min}(x)\right] r_0/\Delta r\right\}$, where we defined $r_0 = \lambda_0/\kappa_t$. Taken together, these relations rescale the response parameter $\alpha = \alpha_F/g_{\min}(x)$ (where α_F is the response parameter for $x = 0$), while the apparent concentration becomes $c' = c/\psi_{\min}$, where

$$\begin{aligned} \psi_{\min} &= \frac{\mathrm{IC}_{50}}{\mathrm{IC}_{50,F}} = \\ &= \frac{\alpha_F^2 + g_{\min}^2(x)}{g_{\min}(x)\left(\alpha_F^2 + 1\right)} \times \left\{1 - \frac{\left[1 - g_{\min}(x)\right] r_0}{\Delta r}\right\}. \end{aligned} \tag{4.21}$$

If we consider that $g_{\min}(x) = 1/(1 + x^n)$, where x is the concentration of $r_{\min}$-varying antibiotic measured in units of IC_{50}, we can calculate the whole dose-response surface as

$$y(c, x) = g_{\min}(x) \times f\left(\alpha_F/g_{\min}(x), c/\psi_{\min}\right), \tag{4.22}$$

where f is a translation inhibitor dose-response curve. Examples are shown in Fig. 4.16.

Model variation discussed above can be expanded in a model in which both $r_{\min}$ and $r_{\max}$ are varied simultaneously (Fig. 4.15). Here, we assume that $r_{\min}$ increases and $r_{\max}$ decreases in concert such that they have the same value at $g_{\Delta r} = 0$ (Fig. 4.15).

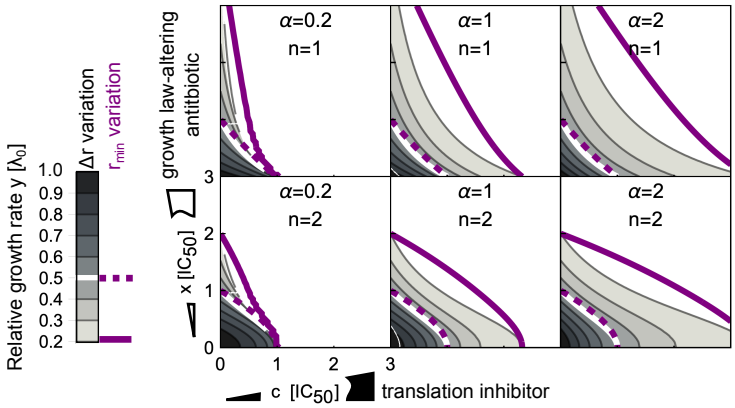

Figure 4.16: Impact of the variation in $r_{\min}$ and Δr on drug interactions. Examples of dose-response surfaces for different translation inhibitors (concentration c; different response parameters α) and different dose-response curves for Δr- and $r_{\min}$-varying antibiotic (concentration x; Hill-function with different steepness parameter n). For easier comparison we overlaid the dose-response surfaces; the purple contours correspond to Δr-varying case.

It follows

$$\begin{aligned}\Delta r' &= r'_{\max} - r'_{\min} = \\ &= \underbrace{r_{\max} g_{\Delta r}(x) + \left[1 - g_{\Delta r}(x)\right](r_0 + r_{\min})}_{r'_{\max}} - \\ &- \underbrace{\left\{r_{\min} + [1 - g_{\Delta r}(x)] r_0\right\}}_{r'_{\min}} = \Delta r\, g_{\Delta r}(x). \end{aligned} \tag{4.23}$$

The response parameter α is rescaled as above; the ratio $\psi = \mathrm{IC}_{50}/\mathrm{IC}_{50,F}$ takes a slightly different form:

$$\psi_{\Delta r} = \frac{\alpha_F^2 + g_{\Delta r}^2(x)}{g_{\Delta r}(x)\left(\alpha_F^2 + 1\right)} \times g_{\Delta r}(x). \tag{4.24}$$

With this at hand, dose-response surfaces can be evaluated (Fig. 4.16). Here we note that the both models give the same result if $r_0 = \Delta r$, which requires $\lambda_0 = \Delta r \kappa_t$. This is intuitive since the ribosome concentration is already at its maximum and only $r_{\min}$ can be varied.

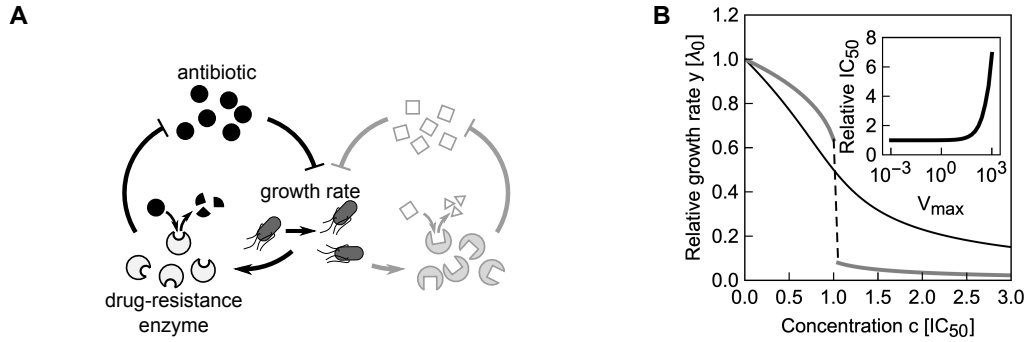

Figure 4.17: **Effects of constitutively expressed resistance genes on the shape of dose-response curve. (A)** Schematic of positive feedback loop for unregulated antibiotic resistance gene. A drug-resistance enzyme degrades the antibiotic, thus reducing growth inhibition and boosting its own expression. However, if the antibiotic concentration exceeds the capacity of removal by the enzyme, growth rate starts to drop and so does the expression of the resistance enzyme, amplifying the growth rate drop. Lightly drawn part (right) illustrates how two antibiotics can get coupled via the growth-rate dependent loop. **(B)** Examples of dose-response curves in the presence or in the absence of a constitutively expressed resistance gene (CERG). Black line shows dose-response curve for $\alpha = 1$. When a CERG is added ($V_{\max} = 1000\ \mu\text{M h}^{-1}$, $K_{\text{rem}} = 0.1\ \mu\text{M}$), the dose-response curve becomes steeper and exhibits an abrupt drop. Inset shows the increase in antibiotic concentration required to halve the growth rate relative to the no-CERG case as a function of $V_{\max}$.

4.3.3 Effect of constitutively expressed resistance genes

Our results show that the steepness of the dose-response curve and the coupling between growth laws and antibiotic response play a key role in determining drug interactions. Recent work showed that dose-response curve steepness can change if genes that convey antibiotic resistance are present [Deris *et al.*, 2013]. Thus, we investigated how the presence of such resistance genes affects the resulting drug interaction.

Bacterial resistance genes often code for dedicated enzymes that degrade the antibiotic or pump it out of the cell. Resistance genes can be constitutively expressed, *i.e.*, they lack specific regulation and their expression depends only on the state of the gene expression machinery. The expression of such constitutively expressed resistance genes (CERGs) under translation inhibition is quantitatively predicted by a theory based on bacterial growth laws [Scott *et al.*, 2010; Deris *et al.*, 2013]: Expression q decreases linearly with decreasing growth rate as $q = q_0\lambda/\lambda_0$, where

q_0 is the expression of the gene in the absence of the drug. An experimentally verified mathematical model that is based on this dependence predicts growth bistability (*i.e.*, coexistence of growing and non- or slowly-growing cells) in bacterial populations that constitutively express resistance genes [Deris *et al.*, 2013]. In this model, the flux of antibiotic removal due to the resistance enzyme is described by

$$j_{\text{rem}} = V_{\max}\left(\frac{\lambda}{\lambda_0}\right) \times \frac{a}{a + K_{\text{rem}}}, \tag{4.25}$$

where K_{rem} is a Michaelis-Menten dissociation constant and $V_{\max}$ is the maximal antibiotic removal rate, which bundles the maximal enzyme abundance and catalytic rate per enzyme.

Due to the linear relation between growth rate and the expression of the resistance gene, the rate of antibiotic removal decreases with decreasing growth rate under translation inhibition. This constitutes a positive feedback loop that leads to growth bistability (Fig. 4.17A,B), which is reflected in a steep dose-response curve of bacterial batch cultures [Deris *et al.*, 2013]. However, note that for very high values of $K_{\text{rem}} \gg a$, Eq. (4.25) becomes linear and the steepness of the dose-response curve decreases, rendering the otherwise bistable system monostable (see Appendix A.1.2).

By extending this scenario to a pair of antibiotics, we can directly test how the presence of resistance genes affects drug interactions. In the most relevant case, there are two CERGs each of which specifically provides resistance to one of the antibiotics. For simplicity, we assume that there is no cross-resistance, *i.e.*, each enzyme specifically degrades only one of the drugs (Fig. 4.17A). We found that the synergistic interaction between two independently binding antibiotics with shallow dose-response curves turns slightly antagonistic due to the presence of resistance genes (Fig. 4.18, top). For competitively binding antibiotics, this effect becomes more pronounced (Fig. 4.18, bottom). In brief, our model predicts drastic qualitative changes in drug interaction type when resistance genes are present.

To test this prediction, we constructed a bacterial strain (see Appendix B) that carries two constitutively expressed resistance genes. We chose TetA [a tetracycline (TET) efflux pump] and CAT [an enzyme that degrades chloramphenicol (CHL)], which were previously characterized in the context of bacterial growth

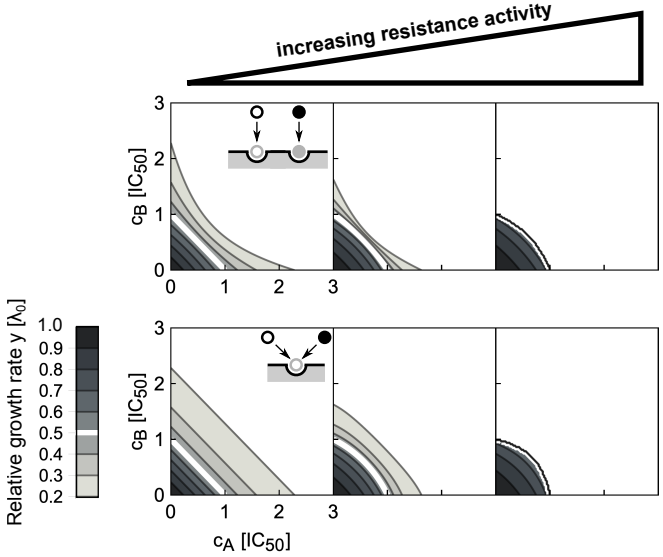

Figure 4.18: **Effects of CERGs on the type of drug interaction.** Dose-response surface for independently (top) and competitively (bottom) binding antibiotics with $\alpha = 1$; resistance activity $V_{\max}$ (assumed to be identical for both antibiotics) increases from left to right: 0, 100, and 950 μM h^{-1}. Concentration axes were rescaled with respect to the increased IC_{50}. Note the qualitative change in dose-response surface shape.

laws (Fig. 4.19A; [Deris *et al.*, 2013]). Furthermore, the interaction between CHL and TET is additive. Our model predicts this interaction to change into antagonism when CERGs are present. Consistent with previous results [Deris *et al.*, 2013], the steepness of the dose-response curve increased upon inclusion of each CERG (Fig. 4.19B). We measured the dose-response surface of the sensitive and the double-resistant strain: Notably, the resistant strain showed a clear antagonistic drug interaction, while this interaction was additive in the strain without CERGs (Fig. 4.19C). This change to antagonism qualitatively agrees with the theoretical prediction (Fig. 4.18). This example shows how resistance genes can drastically alter drug interactions – a phenomenon caused by a non-trivial interplay of gene-expression and cell physiology predicted by our biophysical model.

In future work, this framework could be expanded to include resistance mechanisms other than the efflux and degradation of the drug. Other resistance mechanisms include the target modification, overproduction of the target mimic, and factor-associated protection [Wilson, 2014]. These mechanisms offer attractive mod-

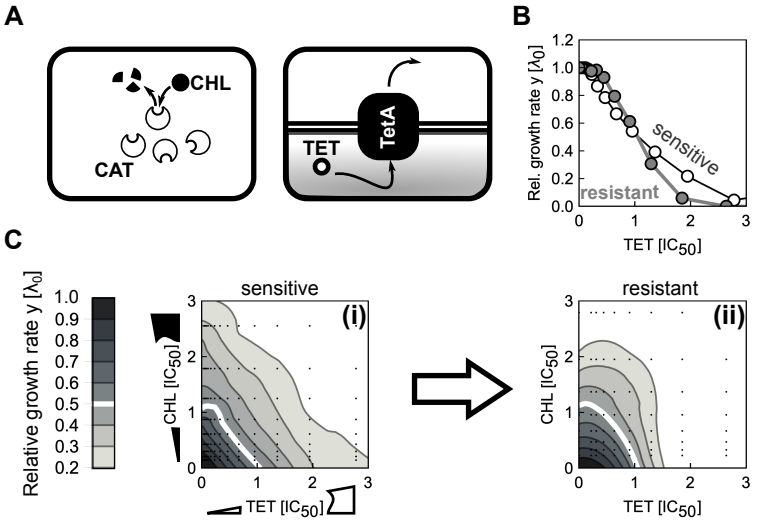

Figure 4.19: **Constitutively expressed resistance genes alter a drug interaction as predicted by theory. (A)** Schematic showing two common resistance mechanisms: Resistance can result from degradation of the drug [left: chloramphenicol acetyltransferase (CAT) degrades chloramphenicol (CHL)] or from drug efflux [right: an antibiotic efflux pump (TetA) removes tetracycline (TET) from the cell]. **(B)** Change in dose-response curve shape due to a constitutively expressed resistance gene. CHL dose-response curves of sensitive (white circles) and resistant strain (gray circles). **(C)** Measured CHL-TET dose-response surfaces for (i) sensitive and (ii) resistant strain. Concentrations were normalized to the IC_{50} of respective strains. The strain with CERGs is 50.5 and 91.5 times more resistant to TET and CHL, respectively, as measured by increase in IC_{50}. Drug interaction changes from additive to antagonistic as suggested by theory (Fig. 4.18).

eling and experimental opportunities. On the modeling side, these additional mechanisms require the introduction of new sub-populations of ribosomes (modified or factor-associated) or target mimics. Experimentally, handling these highly resistant strains is challenging as minimal inhibitory concentrations approach the solubility limits of a particular antibiotic, which requires fine-tuning of the expression system. While these extensions are of high basic and clinical importance, they are outside of the scope of this study. Here we included only the best-characterized examples that required minimal genetic intervention into the system.

4.4 Interim discussion

We constructed a minimal biophysical model of antibiotic interactions that takes into account the laws of bacterial cell physiology. Most parameters in our model are constrained by established results or by the dose-response curves of the individual antibiotics that are combined (Fig. 4.5). Our approach offers a scalable theoretical framework for predicting drug interactions: The number of parameters required for the independent binding model scales linearly with the number of antibiotics. This framework is readily generalized to combinations of more than two antibiotics. Ribosomal growth laws [Scott *et al.*, 2010] were essential for building this predictive framework, highlighting the importance of quantitative phenomenological descriptions of physiological responses to drugs and other perturbations (Fig. 4.2). The discovery of similar quantitative relations between physiological parameters and growth rate for other classes of antibiotics and other types of cells would greatly facilitate more general predictions of drug interactions.

Our work highlights the advantages of a physiologically relevant "null model," which captures all effects that are generally relevant for ribosome-binding antibiotics without trying to describe any molecular details of specific antibiotics (Fig. 4.5). While general multiplicative (Bliss) or additive (Loewe) expectations are simple to construct, our work demonstrates that their utility as a reference has clear limitations. Specifically, our model shows that both are expected to be valid only in certain limits (Figs. 4.6 and 4.8). Moreover, these standard null models do not capture known effects of antibiotic binding and growth physiology, which suffice to produce strong deviations from the standard null models. Our biophysical model captures these effects and thus offers an improved expectation for drug interactions. Generalizing this model to three drugs demonstrated that mechanism-independent predictions of higher-order interactions [Wood *et al.*, 2012] are consistent with simplified first-order kinetics. In summary, our model serves as a bridge between mechanism-independent general predictions of drug interactions and elusive quantitative descriptions of detailed molecular mechanisms that capture the idiosyncrasies of each drug.

We showed that direct physical (or allosteric) interactions of antibiotics on their

target do not necessarily lead to synergy (Figs. 4.8 and A.3). Synergy only occurs if the dose-response curves of the individual drugs are sufficiently shallow. While this insight is not easily applied in the design of drug combinations, the identification of cooperatively binding drug pairs still has considerable potential. Our results highlight that altering the steepness of individual drug dose-response curves may offer under-appreciated opportunities for drug design.

The predictions of our model are directly testable in experiments (Figs 4.19, 4.14, and 4.7). Perhaps the most striking experimental validation of our model is the change in drug interaction type due to the presence of antibiotic resistance genes (Fig. 4.18, Fig. 4.19C). This observation is notable since previous work concluded that most mutations and mechanisms that provide resistance to individual drugs only rescale the effective antibiotic concentrations while preserving the shape of the dose-response curves and surfaces [Chevereau *et al.*, 2015; Wood *et al.*, 2014; Chevereau and Bollenbach, 2015; Chait *et al.*, 2007]. In contrast, our results show that specific resistance genes for two antibiotics targeting the ribosome inevitably alter the drug interaction, even in the absence of more complicated mechanisms.

Discrepancies between experimental results and model predictions can expose cases in which more complicated mechanisms cause the observed drug interaction. A limitation of our model is that it considers fully assembled translating ribosomes as sole targets of the antibiotics, without taking the exact stage of the translation cycle into account. In principle, a model that describes ribosome assembly and more details of the translation cycle and the transitions between its different steps could provide a more detailed mechanistic picture. However, since we currently do not know the *in vivo* parameter values that characterize the translation cycle, such a model would not be predictive, but would rather rely on extensive fitting of free parameters to limited experimental data. Instead, the underlying mechanisms of drug interactions that cannot be captured by the minimal biophysical model presented here, and in particular suppression, can be elucidated by targeted phenomenological approaches, which we focus on next.

5 Inducible genetic bottlenecks in translation

Certain drug interactions clearly deviated from the model predictions. An example is the suppressive/antagonistic interaction between STR and KSG, which was predicted to be additive (Fig. 4.7). Such clear deviations could originate from direct molecular interactions of the drugs on the ribosome, and thus be specific for every drug pair. Alternatively, these drug interactions could result from the multi-step structure of the translation cycle itself, which our model does not take into account. Simple partitioning of ribosomes into different populations that are susceptible to different antibiotics does not alter the drug interaction (Appendix A.5.1). In the most complex cases, drug interactions could result from drug effects that are unrelated to the primary drug target [Chevereau and Bollenbach, 2015], in particular from effects on drug uptake or efflux [Lazar *et al.*, 2013]. We focused on the plausible hypothesis that drug interactions are caused by the interplay of ribosomes halted in different stages of translation cycle such as initiation, translocation, recycling, etc. (Fig. 3.1).

To test this hypothesis, we developed a technique for measuring how halting ribosomes in different stages of the translation cycle affects the efficacy of various antibiotics. Specifically, we imposed artificial bottlenecks in translation by genetically limiting the expression of translation factors that catalyze well-defined translation steps [Cole *et al.*, 1987]. We constructed *E. coli* strains with translation factor genes under inducible control of a synthetic promoter [Lutz and Bujard, 1997]. These genes were integrated into the chromosome outside of their endogenous loci and the endogenous copy of the gene was disrupted (Fig. 5.1A; Methods). This procedure yielded six strains that enable continuous control of key translation processes (Fig. 5.1B): stabilization of the 50S subunit (*der*), initiation (*infB*), delivery of charged tRNAs (*tufA/B*), release of GDP from elongation factors (*tsf*), translocation

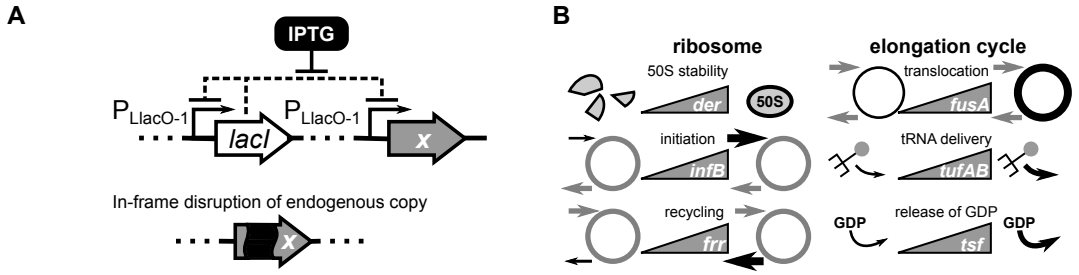

Figure 5.1: **Artificial translation bottlenecks. (A)** Schematic of synthetic regulation introduced to control the expression of a translation factor *x*, which creates an artificial bottleneck in translation at a well-defined stage; *lacI* codes for the Lac repressor, which represses the $P_{LlacO-1}$-promoter (Methods, [Lutz and Bujard, 1997]). **(B)** Constructs were made for six translation factors mediating 50S stability (*der*), initiation (*infB*), recycling (*frr*), translocation (*fusA*), tRNA delivery (*tufAB*) and GDP release (*tsf*), respectively. Higher expression alleviates the artificial bottleneck. Thicker lines or arrows indicate higher rates.

(*fusA*) and recycling of ribosomes (*frr*) [Rodnina, 2018].

Reducing translation factor expression by varying the inducer concentration resulted in a gradual decrease in growth which stopped at almost complete cessation of growth, reflecting the essentiality of translation factors (Fig. 5.2; Appendix B and Fig. E.5). Since the endogenous regulation of translation factors generally follows that of the translation machinery [Maaløe, 1979; Gordon, 1970; Blumenthal *et al.*, 1976; Furano and Wittel, 1975], limiting the expression of a single translation factor imposes a highly specific bottleneck as all other components get upregulated. Any global feedback regulation is left intact as we removed the factor from its native operon. Similar genetic perturbations further conform to bacterial growth laws [Scott *et al.*, 2010; Cole *et al.*, 1987; Olsson *et al.*, 1996], supporting that translation factor deprivation is a suitable means of assessing responses to targeted perturbations of translation. While antibiotics often have secondary targets and other non-specific effects on the cell, thus obfuscating experiments, translation factor deprivation is highly specific. Our synthetic strains offer precise control over artificial translation bottlenecks that determine the rates of different translation steps and enable disentangling phenomena that are caused by the primary mode of action of antibiotics from those that result from other effects of these drugs.

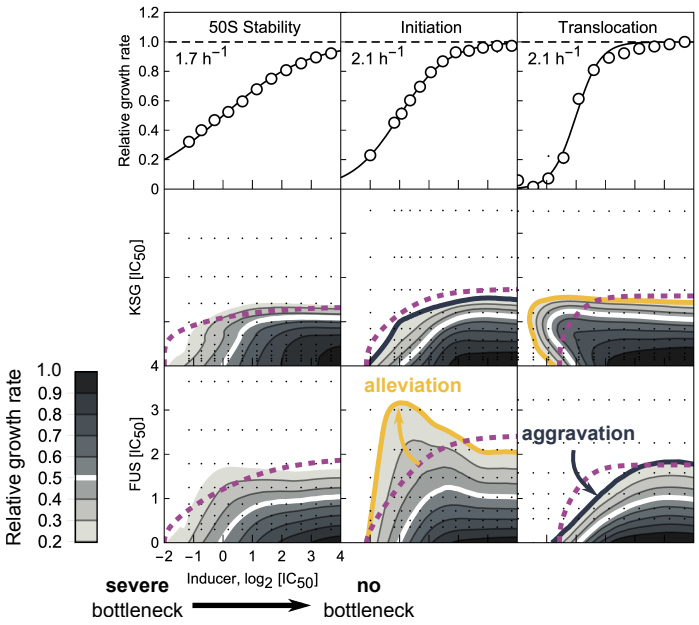

Figure 5.2: **Artificial translation bottlenecks strongly affect antibiotic efficacy.** Translation factor induction curves (upper row) and response surfaces over the inducer-antibiotic grid for different antibiotics (KSG and FUS, middle and bottom row, respectively) in combination with different bottlenecks (50S stability, initiation, and translocation). Full induction of the translation factor rescues wild type growth; increasing bottleneck severity leads to a smooth decrease in growth rate to zero. Induction curves were measured in $n = 8$ technical replicates, and median value of non-zero growth rates was calculated. Comparison of the response surfaces with independent expectation (dashed purple line) identify alleviation (orange line) or aggravation (blue line).

We used these synthetic strains to assess the impact of bottlenecks on antibiotic efficacy. We measured growth rates over a two-dimensional matrix of concentrations of inducer and antibiotic for each of the six strains (Fig. 5.2; Appendix B). To assess if the action of the antibiotic is independent of the translation bottleneck, we analyzed these experiments using a multiplicative null expectation. Note that additivity, as used for antibiotics (Fig. 3.3), is not a suitable null expectation here since the responses to increasing concentrations of antibiotic and inducer are opposite. However, if antibiotic action is independent of the translation bottleneck, the growth rate should be a product of the relative growth rates of each of the two perturbations acting individually. Independence implies that the dose-response surface is obtained as a multiplication of the antibiotic dose-response and the translation factor induction curve. Deviations from independence indicate a nontrivial interaction between the

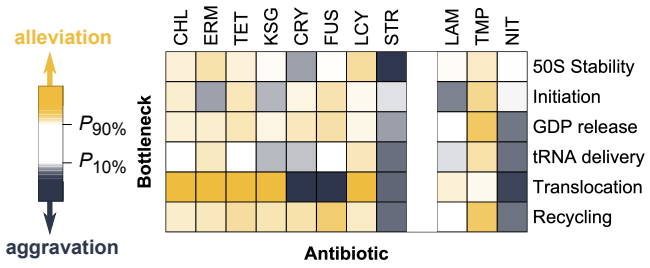

Figure 5.3: **Bottleneck-dependency scores.** Columns show bottleneck dependency vectors in color code; dependency vectors quantify the response of a given antibiotic to the translation bottlenecks (see C.3.2 and Fig. C.2).

bottleneck and the antibiotic action.

We systematically identified interactions between translation inhibitors and bottlenecks by their deviation from independence. In general, antibiotic action can be alleviated or aggravated by a given bottleneck, i.e., the bacteria can be less or more sensitive to the antibiotic due to the bottleneck, respectively. We quantified the magnitude of these effects by bottleneck dependency (BD) scores (Appendix C) and collected them into a single bottleneck dependency vector per antibiotic. The components of this vector describe the interactions between the antibiotic and all six translation bottlenecks. Bottleneck dependency vectors were diverse (Fig. 5.3), indicating that bottlenecks at different stages of the translation cycle differentially affect antibiotic efficacy. These results are consistent with the hypothesis that the high diversity of drug interactions between translation inhibitors (Fig. 3.4) originates in the diversity of translation steps targeted by the drugs (Fig. 3.1).

5.1 Antibiotic fingerprinting

The bottleneck dependency vector of a given antibiotic provides a quantitative, functional summary of its interactions with the translation cycle. In this sense, it is a characteristic "fingerprint" of the antibiotic. Clustering of antibiotics based on their bottleneck dependency vectors (Fig. 5.4) robustly grouped antibiotics with a similar mode of action (CRY and FUS, LCY and CHL in Fig. 5.4, respectively). Notably, this approach separated the translocation inhibitors CRY and FUS from

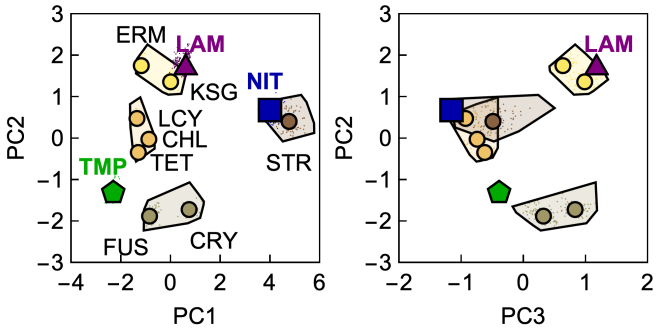

Figure 5.4: **PCA projections of BD vectors.** Clustering of the bottleneck dependency vectors upon dimensionality-reduction by Principal Component Analysis (PCA; see C.3.3). Circles show dependency vectors projected onto the two principal components (PC1,2 and PC2,3 on the left and right, respectively); colors indicate cluster identity. The extended cluster areas shown are convex hulls of bootstrapped projections (denoted by dots). Projections of the three additional antibiotics LAM, NIT, and TMP are denoted by a purple triangle, blue square, and green pentagon, respectively. We estimated the p-value$\approx 3 \times 10^{-4}$ by clustering $n = 10^4$ reshuffled datasets with added noise and counting the fraction of instances that matched the shown clustering result. See Appendix C and Eq. (C.4); we did not use a standard statistical test.

STR, which only weakly affects translocation [Peske *et al.*, 2004]. Drug interactions between antibiotics from the same cluster were strictly additive (Figs. 3.4 and 5.4). These results show that interactions of antibiotics with translation bottlenecks have explanatory power for drug mode of action and can expose antibiotics acting as substitutes for one another.

While the clustering of certain antibiotics can be rationalized from their presumed modes of action, this is more challenging for others. To further assess the value of this analysis, we measured bottleneck dependencies for three additional antibiotics: lamotrigine (LAM), trimethoprim (TMP), and nitrofurantoin (NIT). As we elaborate below, using drugs with a defined mode of action (LAM and TMP) corroborates the utility of clustering by bottleneck dependencies, while the similarity of STR to NIT, which has multiple modes of action, suggests a plausible reason for the separation of STR from other clusters of translation inhibitors.

To challenge the predictive power of translation bottlenecks, we tested whether the mode of action of a partially characterized antibiotic can be inferred from its bottleneck dependency vector. We focused on lamotrigine (LAM), an anticonvulsant

drug which was recently identified to inhibit maturation and in turn reduce the number of translating ribosomes, potentially by interfering with initiation factor 2 (IF2, encoded by *infB*) [Stokes *et al.*, 2014]. The bottleneck dependency vector of LAM was most similar to that of KSG (Fig. 5.4). As for LAM, a reduction of translating ribosomes is a signature of the initiation inhibitor KSG [Kaberdina *et al.*, 2009]. Hence, this observation further corroborates that similar bottleneck dependency vectors for translation inhibitors indicate similar mode of action. Bottleneck dependency vectors indicated an unexpected similarity in effective mode of action between ERM and KSG (Fig. 5.4), an initiation inhibitor. These data suggest that ERM, which cannot block the synthesis of some proteins above a certain length [Kannan *et al.*, 2012], may effectively act as an initiation inhibitor. These results show that bottleneck dependency vectors often confirm established similarities but can also provide complementary insights into effective drug mode of action.

We further tested how an antibiotic with a mode of action unrelated to translation interacts with translation bottlenecks. If drug interactions are primarily determined by their mode of action [Yeh *et al.*, 2006; Brochado *et al.*, 2018], antibiotics interfering with processes unrelated to translation should be affected similarly by all different translation bottlenecks as the net effects of translation bottlenecks are indistinguishable – all lead to cessation of protein synthesis. To test this idea, we chose the antibiotic trimethoprim (TMP), which inhibits folate synthesis by binding to dihydrofolate reductase and is not known to directly perturb translation [Walsh, 2003]. Its bottleneck dependency vector indicates that all bottlenecks alleviated TMP's action to various degrees (Fig. 5.3) – a characteristic that is incompatible with any of the clusters of translation inhibitors (Fig. 5.4). Furthermore, TMP is known to primarily interact antagonistically or suppressively with translation inhibitors [Yeh *et al.*, 2006; Bollenbach *et al.*, 2009]. These results support the idea that the effects of specific translation bottlenecks are diverse for antibiotics targeting translation, but not for antibiotics with modes of action unrelated to translation.

Streptomycin stands out among translation inhibitors, as its action is aggravated by all translation bottlenecks (Fig. 5.3). This might be a consequence of its multiple modes of action: besides interfering with tRNA binding, it slightly lowers the

translocation rate [Peske *et al.*, 2004] and causes protein mistranslation, changes in membrane potential, and membrane permeabilization [Davis, 1987]. These phenomena can lead to unspecific downstream effects in the cell. Therefore, we probed if such unspecific effects can explain its distinct response to translation bottlenecks by measuring the bottleneck dependency vector of the prodrug nitrofurantoin (NIT). Nitrofurantoin has complicated effects on the bacterial cell, including the formation of non-native disulfide bonds in protein structures [Bandow *et al.*, 2003], DNA damage, and oxidative stress [Mitosch *et al.*, 2017]. The similar bottleneck dependency between STR and NIT (Fig. 5.3) is likely due to unspecific effects common to both drugs, such as the production of dysfunctional proteins.

5.2 Drug interactions can be predicted from antibiotic responses to translation bottlenecks

We reasoned that the effects of translation bottlenecks on antibiotic action should also have predictive power for drug interactions between translation inhibitors. We therefore sought a quantitative way of probing the contribution of translation bottlenecks to drug interactions between translation inhibitors.

Ribosomes progress through the translation cycle in a sequence of steps (Fig. 5.5A). Antibiotics and genetic translation bottlenecks hinder this progression by reducing the transition rates between these steps. If an antibiotic specifically targets a single translation step and reduces the same transition rate as a genetic translation bottleneck, the effects of the drug and the bottleneck should be equivalent, i.e., the consequences of any perturbation elsewhere in the translation cycle should be independent of the exact means by which such a reduction is achieved (Fig. 5.5B).

5.2.1 Additive interactions and remapping

To establish the equivalence of specific translation bottlenecks and antibiotic action, we first transformed the measurements of growth rate as a function of translation factor induction into dose-response curves of a corresponding idealized antibiotic

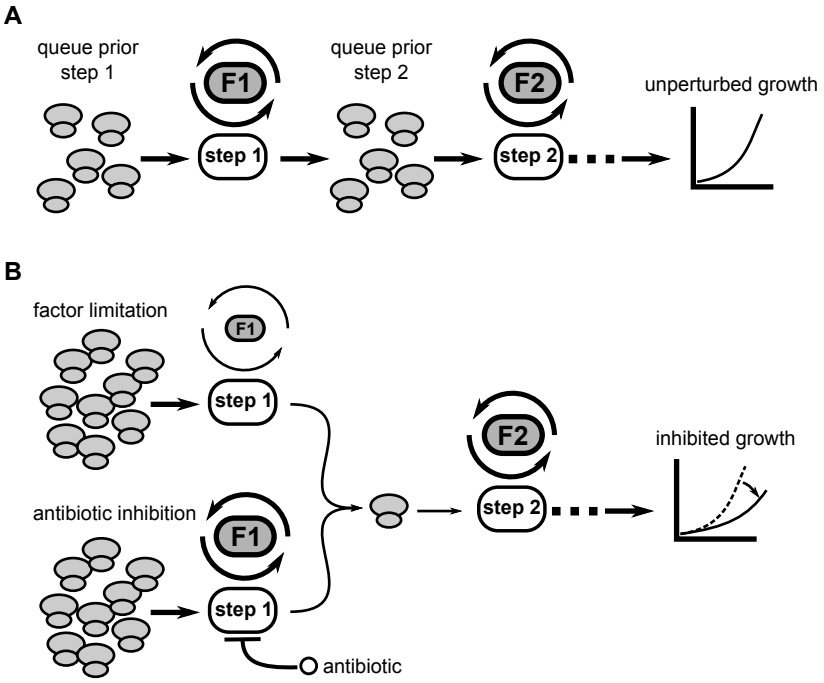

Figure 5.5: **Translation factor deprivation mimics the action of equivalent antibiotics. (A)** Schematic of translation as a sequence of steps (white), catalyzed by translation factors (gray). In the absence of perturbations, ribosomes progress through the steps unimpeded, resulting in unperturbed growth. **(B)** Schematic of perturbed translation. Top: as the abundance of factor F1 is lowered (smaller factor symbol), the rate of step 1 decreases (thinner arrows) and ribosomes queue in front of the bottleneck. Bottom: the same rate is reduced by an antibiotic. The effects of factor deprivation and antibiotic action on growth are equivalent.

that targets a single translation step with perfect specificity. In essence, this procedure converts inducer concentrations into equivalent antibiotic concentrations: the two concentrations are identified as equivalent if they lead to the same relative growth rate (Fig. 5.6A,B; Appendix C). If the perturbations of factor and antibiotic are equivalent, then the true and the idealized antibiotic should act as substitutes for each other, and exhibit an additive drug interaction. Conversely, we can use this comparison (Fig. 5.6C and Fig. E.6) to test systematically if the action of antibiotics is quantitatively equivalent to specific translation bottlenecks.

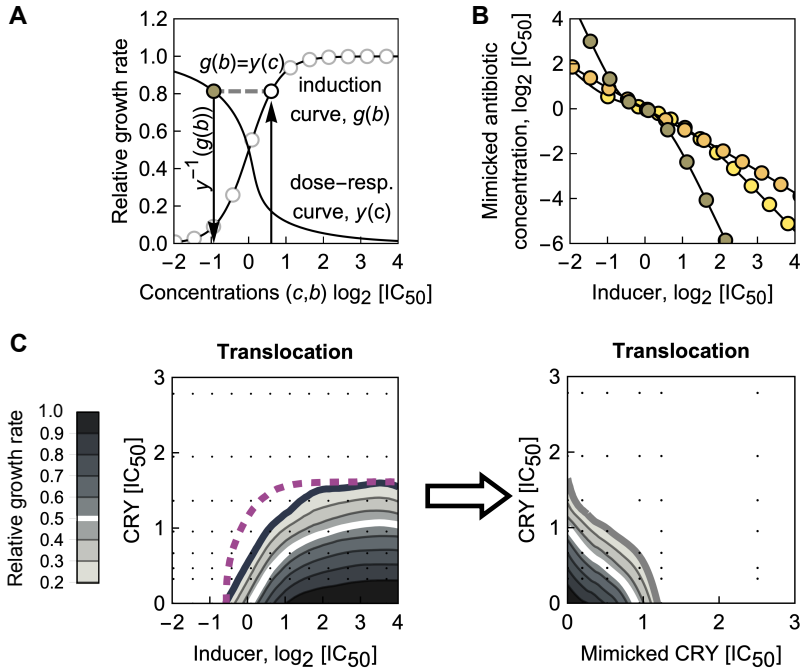

Figure 5.6: **Translation factor deprivation mimics the action of equivalent antibiotics. (A)** Schematic of conversion of inducer concentration b (here for the translocation factor) into the mimicked antibiotic concentration c (here: CRY). For each inducer concentration b, the growth rate from the induction curve $g(b)$ is determined and the same growth rate on the antibiotic dose-response curve $y(c)$ is identified (gray dashed line); the inverse function of the dose-response curve yields the equivalent antibiotic concentration as $c = y^{-1}\left(g(b)\right)$. **(B)** The resulting conversion of inducer concentration b into antibiotic concentration c for three different pairs of equivalent perturbations: CRY-translocation (gray), KSG-initiation (yellow), and TET-tRNA delivery (orange). **(C)** Inducer-antibiotic response surface (left) and mimicked antibiotic-antibiotic response surface (right) upon conversion of inducer concentration as in C and D. Purple dashed line shows isobole for multiplicative responses at relative growth rate 0.2. The remapped response surface is additive, corroborating the equivalence of CRY and translocation factor deprivation.

We found that the effect of certain translation inhibitors is almost perfectly mimicked by translation bottlenecks. Within our selection of antibiotics, several strong candidates for equivalent perturbations exist (Fig. 3.1): CRY, FUS, and potentially STR with EF-G (translocation); KSG with IF2 (initiation); and TET with EF-Tu (tRNA-delivery). For example, remapping the response to CRY and EF-G yields an additive surface (Figs. 5.6C, 5.7A), corroborating that CRY and the EF-G translocation bottleneck are equivalent perturbations. In contrast, if the bottleneck is

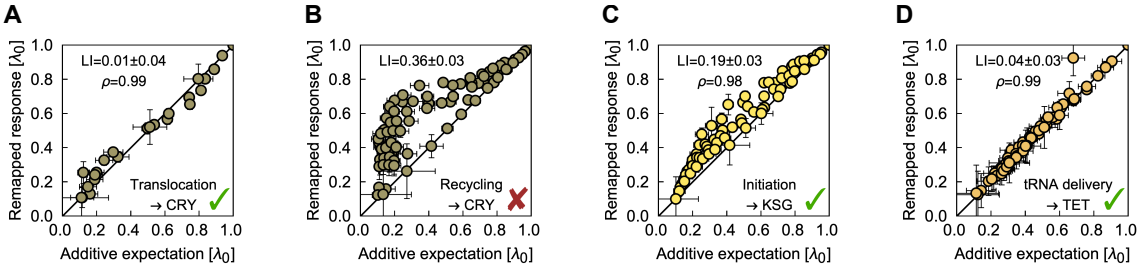

Figure 5.7: **Comparison of response surfaces remapped to the additive expectations.** The bottlenecks and antibiotics are shown on the bottom right, respectively. Errors in LI and in expected and remapped responses were evaluated by bootstrapping (see Sec. C.4.1 and Fig. E.6). **(A)** Additive expectation from Fig. 5.6C and remapped response surface agree ($\rho = 0.99$). **(B)** As A, but for a recycling bottleneck. The large and statistically significant discrepancy in LI from 0 indicates that CRY and a recycling bottleneck are not equivalent. **(C)** As A, but for KSG and an initiation bottleneck ($\rho = 0.98$). **(D)** As A, but for TET and a tRNA delivery bottleneck ($\rho = 0.99$).

not equivalent to the drug, remapping does not yield an additive response surface; an example is CRY and the recycling bottleneck (Fig. 5.7B). Occasionally, marginal effects dominate the apparent equivalence: STR lowers translocation rate only two-fold [Peske *et al.*, 2004], but inhibiting translocation by deprivation of EF-G is still the best mimic of STR. In general, demonstrating that the action of an antibiotic is equivalent to a specific translation bottleneck provides strong quantitative evidence for its primary mode of action, since translation factors control individual steps with high specificity.

In contrast, the common approach of overexpressing the drug target does not provide useful insights into the mode of action of ribosome-targeting antibiotics. Simple overexpression requires a well-defined drug target like a single protein; overexpressing the ribosome is impractical [Jinks-Robertson *et al.*, 1983] and would

not help distinguish the precise action of different ribosome-targeting antibiotics. Even for less complex drug targets, the interpretation of overexpression assays is challenging [Palmer and Kishony, 2014]. Still, we tested if simple overexpression of translation factors can provide similar insights into the mode of action of TET as translation bottlenecks. Overexpression of translation factors only weakly affected antibiotic efficacy (Fig. B.4). The effects of overexpressing different translation factors were not specific for antibiotic mode of action (Fig. B.4). Hence, unlike the depletion of translation factors, their overexpression provides no information about drug interactions with other antibiotics.

5.2.2 Prediction of drug interactions

For antibiotics that are equivalent to specific translation factors (Fig. 5.7), drug interactions with other antibiotics can be directly predicted from translation bottleneck measurements. In practice, this is done by remapping the antibiotic-translation factor response surfaces as described above (Fig. 5.8). Unlike the predictions of

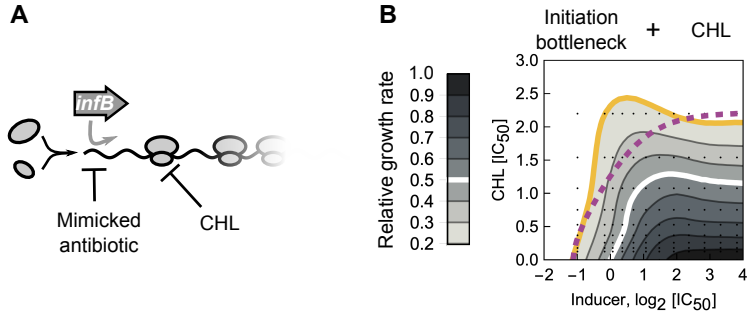

Figure 5.8: **Information drug-interaction is contained in bottleneck-antibiotic interaction. (A)** The drug interaction between CHL and an antibiotic that targets initiation can be predicted through mimicking the initiation inhibition by limiting the expression of initiation factor (*infB*). **(B)** The response surface of CHL combined with the inducer for the initiation (*infB*) bottleneck shows mild alleviation. This response surface contains information about the interaction between CHL and any antibiotic that interferes with initiation. The inducer axis is remapped into mimicked antibiotic concentration (Fig. 5.6).

the biophysical model (Chapter 4), the predictions made in this way are not based on a mathematical model, but rather on empirical effects of genetic perturbations, which are quantitatively converted into equivalent drug effects; in particular, they

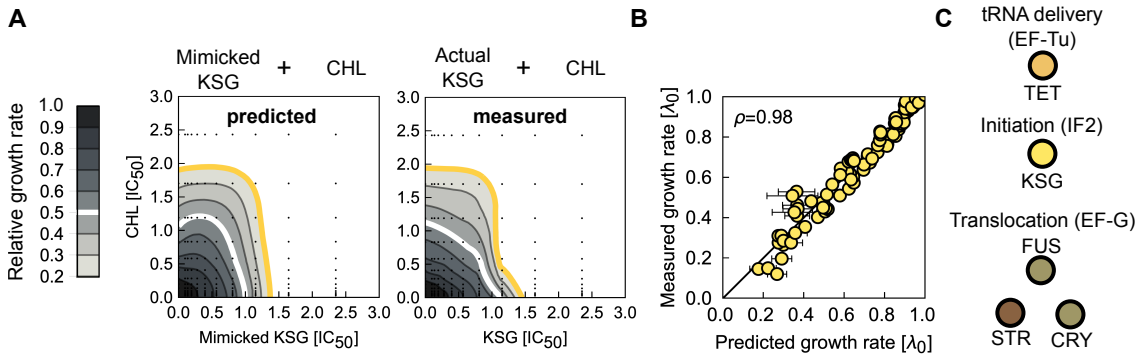

Figure 5.9: **Example of drug-interaction prediction based on the equivalent translation bottlenecks. (A)** Left: resultant prediction of the response surface for the initiation-inhibiting antibiotic KSG and CHL. Right: measured KSG-CHL response surface for direct comparison; strong antagonism is observed as predicted.**(B)** A point-by-point comparison of predicted and measured response surfaces (Pearson's ρ = 0.98).**(C)** Schematic showing antibiotics and their equivalent translation factor bottlenecks. Drug interactions with these antibiotics can be predicted for any antibiotic with a known response to the equivalent bottleneck. Color-code shows cluster identity from Fig. 5.1.

are independent of the assumptions underlying the biophysical model. While the biophysical model is only valid for antibiotics that conform to bacterial growth laws, the predictions based on the observed effects of translation bottlenecks are independent of whether or not the growth laws hold for the specific perturbations of translation used. The resulting prediction will be faithful if the drug interaction originates exclusively from the interplay of two translation bottlenecks.

Drug interactions predicted using this procedure were often highly accurate (Fig. 5.10). In particular, some of the most striking cases of antagonistic and suppressive interactions were correctly predicted. For example, the prediction of antagonism between CHL and KSG was quantitatively correct (Fig. 5.9). The same interactions were correctly predicted for LCY (Fig. 5.10), which is similar to CHL (Figs. 3.1 and 5.4). Remapping qualitatively accounted for nearly all observed interactions of KSG with quantitative agreement in several cases (Fig. E.7), including the previously unexplained KSG-STR interaction (Fig. 5.10). Further, suppression of FUS by CHL was correctly predicted: FUS loses potency when CHL is added (Fig. 5.10). In this way, several drug interactions with previously elusive mechanisms are explained by the interplay of the specific steps in the translation cycle that are targeted by the

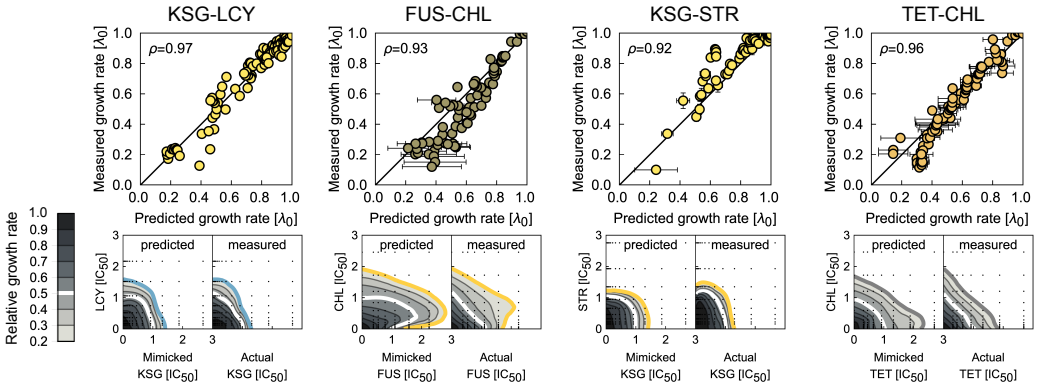

Figure 5.10: **Comparison of predicted and measured response surfaces for different antibiotics in combination with antibiotics that have a factor analog.** Top row: scatter plots as in **(D)**; bottom row: predicted and measured response surfaces, respectively. Remapping correctly predicts antagonism (KSG-LCY), suppression (FUS-CHL), strong antagonism (KSG-STR), and additivity (TET-CHL).

antibiotics involved.

Remapping correctly predicted additive drug interactions between antibiotics that could not be easily explained by the biophysical model. As noted above, additivity between CHL-TET was predicted for the competitive binding scheme; yet, competitive binding is difficult to rationalize as TET and CHL bind to different subunits. Similarly, the additive pair KSG-ERM is even more puzzling since, unlike ERM, KSG does not act within the elongation cycle (Fig. 3.1).

Our remapping approach further explained nontrivial additive interactions. In particular, the additive interaction between CHL and TET is hard to rationalize: these antibiotics have completely different binding sites on the ribosome. However, CHL and TET interacted similarly with translation bottlenecks (Fig. 5.4) and their interaction was faithfully captured by the remapping approach (Fig. 5.10). This observation suggests that the action of CHL is largely equivalent to inhibiting tRNA delivery. As CHL binding interferes with an aminoacyl moiety of tRNA on the A-site [Wilson, 2014; Dunkle *et al.*, 2010], this suggests that perturbation of tRNA dynamics might be at the heart of the drug interaction between TET and CHL. At a more detailed level, CHL was shown to cause context-specific translation arrest by interfering with tRNA delivery only at specific codons [Marks *et al.*, 2016; Choi, 2019]. Our approach cannot capture such more detailed molecular aspects of

antibiotic mode of action; instead, it indicates that the global effect of CHL is largely equivalent to hindered delivery of all tRNAs. The recently suggested effect of TET on initiation [Nakahigashi *et al.*, 2016] is not reflected in our analysis, indicating at least that the effect of TET is not equivalent to initiation inhibition (Fig. E.6).

KSG and ERM constitute another antibiotic pair that interacted additively and was clustered together (Fig. 5.4). Remapping correctly predicted additivity between KSG-ERM (Fig. E.6); however, unlike KSG, ERM does not directly inhibit initiation (Table 1). Yet, ERM's inability to inhibit translation when the nascent peptide chain of some proteins [Kannan *et al.*, 2012] is extended beyond a certain length may effectively lead to a global functional equivalence with KSG, suggesting a possible cause of co-clustering and additivity between ERM and KSG (Fig. 5.4). While plausible, these possibilities require further experimental investigation, especially since ERM selectively blocks the egress of peptide chains and reshapes the proteome [Kannan *et al.*, 2012; Vazquez-Laslop and Mankin, 2018].

For some antibiotic pairs, the predictions based on equivalent translation bottlenecks failed to explain the observed drug interactions (e.g., for LCY-CRY and CHL-CRY; Fig. E.7), indicating that these interactions have origins outside of the translation cycle. We expect that these cases are often due to idiosyncrasies and secondary effects of the drugs, which will require separate in-depth characterization in each case. In contrast, our results show that various non-trivial drug interactions between antibiotics are systematically explained by the interplay of specific translation bottlenecks caused by the antibiotics. While the growth-law based biophysical model already explained ≈57% (16 of 28) of the observed interactions (Fig. E.4), these included many weak or additive interactions; the most striking suppressive interactions were only captured after taking into account the multi-step nature of translation (Fig. E.7), thereby increasing the explained fraction to ≈71% (20 of 28).

6 Simultaneous titration of translation factors and continuous epistasis

If suppressive drug interactions are caused by the interplay of different translation bottlenecks alone, it should be possible to recapitulate these interactions in a purely genetic way. We thus expanded our translation bottleneck approach by introducing multiple genetic bottlenecks in the same cell. We focused on the interactions between initiation inhibitors (such as KSG) and translocation inhibitors (such as CRY and FUS), which were exclusively antagonistic or suppressive (Fig. 3.4). Moreover, the initiation inhibitor KSG alleviated a genetic translocation bottleneck and an initiation bottleneck suppressed the effect of the translocation inhibitor FUS (Fig. 5.2). These observations suggest that a universal mechanism underlies the suppression between initiation and translocation inhibitors.

We constructed a synthetic strain that enables simultaneous independent control of initiation and translocation factor levels. We integrated the initiation and translocation factors outside their native loci under the tight control of promoters inducible by isopropyl β-D-1-thiogalactopyranoside (IPTG) and anhydrotetracycline (aTc), respectively, in a strain in which their endogenous copies were deleted (Fig. E.8 and Appendix B). To maximize the precision of induction that is achievable with different inducer concentrations, we put both factors under negative autoregulatory control by chromosomally integrated repressors [Scott *et al.*, 2010; Klumpp *et al.*, 2009]. The resulting strain showed virtually no growth when at least one of the inducers was absent but unrestricted wild type growth in the presence of both inducers (Fig. 6.1A). These observations confirm that both translation factors are essential and show that their expression can be varied over the entire physiologically relevant dynamic range, thus enabling quantitative genetic control of two key translation processes.

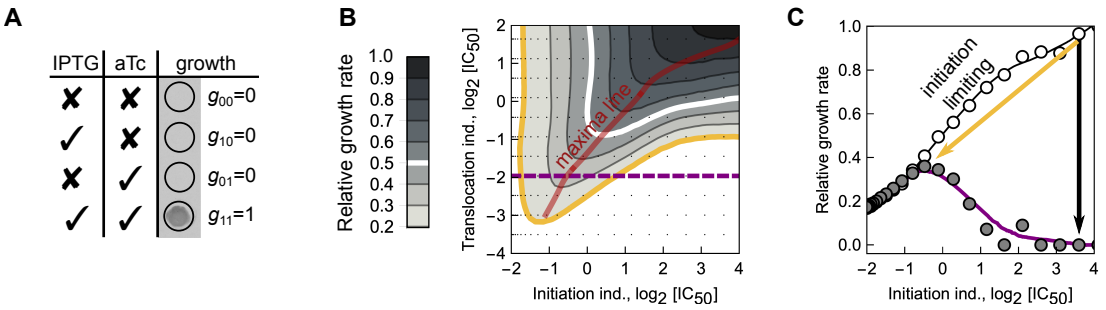

Figure 6.1: **Suppression between inhibition of translocation and initiation. (A)** Results of all-or-nothing growth assay: bacteria grow only when both essential factors are induced. **(B)** Measured growth rate response surface for the dual inducible promoter strain as a function of both inducer concentrations; the red line shows the ridge of maximum growth. **(C)** Cross-section of the response surface along the dashed purple line (gray circles) and at maximal aTc induction (white circles); solid lines are smoothed profiles. Black arrow denotes a decrease in translocation; if initiation is lowered simultaneously with translocation (orange arrow), growth reduction is smaller.

Curtailing translation initiation suppresses the effect of a genetic translocation bottleneck. We determined the bacterial response to varying translocation and initiation factor levels by measuring growth rates over finely resolved two-dimensional concentration gradients of both inducers. The resulting response surface clearly showed that inhibition of initiation alleviates the effect of translocation inhibition (Fig. 6.1 and E.8). This phenomenon exactly mirrors the antibiotic-antibiotic (KSG-FUS, Fig. 3.4) and bottleneck-antibiotic interactions (initiation-FUS, Fig. 5.2). An all-or-nothing approach (Fig. 6.1A), analogous to common genetic epistasis measurements [Constanzo *et al.*, 2010], would miss this suppressive effect, highlighting the importance of using quantitatively controlled perturbations. Taken together, these data show that the interplay of translation initiation and translocation alone is sufficient to produce strong suppression: dialing down initiation cranks up growth stalled by translocation bottlenecks. The widespread suppression between antibiotics targeting initiation and translocation is thus explained as a general consequence of the combined inhibition of specific translation steps alone.

What is the underlying mechanism of the suppressive interaction between initiation and translocation inhibitors? We hypothesized that this suppression results from alleviating ribosome "traffic jams" that occur during translation of transcripts at

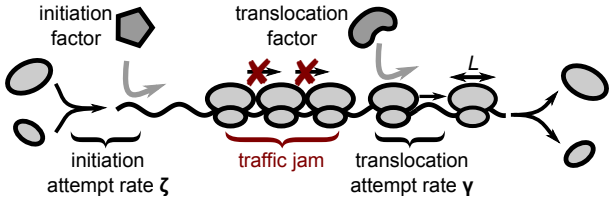

Figure 6.2: **Schematic of ribosomes progressing along a transcript – a stuck ribosome can cause a traffic jam.** Ribosomes undergo factor-mediated initiation events with attempt rate ζ and translocation with attempt rate γ.

low translocation rates (Fig. 6.2). The traffic of translating ribosomes that move along mRNAs can be dense [Mitarai *et al.*, 2008]. When a ribosome gets stuck, e.g., due to a low translocation rate, it blocks the translocation of subsequent ribosomes. The resulting situation is similar to a traffic jam of cars on a road. Traffic jams can form due to the asynchronous movement and stochastic progression of particles in discrete jumps, which is a good approximation for the molecular dynamics of a translating ribosome. If particle progression were deterministic and synchronous, no traffic jams would form. A classic model of queued traffic progression, which can be applied to translation [MacDonald *et al.*, 1968; MacDonald and Gibbs, 1969], is the Totally Asymmetric Simple Exclusion Process (TASEP) [Shaw *et al.*, 2003b; Zia *et al.*, 2011].

6.1 TASEP model of translation within growth law framework

We developed a generalization of the TASEP that describes the traffic of translating ribosomes on mRNAs and takes into account the laws of bacterial cell physiology. There are several differences between the classic TASEP and translating ribosomes moving along a transcript. First, a ribosome does not merely occupy a single site (codon), but rather extends over 25 nucleotides ($\approx$ 8.33 codons) [Mohammad *et al.*, 2019; Woolstenhulme *et al.*, 2015]. Second, the total number of ribosomes in the cell is finite and varies as dictated by bacterial growth laws [Scott *et al.*, 2010; Scott *et al.*, 2014]. Third, translation steps are mediated by translation factors that bind

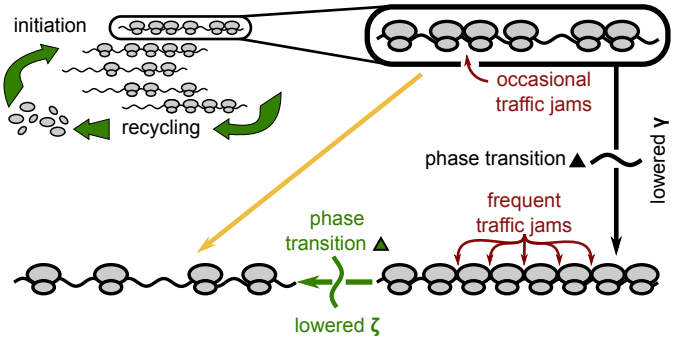

Figure 6.3: **Schematic of the theoretical model of translation.** Translation is described as an ensemble of transcripts competing for the limited and growth-rate-dependent pool of ribosomes. Ribosomes advance on transcripts as described by a generalized totally asymmetric simple exclusion process (TASEP) for particles of size L (see Fig. 6.2 and text). When $\gamma < \zeta(1 + L^{1/2})$, ribosomes saturate and traffic jams develop, resulting in a drop in elongation and growth (black arrow, the transition happens at the black triangle) [Klumpp and Hwa, 2008; Lakatos and Chou, 2003]. When $\zeta < \gamma/(1 + L^{1/2})$, a phase transition occurs (green triangle): traffic jams dissolve – elongation and growth increase (along the green arrow).

to the ribosome in a specific state and push the ribosome into another state [Rodnina, 2018]. These transitions are stochastic with rates that depend on the abundance of ribosomes in a specific state and on the abundance of translation factors available to catalyze the step. Thus, the initiation- and translocation-attempt rates, which are constant in the classic TASEP, depend on the state of the system. We formulated a generalized TASEP that captures these extensions, estimated all of its parameters based on literature, and derived the model equations analytically. The resulting growth rate was calculated numerically. In brief, our generalized TASEP model provides a physiologically realistic description of the factor-mediated traffic of ribosomes on multiple transcripts.

There are several specific differences between the classical open TASEP system and translation in the context of the bacterial cell (Fig. 6.3). Firstly, the pool of ribosomes is finite and variable in size (as dictated by the growth laws). Secondly, the ribosomes span over more than one site – it occupies 25 nucleotides, *i.e.*, $L \approx 8.33$ codons [Mohammad *et al.*, 2019; Woolstenhulme *et al.*, 2015]. Thirdly, steps in translation are mediated by translation factors that bind to the ribosome in a specific state and (stochastically) push the ribosome into another state. The rates

depend on the abundance of ribosomes in a specific state and the abundance of the factor catalyzing the step. Thus, the rates, which are kept fixed in the classical TASEP, become variable and system-state dependent.

6.2 Analytical results for TASEP of extended particles

In the absence of ribosome pausing, established analytical results for the TASEP of extended particles can be used [Klumpp and Hwa, 2008; Lakatos and Chou, 2003; Shaw *et al.*, 2003b; Zia *et al.*, 2011]. If the release of ribosomes at the end of the transcript is not limiting, two different regimes of ribosome traffic exist, namely the initiation- and translocation-limited regime. These regimes are separated by a non-equilibrium phase transition. The current of ribosomes J in the two regimes is given by:

$$J_{\text{init}}(\zeta,\gamma) = \frac{\zeta\left(\gamma-\zeta\right)}{\left[\gamma+\zeta\left(L-1\right)\right]} \quad \text{and} \quad J_{\text{tran}}(\zeta,\gamma) = \frac{\gamma}{\left(1+\sqrt{L}\right)^2}, \tag{6.1}$$

where ζ and γ are initiation and translocation attempt-rates, respectively (Fig. 6.3). The ribosome coverage density ρ reads:

$$\rho_{\text{init}}(\zeta,\gamma) = \frac{L\zeta}{\left[\gamma+\zeta\left(L-1\right)\right]} \quad \text{and} \quad \rho_{\text{tran}}(\zeta,\gamma) = \rho_{\text{max}} = \frac{1}{1+1/\sqrt{L}}. \tag{6.2}$$

The elongation velocity (rate) u depends both on the current and the ribosome density $\rho_r = \rho/L$ via $u = Js/\rho_r$, where s is the step size (1 aa or 1 codon). This in turn yields

$$u_{\text{init}}(\zeta,\gamma) = s(\gamma-\zeta) \quad \text{and} \quad u_{\text{tran}}(\zeta,\gamma) = s\frac{\gamma}{1+1/\sqrt{L}}. \tag{6.3}$$

6.2.1 Distribution of ribosomes across different classes

The total ribosome concentration r_{tot} is

$$r_{\text{tot}} = r_{\text{i}} + r_{\text{tr}} + r_{\text{min}}, \tag{6.4}$$

where r_{i} and r_{tr} are the concentrations of non-initiated and translating ribosomes, respectively. Translating ribosomes are distributed across numerous mRNA transcripts

in the cell and their concentration can be written as:

$$r_{\mathrm{tr}} = \frac{1}{V}\sum_{p}^{M} \rho_{r,p} D_p = \frac{1}{V}\sum_{p}^{M} \frac{\rho_p}{L} D_p \approx \frac{1}{V} M \frac{\rho}{L} \bar{D} = \Xi \rho_r \bar{D}, \tag{6.5}$$

where D_p and $\rho_{r,p}$ are the length and ribosome density of the $p-$th transcript, respectively, M is the total number of transcripts and V the cell volume ($\Xi = M/V$ is the concentration of transcripts). The density of ribosomes $\rho_r = \rho/L$ is a TASEP-derived quantity and depends on the initiation attempt rate ζ and translocation attempt rate γ. In the last step, we assumed for simplicity that the density of ribosomes across the transcripts does not vary significantly between transcripts. However, if transcripts do differ in their ribosomes densities, the ones with higher densities will enter the translocation limiting regime (in which traffic jams form) already at a smaller decrease in translocation attempt rate. If those transcripts code for essential genes, this will correspondingly lead to a decrease in growth rate already at such smaller decreases in translocation attempt rate. Such traffic jams would still be relieved by lowering initiation rate even though traffic jams have not developed on all other transcripts. Thus, the qualitative conclusions of the analysis below would still hold, but the results would be quantitatively different. However, taking differences between transcripts into account would require explicit modeling of individual transcripts and is beyond the scope of this work. Assuming similar ribosomes densities allows replacement of the sum with $M\bar{D}$, where $\bar{D}$ is the average length of transcripts being translated; the proteome-weighted average length is $\bar{D} \approx 209$ [Milo and Phillips, 2016].

The growth rate is proportional to the elongation velocity of ribosomes along the transcript $u(\zeta, \gamma)$ and to the number of translating ribosomes. However, there is a limit for the maximal elongation rate $u_{\max}$ because other processes (*e.g.*, charged tRNA delivery) become limiting at some point in a given nutrient environment. We estimated the maximal elongation rate from the Michaelis-Menten-like relation between RNA/protein (R/P) and translation rate obtained in Ref. [Dai *et al.*, 2016]: $u = k_{\mathrm{el}}(R/P)/[(R/P) + K_{\mathrm{el}}]$, where $k_{\mathrm{el}} = 22$ aa/s and $K_{\mathrm{el}} = 0.11$. We calculated the theoretical $(R/P) = (R/P)_{\min} + \lambda_0/\kappa_t^{R/P} \approx 0.54$, where $\kappa_t^{R/P} = 4.5\ \mathrm{h}^{-1}$ and $(R/P)_{\min} = 0.09$ [Scott *et al.*, 2010]. Plugging this (R/P) into the Michaelis-Menten

function for the translation rate, we obtain $u_{\max} \approx 18$ aa/s. Thus, the growth rate is given as

$$\lambda = \kappa_t r_{\text{tr}} \min\left[\frac{u(\zeta,\gamma)}{u_{\max}}, 1\right]. \tag{6.6}$$

However, the growth rate feeds back into the total ribosome concentration via the growth law as

$$r_{\text{tot}} = r_{\text{i}} + r_{\text{tr}} + r_{\min} = r_{\max} - \lambda\Delta r\left(\frac{1}{\lambda_0} - \frac{1}{\kappa_t \Delta r}\right). \tag{6.7}$$

We can estimate Ξ at λ_0 as

$$\frac{\lambda_0}{\kappa_t} = \Xi\rho_r\bar{D} \implies \Xi = \frac{\lambda_0}{\kappa_t\rho_r\bar{D}}. \tag{6.8}$$

Factor-dependent translocation attempt rate The ribosome will perform a specific step only when the associated factor is bound to it: the step-attempt rate is proportional to the probability P_b of the ribosome being bound by a factor. This probability can be calculated by assuming a population of elongation factors with concentration $c_{\text{ef}} = c_{\text{ef,b}} + c_{\text{ef,n}}$ and translating ribosomes $r_{\text{tr}} = r_{\text{tr,b}} + r_{\text{tr,n}}$, where the indices b and n denote the factor-bound and unbound subpopulations, respectively. Binding is described by

$$\frac{\mathrm{d}r_{\text{tr,b}}}{\mathrm{d}t} = k_{\text{on}}c_{\text{ef,n}}r_{\text{tr,n}} - k_{\text{off}}r_{\text{tr,b}}, \tag{6.9a}$$

$$\frac{\mathrm{d}c_{\text{ef,b}}}{\mathrm{d}t} = k_{\text{on}}c_{\text{ef,n}}r_{\text{tr,n}} - k_{\text{off}}c_{\text{ef,b}}. \tag{6.9b}$$

Solving for steady state, noting that $r_{\text{tr,b}} = c_{\text{ef,b}}$ and defining $K_D = k_{\text{off}}/k_{\text{on}}$ we obtain the probability for a ribosome to be bound as

$$P_b = \frac{r_{\text{tr}} - r_{\text{tr,n}}}{r_{\text{tr}}} = 1 - \frac{(r_{\text{tr}} - K_D - c_{\text{ef}}) + \sqrt{4K_D r_{\text{tr}} + (r_{\text{tr}} - K_D - c_{\text{ef}})^2}}{2r_{\text{tr}}}. \tag{6.10}$$

The binding constant of EF-G to the ribosome complex I (pre-translocation analog with N-Ac-dipeptidyl-tRNA at the A-site and deacylated-tRNA in the P-site) [Yu *et al.*, 2009] is $K_D = 0.27 \pm 0.02$ μM; we used this value in our calculations.

6.2.2 Factor-dependent initiation attempt rate

Successful initiation events are not limited to a single L-codon long slot on a mRNA (that can be free or occupied) but can occur on any transcript; and only the factor-bound ribosomes can attempt an initiation event. Thus, the initiation rate can be described by Michaelis-Menten kinetics:

$$\zeta = \zeta_0[\mathrm{IF}]\frac{r_i}{K_m + r_i}. \tag{6.11}$$

We can estimate K_m from kinetic rates determined by Milon *et al* [Milon *et al.*, 2012] where the free 30S subunit is bound (almost simultaneously) by IF3 and IF2 with rate $(2-10)\times 10^2\ \mu\mathrm{M}^{-1}\mathrm{s}^{-1}$ and dissociates at rate $30\ \mathrm{s}^{-1}$. From these values, we estimate $K_m \approx 0.05\ \mu$M.

6.2.3 Estimation of model parameters

It is useful to estimate if WT translation is in the initiation or translocation limited regime, which we can obtain from the average WT ribosome density. We can estimate the WT ribosome density as $\rho_r = 3\beta_r N_r/(r_m t_m)$, where N_r, β_r, r_m and t_m are the number of ribosomes, the fraction of active ribosomes, the rate of mRNA synthesis per cell, and the average mRNA life-time, respectively [Bremer and Dennis, 1996]. The fraction of translating ribosomes β_r is estimated from fitting a Hill function to data from Ref. [Dai *et al.*, 2016] (Fig. 6.4A).The average lifetime of mRNA is assumed to be growth rate-independent [Klumpp *et al.*, 2009] at $t_m \approx 1.5$ min [Yu *et al.*, 2006]. For higher growth rates, the relation between growth rate and (calculated) WT ribosome density linearizes; extrapolating to $\lambda_0 = 2.0\ \mathrm{h}^{-1}$, we obtain a rounded-up value of $\rho_r \approx 0.07$ (Fig. 6.4B), which yields $\Xi \approx 2.2\ \mu$M. For cells grown in LB, the average number of transcripts per cell was measured as $N_{\mathrm{mRNA}} \approx 7800$ [Bartholomäus *et al.*, 2016]. To estimate the mRNA concentration, we use $\Xi = N_{\mathrm{mRNA}}/V_{\mathrm{cell}} = (N_{\mathrm{mRNA}}/m_{\mathrm{dry}})\times(m_{\mathrm{dry}}/m_{\mathrm{wet}})\times(m_{\mathrm{wet}}/V_{\mathrm{cell}})$, where $m_{\mathrm{dry}}/m_{\mathrm{wet}} \approx 1/3.1$ and $m_{\mathrm{wet}}/V_{\mathrm{cell}} \approx 1.09$ g/mL are growth-rate independent quantities (see Supplementary Information of Ref. [Greulich *et al.*, 2015]). We obtained the dry mass of the cell at $\lambda = 2.0\ \mathrm{h}^{-1}$ by extrapolating from measured data

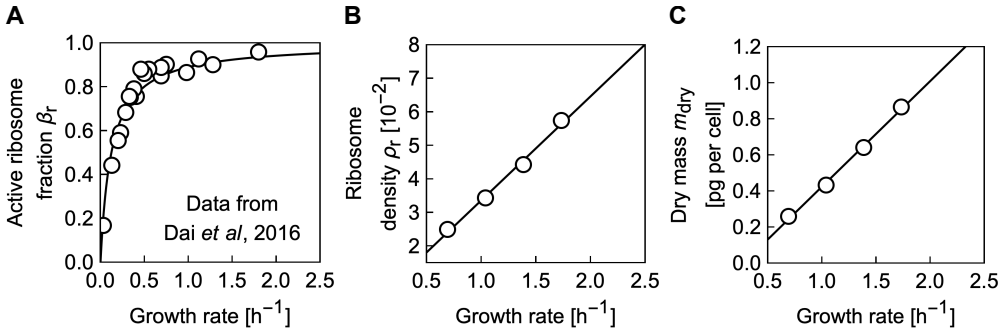

Figure 6.4: **Estimation of TASEP-model parameters. (A)** Active ribosome fraction as a function of growth rate in different nutrient environments. Data is from Ref. [Dai *et al.*, 2016]. The solid line represents a best-fit Hill function $(x/a)/[1+(x/a)]$, where $a \approx 0.12$ h^{-1}. **(B)** Calculated ribosome density $\rho_\mathrm{r} = 3\beta_\mathrm{r} N_\mathrm{r}/(r_\mathrm{m} t_\mathrm{m})$. The solid line shows best fit. **(C)** Dry mass measurements from Ref. [Bremer and Dennis, 1996] and best-fit linear function (solid line). Arrow denotes the density for $\lambda_0 = 2.0$ h^{-1}.

at various growth rates [Bremer and Dennis, 1996] as $m_\mathrm{dry} \approx 1.01$ pg/cell (Fig. 6.4C), which in turn yields $\Xi \approx 4.5$ μM. This value is higher than our estimate, since the latter is skewed towards higher WT ribosome densities, which require fewer transcripts at the same number of translating ribosomes.

The estimated WT ribosome density is $\rho_r \approx 0.07$, which is lower than the maximal attainable ribosome density of $\rho_{\mathrm{r,max}} = \rho_\mathrm{max}/L = 1/(L+\sqrt{L})|_{L=25/3} = 0.089$. Thus, translation in the WT is likely in the initiation-limited regime. Therefore, the equations for ribosomal density and elongation velocity for the initiation limiting regime are used to estimate the apparent initiation and translocation attempt rates:

$$\rho_r(\zeta) = \frac{\zeta}{\gamma + \zeta(L-1)} \approx 0.07 \quad \text{and} \quad u = (\gamma - \zeta)s \approx 18 \text{ aa/s}. \tag{6.12}$$

The apparent rates are $\gamma \approx 21.0$ s^{-1} and $\zeta \approx 3.0$ s^{-1}. In the case of WT regulation there are ~ 0.83 EF-G molecules per ribosome and the expression of the factor is coupled to the ribosome number (*i.e.*, their ratio is constant) [Dai *et al.*, 2016]. This allows us to estimate $\gamma_0 = \gamma/P_b$, where we note that $c_{\mathrm{ef,WT}} \approx 43.0$ μM (estimated from 0.83×51.9 μM where the ribosome concentration is calculated from the growth law). Next, we estimate the number of translating ribosomes from Eq. (6.6) as 32.6 μM, which yields $P_b \approx 0.98$ [Eq. (6.10)] and finally $\gamma_0 \approx 21.5$ s^{-1}. We further note that there are 0.3 IF2 molecules per ribosome [Bremer and Dennis, 1996],

implying $[\mathrm{IF}]_{\mathrm{WT}} \approx 15.6\ \mu\mathrm{M}$, from which we estimate $\zeta_0 \approx \zeta/[\mathrm{IF}]_{\mathrm{WT}} \approx 0.19\ \mu\mathrm{M}^{-1}\mathrm{s}^{-1}$. With these parameter values, our model is fully defined and the growth rate is calculated (Mathematica function `NSolve`) as its output based on the concentration of translation factors.

We further explored the effects of parameters on the model results. First, we verified the impact of WT ribosome density ρ_r (one that supports maximal growth rate at saturating factor concentrations), we systematically calculated the response surfaces for different values of ρ_r between 0.0117 and 0.0817 (6.5A). With decreasing WT ρ_r, the concentration of mRNA Ξ increases according to Eq. (6.8). When $\Xi \gg \Delta r L/\rho_{\max}\bar{D}$, the traffic jams of ribosome are not possible anymore as there are too many mRNAs that can carry more ribosomes than available. The critical WT ribosome density is $\rho_{\mathrm{r,crit}} = \lambda_0/(\kappa_t \Delta r) \times \rho_{\mathrm{r,max}}$ (6.5A).

Next, we systematically calculated the response surfaces for different values of ribosome footprint size L and WT ribosome density ρ_r. Here, we varied ribosome footprint size L since: (i) a small increase in L could be caused by the space required by the movement of the ribosomal subunits during different phases of progression along mRNA, and (ii) size estimates in the literature vary [Kang and Cantor, 1985; Mitarai *et al.*, 2008; Shaw *et al.*, 2003b; Mohammad *et al.*, 2019]. We varied L between 5 and 20 codons. We calculated the phase diagram of BD scores (6.5B,C). By doing so, we checked the impact of physiological parameters on the outcome of the model, and verified the mathematical relations discussed above more generally.

Without any free parameters, this generalized TASEP qualitatively reproduced the suppressive effect of lowering the initiation rate under a translocation bottleneck (Fig. 6.6A). This suppression results from a phase transition between the translocation- and the initiation-limited regime. In the translocation-limited regime (black arrow in Fig. 6.6A), ribosome traffic is dense and cannot be further increased by boosting the initiation attempt rate. Upon decreasing the initiation attempt rate ζ (green arrow in Fig. 6.6A), a phase transition to the initiation-limited regime occurs. Beyond the critical point of this phase transition (green triangle in Fig. 6.6A), the elongation velocity, and with it the growth rate, begins to increase with decreasing initiation attempt rate. Hence, ultimately, a non-equilibrium phase transition in

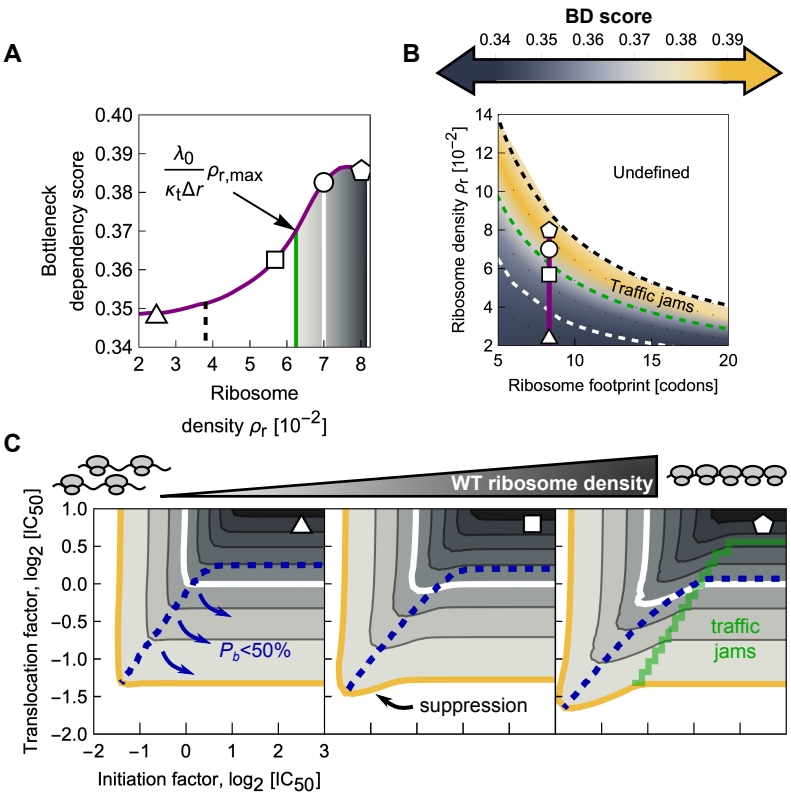

Figure 6.5: **Variation of TASEP-model parameters. (A)** Impact of varying the initial ρ_r on resulting bottleneck dependency score for $L = 25/3$. White symbols correspond to the examples showcased in B,C. The white circle shows the result from the main text for the estimated value of WT $\rho_r = 0.07$. The solid green vertical line denotes the critical value $\lambda_0 \rho_{r,max}/(\kappa_t \Delta r)$ above which traffic jams due to translocation limitation can form. The dashed vertical line indicates the approximate point at which suppression starts to develop due to factor sequestration (as obtained by $\partial \mathrm{BD}/\partial \rho_r = 0.3$). **(B)** Phase diagram of BD score as a function of WT ribosome density ρ_r and ribosome footprint size L. Purple line and symbols corresponds to the cross-section in A. The "undefined" area corresponds to the example in which translation is already in the regime with traffic jams and Eqs (6.12) do not have a unique solution. White dashed line corresponds to $\partial \mathrm{BD}/\partial \rho_r = 0.3$, above which (approximately) suppression starts to develop. Green dashed line shows the $\lambda_0 \rho_{r,max}/(\kappa_t \Delta r)$, above which traffic jams can develop. **(C)** Response surfaces for $\rho_r \approx 0.025,\ 0.057,$ and 0.080 [from left to right; symbols shown as in A,B]. Symbols in the upper-right corner correspond to the values shown in A,B. Dashed blue lines show where 50% of the translating ribosomes are bound by the elongation factor; below this line, this fraction decreases along the arrows. When ρ_r increases, suppression starts to develop. Increasing ρ_r further facilitates strong suppression by the formation of traffic jams (below green line).

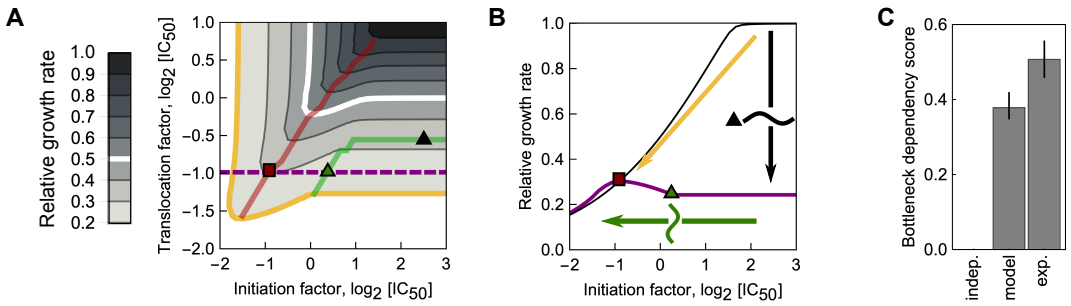

Figure 6.6: **TASEP-model predicts suppression between inhibition of translocation and initiation. (A)** The growth rate predicted by the generalized TASEP model recapitulates suppression of translocation inhibition by lowered initiation; note that, unlike in Fig. 6.1A, axes show the concentrations of translation factors. States below and to the right of the green line are in the translocation limiting regime. **(B)** Cross-sections of the response surface. As the initiation factor level is decreased, the critical point of the phase transition (green triangle) is reached; growth starts increasing after passing the critical point, and decreases again after passing the maximum (red square) as the number of translating ribosomes becomes limiting. **(C)** Bottleneck dependency (BD) score quantifies the deviation from independent expectation (BD = 0) for the response surfaces in Fig. 6.1A and A; heights of bars corresponds to the medians and error bars are 90% bootstrap confidence intervals. Medians and confidence intervals were estimated from $n = 100$ bootstrap data points.

which ribosome traffic jams dissolve underlies the suppressive effect.

The densification of ribosomes on transcripts has an additional consequence: as the number of ribosomes that are stuck on transcripts increases, more elongation factors are sequestered by ribosomes. This in turn reduces the probability that an individual ribosome is bound by a factor – a necessary condition for the ribosome to attempt a translocation step. This situation results in a positive feedback loop in which the reduced translocation attempt rate further amplifies ribosome congestion.

To compare measured and predicted surfaces, which have different axes, we calculated their respective deviation from independence as for the bottleneck dependency score (Fig. 5.3). By this measure, the model faithfully captured the clear deviation from the multiplicative expectation (Fig. 6.6C); the agreement with the experimental data is good, especially considering that the model results are parameter-free and not a fit to the experimental data.

Taken together, these results show that suppressive drug interactions between translation inhibitors are caused by the interplay of two different translation bottle-

necks. Close agreement of the experiments with a plausible theoretical model of ribosome traffic, which captures physiological feedback mediated by growth laws, strongly suggests that suppression is caused by ribosome traffic jams. Such traffic jams result from imbalances between translation initiation and translocation; they dissolve in a phase transition that occurs when one of these processes is slowed, leading to an overall acceleration of translation and growth. Stalled ribosomes facilitate the formation of traffic jams by sequestering elongation factors. We conclude that a non-equilibrium phase transition in ribosome traffic is at the heart of suppressive drug interactions between antibiotics targeting translation initiation and translocation.

6.3 Effect of mRNA growth-rate dependence

The concentration of mRNA could in principle be growth rate-dependent. However, direct dependence of mRNA on the growth rate is difficult to estimate from existing literature as total RNA is mostly composed of rRNA and tRNA [Scott *et al.*, 2010; Dai *et al.*, 2016]; estimation of the mRNA fraction is thus prone to errors. However, if we assume proportionality between ribosome and mRNA concentration, a simplified form can be written down as $\Xi = \Xi_0 r_{\mathrm{tot}}/r_{\mathrm{tot},0}$, where Ξ_0 and $r_{\mathrm{tot},0} = r_{\mathrm{min}} + \lambda_0/\kappa_{\mathrm{t}}$ are the estimates of mRNA concentration from the previous section and total ribosome concentration in the unperturbed case, respectively. Plugging this dependence into the model does not qualitatively change the suppressive interaction between inhibition of initiation and translocation (Fig. 6.7). In this scenario, the increasing number of mRNA transcripts partially alleviates the densification of ribosomes on transcripts. However, the overall increasing number of translating ribosomes sequesters the elongation factors – this effect is still alleviated by lowering the initiation rate and in turn the density of ribosomes.

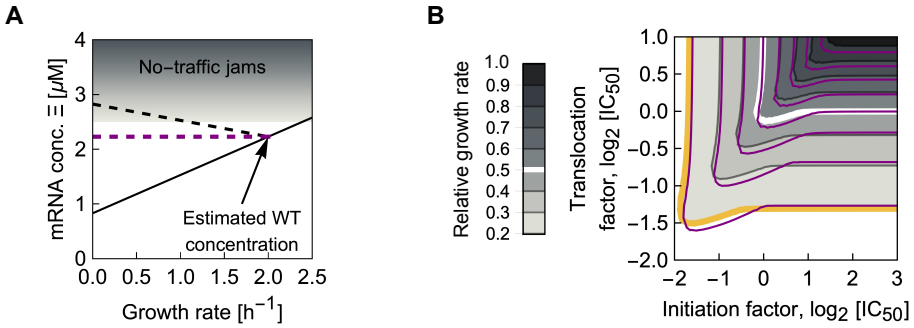

Figure 6.7: **Variation of TASEP-model parameters. (A)** Two models of mRNA concentration dependence. Black lines denote the dependence of mRNA on growth rate if the co-regulation between total RNA and mRNA is assumed; solid and dashed lines correspond to variation of the nutrient quality and translation perturbation, respectively. The arrow denotes the estimated mRNA concentration; this concentration is assumed constant (dashed purple line) in the model shown in the main text. If the mRNA concentration exceeds $\Delta r/\left(\rho_{\mathrm{max,r}}\bar{D}\right)$, traffic jams do not develop. Elongation factors are still sequestered as the number of translating ribosomes increases, which in turn decreases the growth rate. **(B)** Direct comparison of model predictions. Prediction with growth-dependent mRNA concentration Ξ is depicted in grayscale; isoboles from the prediction assuming a constant pool of mRNA are shown in purple. Both results are qualitatively equivalent.

6.4 Rescue mechanisms and inefficiency of a direct response to translocation inhibition

Bacteria have evolved rescue mechanisms for stalled ribosomes (tmRNA, ArfA and ArfB). However, these mechanisms are mostly aimed at the rescue of ribosomes that were stalled due to limiting supply of building blocks or those in non-stop complexes. The former is an unlikely scenario during translocation limitation; as the building blocks are under-consumed, non-stop complexes can form via the formation of damaged or truncated mRNA (e.g., via cleavage by RNases) or via collision-induced frame-shifts [Simms *et al.*, 2019; Keiler, 2015]. However, the tmRNA pathway requires an empty A-site on the ribosome, which is occupied in the pre-translocation complex, thus hindering the rescue initiation. Likewise, the ArfA pathway is hindered by an occupied A-site – it requires release factor 2 to bind to the A-site of the ribosome to initiate premature release and recycling. ArfB on the other hand, can recover the lack of tmRNA and ArfA pathways only when heavily

overexpressed [Chadani *et al.*, 2011] and is considered ineffective in the WT regime. In sum, established rescue mechanisms are unlikely to recover stuck ribosomes and we therefore omit these mechanisms from the analysis.

Additionally, the cell could have an initiation-inhibiting mechanism in place as a response to translocation inhibition. However, the observed responses of bacteria to translation inhibition show global derepression of the translation machinery by reducing the levels of ppGpp. Besides the upregulation of all translation components mentioned in the main text [Maaløe, 1979; Gordon, 1970; Blumenthal *et al.*, 1976; Furano and Wittel, 1975], an additional effect of lower levels of ppGpp is a direct increase of initiation. The catalytic function of the initiation factor is lowered when ppGpp levels are high, and higher when ppGpp is reduced [Milon *et al.*, 2006]. These arguments show that an alleviating response of translocation inhibition by either rescue mechanisms or by direct down-regulation of initiation is unlikely.

7 Tools for quantitive characterization of translation

In previous chapters, we focused on growth rate as the macroscopic response to translation perturbation. While it comprehensively reflects the impact on the overall physiology, it lacks a level of detail that allows a deeper understanding of the perturbation effects. Therefore, we aimed to (i) develop tools to gain deeper insight into translation and (ii) develop a model that would be based on measurable parameters and would consolidate the measurements. In comparison to previous chapters, this one will be more conceptual/technical and will illustrate an approach rather than a complete solution.

While the growth laws proved to be remarkably robust, measuring ribosome abundance for a particular perturbation would be useful as it would challenge the validity of the growth laws and provide a numerical scale for comparing the abundances of a particular protein (as in: how many translation factors per ribosome are in the cell?). Next, if we perturb the translation genetically by titrating the translation factor, it is of importance to know the abundance of said factor. Here, we aim to obtain a physical quantity (*i.e.*, number of molecules per cell), rather than a value expressed in relative terms or proxy units (*e.g.*, fluorescence or photon-counts-per-second). Physical quantities allow us to evaluate the model in quantitative terms and make the model independent of the particular measurement technique. Additionally, to get a broad overview of the cellular physiology, we aim to determine some macromolecular parameters of the cell, such as protein and RNA content.

We illustrate these approaches and techniques by investigating the effects of initiation factor titration. Initiation – as we discussed in the Introduction – is a process with many steps that are orchestrated by several auxiliary factors. Describing the whole process in detail would require multiple parameters and would make the

analysis highly complex. Similar to the TASEP model we introduced in the previous chapter, we can use certain approximations that will simplify the analysis.

7.1 Impact of sub-saturating levels of initiation factors on the growth rate

Below we describe a model in which the translation is perturbed by sub-saturating levels of initiation factor. In the model, we divide total ribosome concentration r_{tot} into translating ribosomes r_u and non-initiated ribosomes r_i. We consider only a few processes: initiation, elongation, and recycling. Because we consider the case in which we throttle down initiation, we assume that the initiation is the only limiting process. We in turn assume that the recycling of the ribosome is instantaneous, *i.e.*, the ribosomes do not transit through a sub-population of terminated, yet not recycled ribosomes.

Here we do not take into account the full molecular complexity of the translation initiation. We assume simple kinetics in which rate f_c of the reaction $r_i \rightarrow r_u$ is given by Michaelis-Menten kinetics

$$f_c = [\text{IF}]\zeta_0 \frac{r_i}{K_m + r_i}, \tag{7.1}$$

where [IF] is an intracellular concentration of initiation factor, ζ_0 is a rate constant and K_m is a Michaelis constant of the reaction, as in Eq. (6.11).

Recycling rate of the ribosomes is much faster than the synthesis of new ones.

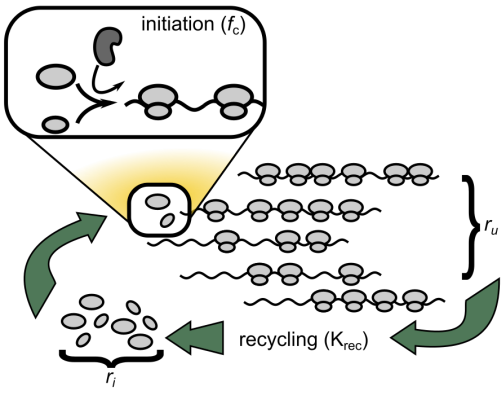

Figure 7.1: **Modeling impact of sub-saturating levels of initiation factors on the growth rate.** In the model, we distinguish translating r_u and inactive ribosomes r_i. Rate of initiation f_c depends on the abundance of both non-initiated ribosomes and initiation factor [see Eq. (7.1) and rounded rectangle]. Ribosomes are recycled at the rate K_{rec}.

We can obtain a proxy for the rate of ribosome recycling from the equality

$$\lambda M_p = k_{\text{rec}} \langle m \rangle, \tag{7.2}$$

where M_p, k_{rec}, and $\langle m \rangle$ are (growth rate-dependent) protein mass, recycling rate, and a typical mass of a protein, respectively. This expression states that the total rate of protein synthesis equals the rate at which the peptide chains are completed (which equals to recycling rate) multiplied by some typical mass of the protein. Further, dividing by cell volume (which is growth rate-dependent) we obtain concentration flux that we can later use in the dynamical system. We note that $1/V = (1/M_{\text{cd}}) \times (M_{\text{cd}}/M_{\text{cw}}) \times (M_{\text{cw}}/V)$, where M_{cw} and M_{cd} are the wet and the dry cell mass, respectively. Since $M_{\text{cw}}/V = 1.09$ g/mL [Kubitschek *et al.*, 1984] and $M_{\text{cd}}/M_{\text{cw}} = 1/3.1$ [Cayley *et al.*, 1991] are independent of the growth rate, inverse volume equals $1/V = \rho/M_{\text{cd}}$, where $\rho = 0.352$ g/mL. We define recycling concentration flux as

$$K_{\text{rec}} = \frac{k_{\text{rec}}}{V} = \lambda \frac{M_p}{\langle m \rangle V} = \lambda \rho \frac{M_p}{M_{cd} \langle m \rangle} = \lambda \xi. \tag{7.3}$$

To estimate the value of $\xi = \rho M_p/(M_{\text{cd}} \langle m \rangle)$ and its possible dependence on the growth rate, we calculated the ratio M_p/M_{cd} at different growth rates [Bremer and Dennis, 1996]. We note that ratio is only weakly growth rate-dependent (in line with Ref. [You *et al.*, 2013]) and we therefore assumed it to be constant at $M_p/M_{\text{cd}} \approx 0.574$. To estimate the typical protein mass $\langle m \rangle$ in the *E. coli*, we assume that the distribution of the protein lengths does not change as a function of the growth rate and we calculate the molecular weight of the typical protein $W_{\langle m \rangle} = \tilde{\ell} W_{\text{aa}}$, where $\tilde{\ell} = 209$ aa is a median length obtained from proteomic abundance weighted distribution (in contrast to genomic length distribution) [Milo and Phillips, 2016] and $W_{aa} = 108$ g/mole is an average molecular weight of the amino acid residue [Bremer and Dennis, 1996]. This yields $\xi = 8.95 \times 10^3$ μM. If we consider a bacterial cell with a volume of ≈ 1 fL, we can calculate that there are $\approx 3.7 \times 10^6$ finished proteins per division. This is in line with the estimated number of proteins per bacterial cell ($2 - 4 \times 10^6$) [Milo and Phillips, 2016] and the agreement between these two independent estimates suggests that the estimated value for ξ is reasonable.

With these considerations at hand, we can write the dynamical system by adding ribosome recycling rates $\lambda\xi$ with opposite signs in differential equations for both r_u and r_i:

$$\dot{r}_u = -\lambda r_u + [\mathrm{IF}]\zeta_0 \frac{r_i}{K_m + r_i} - \lambda\xi, \tag{7.4a}$$

$$\dot{r}_i = -\lambda r_i - [\mathrm{IF}]\zeta_0 \frac{r_i}{K_m + r_i} + s(\lambda) + \lambda\xi. \tag{7.4b}$$

This system of ODEs resembles the one used for describing the binding of antibiotics. Setting both time derivatives to 0 and summing the equations yields:

$$\lambda(r_u + r_i) = \lambda r_{\mathrm{tot}} = s(\lambda), \tag{7.5}$$

which together with Eq. (4.2) gives the expression for the rate of ribosome synthesis:

$$s(\lambda) = \lambda \left[r_{\max} - \lambda\Delta r \left(\frac{1}{\lambda_0} - \frac{1}{\kappa_t \Delta r} \right) \right]. \tag{7.6}$$

From the steady-state Eq. (7.4a) and Eq. (7.1) we note that

$$\lambda(r_u + \xi) = f_c = [\mathrm{IF}]\zeta_0 \frac{r_i}{K_m + r_i} = f_c, \tag{7.7}$$

which allows rewriting the steady-state Eq. (7.4b) into

$$\lambda r_i = -\lambda(r_u + \xi) + \lambda \left[r_{\max} - \lambda\Delta r \left(\frac{1}{\lambda_0} - \frac{1}{\kappa_t \Delta r} \right) \right] + \xi\lambda. \tag{7.8}$$

Since $r_u = \lambda/\kappa_t + r_{\min}$, we can rewrite the expression above into

$$\lambda r_i = \underbrace{\lambda \left[r_{\max} - \lambda\Delta r \left(\frac{1}{\lambda_0} - \frac{1}{\kappa_t \Delta r} \right) \right]}_{s(\lambda)} - \underbrace{\lambda \left(\frac{\lambda}{\kappa_t} + r_{\min} \right)}_{\lambda r_u = f_c}. \tag{7.9}$$

Dividing by λ and rearranging we find

$$r_i = \Delta r \left(1 - \frac{\lambda}{\lambda_0} \right). \tag{7.10}$$

This expression is a mathematical formulation of the following: when there are no translating ribosomes ($r_u = 0$ and $\lambda = 0$) then the whole dynamic range of the ribosomes Δr is allotted to the inactive ribosomes r_i. However, when the inactive ribosomes are immediately converted to the translating ribosomes, then the growth

rate equals the unperturbed one, *i.e.*, $\lambda = \lambda_0$. We insert the Eq. (7.10) into the expression for the initiation rate [Eq. (7.7)], which yields

$$\lambda \left(\frac{\lambda}{\kappa_t} + r_{\min} + \xi \right) = [\mathrm{IF}]\zeta_0 \frac{\Delta r(1 - \lambda/\lambda_0)}{K_m + \Delta r(1 - \lambda/\lambda_0)}. \tag{7.11}$$

After the multiplication of the expression above with the denominator of the right-hand side and rearranging of the terms, we obtain an implicit expression for the dependence of the growth rate on the concentration of the initiation factor:

$$\begin{aligned} - & \frac{\lambda^3}{\kappa_t \lambda_0}\Delta r + \lambda^2 \left[\frac{K_m}{\kappa_t} + \frac{\Delta r}{\kappa_t} - \frac{(r_{\min} + \xi)\,\Delta r}{\lambda_0} \right] + \\ + & \lambda \left[(r_{\min} + \xi)\,(K_m + \Delta r) + [\mathrm{IF}]\frac{\zeta_0 \Delta r}{\lambda_0} \right] - [\mathrm{IF}]\zeta_0 \Delta r = 0, \end{aligned} \tag{7.12}$$

which is after multiplying with $-\kappa_t/(\Delta r \lambda_0^2)$ rewritten into

$$\begin{aligned} & \left(\frac{\lambda}{\lambda_0} \right)^3 - \left(\frac{\lambda}{\lambda_0} \right)^2 \left[1 + \frac{K_m}{\Delta r} - \frac{(r_{\min} + \xi)\,\kappa_t}{\lambda_0} \right] - \\ - & \left(\frac{\lambda}{\lambda_0} \right) \left[\frac{(r_{\min} + \xi)\,\kappa_t}{\lambda_0} \left(1 + \frac{K_m}{\Delta r} \right) + [\mathrm{IF}]\frac{\zeta_0 \kappa_t}{\lambda_0^2} \right] + [\mathrm{IF}]\frac{\zeta_0 \kappa_t}{\lambda_0^2} = 0. \end{aligned} \tag{7.13}$$

Taking [IF] towards either 0 or ∞ reveals two limiting cases, where $\lambda = 0$ and $\lambda = \lambda_0$, respectively, are the solutions to the Eq (7.13). We can further determine $[\mathrm{IF}]_{50}$, *i.e.*, the concentration of the initiation factor needed to support $\lambda = \lambda_0/2$, and its dependence on other parameters:

$$[\mathrm{IF}]_{50} = \frac{\lambda_0^2}{4\zeta_0 \kappa_t} \left(1 + \frac{2K_m}{\Delta r} \right) \left[1 + 2\frac{(r_{\min} + \xi)\,\kappa_t}{\lambda_0} \right]. \tag{7.14}$$

We note that at conditions allowing for faster growth (higher λ_0), higher concentration of the initiation factor is required. Alternatively, for high catalytic rates [$\zeta_0 \gg \lambda_0^2/(4\kappa_t)$], a lower concentration is required. Both make an intuitive sense, because at rapid growth initiation has to be more rapid; however, if the catalytic rate is higher (*i.e.*, enzyme is more efficient), fewer initiation factors are required. With these expressions at hand and by defining $b = [\mathrm{IF}]/[\mathrm{IF}]_{50}$, $R_0 = (r_{\min} + \xi)\,\kappa_t/\lambda_0$, and $y = \lambda/\lambda_0$, we can rewrite the Eq. (7.13) to express initiation factor concentration as:

$$\begin{aligned} b &= \frac{4}{(1 + 2R_0)(1 + 2K_m/\Delta r)(1 - y)} \times \\ &\times \left[-y^3 + y^2 \left(1 + \frac{K_m}{\Delta r} - R_0 \right) + yR_0 \left(1 + \frac{K_m}{\Delta r} \right) \right]. \end{aligned} \tag{7.15}$$

We note that the expression breaks down in the limit $K_m \to 0$, as the divergence at $y \to 0$ [caused by $(1 - y)$ in the denominator of the first factor] disappears, thus allowing the growth rates exceeding λ_0. Limiting both R_0 and K_m to ∞, the expression simplifies into Michaelis-Menten function, *i.e.*, $y = b/(b + 1)$, while for $R_0 \to \infty$ and $K_m \to 0$ we obtain a linear increase in growth rate, *i.e.*, $y = b/2$ for $b < 2$. Figure 7.2 shows that curves for $R_0 \gg 1$ fall in-between these two limits,

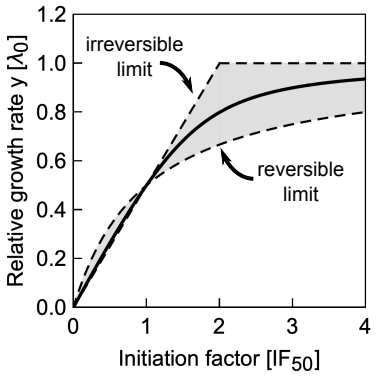

Figure 7.2: **Induction curve for initiation factor.** Figure shows an example of Eq. (7.13) for $R_0 = 100$ and $K_m/\Delta r = 0.1$ (solid line). Gray area is bounded by two limiting cases discussed in the text and shown as dashed lines. Since concentrations are measured in units of $[\mathrm{IF}]_{50}$, both curves go through the point $(1, 1/2)$. Note, that the chosen example lies within the boundaries determined by the limiting cases.

which we term reversible and irreversible for $K_m \to \infty$ and $K_m \to 0$, respectively.

To adjust the parameters in the Eq. (7.13) we need the measurements of intracellular concentration of the initiation factor. For that, we need to establish a precise technique for determination of absolute abundances in the cell.

7.2 Scarless tagging of chromosomal genes

Quantitative measurements of particular physiological parameters are always a tug-of-war between precision and ease of handling/throughput. Furthermore, various methods differ in the level of invasiveness, *i.e.*, whether the measurement requires alteration of a native protein of interest, which might lead to fitness defects. Additionally, not all methods allow convenient conversion of measured quantity (*e.g.*, fluorescence) into a physical quantity (*e.g.*, number of proteins per cell.

The genome-wide techniques (*e.g.*, quantitative proteomics) present a powerful tool that gives an overview of the whole proteome [Hui *et al.*, 2015]. However, the handling of such rich datasets requires careful curation and might fail when the

abundances of specific proteins are very low, which are often simply excluded from the analysis. This is particularly problematic in our case, as we aim to lower the abundance of an essential protein. Techniques that focus on the quantification of a specific protein are based on various approaches. Immunostaining methods, for example, require the development of specific antibodies, which are then hybridized with the protein of interest. Alternatively, common protein tags, such as His- or Flag-tag can be added to the protein and targeted with appropriate antibodies. Protein-bound antibodies can be either directly or indirectly used in the measurement of the amount of the protein, which is either based on colorimetry, chemiluminescence, and radioactive- and fluorescence detection. Such immunostaining methods are powerful tools for determining the presence of a specific protein but are deficient in detecting small changes in protein abundances. Alternatively, a protein of interest can be fused directly with a reporter. If we attach, for example, a fluorescent reporter (that is $\approx$ 330 amino acids in size) on one end of the protein, we can in principle measure its abundance directly since the latter is proportional to detected fluorescence. However, this might come at the price of reduced catalytic activity of the protein as well as disrupted physical properties (mobility, rotational defects). Yet, it is relatively easy to perform high-throughput measurements as the measurements can be effectively automatized. We demonstrate the effects of the problematic reduced catalytic efficacy in the Appendix, where we describe the construction of a strain with in-frame titratable GFP-fused initiation factor.

As we discussed in the Introduction, proteins involved in the translation enter into this highly dynamic process in which the structure of a particular protein plays an important role. Therefore, we developed a method with low invasiveness, high precision of detection, and medium convenience of handling. Below we describe the construction of the auxiliary tools and demonstrate the use of the method on the quantification of initiation factor. Sections denoted with an asterisk ($*$) are more technical. Our method is based on commercially available HiBit technology (Promega). The method is conceptually similar to immunostaining methods, as it requires an eleven-amino acid long tag to be added to either end of the protein. Quantification is performed by (i) lysis of cells, (ii) hybridization of the tagged

protein with a complementary fragment, and (iii) measurement of the luminescence. Due to wide dynamic range of detecion and lack of background, luminescence measurement offers a broad and linear dynamic range, as we show below.

We describe the technique to attach the HiBit tag to the carboxyl-end of proteins by scarless in-frame integration. We additionally add a flexible linker between the endogenous protein and the HiBit tag to decouple these two parts as much as possible and minimize the detrimental effects of tagging on the catalytic activity of the protein. We based the method on galactose selection-counter selection method, which allows us to remove the selection marker upon the integration of the tag.

7.2.1 Development of the technique for scarless tagging of chromosomal genes

We developed the method for scarless chromosomal integration of genetic fragments. The efficient fusion of the tag-encoding sequence to the 3'-end of the gene of interest requires high specificity and ideally should leave no scar behind. However, as the immediate neighborhood of the gene might be different from case to case, we aimed to develop a flexible system for scarless chromosomal in-frame insertions of the tag. We chose to use a recently developed galactose selection-counterselection [Warming *et al.*, 2005] method with modifications.

The basis of the galactose selection-counterselection is the double function of galactokinase (encoded by *galK*). Galactokinase is involved in the first step of galactose metabolism as it phosphorylates the galactose, which is then further processed by other components of the system. Therefore, in the strain devoid of *galK* will grow in galactose minimal medium only if the *galK* is successfully introduced into the chromosome. This way, we can select for the presence of *galK*.

However, GalK phosphorylates galactose analog, 2-deoxy-galactose (DOG), as well. The buildup of the phosphorylated analog is deleterious to the cell. In this case, only the cells that lack *galK* can grow in the medium with DOG present. Therefore, we can use the DOG to counterselect for the presence of *galK*. This dual-nature of *galK* can be used in recombineering [Warming *et al.*, 2005] or in fluctuating the

selection pressure in studies of evolution [Tomanek *et al.*, 2020].

Required strains

To use a galactose selection-counterselection, a strain that is deficient in *galK* is required in the initial step. When attempting the deletion of the *galK*, the 3'-end of *galK* should be left intact – there is a 7-nt overlap with a downstream *galM*. The in-frame gene disruption strategy employed in the construction of the Keio collection [Baba *et al.*, 2006] leaves the last 21-nt intact and is suitable for this purpose – this strategy also leaves the translation signals of the downstream gene unperturbed. The deletion can be readily moved by using generalized P1 transduction and the transduced cassette can be efficiently resolved by FLP-resolvase from the plasmid pCP20. We verified the deletion by PCR in which primers bind in regions flanking the deletion region. The *galK*-deficient strain should be checked for growth on galactose minimal plates as well as for the loss of catalytic activity on MacConkey galactose indicator plates (colonies should not appear pink but rather white). The obtained strain serves as the platform for the recombineering. In establishing the technique we used a derivative of laboratory strain MG1655 with the following additional genotypic differences Δ*lacIZYA*::*frt* Δ*galK*::*frt*.

7.2.2 ∗Auxiliary plasmids

We aimed to construct a plasmid bearing a selection-counterselection cassette and a linker-tag tandem upstream. This plasmid would serve as a PCR template to yield a double-stranded DNA fragment used in recombineering. We aimed to build the plasmid using modified Gibson assembly (HiFi-builder, New England Biolabs), from four fragments: (i) the *pir*-dependent origin of replication and ampicillin resistance cassette, (ii) *TrrnB* terminator with flexible linker [$(GGGS)_2$]-HiBit tag tandem introduced as its upstream overhang, (iii) strong λ-P_R, and (iv) *galK* gene (Fig. 7.3). The *pir*-dependent origin of replication prevents the recombineering interference by template carry-over as it cannot replicate in the strains of interest (it shall be maintained in pir^+ strain, *e.g.*, DH5α λpir). The plasmid has an excisable terminator

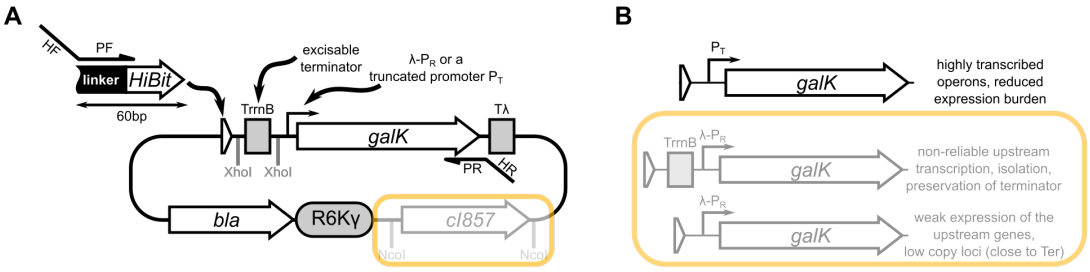

Figure 7.3: **Auxiliary plasmids used in scarless tagging of chromosomal genes. (A)** Main features of the plasmid. Multiple variants of the plasmid were attempted, each suited for different properties of the tagged gene (see B) Orange semi-opaque square denotes part that misses from the plasmid used in the text but will be included in future variants. **(B)** Different variants of the tagging segment with a brief description of intended use. Orange semi-opaque square denotes variants under construction.

between the tag and *galK* promoter.

We PCR-amplified all fragments for the isothermal assembly except the λ-P$_R$ promoter, which we obtained by annealing complementary synthetic oligonucleotides (annealing was performed in TSE buffer: Tris 10 mM, NaCl 50 mM and EDTA 1 mM with pH 7.7). Due to inefficient assembly of multiple fragments, we performed a sequential assembly followed by PCR amplification of the assembled fragment, which improved the efficiency. However, during the plasmid construction, we noted multiple occurrences of mutation in the promoter, leading us to the conclusion that the expression of the *galK* from a strong and constitutive λ-P$_R$ promoter presents a burden for a host cell when expressed from a plasmid. In the plasmid that is currently under development, we plan to introduce the temperature-dependent repressor *cI*857 to inhibit the expression of the *galK* from λ-P$_R$ when cultivated below 32°C.

7.2.3 ⋆Design of recombineering primers, recombineering, and chromosomal modifications

The chief objective of our technique is to allow for a flexible design of integration fragments without the need to construct new plasmids for every integration. Therefore, with the template plasmid described above at hand, we only need to redesign

the PCR primers that determine the chromosomal target. We illustrate the design of primers whose 5′-overhangs serve as "landing pads" in recombineering.

We need to design the recombineering primers such that the proper open reading frame is left intact after the integration of the tag. Both recombineering primers have an annealing part to the auxiliary plasmid and a 5′-overhang that is homologous to the targeted chromosomal. Forward primer begins with the last 50-bp before the stop codon of the gene of interest (HF part) and continues with 40-bp that anneal to the linker (PF: GGTGGTGGTTCTGGTGGTGGTTCTGTGAGCGGCTGGCGGC, Fig. 7.3). Reverse primer begins with a reverse complement of the region downstream of the stop codon of the gene of interest (HR). This part has more flexibility as the frame was preserved with the forward primer. However, HR has to be designed such that the downstream gene is not perturbed. For tagging, reverse complement of the 50-bp immediately after stop codon can be used. The primer continues with a 45-bp long reverse annealing region (PR: TTATCGTGAGGATGCTAGCTCAGCACTGTCCT-GCTCCTTGTGATG, Fig. 7.3). Long primers make the PCR amplification the most challenging part of the whole procedure. However, when successful, the fragment is relatively short ($\approx$ 1.5-kbp) which favorably improves the transformation and recombineering efficiency. The fragment is recombined into the region of interest using λ-red recombineering [Datta *et al.*, 2006]. The obtained strain is selected on agar plates containing D-galactose as the only carbon source. Grown colonies are picked and restreaked on MacConkey indicator plates, where correct colonies should turn pink (as opposed to white) thus confirming the GalK activity. After PCR verification, a recombineering plasmid is reintroduced to allow for the removal of the *galK* cassette.

Scarless removal of the selection cassette is attempted by recombineering a short fragment that replaces the selection cassette. In this step, we design a 100-bp DNA fragment whose initial 50-bp are the same as the last 50-bp of the linker-tag segment [common removal fragment (RF): CTGGTGGTGGTTCTGTGAGCGGCTGGCGGCT-GTTCAAGAAGATTAGCTAA] and the final 50-bps are reverse-complement to segment HR from above. The fragment is assembled by annealing two complementary synthetic oligonucleotides in TSE buffer. Short fragments have superior trans-

formation efficiency; while recombineering can be performed by single-stranded oligonucleotides we opted for double-stranded fragments out of concern of unwanted structures formation and differences in recombination efficiencies between lagging and leading strands. Upon electroporation, an extended outgrowth period is necessary to completely segregate the unmodified chromosomal loci (due to multiple replication rounds in the cell, not all loci are modified in recombination) and to dilute out GalK. The latter would be detrimental in the counterselection even though the gene has been eliminated. Counterselection is performed on agar plates with glycerol as a carbon source and DOG as a counterselection compound. Grown colonies are picked and restreaked on MacConkey indicator plates to verify the loss of *galK* cassette as indicated by white colonies. After PCR verification and sequencing, the strain should contain a modified locus with no residual chromosomal alterations.

7.2.4 ∗Scarless tagging of initiation factor 2 and measurement of its abundance

We illustrate this procedure by describing the construction of the fusion between endogenous *infB* and [$(GGGS)_2$]-HiBit. We used this construct to determine the native level of initiation factor and verify the integration technique. We started with a galactose-auxotrophic strain. We designed the primers according to the description above. Forward recombineering primer 5′-overhang contained the forward homology (HF) to *infB* (GCGATGTGATCGAAGTATTCGAAATCATCGAGATCCAACGTACCATTGCT), followed by the PF segment that anneals to the auxiliary plasmid described above (Fig. 7.3). Reverse primer 5′-overhang determined the second arm of the landing pad, which we chose as the immediate 50-nt after *infB* (CATGCCGGATGCAGCGTAAACGCCTTATCCCGCATGGAACCCTAAAAACC). The annealing region of the reverse primer continued with the PR segment described in the previous section (Fig. 7.3).

After the PCR amplification of the fragment, it was recombined into the chromosome. Correct recombinants were selected on galactose (as described above) and

verified by PCR and by streaking on MacConkey indicator plates. Correct clones were transformed with recombineering plasmid in preparation for the removal of the selection cassette. Here, we designed two complementary oligonucleotides. The first half of the sense oligonucleotide is the common removal fragment RF and the second half is reverse-complemented HR. This fragment was recombined into the strain [Datta *et al.*, 2006] and counterselected on DOG-glycerol plates. We verified the cassette removal by streaking on MacConkey indicator plates and PCR. Taken together, PCR confirmed the desired 60-nt alteration of the chromosomal region. The tagging of the carboxyl-end of the protein captures potential isoforms of a particular protein. Concretely, the transcript for *infB* gets translated as three isoforms: IF2α, IF2β, and IF2β′ (full-length protein and start codons at positions 158 and 165, respectively). These isoforms do not have the same start codon but share the same stop codon and with it a HiBit tag. This way, the quantification of the tagged proteins lumps together all isoforms.

Next, we tested the precision of protein quantification and potential fitness defects of the tagged strain. We grew WT and tagged strain in minimal medium in shaking flasks immersed into a water bath with shaking. We measured OD periodically; after each measurement, we replenished the removed medium with fresh prewarmed one and corrected the measured OD accordingly. We noted that there is only a small difference in the growth rate (Fig. 7.5). After cultures approached

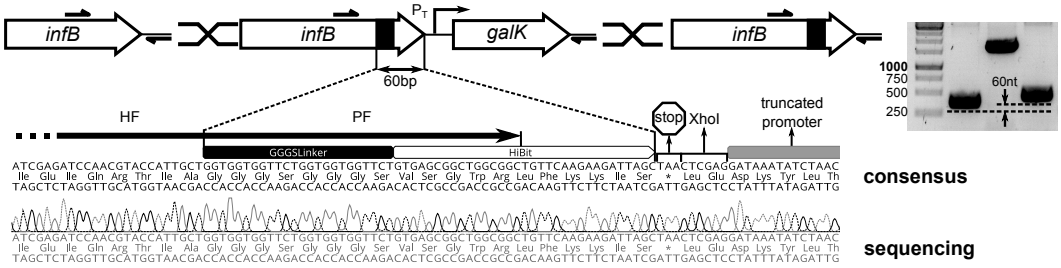

Figure 7.4: **Progression of the modifications of *infB* locus.** Top: Schematic of the progression. Shown are approximate position of the PCR primers. Black region indicates a linker. Bottom: Sequencing electropherogram result compared to the consensus. Shown are more details of the immediate neighborhood of the tag. Right: DNA bands corresponding to the PCR reactions for individual steps shown on the right.

the late exponential phase, we collected the bacteria, adjusted their density to the same value and lysed the cells.

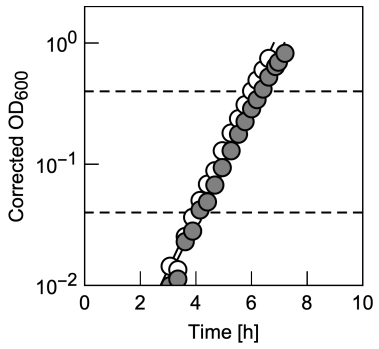

Figure 7.5: **Growth curves of tagged and WT strain.** Time tracks of OD for WT (white circles) and tagged (gray circles) strain reveal that there is only a marginal fitness defect caused by tagging (growth rates in minimal M9 medium with casamino acids and glucose: 1.13 ± 0.02 and $1.07 \pm 0.02\ h^{-1}$, respectively).

After obtaining the lysates of WT and tagged strain, we constructed a serial dilution of the tagged lysate in WT lysate, thus mixing the proteomes of both such that the ratio of the tagged-strain proteome halves in every step (Fig. 7.6). If strains have globally the same proteomes except that the tagged strain contains a detectable tag, such dilution will keep the amount of non-specific detection constant, yet it will decrease the specific detection of the tagged protein accordingly. To obtain the abundance of the tagged protein rather than just a readout, we constructed another dilution series of WT lysate, which we spiked with a known quantity of control protein (HiBit Control protein, Promega). By fitting a linear function to a scatter plot of the readouts of both dilution series we obtain the ratio between the initial concentrations of the standard and tagged protein (Fig. 7.6). Furthermore, by including the control in which we perform the assay solely using the lysate of WT cells, we can estimate the background and the sensitivity of the assay.

We additionally estimated the density of bacteria by plating a series of diluted samples. This allowed us to obtain an estimate for the number of molecules per cell. In so doing we estimated that there are around 2.2×10^3 initiation factor molecules per colony-forming unit (CFU) (Fig. 7.6). Here, we must point out that the estimate of cell density can vary significantly between technical replicates. In the next section, we will recalculate the concentration of the factors per ribosome.

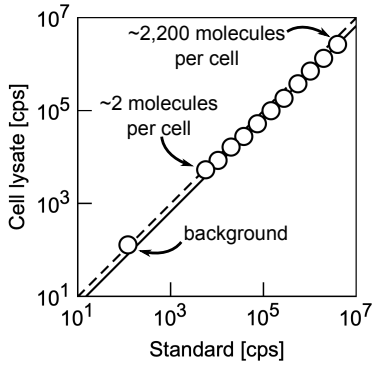

Figure 7.6: **Standard curve for quantification of HiBit-tagged protein.** By measuring the luminescence of the dilution series of known concentration of control protein and the dilution series of the tagged-strain lysate. If the concentrations of both are the same, the slope would be 1 (dashed line), otherwise, the slope is different. Note, that the difference between background and point with the lowest signal is nearly a hundred-fold.

7.3 Model meets the experiment: initiation perturbations

The aim of developing the precise technique for quantifying the abundance of translation factors in physical units was to analyze the model from Sec. 7.1. Below we illustrate the process of inferring phenomenological parameters that constrain the induction curve [Eq. (7.13)]. We designed the experiment around a variation of the initiation factor as in Chapter 5. To vary the expression of the initiation factor, we recombined the tagged initiation factor into the *galK* locus under the control of the $P_{\mathrm{LlacO-1}}$ promoter. Besides measuring the abundance of the initiation factor, we aimed to determine the RNA and protein content to get a closer look into the physiological state of the cell.

7.3.1 The growth conditions

We grew the strain with the titratable initiation factor at five different inducer concentrations, which we chose to cover growth rates roughly between 50-100% of the maximal one. We measured the growth rates of batch cultures by sampling the cultures periodically and measuring the OD (Fig.7.7A). Besides five conditions in which we grew the strain with titratable tagged initiation factors, we prepared two separate cultures for a strain with a tagged endogenous copy of the initiation factor as well as a WT strain. All strains were grown in M9 minimal medium with casamino acids and glucose, supporting a growth rate of $\lambda_0 \approx 1.0$ h^{-1}. By measuring the

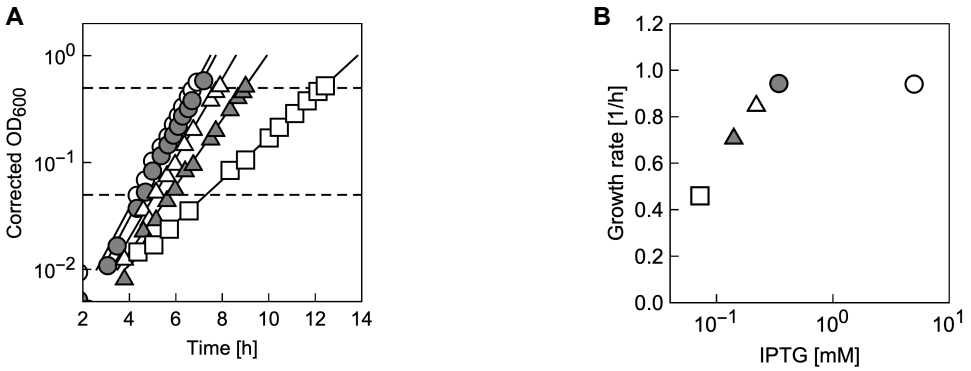

Figure 7.7: **Growth curves and a resulting induction curve for the strain with titratable initiation factor. (A)** Time tracks of OD for five different conditions. Note how the slope of the curves decreases as a result of lowered initiation factor expression. **(B)** The induction curve shows the dependence of growth rates on inducer concentration. Symbols correspond to the growth curves shown in A.

growth rate we determined its dependence on the inducer concentration (Fig. 7.7B).

7.3.2 Quantification of the initiation factor abundance

With the factor-quantification method at hand (see Sec 7.2.4), we moved a step closer to having the necessary data for constraining the parameters ζ_0 and K_m in Eq. (7.13). We constructed factor-dilution curves using WT strain lysates and standard proteins (Fig. 7.8).

The assay provided information on how many initiation factor molecules are present per given density of cells (specified by measured optical density). However, to obtain the intracellular factor concentration we needed to find a reasonable proxy for calculating the cellular volume. Because we can calculate the ribosome concentration from Eq. (7.13), we aimed to calculate how the initiation factor abundance changes relative to ribosome abundance. To obtain ribosome abundance we quantified the RNA as well as protein content.

7.3.3 Quantification of the protein and RNA content

To quantify the ribosome content, we determined the total RNA content by performing perchloric acid ($HClO_4$) extraction as described in Ref. [Benthin *et al.*, 1991] with minor modifications (as communicated by M. Scott, University of Waterloo). Briefly,

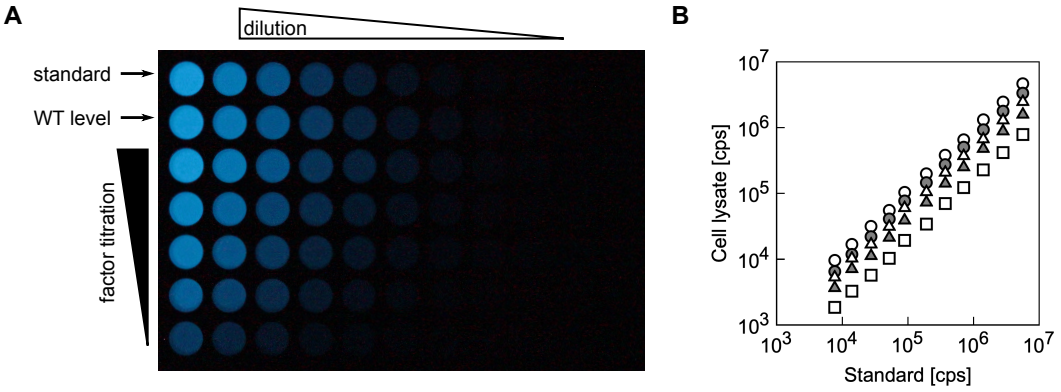

Figure 7.8: **Quantification of the initiation factor abundance in factor-titration experiment. (A)** A photo shows a microtiter plate with luminescent samples in the wells. It showcases the strength of the signal in comparison to the background and how signal decreases by serial dilution. We obtained the photo using a macroscope camera with 30 s exposure without any filters. **(B)** Concentration of the initiation factor is obtained from a scatter plot. See Sec. 7.2.4 and Fig. 7.6. Symbols are as in Fig. 7.7. Lower abundance is reflected in a lower offset (due to log-log plot).

the cell pellet is washed with cold $HClO_4$, followed by hydrolysis in KOH at 37°C. Supernatant is neutralized by cold $HClO_4$ (which yields potassium perchlorate used in rocketry) and the precipitate is washed again with perchloric acid. Spin-cleared supernatant contains RNA, which is quantified by measuring the absorbance at 260 nm. The concentration of RNA is obtained by noting that the molar extinction coefficient is $10.8{\times}10^3$ $M^{-1}cm^{-1}$ and molecular weight of average RNA nucleotide weight of 324 Da, thus yielding $c_{\mathrm{RNA}} \approx 31 \times \mathrm{OD}_{260}$ μg/mL.

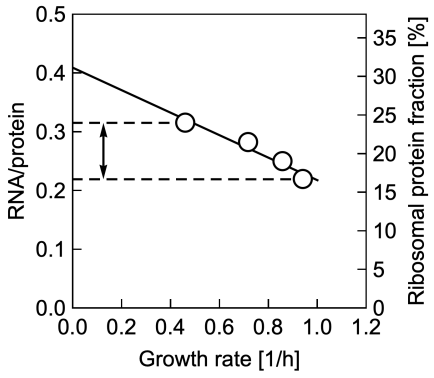

Figure 7.9: **RNA to protein ratio reflects ribosome upregulation.** By measuring the RNA and protein content we can observe the upregulation of the ribosome expression. Here, our measurements reproduce the negative correlation between the growth rate and RNA/protein. We excluded one point due to issues with protein quantification.

We quantified the protein content by using colorimetric bicinchoninic acid assay (also known as Smith assay, Sigma-Aldrich BCA1-1KT). This colorimetric assay is based on the change in the color due to protein bonds reducing Cu^{2+} ions, which is

reflected in changed color (similar to biuret test). To translate the change in color (as measured by absorbance at 562 nm) to protein concentration, we performed the assay on a series of protein samples (bovine serum albumin) of known concentrations; such standard curve is well described by a quadratic function.

With these two quantifications at hand, we determined the RNA/protein ratio (Fig. 7.9). This ratio reflects the ribosome content relative to the whole proteome (see Introduction). Here, we observed the increase in RNA/protein ratio as we lowered the expression of the initiation factor. We converted the RNA/protein ratio to protein fraction by accounting 86% of the RNA is rRNA, the ratio of r-proteins to rRNA $m_{\mathrm{r-protein}}/m_{\mathrm{rRNA}} = 0.53$, and the ratio of r-proteins and extended translation machinery proteins is around 1.67 [Bremer and Dennis, 1996; Maaløe, 1979; Scott *et al.*, 2010]. This yields the conversion $\phi_R = (R/P)\rho$, where R, P, and $\rho = 0.76$ are RNA-, protein content, and conversion factor from R/P to ϕ_R, respectively. We, however, observed a lower increase in protein fraction allotted to a ribosomal fraction as reported in Ref. [Scott *et al.*, 2010].

7.3.4 Inference of physiological parameters

The model presented in Sec. 7.1 requires two parameters: ζ_0 and K_m. To adjust these two parameters, we first calculated the abundance of initiation factors relative to the number of ribosomes. If we know the amount of total RNA, we can estimate the number of ribosomes by noting that there are 4,566 RNA nucleotides per ribosome with the average nucleotide molecular weight of 324 Da. In so doing, we estimated how the growth rate changes with the ratio between initiation factor molecules per ribosome (Fig. 7.10A).

Obtaining the ratio of initiation factor molecules per ribosome has the added benefit of being easily convertible to the intracellular concentration of translation factors. Here, we estimate the intracellular concentration of translation factors by multiplying the ratio and the concentration of the ribosomes, which we estimate from the growth law [Eq. (4.2)] (Fig. 7.10B). With this data at hand, we can fit the model [Eq. (7.13)]. We obtained the values $K_m = 0.36$ μM and $\zeta_0 = 2.21$ $\mu\mathrm{M}^{-1}\mathrm{s}^{-1}$.

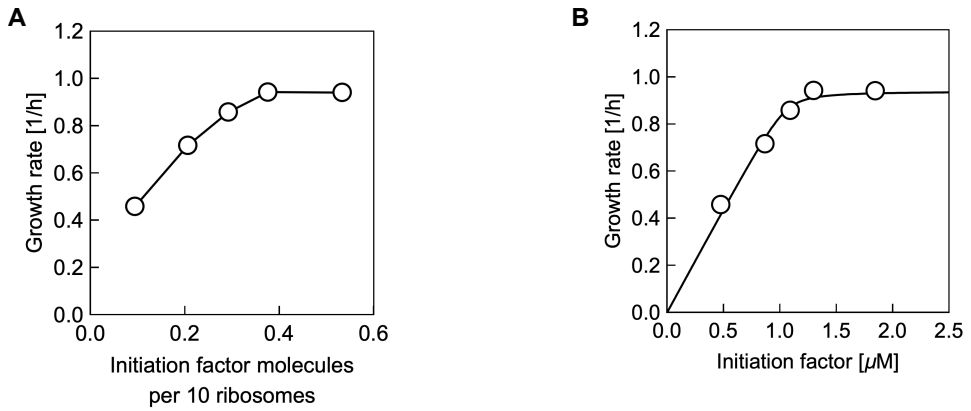

Figure 7.10: **Growth rate dependence on number of initiation factors in relation to ribosomes and on concentration of factors. (A)** Growth rate monotonically increases with the number of initiation factor molecules per ribosome. Full growth rate is recovered already at ≈ 0.4 factors per ten ribosomes. **(B)** Intracellular concentration of the initiation factor can be mapped to the growth rate using the model [Eq. (7.13), solid line].

Coincidentally, the dissociation constant K_m we obtained from the fit is higher than the estimate we used in the TASEP modeling. In the latter case we used a value obtained *in vitro* [Milon *et al.*, 2012]. As we noted in the Introduction, the crowded environment of the cell causes the slower diffusion of bulky proteins [Klumpp *et al.*, 2013; Milo and Phillips, 2016]. Here, the ratio between inferred and *in vitro* measured value is ≈ 7.2, roughly comparable between the ratio of diffusion constants in water and cytoplasm. The parameter values are burdened by measurement and fitting imperfections, but it is still reassuring that the order-of-magnitude for the ratio is in line with the expected estimates as based on Smoluchowski limit, *i.e.*, $K_m \geq k_{\text{init}}/(4\pi D a) \propto 1/D$, where D is a diffusion constant, a is typical linear dimension, and k_{init} is an initiation rate per ribosome [Klumpp *et al.*, 2013]. The low value of $K_m/\Delta r$ also suggest that the Eq. (7.13) will be close to the irreversible limit since $R_0 \approx 541$ and $K_m/\Delta r \approx 0.008$. We further estimate the initiation factor concentration that supports a 50% growth rate as $[\text{IF}]_{50} \approx 0.57$ μM. We can further explain higher value for ζ_0 compared to the estimate in Chapter 6. Figure 7.10 shows that the full growth rate is recovered already at ≈ 0.4 initiation factors per ten ribosomes, which is roughly ten times less than the estimate we used previously [Bremer and Dennis, 1996]. Because we estimate the rate as $\zeta_0 = \zeta/[\text{IF}]$,

where $\zeta = 3.0\ s^{-1}$, this approximately ten-fold decrease results in the same fold-increase in the estimate.

Predicting the effect of hyper-accurate ribosomes on the induction curve

Here, the advantage of such a model over a simple fit of a generic function can be illustrated. Because the parameters have a physiological interpretation, we can predict the change in the induction curve when parameters alter. The translation rate of ribosomes can be reduced by specific mutations in the ribosomal proteins. By fitting a sigmoidal function to the data in Fig. 7.10B, we can indeed map the initiation factor concentration to the growth rate. However, we do not obtain a mechanistic understanding of the fitted-function parameters.

Mutations in the ribosomal protein *rpsL* of the small ribosome subunit can render ribosomes hyper-accurate to the extent that proof-reading becomes limiting in translation [Ruusala *et al.*, 1984]. The addition of streptomycin (which increases the rate of mistranslation) increases the growth rate. Because κ_t is proportional to the translation rate (see Introduction), we denote $\kappa_{t,\varphi} = \kappa_t \times \varphi$, where φ is a relative translation rate ($\varphi = 1$ corresponds to WT translation rate). Put together, the growth rate as a function of relative translation rate is $\lambda_\varphi = \lambda_{\max}\lambda_0\varphi/[\lambda_0(1-\varphi) + \varphi\lambda_{\max}]$, where $\lambda_{\max} = \Delta r\kappa_t \approx 2.8\ h^{-1}$ and λ_0 is a WT growth rate in this particular medium. Additionally, we can predict the change in IF_{50} from Eq. (7.14) thus fully constraining the induction curve without any free parameters. In the limit of $R_0 \gg 1$ and $K_m/\Delta r \ll 1$, $IF_{50} \approx \lambda_\varphi(r_{\min} + \xi)/2\zeta_0 \propto \lambda_\varphi$, which offers a prediction for scaling of the initiation factor concentration required to achieve 50% of the λ_φ.

This showcases the benefit of having a physiology-based model that offers a mechanistic prediction, which we can trackback to a genetic perturbation. Here, the effects of mutations that perturb catalytic rate ζ_0 can be predicted as well. Here we demonstrated how the reduced translation rate can alter the induction curve. If we would like to pursue this further and investigate the effects of the translation rate perturbations, it is of the essence to develop tools to measure the translation rate.

7.4 Gene expression dynamics and the measurements of the translation rate

In previous chapters, we focused primarily on the steady-state solutions. While studying steady-state behavior is insightful for inference of global dependencies between physiological processes, the dynamics of said processes can offer additional information about the system. Furthermore, as we discussed in the Introduction, many parameters that describe the steady-state behaviors are dependent on parameters describing the dynamics [Dai *et al.*, 2016]. The dynamical properties of the gene expression are directly connected with translation. Therefore, studying the dynamics of gene expression can provide additional information about translation parameters (*e.g.*, translation rate) and those of related processes (*e.g.*, mRNA transcription or decay rate). Below we briefly discuss a simple model that describes the dynamics of gene expression and experimental design that allows us to infer crucial physiological parameters.

7.4.1 The dynamical system describing gene expression

We consider the following scenario: the transcription of a gene starts at $t = 0$ when new 5′-ends start appearing. These mRNA transcripts get degraded with the rate proportional to their abundance, while non-degraded transcripts are translated. However, a certain amount of time between the start and finish of translation is required, since the ribosome processes a certain number of codons per second (defined as a translation rate). On top, other processes (*e.g.*, ribosome translation initiation, ejection of a completed protein, *etc.*) delay the protein production. We can lump all these contributions into a characteristic delay t_0. Therefore, the rate of new proteins appearing becomes proportional to the mRNA concentration at the time $t - t_0$. We note, that a different derivation that arrives to similar results is in Ref. [Liang *et al.*, 1999].

Let m be a concentration of mRNA; starting at the time of the induction, its time

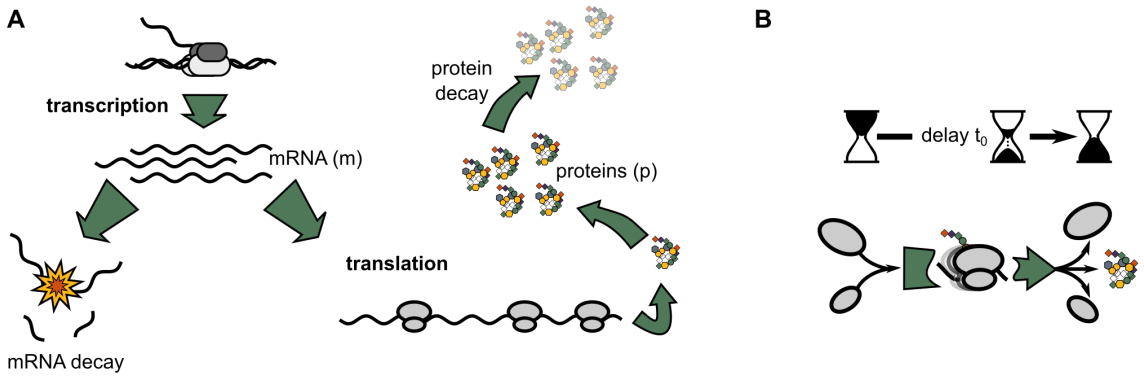

Figure 7.11: **Main components of the model describing gene expression dynamics. (A)** In the model, we consider only simplified transcription and translation. In the transcription and translation part, we consider synthesis and decay of mRNA and proteins, respectively. **(B)** The delay between the start and the end of translation means that the rate of protein synthesis is proportional to the abundance of mRNA at an earlier time.

derivative is

$$\dot{m}(t) = \omega - m(t)\varepsilon, \tag{7.16}$$

where ω and ε are an mRNA transcription and decay rate, respectively. Solving for $m(0) = 0$ yields

$$m(t) = \frac{\omega}{\varepsilon}\left(1 - e^{-t\varepsilon}\right). \tag{7.17}$$

Here, we assumed that the transcription starts at $t = 0$; in practice, induction of transcription is also delayed relative to the "start" signal (*i.e.*, the addition of the inducer) – inducer has to enter into the cell and bind to the transcription factor, RNAP initiates transcription, *etc.* As we discuss later, this delay can be accounted for in delay time t_0 as well. Equation (7.17) has the expected sigmoidal shape with the limit $\lim_{t\to\infty} m(t) = \omega/\varepsilon$, which is expected for a birth-death process.

We describe the time evolution of the protein concentration with a delay differential equation; protein synthesis rate at the time t is proportional to the amount of mRNA at the time $t - t_0$. The proportionality constant equals the initiation rate Σ and the protein decay rate is given by Υ:

$$\dot{p}(t) = \Sigma m(t - t_0) - \Upsilon p(t). \tag{7.18}$$

Here, we can mathematically delineate the sources of t_0. Delay time t_0 can be separated into a variable and fixed component relative to the length of the ORF.

Certain processes (*e.g.*, ribosome binding to 5′-UTR and translation initiation) will take the same time, invariant of the length of the downstream ORF: we lump all these delays into a single number t_{lump}. Because this number is the same for all transcripts, it can account for delay times in transcription as well. On the other hand, ribosomes will need a longer time for completing the translation of longer ORFs, *i.e.*, $t_L = L/k$, where L and k are lengths of the ORFs (in codons) and translation speed. Parsing the onset time into a fixed and variable component (*i.e.*, $t_0 = t_{\text{lump}} + L/k$) is useful in comparison of the onset times of proteins of different lengths. Taking the difference between the onset times of proteins A and B becomes $\Delta t = t_{0,\text{A}} - t_{0,\text{B}} = (L_\text{A} - L_\text{B})/k = \Delta L/k$, from which t follows that $k = \Delta L/\Delta t$. Hence, knowing the onset times of proteins of different (known) lengths can uncover the translation rate [Schleif *et al.*, 1973; Zhu *et al.*, 2016]. Equation (7.18) is linear and its solution for times $t \geq t_0$ is

$$p(t) = \frac{\omega\Sigma}{\varepsilon\Upsilon(\varepsilon - \Upsilon)} \left\{ \varepsilon \left[1 - e^{(-t+t_0)\Upsilon} \right] + \Upsilon \left[e^{(-t+t_0)\varepsilon} - 1 \right] \right\}, \tag{7.19}$$

and is zero for $t < t_0$. The limit $\lim_{t\to\infty} p(t) = \omega\Sigma/(\varepsilon\Upsilon)$ is as expected for a steady-state solution and represents the maximal attainable expression level at which mRNA and protein synthesis (ω, Σ) and decay (ε, Υ) balance-out (Fig. 7.12A).

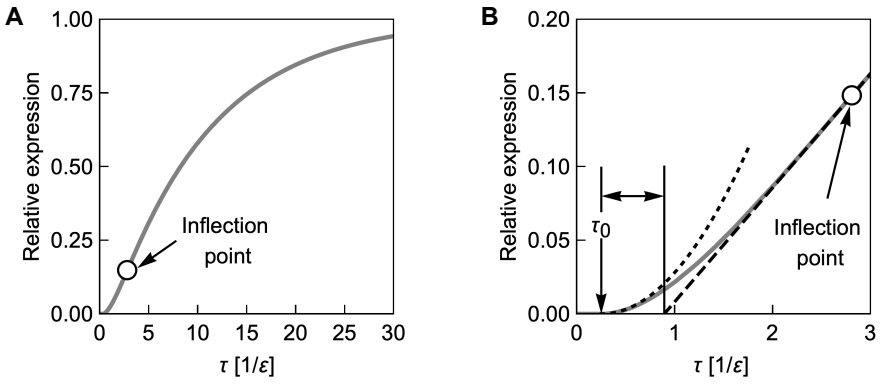

Figure 7.12: **Theoretical model of induction dynamics. (A)** Time dependence of gene expression. Rapid increase in gene expression slows down after passing the inflection point. We rescaled the expression relative to its maximum $\omega\Sigma/(\varepsilon\Upsilon)$ and used mRNA lifetime $t_{\text{mRNA}} = 1/\varepsilon$ as a time scale. **(B)** Early stages of gene expression dynamics (before the inflection point). After $\tau_0 = t_0\varepsilon$ a quadratic increase (dotted line) is followed by gradual transition into a linear increase (dashed line). We used $\tau_0 = 0.25$ and $\Sigma/\varepsilon = 0.1$.

Since we are interested in the dynamics of the induction, we investigate the early

behavior of the system, specifically around the time when the first proteins start to appear. Expanding the Eq. (7.19) around t_0, we obtain

$$p(t) \approx \frac{\omega\Sigma}{2}(t - t_0)^2 . \tag{7.20}$$

The quadratic behavior and independence of the degradation constants arise due to low abundances of mRNA and proteins. Because degradation is proportional to said abundances, it is low in comparison to the synthesis rates. We can heuristically explain quadratic behavior by noting that if the mRNA abundance increases linearly with time (in the absence of degradation) as $m(t) \approx \omega t$, protein synthesis then equates $\dot{p} \approx \Sigma\omega(t - t_0)$. Integrating the latter between t_0 and an arbitrary time $t \geq t_0$ yields $p(t) = (\omega\Sigma/2) \times (t^2 - 2t_0 t - t_0^2) = (\omega\Sigma/2) \times (t - t_0)^2$ as in Eq. (7.20) [Schleif *et al.*, 1973]. In the early stages of the induction, we thus expect the quadratic increase in expression (Fig. 7.12B).

Expression saturates after a long enough time. However, if in the early stages expression increases quadratically (therefore with an upward concavity since $\ddot{p}(t) > 0$) and flattens in the long term, it has to pass through the inflection point (Fig. 7.12). We find the inflection point by equating the second time derivative

$$\ddot{p}(t) = \frac{\omega\Sigma}{\varepsilon\Upsilon(\varepsilon - \Upsilon)}\left[\Upsilon\varepsilon^2 e^{(-t+t_0)\varepsilon} - \varepsilon\Upsilon^2 e^{(-t+t_0)\Upsilon}\right], \tag{7.21}$$

with 0. This yields a solution $t_{\text{inf}} = [t_0\varepsilon - t_0\Upsilon + \ln(\varepsilon/\Upsilon)]/(\varepsilon - \Upsilon)$. Taylor expansion of a function around the inflection point yields a linear approximation due to vanishing second derivative. As we show later, this approximation contains additional information about the system parameters. If we calculate the intercept of this linear expansion with the time axis, we obtain

$$t_\varepsilon = t_0 + \frac{1}{\varepsilon} + \underbrace{\frac{1}{\Upsilon} - \frac{(\varepsilon/\Upsilon)^{\frac{\Upsilon}{\varepsilon-\Upsilon}}}{\Upsilon} + \frac{\ln(\varepsilon/\Upsilon)}{\varepsilon - \Upsilon}}_{\frac{[(\varepsilon/\Upsilon)^{\Upsilon/(\varepsilon-\Upsilon)}-1](\varepsilon-\Upsilon)-\Upsilon\ln(\varepsilon/\Upsilon)}{\Upsilon(\Upsilon-\varepsilon)}} . \tag{7.22}$$

In the limit $\varepsilon \gg \Upsilon$, Eq. (7.22) simplifies to $t_\varepsilon = t_0 + 1/\varepsilon$. Consequently, this means that if we determine the t_0 [Eq. (7.20)] and the intercept t_ε [Eq. (7.22)], we can estimate the average lifetime of mRNA, *i.e.*, $t_{\text{mRNA}} = 1/\varepsilon$. Typically, proteins in *E. coli* are relatively stable and are mostly diluted by the growth of cells. Therefore,

the protein decay rate becomes $\Upsilon \approx \lambda$, which is in the order of 0.01-0.1 min^{-1}. Estimates of mRNA degradation are around 0.3-1 min^{-1} [Liang *et al.*, 1999; Yu *et al.*, 2006], thus making these rates at most an order of magnitude apart. Thus, this approximation essentially serves as an estimate for an upper bound of the lifetime of mRNA. Thus, such a dynamic measurement can estimate the mRNA lifetime as well as the translation rate.

Besides mRNA lifetime and translation rate, translation initiation rate is one of the crucial parameters of translation as we have shown in Chapters 5,6, and Sec. 7.3. In the following, we propose that as the variation of the ORF length uncovered the translation rate, the variation of the transcript-specific initiation rate holds the potential to reveal the relative changes in the initiation rates between different conditions.

On the level of mRNA, multiple properties determine the initiation rate. The contributions arise from: (i) energetics of hybridization between mRNA and rRNA (SD-aSD) as well as the codon-anticodon pairing on the start site, (ii) energy penalty of the suboptimal distance between rRNA binding site and start codon, and (iii) energetics of the mRNA unfolding [Salis *et al.*, 2009]. These properties are directly determined by the sequence of mRNA and can be varied genetically. From the point of statistical physics, the problem of the ribosome binding and initiating the translation is similar to the polymerase binding to the promoter and starting transcription. In the same spirit as in *e.g.,* Ref. [Kinney *et al.*, 2010], we can describe the translation initiation using equilibrium statistical thermodynamics. In this case, the initiation rate is proportional to the probability of binding given with a Boltzmann weight, *i.e.,* $\propto \exp(-\Delta E_{\text{tot}}/k_B T)$, where ΔE is the sum of all energy contributions described above [Salis *et al.*, 2009].

With these considerations at hand, we can further parse the length-invariant component t_{lump} in the onset time t_0. Namely, let us assume that

$$t_0 = t_{\text{lump}} + \frac{L}{k} = \frac{\vartheta_i}{u_{\text{ti}}(\lambda)} + t_{\text{steps}}(\lambda) + \frac{L}{k} = \frac{\vartheta_i}{u_{\text{ti}}(\lambda)} + t_{\text{rest}}(\lambda), \tag{7.23}$$

where $t_{\text{rest}}(\lambda) = t_{\text{steps}}(\lambda) + L/k$ is the total time associated with all other required translation steps except initiation. Denominator $u_{\text{ti}}(\lambda)$ is an intrinsic translation

initiation rate, which we aim to determine. Here, λ encapsulates the growth condition as well as the choice of the strain and is therefore variable. In Eq. (7.23), coefficient ϑ_i denotes a characteristic weight, specific for i-th transcript. The value of this weight is inversely proportional to the Boltzmann factor and is mRNA sequence-dependent, specifically on the details of 5′-UTR.

In contrast to variation of the ORF lengths, modifications of the 5′-UTR do not have a direct quantitative interpretation. As the actual values of ϑ_i are not known, the direct inference of t_{rest} and u_{ti} is not possible. However, if we consider two conditions (λ and λ'), we can infer the relative difference between $u_{\text{ti}}(\lambda)$ and $u_{\text{ti}}(\lambda')$. We start by inverting the Eq. (7.23) to express

$$\vartheta_i = u_{\text{ti}}(\lambda)\,[t_0(\lambda, \vartheta_i) - t_{\text{rest}}(\lambda)]\,. \tag{7.24}$$

Next, we plug the expression for ϑ_i [Eq. (7.24)] into the Eq. (7.23), but this time for λ':

$$\begin{aligned} t_0(\lambda', \vartheta_i) &= t_{\text{rest}}(\lambda') + \underbrace{\frac{u_{\text{ti}}(\lambda)}{u_{\text{ti}}(\lambda')}}_{1/\Gamma}\,[t_0(\lambda, \vartheta_i) - t_{\text{rest}}(\lambda)] = \\ &= \underbrace{t_{\text{rest}}(\lambda') - \frac{1}{\Gamma} t_{\text{rest}}(\lambda)}_{\chi \perp \vartheta_i} + \frac{1}{\Gamma} t_0(\lambda, \vartheta_i) = \\ &= \chi + \frac{1}{\Gamma} t_0(\lambda, \vartheta_i). \end{aligned} \tag{7.25}$$

This expression allows the determination of the relative intrinsic initiation rate Γ. The offset χ is independent of ϑ_i. If we consider a series of N transcripts of a fixed length but with different 5′-UTR (different ϑ_i) with known onset times in both conditions (λ and λ'), we can extract the Γ by fitting a line to a scatter plot of onset times $\{(t_0(\lambda, \vartheta_1), t_0(\lambda', \vartheta_1)), \ldots, (t_0(\lambda, \vartheta_N), t_0(\lambda', \vartheta_N))\}$. Experimentally, this approach requires the determination of the onset times for a series of 5′-UTR variants in a reference and studied condition. Fitting a line gives a slope, whose inverse value is $\Gamma = u_{\text{ti}}(\lambda)/u_{\text{ti}}(\lambda')$, which reports on the relative change in intrinsic initiation rate between conditions.

7.4.2 Experimental concept

The model we described above suggests a way of determining the translation parameters if we can precisely measure the dynamics of gene expression. Specifically, we require the measurement technique to have high sensitivity because we aim to detect the emergence of first proteins. In turn, this requires low background. Furthermore, high temporal precision is important to track events that have a typical timescale of seconds to minutes. A classical method for determining low amounts of proteins is using β-galactosidase (LacZ). This method has been used studies of the induction kinetics of L-arabinose operon [Schleif *et al.*, 1973] as well in later refinements of the method for determining the translation rate [Zhu *et al.*, 2016; Liang *et al.*, 1999; Liang *et al.*, 2000]. While the β-galactosidase assay is highly precise, it is also somewhat demanding to perform: it requires sampling of the culture in regular intervals and lengthy processing of samples. Therefore, we aimed to establish a technique that beside precision offers minimally invasive handling as well.

We considered different reporters to replace the use of β-galactosidase assay. Fluorescent proteins, for example, offer convenient measurements. However, tracking dynamical processes by measuring the fluorescence of proteins has a disadvantage: fluorescent proteins are not fluorescent immediately after they exit the ribosome. It can take many tens of minutes of maturation before fluorescence can be detected [Iizuka, 2011]. Because we expect the typical time scale for translation of a particular transcript to be in tens of seconds [Zhu *et al.*, 2016; Bremer and Dennis, 1996; Dai *et al.*, 2016], this maturation process renders the fluorescent proteins less apt for measurement of induction kinetics. We thus aimed to implement an induction assay using bacterial luminescence.

Bacterial luminescence from *Photorhabdus luminescens* [Bjarnason *et al.*, 2003] requires an operon *luxCDABE* consisting of five genes, where genes *luxC*, *luxD*, and *luxE* provide substrates (flavin mononucleotide $FMNH_2$ and long-chain fatty aldehyde) that bind to the heterodimeric complex of subunits α and β encoded by *luxA* and *luxB*, respectively [Gregor *et al.*, 2017]. The active site is located on the

α subunit, whose light yield depends on the presence of the β subunit. Thus, the absence of the catalytic subunit α renders the cells non-luminescent. Therefore, to track the induction kinetics, we aimed to put the *luxA* under inducible control. This would allow us to cultivate a strain in the absence of an inducer and track the induction kinetics upon the addition of a high concentration of the inducer. Measuring luminescence can be done conveniently in an appropriate plate reader and does not require manual sampling; thus, smaller sample volumes are required and measurements can be done repeatedly. Furthermore, LuxA does not have to undergo maturation after completing folding, which is faster (μs to ms [Kubelka *et al.*, 2004]) in comparison to GFP maturation times (minutes [Iizuka, 2011]). It is, however, unclear how formation of a LuxA-LuxB dimer affects the measurements. Additionally, as the model discussed above suggests, we wanted to make the expressed gene longer by extending the 5'-end of the open reading frame. Further, we required the system to allow quick modifications of the 5'-UTR. Therefore, we aimed to build a compact genetical system that would allow convenient alterations of the open reading frame as well as UTR. Below we describe the construction and verification of such a system based on two plasmids and its eventual merger into a compact one-plasmid platform. More technical sections are denoted with an asterisk (∗).

7.4.3 ∗Construction of the platform

∗Deletion of *luxA* gene and inducible control

We began the construction of the plasmid platform by deleting the gene *luxA* from the pCS-λ plasmid [Kishony and Leibler, 2003]. We deleted the *luxA* This was done by site-directed mutagenesis using phosphorylated primers PCSdelLuxA-F and PCSdelLuxA-R (Table 7.1). We DpnI digested gel-purified PCR product. Ligation yielded pCS-λ plasmid Δ*luxA*, which we selected for by platting on LB agar plates with 50 μg mL^{-1} kanamycin. Successful deletions were checked for the absence of luminescence and verified by sequencing with primers PCSdelSeqUp and PCSdelSeqDn.

pCS-λ Δ*luxA*

PCSdelLuxA-F	5′-CTAAGGAGAAAGAAATGAAATTTG-3′
PCSdelLuxA-R	5′-AGAGAGTCCTTATATTGC-3′
PCSdelSeqUp	5′-ACGATAATTGGGTCAAGCAAGATG-3′
PCSdelSeqDn	5′-CCAATAAGCAAGCTTCCTCCG-3′

pBAD24-luxA, pBAD24-lacZluxA

luxA-2-pBAD24-Fkpn	5′-ggg**g**gtaccccaacctagg ggtggtggttctggtggtggttct- -AAATTTGGAAACTTTTTGCTTACATACCA-3′
luxA-2-pBAD24-Rhind	5′-cccaagctt**CTA**ATATAATAGCGAACGTTGTTTTTCTTT-3′
kpn-lacZ-2-luxA-F	5′-ggggtaccaACCATGATTACGGATTCACTGGC-3′
avr-lacZ-2-luxA-R	5′-agtccctaggTTTTTGACACCAGACCAACTG-3′

Table 7.1: **Oligonucleotides used in the construction of plasmids pCS-λ Δ*luxA*, pBAD24-luxA, and pBAD24-lacZluxA.** Annealing regions are printed in uppercase, underlined are the restriction sites and bolded are start and stop codons (or the nucleotide, which will give either after subcloning). Dashed underline indicates the linker.

Further steps require the introduction of *luxA* downstream of the P_{BAD} promoter. At this stage, we also included a $(\mathrm{GGGS})_2$ linker (BioBrick identification: K1486003, sequence GGTGGTGGTTCTGGTGGTGGTTCT) and the additional restriction site AvrII for subsequent in-frame subcloning of *lacZ* upstream of the linker-*luxA* tandem (additional bases CCAA between restriction sites in luxA-2-pBAD24-Fkpn promote double-digestion and constrain the open reading frame). We amplified the linker-flanked *luxA* gene from pCS-λ by primers luxA-2-pBAD24-Rhind and luxA-2-pBAD24-Fkpn. PCR product was purified and digested with KpnI and HindIII; plasmid pBAD24 [Guzman *et al.*, 1995] underwent the same digestion reaction but was additionally treated with rSAP to prevent spurious religation. The ligation yielded pBAD24-luxA with an ampicillin resistance cassette (*bla*) and pMB1 origin (15-20 copies per cell) [Guzman *et al.*, 1995]. Introduced restriction sites in the primer luxA-2-pBAD24-Fkpn enabled subsequent digestion of pBAD24-luxA

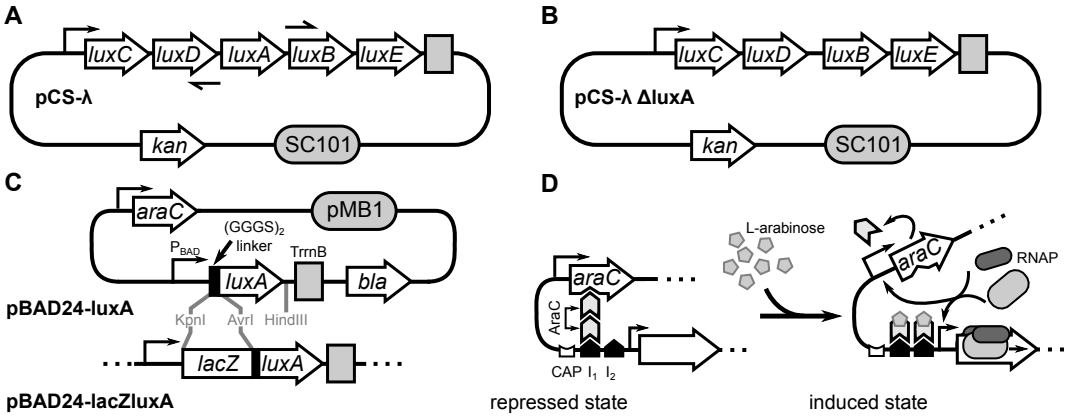

Figure 7.13: **Construction of plasmids used in the measurement of the translation rate. (A,B)** We deleted *luxA* from the luminescence plasmid pCS-λ [Kishony and Leibler, 2003] by using site-directed mutagenesis, yielding a plasmid pCS-$\lambda\Delta luxA$. **(C)** We put the gene *luxA* under inducible control by subcloning into pBAD24; this step introduced an eight amino acids long linker, enabling a fusion with *lacZ*, yielding pBAD24-lacZluxA in the process. See the main text for details. **(D)** Promoter P_{BAD} is repressed by AraC dimer by forming a loop in DNA. When L-arabinose is added, AraC acts as an activator, which with the help of cAMP-bound CAP recruits the RNA polymerase (RNAP) for transcription of the downstream gene.

with KpnI and AvrII, which opened the cloning site to accept *lacZ* gene that was amplified by primers kpn-lacZ-2-luxA-F and avr-lacZ-2-luxA-R. The overhang in kpn-lacZ-2-luxA-F introduced additional adenine right after KpnI site to put the gene into the correct reading frame. This yields a generic way for creating gene-*luxA* fusions: forward primer begins with GGGGTACCA and continues with the sequence of a gene after the start codon, while the reverse primer begins with AGTCCCTAGG and continues with reverse-complemented sequence before the stop codon.

7.4.4 Experimental determination of the translation rate

We first tested whether the expression of *luxA* is tightly repressed in the absence of arabinose and whether the addition of arabinose quickly derepresses the expression; additionally, this verified that we can obtain high temporal precision of luminescence

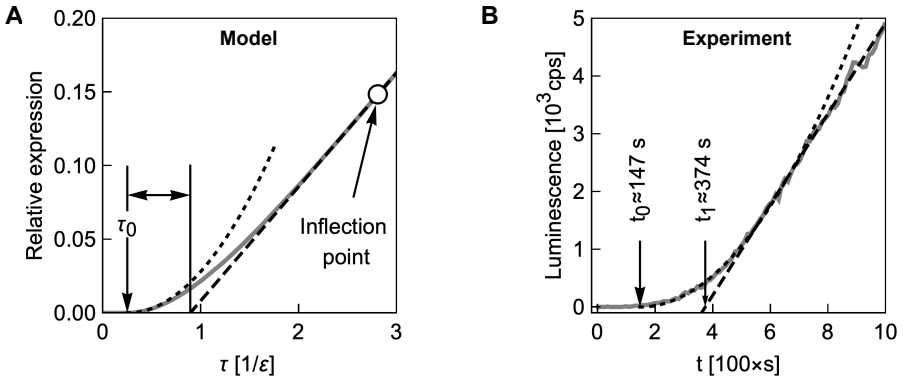

Figure 7.14: **The measurement of induction dynamics reveals two distinct phases in early expression. (A)** The plot from Fig. 7.12 showing model results for easier side-by-side comparison with the experiment. **(B)** Example of experimentally observed induction dynamics. We added arabinose at $t = 0$. After $t_0 = 147$ s, a quadratic increase (dotted line) in expression was recorded, followed by a smooth transition into a linear increase (dashed line). The intersection of the linear approximation with the time axis is at $t_1 = 374$ s.

measurements. However, because the P_{BAD} promoter contains the CAP[1]-binding site, we additionally verified the effect of adding cyclic-AMP (cAMP) before the induction (Fig. B.7). The addition of cAMP before (but not at) induction makes the expression stronger, but not quicker.

We showed that the promoter is tightly repressed in the absence of arabinose and that we can detect the early stages of protein occurrence. We then compared the experimentally observed induction dynamics with the model predictions (Fig. 7.12). Specifically, we wanted to see whether the expression time track exhibits an initial quadratic increase that smoothly transitions into a linear increase. Our experiments confirmed the existence of two different regimes in the expression dynamics (Fig. 7.14). Concretely, after the delay of t_0 we observed a quadratic increase that gradually changed into linear. Further, we can now estimate the mRNA lifetime from inferred times t_0 and t_1 as $t_{\mathrm{mRNA}} \approx t_1 - t_0$. The difference is $t_1 - t_0 = 227$ s or roughly 3.8 minutes, which is in line with current estimates of mRNA lifetime that range between 1-5 minutes [Liang *et al.*, 1999; Yu *et al.*, 2006]. However, mRNA lifetime is transcript-dependent as well, as demon-

[1]cAMP receptor protein

strated for the toxin-antitoxin systems [Nikolic *et al.*, 2018].

Next, we aimed to determine the translation rate in line with previously proposed methods [Zhu *et al.*, 2016]. We transformed HG105 with a supporting plasmid pCS-$\lambda\Delta luxA$ whose encoded proteins provide saturating amounts of LuxB and substrate $FMNH_2$. On top of the supporting plasmid, we transformed the strain with the plasmid pBAD24-luxA or pBAD24-lacZluxA, *i.e.,* reporter only or the extended reporter (fusion *lacZ-luxA*), respectively. The addition of *lacZ* lengthens the open reading frame by additional 1,022 codons. Therefore, by measuring the onset times for reporter and extended reporter, we can determine the translation rate by dividing the difference in length by the difference between the onset times (Fig. 7.15) [Zhu *et al.*, 2016].

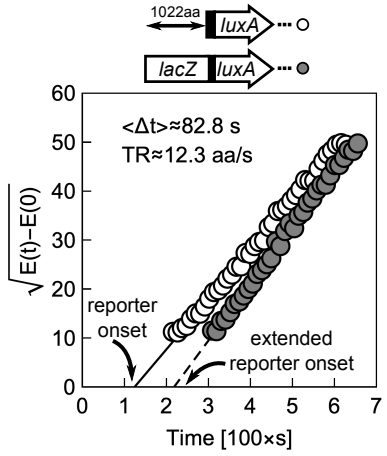

Figure 7.15: **The difference between onset times for proteins of different length reveals the translation rate.** By examining the quadratic increase in expression in the early stages of induction, we inferred the onset times for reporter and extended reporter. Time tracks (white and gray disks for reporter and extended reporter, respectively) follow quadratic increase as demonstrated by linear dependency upon square-root transformation.

We applied square-root transformation to the time traces of the expression of the reporter and extended reporter. We observed that both traces complied with the expected early-time dependency dictated by Eq. (7.20) – Fig. 7.15. The average time difference between onsets amounted to $\langle \Delta t \rangle \approx 82.8$ s; because the difference in lengths is 1,022 amino acids, we estimated the translation rate to be ≈ 12.3 amino acids per second. This estimate is below the expected 18 amino acids per second at $\lambda_0 \approx 2\ \mathrm{h}^{-1}$ [Dai *et al.*, 2016; Zhu *et al.*, 2016]. However, our measurement technique requires more optimization regarding the exact conditions of the induction, *e.g.,* cell density at the time of the measurement, pretreatment, *etc.* Importantly, we demonstrated that the observed dynamics is consistent with a mathematical model that predicts two distinct phases. Additionally, the values

for physiological parameters (translation rate, mRNA lifetime) come close to the previous estimates. Together with a convenient measurement approach (mix-and-measure), this technique holds the potential to be readily used in the measurements of translation parameters. However, our approach still requires two plasmids to be simultaneously present in the cell.

***Single-plasmid platform**

Merging of the supporting plasmid and the induction-module bearing plasmid into a single one would offer multiple benefits. It would decrease the burden plasmid maintenance and expression of antibiotic cassettes. Additionally, it would require a single transformation, thus making it useful for screening of translation rates in various strains. Likewise, if designed appropriately, a single-plasmid platform makes the genetic manipulations easier. Therefore, we aimed to construct a platform for measuring translation rates that: (i) has a single antibiotic resistance cassette, (ii) contains multiple cloning site for in-frame fusion with *luxA*, (iii) enable rapid exchange of ribosome binding site (RBS) by flanking it with two unique restriction sites, (iv) contains regulatory elements that lower the spurious read-throughs, and (v) has a low-copy origin of replication. We aimed to construct such plasmid by using Gibson assembly since it allows remarkable flexibility in designing new genetic constructs (Fig. 7.16).

This process yielded a plasmid pTR-luxA that meets the requirements stated above. Ribosomal binding site – specifically its SD – is flanked by NheI and EcoRI restriction sites. This flanking allows rapid replacement of RBS with an oligo-duplex made of annealed sense-antisense oligonucleotides. We can design the annealing oligonucleotides such that they yield overhangs that are compatible with EcoRI-NheI opening. Below we illustrate the procedure for the construction of RBS variants that differ in two nucleotides of the SD.

We design the annealing nucleotides such that they anneal in 5′-CAGGNNG-3′ on the sense strand; the sites NN differ between SD variants. We can choose the two variable nucleotides to vary the strength of the RBS. There are sixteen variants, all of which we plugged into RBS-calculator, which calculates a translation

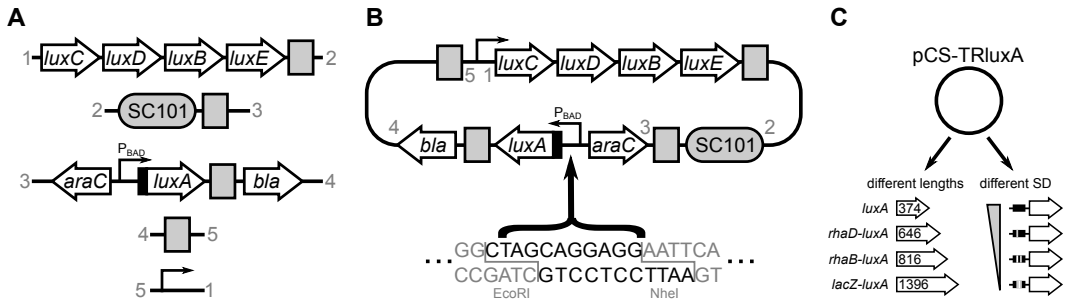

Figure 7.16: **Gibson-assembled plasmid pTR-luxA enables the rapid creation of protein fusions and the exchange of RBSs. (A,B)** Fragments used in Gibson assembly. Matching ends are denoted by numbers. This assembly removed EcoRI and AvrII restriction sites, flanked the promoters with terminators, provided the low-copy number origin of replication, and the ampicillin resistance cassette. Replacement of the RBS is based on ligation of the duplex into the plasmid (B; bottom, typeset in black). **(C)** Plasmid provides a platform for creating gene-*luxA* fusions (useful for determining translation rate) and quick exchange of RBSs with annealed oligonucleotide duplexes with EcoRI and NheI overhangs. On the left are shown candidate genes of different lengths.

initiation rate using a thermodynamic model [Salis *et al.*, 2009]. From the calculated translation initiation rates, we chose four variants whose calculated initiation rates differ ~ 2-fold (Table 7.2). With these variants at hand, we add CTAG and AATT to 5′-ends of the sense and antisense oligonucleotides. The overhangs of such duplex are compatible with the sticky ends of digested pTR-luxA and new SD variants can be efficiently ligated into the plasmid in a single step.

SD	sense	antisense	init. rate [a.u.]
RBS1	5′-CTAGCAGGGAG-3′	5′-AATTCTCCCTG-3′	0.577
RBS2	5′-CTAGCAGGTGG-3′	5′-AATTCCACCTG-3′	0.182
RBS3	5′-CTAGCAGGGTG-3′	5′-AATTCACCCTG-3′	0.087
RBS4	5′-CTAGCAGGCCG-3′	5′-AATTCGGCCTG-3′	0.036

Table 7.2: **Variants of Shine-Dalgarno sequence, corresponding sense-antisense oligonucleotides, and relative initiation rate.** Underlined is the annealing region. Calculated initiation rates are obtained from RBS-calculator [Salis *et al.*, 2009].

The experiment presented at the beginning of this section illustrated how we can determine the translation rate from a comparison of the onset times for reporter and extended reporter. However, the translation rate we determine this way is specific for a particular gene used in the extension. Therefore, to determine the global translation rate, several genes should be used.If these are of different lengths (Fig. 7.16C), we can fit a line to the onset times as a function of gene lengths. The slope would represent the translation rate. The gene-specific translation rate, on the other hand, is useful in dissecting the intricacies of specific genes and properties of their translation. For example, a gene with many rare codons can be subcloned in-frame with the reporter and we can infer its translation rate. We can deduce the best conditions for its expression by varying the conditions or the expression strain. As such, this tool can be of use beyond the basic studies of translation and can prove useful in optimization processes in biotechnology.

7.5 Towards quantitative understanding of physiological role of translation

This chapter illustrated efforts aimed at quantitative parsing of translation within the context of physiology. As such, the presented results were conceptual rather than conclusive. However, the chapter showcases that by using a simple theoretical framework, we can analyze the observations tractably. Additional tools that allow targeted changes in translation machinery would likewise reveal further relationships between processes.

While the tools presented in this chapter still require optimization, preliminary results are promising. We aimed at keeping the number of inferred parameters low (one parameter per feature). If we balance the number of predictions with inferred parameters, we can keep a constant check on used models.

If successful, a fully-characterized and verified quantitative model of translation would offer a predictive tool that can explain multiple phenomena at once [Gregor, 2017]. As we elaborate in the next chapter, understanding of gene expression and

its physical and biological constraints is crucial for many aspects of life sciences, including evolution and synthetic biology.

8 Discussion and outlook

We established a framework that combines mathematical modeling, high-throughput growth rate measurements, and genetic perturbations to elucidate the underlying mechanisms of drug interactions between antibiotics inhibiting translation. Kinetics of antibiotic-target binding and transport together with growth laws, *i.e.*, the physiological response to translation inhibition (Introduction), form a biophysically realistic baseline model for predicting antibiotic interactions from properties of individual antibiotics alone (Chapter 4). This model explained many interactions, but not all, failing specifically for suppressive interactions. Predictions improved by taking into account the step-wise progression of ribosomes through the translation cycle (Chapter 5). This was achieved by mimicking antibiotic perturbations of this progression genetically, which directly identified the contribution of antibiotic-imposed translation bottlenecks to the observed drug interactions. Finally, to explain the origin of suppressive interactions unaccounted for by the biophysical model, we modeled the traffic of translating ribosomes explicitly. Our results show that translocation inhibition can cause ribosomal traffic jams, which dissolve in a non-equilibrium phase transition when initiation is inhibited simultaneously with translocation, thereby restoring growth (Chapter 6). This phase transition explains the suppressive drug interactions between antibiotics targeting initiation and translocation.

Taken together, our framework mechanistically explained 20 out of 28 observed drug interactions, as classified based on stringent criteria. While 16 out of 28 of interactions were already explained by the biophysical model, these include many weak and additive interactions; in contrast, only the translation bottleneck approach correctly predicted some of the strongest interactions and, in particular, suppression. Furthermore, we only classified predictions as correct if the majority of growth

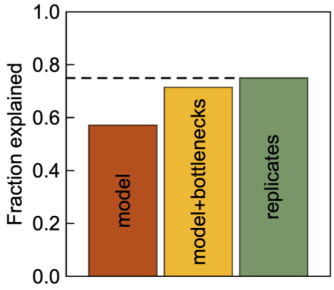

Figure 8.1: **Fraction of drug interactions explained.** Biophysical model explained ≈ 57% of interactions (orange), while including the bottlenecks-based remapping (yellow) increased this fraction to ≈ 71%. This is only slightly below the empirical upper bound (75%, dashed line) obtained by considering replicates as predictions.

rates across the dose-response surface quantitatively matched the prediction. As a result, cases where the predicted and observed drug interaction type agree are often still classified as false because the agreement is not quantitative. If the same stringent criteria are applied to replicate measurements of drug interactions (shown in Fig. E.2), only 75% of measurement replicates are classified as faithful predictions. Thus, our conservative estimate of the fraction of explained interactions (71%) is close to the maximum achievable at our measurement precision. Notably, even cases rejected as quantitatively different can provide valuable insights. For example, the remapping-based prediction of the CHL-FUS interaction (Fig. 5.10) is rejected because it quantitatively exaggerates the suppression between these drugs. Nevertheless, remapping correctly predicts the occurrence of suppression as well as its direction. Qualitative observations like these still advance our understanding of drug interactions by highlighting drug interaction mechanisms that are distorted by additional effects of unknown origin.

While we focused on translation inhibitors, key elements of our framework can be generalized to drugs with other modes of action. Specifically, when considering a drug that targets a specific process mediated by an essential enzyme, our approach of equating the deprivation of the enzyme with the action of an antibiotic is readily applicable. Depriving the cell of an essential enzyme would cause the formation of a physiological bottleneck. Our observations also highlight the advantages of factor deprivation compared to simple overexpression: the former produced a quantitative prediction for drug interactions, while no meaningful prediction could be made from overexpression data (Fig. B.4). The general approach of depleting key

accessory proteins is particularly useful for antibiotics targeting multi-component complexes or in cases where the effects of overexpressing the drug target are difficult to interpret [Palmer and Kishony, 2014].

Similar to translation, transcription is a crucial step in gene expression and is a target of antibiotics. The molecular machine at the core of transcription is a multi-component enzyme RNA polymerase (RNAP). The rates of transcription depend on the abundance of RNAP. Similarly to the translation apparatus, the expression of RNAP and its activity are growth rate-dependent [Bremer and Dennis, 1996; Shepheard *et al.*, 1980]. Besides the synthesis of mRNA, RNA polymerases synthesize crucial components of translation apparatus such as the ribosomal RNA. Because ribosomes synthesize RNAP proteins, this interdependence constitutes another branch of the autocatalytic process underlying ribosome biogenesis. Together, these considerations result in another growth law that connects the number of ribosomes and the number of polymerases with the growth rate [Kostinski and Reuveni, 2020]. By titrating the amount of RNAP (by controlling the expression of its subunits), the global effects of transcription inhibition would occur [Izard *et al.*, 2015]. Similarly, transcription-targeting antibiotics (*e.g.*, rifampicin) are expected to elicit similar global effects and could be mimicked by titration of RNAP. As such, the titration of RNAP would offer an insight into the idealized interference with the global rate of transcription and its impact on physiology.

Several tempting antibiotic targets could be additionally considered within the framework of physiological bottlenecks. Folate biosynthesis, for example, is a target of multiple antibiotics (Introduction). Here, titration of targeted enzymes (*e.g.*, dihydrofolate reductase or dihydropteroate synthase [Walsh, 2003]) would reveal the physiological consequences of inhibitions of various steps in the folate biosynthesis. Importantly, in the case of sulfa drugs that target dihydropteroate synthase, pools of essential metabolites are drained as the antibiotics divert the flux towards nonproductive compounds [Walsh, 2003]. Titration of the enzyme would help delineate the effects of an overall reduction in folate biosynthesis compared to the accumulation of nonproductive compounds and drainage of the metabolite pools. Further, titration of gyrase (encoded by *gyrA,B*) would mimic

a canonical gyrase inhibitor like coumermycin A1 [Sugino *et al.*, 1978]. Beyond antibiotics, environmental conditions such as nutrient limitations and their interplay with the action of antibiotics can be mimicked using similar genetic interventions. For example, underexpression of lactose permease and glutamate dehydrogenase mimic carbon or anabolic limitation, respectively [You *et al.*, 2013; Hui *et al.*, 2015]. In general, genetic perturbations enable precise investigations of essential cellular processes – including those that cannot be currently targeted by drugs. In sum, there are several attractive opportunities for mimicking the antibiotic effects with equivalent physiological bottlenecks that could be explored in the future.

Mimicking the effects of two drugs with controllable genetic perturbations generalizes the concept of genetic epistasis to continuous perturbations. Epistasis studies compare the effects of double gene knockouts to those of single knockouts and identify epistatic interactions – an approach that can reveal functional modules in the cell [Segre *et al.*, 2005; Constanzo *et al.*, 2010; Tong *et al.*, 2004]. Our results show that continuous genetic perturbations provide valuable additional information on genetic interactions (Chapters 5 and 6). Firstly, the direction of epistatic interactions cannot be extracted from measurements of single and double mutants (Fig. 8.2). Secondly, the quantitative information obtained from such "continuous epistasis"

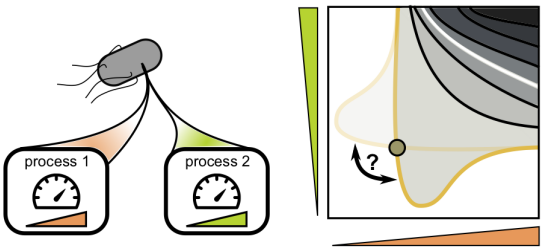

Figure 8.2: **Continuous variation of two rates reveals relationships between cellular processes.** While a point measurement (brown circle) can detect suppression, its direction remains unclear. A gradual change in rates specifies the direction of suppression and offers quantitative insights into the intertwining of processes.

measurements provides more stringent constraints for mathematical models of biological systems. In particular, continuous epistasis data can be powerful for the development of whole-cell models that describe the interplay of different functional modules in the cell. Thirdly, this approach allows including essential genes in epistatic interaction networks even for haploid organisms, which otherwise requires the use of less well-defined hypomorphs. Hence, continuous epistasis measurements

augment all-or-nothing genetic perturbations.

Continuous epistasis measurements further enable a deeper understanding of previously mysterious antibiotic resistance mutations. Specifically, translation bottlenecks that alleviate the effect of an antibiotic expose a latent potential for resistance development. Indeed, mutations with effects equivalent to factor-imposed bottlenecks occur under antibiotic selection pressure. For example, resistance to ERM in *E. coli* can be conferred by mutations in proteins of the large ribosomal subunit, that hinder its maturation and lower its stability [Zaman *et al.*, 2007]. Consistent with this observation, our results indicate that the action of ERM is alleviated by lowering the stability of the 50S subunit (Fig. 5.3). Mutations in recycling factor were observed in *Pseudomonas aeruginosa* evolved for resistance to the TET derivative tigecycline [Sanz-Garcia *et al.*, 2018]. The observed alleviation of TET action by a recycling bottleneck (Fig. 5.3) offers a mechanistic explanation for the beneficial effects of these mutations. Mutations in other genes predicted based on the effect of translation bottlenecks may be difficult to observe, especially in clinical isolates, due to the associated fitness cost and selection pressure for reverting the mutations in the absence of antibiotic selection. Beyond mutations conferring resistance to individual drugs, consistent or conflicting dependencies of different antibiotics on translation bottlenecks may further indicate the potential for evolving cross-resistance and collateral sensitivity, respectively [Baym *et al.*, 2016]. Likewise, the framework could facilitate the development of better strategies for antibiotic cycling.

Our work also demonstrated the potential of improved null models for drug interactions that are based on generic biophysical and physiological considerations. The number of parameters is minimal and the biophysical model we presented makes parameter-free predictions. This model is readily extended to capture phenomena such as an inactive fraction of ribosomes (Sec. A.5.1) or physical interactions between antibiotics on the ribosome (Chapter 4. Including more detailed mechanisms, *e.g.*, interplay between different ribosome states that are targeted by different antibiotics, would require additional parameters with unknown values. In essence, such a detailed model and its parameters would have to be fine-tuned for every antibiotic combination. Meaningful predictions would require independent

quantitative measurements of multiple kinetic parameters such as the rates of antibiotic binding to the ribosome in different states; for all practical purposes, such a more detailed model would not be predictive. In contrast, the minimal biophysical model we presented provides an improved null expectation for drug interactions. Deviations from this expectation expose drug interactions for which additional details of the antibiotic-ribosome interaction are important. We showed examples of the latter experimentally by halting the ribosome in specific stages of the translation cycle. Developing a fully parameterized mathematical model of the translation cycle and how it is affected by different antibiotics is a formidable challenge for decades to come.

Crucial to both the minimal biophysical and the TASEP-translation model (Chapters 4 and 6) is the validity of the growth laws. By experimental validation of such models, we showed that capitalizing on growth laws in theoretical models can offer valuable insights into the interplay of cell physiology and antibiotic action. Unexplained deviations are good starting points for the identification of situations in which growth laws are violated. This underscores the importance of elucidating such growth laws in other organisms.

In conclusion, we presented a systematic approach for discovering the mechanistic origins of drug interactions between antibiotics targeting translation. As illustrated above, our approach of mimicking drug effects with continuous genetic perturbations is general and can be extended to antibiotics with other primary targets, other types of drugs, and other organisms. As the translation machinery is highly conserved, the interaction mechanisms for drugs targeting specific steps of translation we uncovered may generalize to diverse other organisms. Crucially, both the biophysical model and bottleneck-mimicking of antibiotics have different scaling than the brute-force measurement of all drug interactions between antibiotics. Minimal model – for independent or competition binding scheme – requires only parameters that are inferable from individual dose-response curves. As such, a number of measurements that are needed to predict an interaction scales linearly rather than quadratically with the number of antibiotics. The required number of experiments within the bottlenecks framework scales quadratically with the number

of targeted processes rather than with the number of antibiotics. Different scaling offers physiologically-informed predictions for drug interactions at the reduced experimental efforts. This advantage could facilitate the discovery of more powerful antibiotic combinations and further strengthen the analogy between antibiotics and genetics. In the long run, extending our combined experimental-theoretical approach to other types of drugs and other biological systems will enhance our understanding of drug modes of action and interaction mechanisms and provide deeper insights into cell physiology.

Outlook

The aim of this thesis was a broad-stroke quantitative description of the translation perturbations. However, many additional aspects of translation and the impact of antibiotics remain elusive. The thesis (specifically Chapter 7) suggests that further quantitative characterization and formulation of quantitative models could offer testable predictions that lead to additional insights into the biology of bacteria. Specifically, by investigating translation as a core process, we make the next steps towards the understanding of genetic circuits, metabolic control, and growth physiology. As we sketch below in more detail, a tandem of modeling and experimentation is instrumental in discerning the answers to evolutionary and physiological questions.

Physical constraints and numerous tradeoffs shape the biological processes across scales. For example, translating ribosomes are slower upon the introduction of hyper-accuracy conveying mutations, which in turn inhibits the growth of bacteria [Ruusala *et al.*, 1984]. From an evolutionary point of view, this growth deficit represents a fitness disadvantage – yet, for an isolated bacterium this "take-your-time" approach might be beneficial if highly precise translation of proteins is more beneficial over rapid growth. Additionally, the doubling time of the ribosome represents a hard-bound on doubling time of bacteria; the smallest and fastest ribosomes can translate their constituent proteins in approximately six minutes [Reuveni *et al.*, 2017]. The autocatalysis of ribosome synthesis is thus of particular importance: how is the

replication of translation machinery by itself constrained? Recent work revealed that the ribosomes appear optimized for the autocatalytic production by having a predominant fraction of mass in a few ribosomal RNAs and multiple small proteins. This suggests that minimizing the time ribosomes spend making themselves might have been one of the utilities for which translation is optimized. Yet, it is far from clear what are the other relevant utility functions. Successful establishment of a fully-specified phenomenological model of translation offers the advantage of probing multiple such questions simultaneously – utilities operate across a tightly-knit net of constraints and tradeoffs, such as the proteome allocation.

Translation machinery can account for nearly half of *E. coli*'s proteome; as we discussed in the Introduction, the expression of components of translation machinery is regulated. While plentiful data is describing the stringent response in the transition to a poor growth environment and its association with regulation by ppGpp, it is still not fully understood how the regulation of translation is implemented. Specifically, which translation parameters can the cell detect and respond to? Importantly, a large part of regulation might arise – at least partially – from passive, physical mechanisms. Here, the future aim should be the targeted perturbations of particular steps in translation using genetics as presented in Chapters 5-7. Systematic measurement of all targeted genetic perturbations would consequently allow full quantitative characterization of the translation cycle. Not only would the underlying mathematical model offer predictions on the behavior of translation upon perturbations and environmental changes, but it would reveal the physical and physiological constraints.

Probing the effects of translation bottlenecks in more detail would allow uncovering additional constraints. Not only that the translation requires significant resources in proteome terms, but it is also one of the most energy-demanding processes in the cell [Maaløe, 1979]. Therefore, the interplay between energetics and protein synthesis is of importance. While theoretical studies [Weisse *et al.*, 2015] have revealed the interplay of trade-offs, gene expression, and growth, a more comprehensive experimental study of protein synthesis energetics is required. Precise quantitative measurements of ATP levels are necessary; while challenging, these

suggest that ATP levels are roughly independent of the nutrient-dependent growth rate [Schneider and Gourse, 2004]. Recent advances in the development of ATP ratiometric sensors [Yaginuma *et al.*, 2014] could aid the measuring of ATP levels in multiple conditions. Furthermore, levels of ATP and GTP are not only involved in providing the energy required in translation but might affect protein synthesis by skewing homeostatic parameters. Specifically, NTPs chelate Mg^{2+} ions required for the normal function of protein synthesis and stability of ribosomes [Pontes *et al.*, 2015]. Exploring the effects of pools of essential metabolites (such as ATP) and their effects on translation would allow the construction of a more holistic picture of protein synthesis within a physiological context. Additionally, these constraints and interplay of trade-offs shaped the evolution of translation components and translation regulation.

A multitude of intertwining processes makes classic epistasis measurements challenging. While point-epistasis is certainly informative, continuous epistasis provides richer information on the interplay between processes. As such, it has important connotations in the understanding of the evolution of translation. As we illustrated in Chapter 6, intricate relationships exist between cellular processes that a smooth variation of them can reveal. By considering the growth rate as fitness, a dose-response surface becomes a fitness landscape. If it arises from physical constraints, selection could drive the evolution of translation machinery according to these landscapes. Conversely, this can explain why some evolutionary trajectories appear nonintuitive. As illustrated in Fig. 8.3, the shape of the fitness landscape might transiently drive certain rates down to speed-up the evolution even though

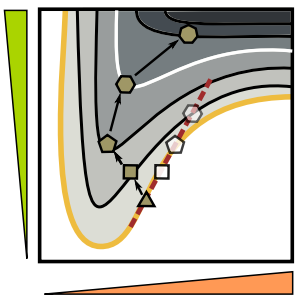

Figure 8.3: **Evolution on complex fitness landscapes.** Fitness landscape determines the evolutionary trajectory. As the rates of two processes (green and orange wedges) can either evolve independently (brown symbols, arrows) or in concert (white symbols, dashed line), relationship between the processes will steer the evolutionary trajectory.

the highest fitness is achieved when both rates are high. Such a conceptual picture is based on largely homogeneous populations in which a fixed mutant quickly overtakes the entire population. However, the populations in the wild are rarely as homogenous as tacitly assumed above. Not only can the populations be genetically heterogenous, but can additionally exhibit a phenotypic heterogeneity. Departing from an isogenic and average cell is of particular importance when we consider evolution in niche environments.

To account for heterogeneity, we need to change the scale of our investigation. While the modeling of bacterial physiology by deterministic differential equations is a useful tool, it does not reflect the inherent randomness and discreteness of the underlying processes [Samoilov and Arkin, 2006]. So-called deviant effects can cause substantial differences between deterministically predicted average response compared to the one obtained in a fully stochastic description [Kuwahara and Gao, 2013]. These stochastic effects in the context of antibiotic treatment might manifest as the "growth rate-switching" between different growth modes (*e.g.*, growing and non-growing) or in increased variability of growth rates. Even for cellular components with lower intrinsic noise (*e.g.*, due to a high number of molecules) stochastic events – such as component partitioning after a cell division – might greatly affect cell physiology and the growth rate. While the growth rate has been shown to be stable over many generations [Wang *et al.*, 2010], this robustness becomes questionable under antibiotic or other stress. Specifically, if the growth rate distribution under stress becomes multimodal, further single-cell level implications are of interest. For example, hysteresis effects can cause switching between growth rates to be history-dependent and thus affect the dynamics of antibiotic therapy. Additionally, connecting the results of the deterministic description with stochastic phenomena could streamline the analysis. Associating the stochastic effects with microscopic mechanisms would be of fundamental importance in going beyond population level-studies.

By considering every bacterium as an independent unit, we can ask fundamental questions of translation on the microscopic level. To start: it is not clear that the growth laws, rates of translation kinetics, *etc.* measured in batch-cultures directly

mirror the intricacies of a single cell. Thus, the development of tools allowing single-cell quantitative characterization of translation and growth rate parameters is necessary. On a batch-culture level, subpopulations with the highest growth rate overtake the rest. However, these outcompeted subpopulations are a meaningful part of bacterial biology. This is not only critical for bacterial response to antibiotics but becomes crucial in ecological and evolutionary considerations. Especially when we consider the utility of translation, single-cell experimentation can highlight additional aspects of translation. How noisy is the translation and which step in the translation cycle is the noisiest? How does the high number of components involved in translation manifest in the overall performance of translation?

Physical constraints do not only embody the physiology of bacteria but will affect our efforts towards the engineering of living organisms. These challenges would be of particular importance in building of the minimal cell. In particular, the construction of a synthetic cell necessitates a deep understanding of translation. The translation is a core process that requires a multitude of components to work in concert. Building a minimal cell is based on finding a minimal set of components that support a self-replicating, functional cell; as such, it necessitates going beyond the "black box" approach when trying to reconstitute translation systems. Yet, this forward engineering predominantly uses *in vitro* approaches that often aim to characterize individual components in detail rather than whole systems. As demonstrated in Chapter 6, certain phenomena only emerge when we consider several processes simultaneously rather than their components in isolation. The reconstitution of a particular cellular module from its components in a bottom-up fashion is a formidable challenge. Yet, this challenge has been solved by millions of years of evolutionary tinkering. Therefore, studies of *in vivo* systems aid the understanding of both evolutionary and engineering approaches. Mathematical modeling can overarch both; importantly, a systemic approach can reveal the physical constraints that affect both the engineering and evolutionary systems.

The central dogma of molecular biology is the basis of our current understanding of life processes. The translation is a crucial process in central dogma and has been investigated heavily. Yet many mysteries still remain; some questions are

revisited and answers can change our interpretation of translation. While central to translation, the ribosomes were long considered as "black boxes" converting the information stored in mRNA into proteins. Many considered ribosomes and mechanistic understanding of their function to be either of little value or simply too complex to be solved [Ramakrishnan, 2018]. The structure of the ribosome was eventually cracked and antibiotics proved remarkably useful in establishing the dynamical landscape of translation progression on a structural level. In this thesis, we demonstrated (albeit to a much more modest degree) that antibiotics can be insightful even on higher levels of the physiological organization. Specifically, a combination of both genetics and antibiotics offers an attractive approach for deepening our understanding bacterial physiological regulation and how the biophysical constraints shape these regulatory responses.

* * *

Nowadays, presented with abundant data, we can decide on the level of complexity at which we would like to answer the question of the origin and mechanics of life. However, current approaches often increase the dimensionality of data rather than its ampleness [Młynarski *et al.*, 2019]. Thus, our efforts should not only increase the rate of data collection but also propose efficient methods of data analysis and interpretation. The efficient coarse-grained models are of high practical value as we can – due to clear assumptions – associate the deviations with processes included in the model. As highlighted in Ref. [Młynarski *et al.*, 2019], we need to define the balance between inference and utility of proposed models. Especially crucial are the models arising from first principles, which are common in physics but are still scarce in biology. High-quality data motivates the construction of such models, which we can illustrate with an analogy from history of physics [Jun *et al.*, 2018]: as Brahe's precise measurements of the planetary orbits led Kepler to *infer* the laws of planetary motions (which were phenomenological but correct and much simpler than the "epicycles"). Newton, on the other hand, was able to *derive* these laws from a single equation describing the dynamics of motion (a first principle). We should hope for the latter but embrace the former.

A Analysis of a mathematical model

A.1 Parameter reduction and the bifurcation point

In the following we derive expressions that constrain the parameter space in which the system is bistable. We start by rewriting the steady-state solution with new variables, which will facilitate reduction of parameters. We recast Eq. (4.4) so as to express $a_{\mathrm{ex}}/2\mathrm{IC}_{50}^{*}$ as function of growth rate; this is possible since $a_{\mathrm{ex}}/2\mathrm{IC}_{50}^{*}$ occurs linearly in the equation. At this stage we introduce new variables and rewrite parameters in a dimensionless form:

$$a_{\mathrm{ex}} = c \times \mathrm{IC}_{50}, \tag{A.1a}$$

$$\lambda = y \times \lambda_0, \tag{A.1b}$$

$$\lambda_0^{*} = \alpha \times \lambda_0, \tag{A.1c}$$

where IC_{50} is concentration needed to halve the growth rate and λ_0 is a drug-free growth rate. These definitions lead to:

$$y\left[\frac{1}{4}\alpha^2 + \frac{1}{2}\frac{\mathrm{IC}_{50}}{\mathrm{IC}_{50}^{*}}c\alpha\right] = \frac{1}{4}\alpha^2 + y^2 - y^3. \tag{A.2}$$

To remove the ratio $\mathrm{IC}_{50}/\mathrm{IC}_{50}^{*}$ from the equation, we use the expression from Ref. [Greulich *et al.*, 2015] that states

$$\begin{aligned}\frac{\mathrm{IC}_{50}}{\mathrm{IC}_{50}^{*}} &= \frac{1}{2}\left(\frac{\lambda_0}{\lambda_0^{*}} + \frac{\lambda_0^{*}}{\lambda_0}\right) = \frac{1}{2}\left(\alpha + \frac{1}{\alpha}\right) = \\ &= \frac{1}{2}\left(\frac{\alpha^2+1}{\alpha}\right).\end{aligned} \tag{A.3}$$

This relation is obtained by plugging $y = 1/2$ and $c = 1$ into Eq. (A.2). Finally, we recast Eq. (A.2) into

$$c = \frac{1}{\alpha^2+1}\left(\frac{\alpha^2}{y} - \alpha^2 + 4y - 4y^2\right). \tag{A.4}$$

This equation expresses the relative concentration c as a function of relative growth rate y in which α is the sole parameter. Fitting an implicit function can be challenging; we can estimate α from equating the implicitly calculated derivative of Eq. (A.4) to the derivative of the Hill function with steepness parameter n, when both derivatives are evaluated at $c = 1$. An estimate for the response parameter is then $\alpha \approx \sqrt{1/(n-1)}$.

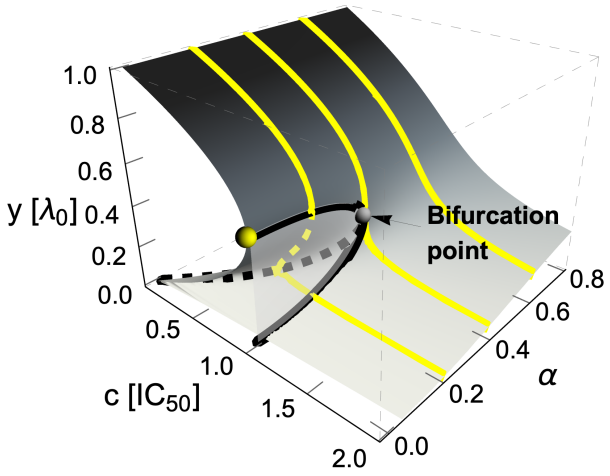

Figure A.1: **Surface of response curves as a function of a response parameter.** With increasing response parameter the dose-response curves become shallower. Below a critical value of a response parameter, more than one growth rate y can correspond to a particular concentration.

A.1.1 Bifurcation point

To determine the critical value of the parameter α below which bistable concentration region exists, we consider the stationary points of Eq. (A.4). The derivative reads:

$$\frac{\mathrm{d}c}{\mathrm{d}y} = \frac{1}{\alpha^2+1}\left(-\frac{\alpha^2}{y^2} + 4 - 8y\right). \tag{A.5}$$

Considering the equation

$$8y^3 - 4y^2 + \alpha^2 = 0, \tag{A.6}$$

we can determine values of y where the derivative of Eq. (A.5) is 0. Since the equation is of third order, we expect either three real roots or one real together with a conjugated pair of complex roots. The solutions [found using Mathematica

(Wolfram Research, 11.3) function `Solve`] are:

$$y_1 = \frac{1}{6}\left[\sqrt[3]{\frac{3}{2}\alpha\left(\sqrt{81\alpha^2-12}-9\alpha\right)}+1+ \right.$$
$$\left. + \frac{1}{\sqrt[3]{(3/2)\alpha\left(\sqrt{81\alpha^2-12}-9\alpha\right)+1}}+1\right], \tag{A.7a}$$
$$y_2 = \frac{1}{24}\left[2(-2)^{2/3}\sqrt[3]{3\alpha\left(\sqrt{81\alpha^2-12}-9\alpha\right)+2}- \right.$$
$$\left. - \frac{4\sqrt[3]{-2}}{\sqrt[3]{3\alpha\left(\sqrt{81\alpha^2-12}-9\alpha\right)+2}}+4\right], \tag{A.7b}$$
$$y_3 = \frac{1}{24}\left[-2\sqrt[3]{-1}2^{2/3}\sqrt[3]{3\alpha\left(\sqrt{81\alpha^2-12}-9\alpha\right)+2}+ \right.$$
$$\left. + \frac{4(-1)^{2/3}}{\sqrt[3]{(3/2)\alpha\left(\sqrt{81\alpha^2-12}-9\alpha\right)+1}}+4\right]. \tag{A.7c}$$

We note that whether all roots are real is determined by the sign of $27\alpha^2-4$; this leads to a critical value of $\alpha_{\text{crit}} = 2/(3\sqrt{3}) \approx 0.385$ – the system has a bistable region when $\alpha < \alpha_{\text{crit}}$. To obtain the span of concentrations at which two bistable growth rates exist (Fig. 4.2d), we plug Eqs. (A.7a) and (A.7c) into Eq. (A.4).

A.1.2 Linearized case of constitutively expressed resistance gene

As noted in the main text (Sec. 4.3.3), for high values of K_{rem} the Michaelis-Menten equation linearizes. In this case we can reuse the expression for growth-dependent efflux from Ref. [Greulich *et al.*, 2015]. Using the parameter reduction from above, the generic solution is

$$y^3 - y^2\left(1-\frac{1}{4}\Omega\alpha^2\right) + y\left[\frac{a_{\text{ex}}}{2\text{IC}_{50}^*}\alpha + \frac{1}{4}(1-\Omega)\alpha^2\right] - \frac{1}{4}\alpha^2 = 0. \tag{A.8}$$

where $\Omega = V_{\max}/(p_{\text{out}}K_{\text{rem}})$. This expression can be rewritten into reduced form as

$$c = \frac{1}{1+\alpha^2(1+\Omega/2)} \times \left[\frac{\alpha^2}{y} - (1-\Omega)\alpha^2 + 4y\left(1-\frac{\Omega\alpha^2}{4}\right) - 4y^2\right]. \tag{A.9}$$

Here, we used the relation that follows directly from Eq. (A.8); $\mathrm{IC}_{50}/\mathrm{IC}^{*}_{50} = (1/2\alpha) \times \left[1 + \alpha^2 (1 + \Omega/2)\right]$. By solving $\mathrm{d}c/\mathrm{d}y = 0$ we obtain a condition $-64\alpha^2 + 432\alpha^4 + 48\alpha^4\Omega - 12\alpha^6\Omega^2 + \alpha^8\Omega^3 \leq 0$ for bistability to exist; heuristically, we note that the leading term in Ω is of the third power and positive and will for high values of Ω make the expression necessarily positive and will thus make the system monostable. This illustrates the importance of non-linearity in the expression describing antibiotic removal [Eq. (4.25)]; the presence of positive feedback alone is not sufficient for the occurrence of bistability. In the limit $\Omega \to \infty$, Eq. (A.9) becomes simply $y = 1 - c/2$ for $c \leq 2$ and $y = 0$ otherwise.

A.2 Calculation of dose-response surface for additive interaction and Loewe interaction score

An additive interaction is characterized by linear isoboles. In this section we briefly sketch the derivation. Let c_A and c_B be relative concentrations (measured in IC_{50} of respective antibiotics) of antibiotics A and B, respectively. Individual dose-response curves are given by f_A and f_B. To construct the additive surface, the growth rate in any point (c_A, c_B) has to be calculated solely from known responses to individual drugs. As isoboles are linear, there is an isobole that passes through this point but terminates in some unique $(c_{A,0}, 0)$ and $(0, c_{B,0})$, from which it follows that $c_B = c_{B,0}(1 - c_A/c_{A,0})$. Since $c_{B,0} = f_B^{-1}\left(f_A(c_{A,0})\right)$, the solution of $c_B = f_B^{-1}\left(f_A(c_{A,0})\right) \times (1 - c_A/c_{A,0})$ for $c_{A,0}$ is sought, which depends on c_A and c_B. If such solution is termed $\hat{c}_{A,0}(c_A, c_B)$ then the whole dose-response surface is given as $f_A\left(\hat{c}_{A,0}(c_A, c_B)\right)$. Integration of Eq. (4.10) is performed over an area where growth rate is above a chosen threshold. Throughout the systematic calculation of phase diagrams, this threshold is set to $y = 0.2$. Positive or negative values of LI suggest antagonistic or synergistic interaction, respectively.

A.3 Numerical solutions

We evaluated the steady-state solution of the system Eqs. (4.6) by forward time integration of the differential equations. We used $\lambda_0 = 2\ \mathrm{h}^{-1}$, which is the drug-free growth rate in rich lysogeny broth (LB) medium at 37°C. We rescaled the time by defining $t = T\tau$, where $T = (\alpha_A + \alpha_B)^{-1} \times (1/\lambda_0)$ and τ is a real number. Similarly, we rescaled concentrations by defining a reference concentration as $M = \left(1/\mathrm{IC}^*_{50,A} + 1/\mathrm{IC}^*_{50,B}\right)^{-1}$; concentrations of all species were rescaled by M. To automatically scale the antibiotic concentrations axes in units of IC_{50}, we set $\mathrm{IC}^*_{50} = 2\alpha/\left(\alpha^2 + 1\right)$. To mimic the situation in which exponentially growing unperturbed bacterial culture is exposed to antibiotic, we set the initial condition to $y = 1$; the rest of the species were set to 0. We integrated the rescaled differential equations forward in time until $\tau = 9 \times 10^3$ for by using Mathematica function `NDSolve`. In computations, K_D and k_{on} values were set for both antibiotics to 0.1 μM and 100 $\mu\mathrm{M}^{-1}\mathrm{h}^{-1}$, respectively. The results are largely invariant of the choice of these numeric constants as long $k_{\mathrm{on}} \gg \kappa_t$ and K_D is roughly between $0.01 - 1$ μM.

Upon fitting α to the normalized dose-response curves, we fixed $k_{\mathrm{on}} = 100\ \mu\mathrm{M}^{-1}\mathrm{h}^{-1}$ (which gave consistent results for all dose-response curves). For each dose-response curve, we determined the optimized value of K_D (Fig. A.2). We used these optimized values in all computations used in comparison between the model and the data. We verified the impact of uncertainties in fitted response parameters by bootstrapping.

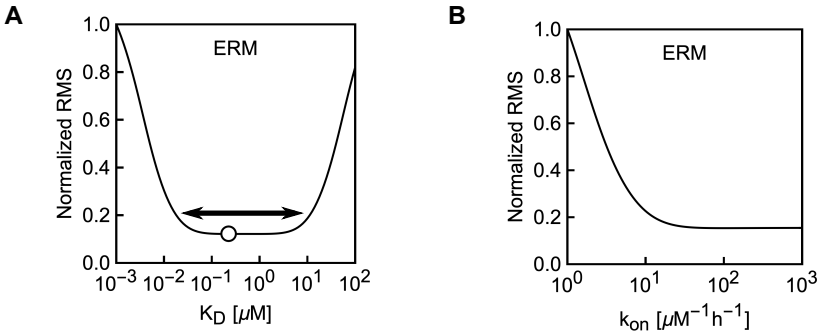

Figure A.2: **Example of an effect of numerical parameters (K_D and k_{on}) on root-mean-square error (in comparison to the experimental data)**. These parameters are required for forward time integration. The root-mean-square error was normalized relative to the maximal error in the scanned interval. **(A)** Effective dissociation constant K_D exhibits roughly two orders of magnitude wide plateau (double-headed arrow; minimum is denoted by a circle). **(B)** First-order binding rate constant k_{on} does not exhibit a plateau but rather flattens out – -consistently with the requirement that $k_{\mathrm{on}} \gg \kappa_{\mathrm{t}}$.

A.4 Analytical solution in the limit of strong inhibition and reversible binding

The system of ODEs [Eqs. (4.6a-d)] can be linearized for near-zero growth rates (*i.e.*, $\lambda \ll \lambda_0^*, \lambda_0$) which is the case when the external concentrations of antibiotics are high enough ($a_{\mathrm{ex},i} \gg \mathrm{IC}_{50,i}$). In the latter case one can postulate two constraints: (i) Ribosome synthesis is up-regulated to the theoretical maximum, *i.e.*, $r_{\mathrm{tot}} = r_{\mathrm{max}}$ and (ii) internal concentration of the i-th antibiotic is $a_i' \approx a_{\mathrm{ex},i} p_{\mathrm{in},i}/p_{\mathrm{out},i}$. These constraints eliminate the dynamical equations for internal concentrations of antibiotics [Eq. (4.6a)]. The fully specified and expanded system of equations reads

$$\dot{r}_u = -(r_u - r_{\mathrm{min}})(k_{\mathrm{on},A} a_A' + k_{\mathrm{on},B} a_B') + r_{b,A} k_{\mathrm{off},A} + r_{b,B} k_{\mathrm{off},B}, \tag{A.10a}$$

$$\dot{r}_{b,A} = k_{\mathrm{on},A}(r_u - r_{\mathrm{min}}) a_A' + \delta_{\mathrm{off},B} k_{\mathrm{off},B} r_d - \delta_{\mathrm{on},B} k_{\mathrm{on},B} r_{b,A} a_B' - k_{\mathrm{off},A} r_{b,A}, \tag{A.10b}$$

$$\dot{r}_{b,B} = k_{\mathrm{on},B}(r_u - r_{\mathrm{min}}) a_B' + \delta_{\mathrm{off},A} k_{\mathrm{off},A} r_d - \delta_{\mathrm{on},A} k_{\mathrm{on},A} r_{b,B} a_A' - k_{\mathrm{off},B} r_{b,B}, \tag{A.10c}$$

$$\dot{r}_d = \delta_{\mathrm{on},A} k_{\mathrm{on},A} r_{b,B} a_A' + \delta_{\mathrm{on},B} k_{\mathrm{on},B} r_{b,A} a_B' - r_d \left(\delta_{\mathrm{off},A} k_{\mathrm{off},A} + \delta_{\mathrm{off},B} k_{\mathrm{off},B}\right). \tag{A.10d}$$

The system is linear and thus the steady-state solution exists in a closed and unique form. We initially derive the stationary solution for independent binding, *i.e.*, $\delta_{\sigma,i} = 1$:

$$r_u = \frac{\Delta r}{\left(1 + a'_A/K_{D,A}\right)\left(1 + a'_B/K_{D,B}\right)} + r_{\min}, \tag{A.11a}$$

$$r_{b,A} = \Delta r \frac{a'_A}{a'_A + K_{D,A}} \frac{1}{1 + a'_B/K_{D,B}}, \tag{A.11b}$$

$$r_{b,B} = \Delta r \frac{1}{1 + a_A/K_{D,A}} \frac{a'_B}{a'_B + K_{D,B}}, \tag{A.11c}$$

$$r_d = \Delta r \frac{a'_A}{a'_A + K_{D,A}} \frac{a'_B}{a'_B + K_{D,B}}. \tag{A.11d}$$

Each product term can be rewritten as a function of $a'_i/K_{D,i}$, which can be further transformed by noting that $K_{D,i} p_{\mathrm{out}_i} = (\lambda_0 \alpha_i)^2 / (4\kappa_t)$ and $a_{\mathrm{ex},i} p_{\mathrm{in},i} = c_i \times \left[\Delta r \lambda_0 \left(\alpha_i^2 + 1\right)\right] / 4$. Together, these expressions allow rewriting Eq. (A.11a) using variables $c'_i = c_i \times \left[(\alpha_i^2 + 1)\lambda_{\max}\right] / (\alpha_i^2 \lambda_0)$, which finally leads to the Eq. (4.11). To obtain Eq. (4.12) the general solution of Eqs. (A.10) is evaluated; the latter is further simplified by assuming that $k_{\mathrm{off},A} \approx k_{\mathrm{off},B}$, which approximately holds for reversibly binding antibiotics.

A.5 Effect of dose-response curve concavity on the shape of isoboles

For intermediate values of $\alpha \sim 1$ and increasing δ, we observed that the isoboles of the dose-response surface at lower drug concentrations indicate strong antagonism, whereas at higher concentrations, they indicate synergism (Fig. A.3A). Is it possible to determine a concentration value above which increasing δ will cease to increase antagonism but rather increase synergism? Intuitively, the interaction-characteristic shape of isoboles is determined by the sign of the mean curvature, the latter being defined as

$$K_a = (k_1 + k_2)/2 \tag{A.12}$$

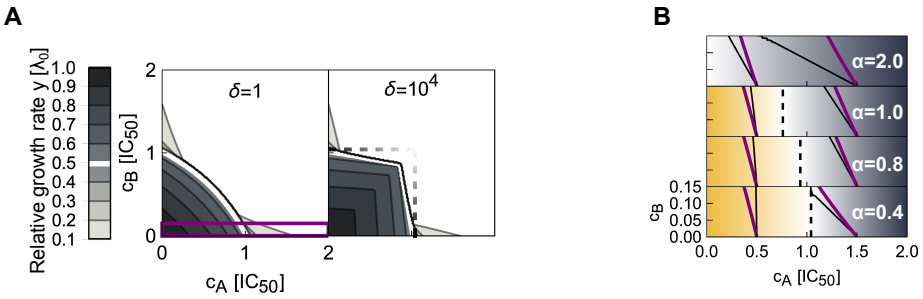

Figure A.3: **Dose-response surface can locally have both antagonistic and synergistic isoboles, depending on the concavity of the individual dose-response curves. (A)** Examples of dose-response surfaces with $\alpha = 0.4$ and with either independent (left, $\delta = 1$) or strongly cooperative binding (right, $\delta = 10^4$). Purple box highlights the area showcased in (B). Dashed black lines denote an approximate area in which increasing δ increases antagonism. **(B)** A detail [highlighted rectangle in (A)] of dose-response surfaces for different values of α. For $\alpha < 2$ black dashed line denotes the boundary below which the increasing cooperativity δ increases antagonism (shades of yellow); above it synergistic character is enhanced (blue). Two isoboles are showcased for each example: purple and black lines correspond to $\delta = 1$ and $\delta = 10^4$, respectively. Note, that below c_{inf} isoboles in the case of strong cooperativity become steeper than the independent ones; above c_{inf} isoboles become shallower, which is indicative of synergy.

where k_1 and k_2 are principal curvatures. Full dependency of K_a is not accessible as an analytical expression for $y(c_A, c_B)$ is not known; however in the limit $\delta \to \infty$ the antagonistic isoboles become nearly perpendicular to the axes, thus rendering all derivatives along perpendicular directions equal to zero. Hence, the expression for K_a is simplified into:

$$K_a\big|_{c_B \to 0} \approx \frac{\mathrm{d}^2 y / \mathrm{d}^2 c_A}{2\left[1 + \left(\mathrm{d}y/\mathrm{d}c_A\right)^2\right]}. \tag{A.13}$$

As the denominator is always positive the sign of K_a depends only on the sign of the second derivative along the axis.

To find this point, we need to determine the inflection point of the relative growth rate y along either of the axes. Here, we need to solve $\mathrm{d}^2 y/\mathrm{d}^2 c = 0$ for α; since y is given only implicitly in Eq. (4.5), the second implicit derivative is calculated. This leads to inflection point at relative growth rate $y_{\text{inf}} = \sqrt[3]{\alpha^2/4}$ for $\alpha > \alpha_{\text{crit}}$, at which second derivative vanishes. Using Eq. (4.5) the inflection concentration is evaluated

as:

$$c_{\mathrm{inf}} = \frac{-\alpha^2 + 2^{4/3}\alpha^{2/3}}{1+\alpha^2}. \tag{A.14}$$

From the expression for y_{inf} we observe that we have a relevant solution only for $\alpha < 2$; this leads to the first conclusion – the intermediate regime of surfaces having both antagonistic and synergistic contours exists only up to $\alpha = 2$. This also implies that for every response parameter α, given a high enough concentration of an antibiotic, the isoboles will become synergistic. However, at low growth rates at high concentrations the approximation [Eq. (4.14)] becomes relevant (Fig. A.3B). Numerically computed dose-response surfaces for $\delta = 1$ and $\delta = 10^4$ illustrate that indeed above the c_{inf} character of the isoboles is different and that the transition happens due to vanishing second derivative.

A.5.1 Ribosome subpopulations

If we consider that translation inhibitors can bind only to a specific subpopulation of ribosomes, we can extend the model from above to incorporate this effect. In the following, we assume for simplicity that there are only two distinct subpopulations of ribosomes ($r_{\mathrm{t,A}}$ and $r_{\mathrm{t,B}}$) that can be bound by different antibiotics (A and B, respectively). Ribosomes cycle between two stages as per

$$\frac{\mathrm{d}r_{\mathrm{t,A}}}{\mathrm{d}t} = -k_{\mathrm{A}} r_{\mathrm{t,A}} + k_{\mathrm{B}} r_{\mathrm{t,B}}, \tag{A.15}$$

$$\frac{\mathrm{d}r_{\mathrm{t,B}}}{\mathrm{d}t} = k_{\mathrm{A}} r_{\mathrm{t,A}} - k_{\mathrm{B}} r_{\mathrm{t,B}}, \tag{A.16}$$

where k_{A} and k_{B} are the cycling rates. Here, assuming that cycling equilibrates quickly, the steady-state solution is simply $r_{\mathrm{t,A}} = \eta r_{\mathrm{t,B}}$, where $\eta = k_{\mathrm{B}}/k_{\mathrm{A}}$; because $r_{\mathrm{u}} - r_{\mathrm{min}} = r_{\mathrm{t,A}} + r_{\mathrm{t,B}}$ it follows that $r_{\mathrm{t,B}} = (r_{\mathrm{u}} - r_{\mathrm{min}})/(1+\eta)$ and $r_{\mathrm{t,A}} = (r_{\mathrm{u}} - r_{\mathrm{min}})\eta/(1+\eta)$. This effectively means that the binding rates are simply rescaled by these factors accordingly, namely $k'_{\mathrm{on,A}} = k_{\mathrm{on,A}}\eta/(1+\eta)$ and $k'_{\mathrm{on,B}} = k_{\mathrm{on,B}}/(1+\eta)$, where the primed constants are those that would be observed *in vivo*, whereas rates without a prime would be observed if a particular population of ribosomes in a specific stage is exposed to the antibiotic *in vitro*. As these considerations are valid for the individual antibiotics as well, these effects are already taken into account by fitting

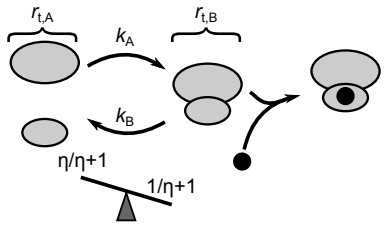

Figure A.4: **Ribosome subpopulations and translation inhibitors.** Two subpopulations of ribosomes $r_{t,A}$ and $r_{t,B}$, here exemplified as non-initiated and initiated ribosomes, are being cycled between as per rates k_A and k_B. The fraction of the total translation-capable ribosomes ($r_u - r_{\min}$) in a particular stage is determined by the ratio of rates $\eta = k_B/k_A$. These two subpopulations of ribosomes are bound by specific antibiotics, here exemplified by antibiotic binding only to subpopulation B (black disk).

the response parameter α. Together with the assumption that the antibiotics bind only ribosomes in a specific stage, these considerations are equivalent to setting the $\delta_{\text{on},i} = 0$, which results in additivity. This example suggests that the possibility of partitioning ribosomes is already implicitly taken into account, yet it does not recover any secondary effect such as traffic jams, factor deprivations, etc. from which complex interactions might arise.

B Experimental methods

B.1 Bacterial strains

Escherichia coli K-12 MG1655 strain was used as a wild-type (WT) strain. When necessary, the selection on kanamycin was performed at 25 μg mL^{-1} (for post-recombineering selection, see below) or at 50 μg mL^{-1} (for P1 transduction and plasmid selection). A concentration of 100 μg mL^{-1} was used for ampicillin (pCP20, resistance cassette resolution) and spectinomycin (pSIM19, recombineering). The selection for overexpression plasmids was done at 35 μg mL^{-1} of chloramphenicol.

To measure the bioluminescence time traces, pCS-λ encoding the bacterial *lux-CDABE* operon driven by the constitutive λ-P$_R$ promoter was transformed into the strains of interest [Kishony and Leibler, 2003]. Selection for the luminescence plasmid was used during the preparation of glycerol stocks (kanamycin 50 μg mL^{-1}) but was omitted during the measurements to avoid unknown interactions between the antibiotics used. The plasmid was stably maintained as we observed no significant fitness defect due to pCS-λ and no apparent spontaneous loss of the plasmid as verified by plating on selective and non-selective plates (Fig. B.1). To this end, we tracked the growth of bacterial cultures in flasks, shaking in a water bath in four conditions. We either actively selected for plasmid maintenance and/or applied antibiotic stress by adding 2 μg mL^{-1} of CHL, which led to $\approx$ 50% inhibition. We measured optical density by standard methods (using Hitachi U-5100 cuvette spectrophotometer); after each measurement, we replenished 1 mL of removed medium with fresh, prewarmed medium and corrected the optical density measurements accordingly. After reaching the late exponential phase, we promptly diluted the culture serially and plated equal volumes on both selective and non-selective plates.

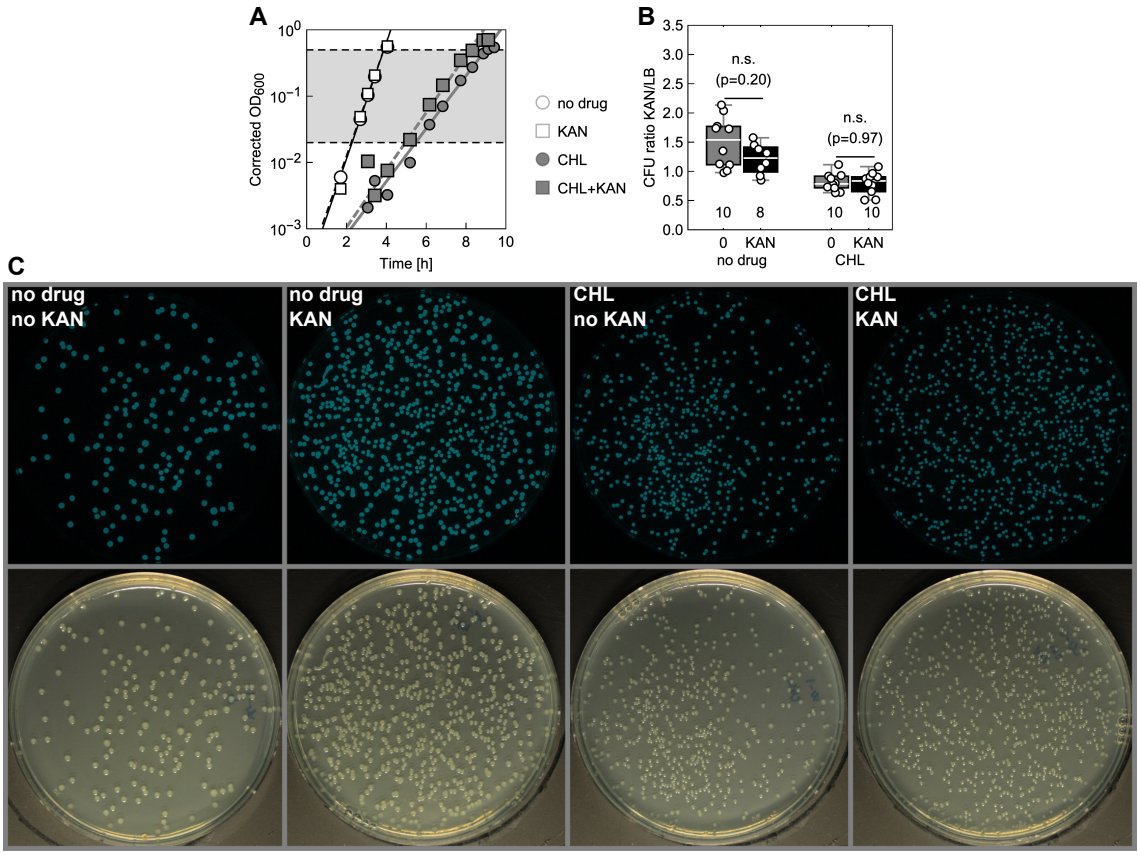

Figure B.1: **Stacker-based setup and incubator box. (A)** Time courses of optical density (OD) measurements of batch cultures in shaking flasks with or without selection for pCS-lambda by kanamycin (KAN) and with or without antibiotic stress [2 μg/mL chloramphenicol (CHL)]. Selection does not alter the response to the CHL. Lines shown in the plot were fitted to log-transformed OD values from the shaded area. **(B)** The ratio of colony-forming units (CFUs) on selective (KAN) and non-selective (LB) agar plates obtained from batch cultures from (A). Cultures grown in the absence of selection do not significantly differ from those with applied selection, indicating that the loss of plasmid is non-significant (p-values obtained by the two-sided Mann-Whitney test, Mathematica function `MannWhitneyTest`). Box-and-whisker charts: whiskers extended to the full range of data points, box edges show a 25%-75% range, and centerline is a median value. The number under the boxes denote the number of independent technical replicates, whose values are overlaid on the boxes. **(C)** Examples of LB agar plates for four different conditions in (A), imaged with a camera in bright field with a long-exposure time (30 s) to detect luminescence; all colonies are luminescent.

The translation factor titration platform was established in strain HG105 (MG1655 Δ*lacIZYA*) [Garcia *et al.*, 2011]. Briefly, endogenous genes encoding for translation factors were first sub-cloned into the pKD13 vector under the control of $P_{LlacO-1}$ promoter with FRT-flanked kanamycin resistance cassette (kan^R) and *TrrnB* termina-

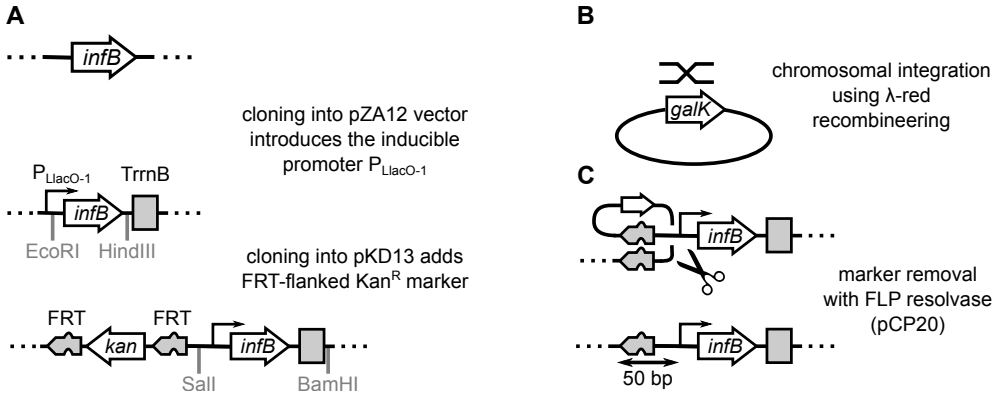

Figure B.2: **Construction of a strain with a titratable initiation factor. (A)** Regulatory elements (the promoter $P_{LlacO-1}$ and the *rrnB* terminator) are introduced through cloning into pZA12 vector. Subsequent cloning into pKD13 next to the FRT flanked Kan^R cassette is needed for removal of the marker upon chromosomal integration. **(B,C)** Upon integration into the *galK* locus using λ-red recombineering, Kan^R cassette is removed by the action of FLP resolvase. Used restriction sites are denoted in grey. Symbols are not to scale.

tor upstream and downstream of the gene, respectively (Fig. B.2) [Scott *et al.*, 2010; Lutz and Bujard, 1997; Klumpp *et al.*, 2009; Datsenko and Wanner, 2000]. The tandem of kan^R and a gene with all regulatory elements was integrated into the chromosome (*galK* locus) using λ-red recombineering (plasmid pSIM19 [Datta *et al.*, 2006]). The kanamycin resistance cassettes here and in the following steps were resolved using yeast FLP resolvase expressed from pCP20 [Cherepanov and Wackernagel, 1995]. Loss of the resistance cassette and curing of the pCP20 plasmid were checked by streaking on selection agar plates with antibiotics and by junction PCR (for resolution). Following the resolution of kan^R, the endogenous factor was inactivated by in-frame deletion: kan^R was integrated into the gene locus and then resolved, which left a 34 residue peptide [Datsenko and Wanner, 2000]. We were unable to introduce kan^R directly into the strain with $P_{LlacO-1}$ driven *frr*; therefore, we first performed the deletion in an auxiliary strain MG1655 Δ*frr*::kan^R bearing the ASKA plasmid with *frr* [Kitagawa *et al.*, 2005] [JW0167(-GFP)], which complemented the chromosomal deletion when IPTG was added. The deletion was possible in the auxiliary strain. We then moved the deletion by generalized P1 transduction [Lennox, 1955]. For *tufAB*, we P1-transduced the deletions (Δ*tufA*::kan^R and Δ*tufB*::kan^R)

sequentially from the respective gene deletion strains from the KEIO collection [Baba *et al.*, 2006]. All other deletions were performed directly in the strains of interest using λ-red recombineering using pKD13 as a template for the cassette amplification [Datsenko and Wanner, 2000]. In the last step, *lacI* driven by the $P_{LlacO-1}$ promoter (yielding growth-rate independent negative autoregulation [Scott *et al.*, 2010; Klumpp *et al.*, 2009]) together with the FRT-flanked kan^R was integrated into the *intS* locus and the resistance cassette was resolved. The allele Δ*intS*::kan^R-$P_{LlacO-1}$-*lacI*-*TrrnB* was moved into the strains by generalized P1 transduction. All chromosomal modifications were validated by PCR. The factor titration platform and the repressor operon were Sanger-sequenced at the integration junctions using PCR primers or a primer binding into the kan^R promoter region (which is upstream of the $P_{LlacO-1}$ promoter prior the resolution). The final genotype for the strains bearing the factor titration platforms is HG105 Δ*galK*::frt-$P_{LlacO-1}$-*x* Δ*x*::frt Δ*intS*::frt-$P_{LlacO-1}$-*lacI*, where *x* denotes the chosen factor. These strains contained no plasmids and no antibiotic resistance cassettes but had a single copy of a translation factor under inducible control.

To generate the strain with independently regulated initiation and translocation factors, we started with a strain carrying a single *infB* copy driven by $P_{LlacO-1}$ (Fig. B.3). Then, the negatively autoregulated *tetR* repressor was integrated into the chromosome, followed by FLP resolvase-mediated resolution of the selection marker. This enabled the integration of $P_{LtetO-1}$-driven *fusA* into the *intS* locus; the resolution was followed by the disruption of the endogenous copy of *fusA*. Furthermore, we introduced a negatively auto-regulated *lacI* into the *xylB* locus. This yielded a marker-less strain with the two essential genes *infB* and *fusA* under inducible, negatively autoregulated, and independent control. The final genotype is: HG105 Δ*galK*::frt-$P_{LlacO-1}$-*infB* Δ*infB*::frt Δ*ycaCD*::frt-$P_{LtetO-1}$-*tetR* Δ*intS*::frt-$P_{LtetO-1}$-*fusA* Δ*fusA*::frt Δ*xylB*::frt-$P_{LlacO-1}$-*lacI*.

Oligonucleotide sequences, targeted template, restrictions sites (when used), and a brief description of use are listed in Table F.4. All DNA modifying enzymes and Q5 polymerase used in PCR were from New England Biolabs.

To construct the double-resistant strain we modified the methods described

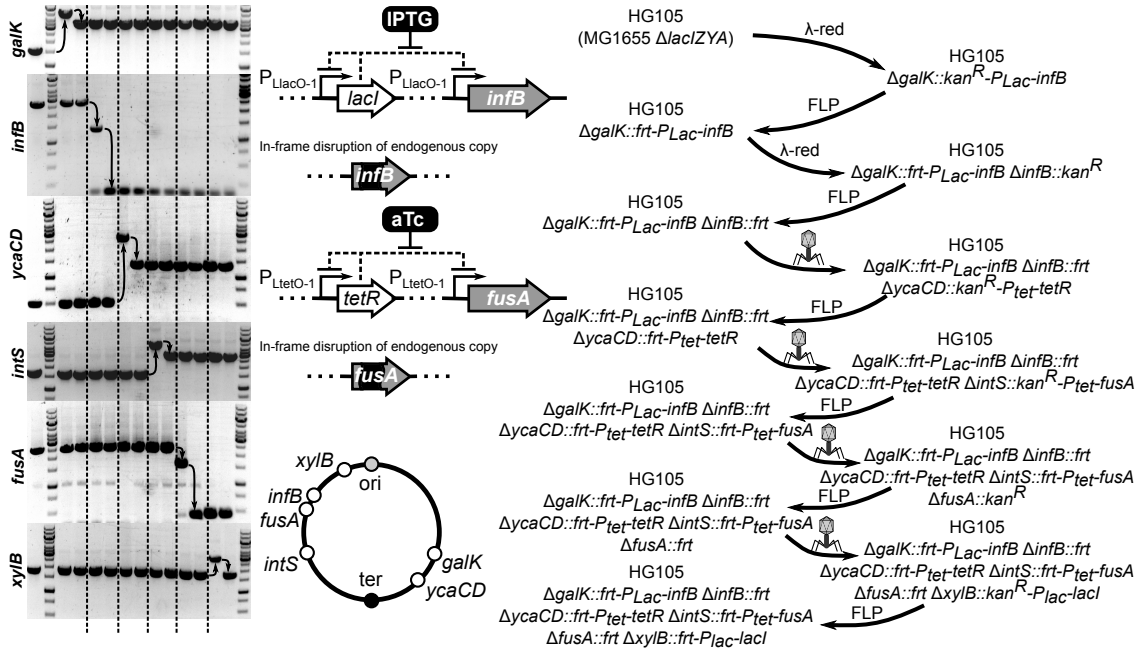

Figure B.3: **Construction of a double titration strain.** Ladder is GeneRuler 1kB. Phage symbol, FLP, and λ-red denote a step based on P1 transduction, FLP-resolution, and λ-red recombineering, respectively. Here, we useda shorthand P_{Lac} for $\mathrm{P_{LlacO-1}}$.

above. We have cloned *cat* gene into a plasmid with pKD13 background, in which resistance gene was driven by a synthetic promoter $\mathrm{P_{LlacO-1}}$ [Lutz and Bujard, 1997]. Promoter was unregulated (constitutive) as the background strain HG105 (MG1655 Δ*lacIZYA*) [Garcia *et al.*, 2011] is devoid of the entire *lac* operon, including the *lac*-repressor. We amplified the *tetA* and *cat* from the strain MS004A [Steinrück and Guet, 2017] and plasmid pZA32 [Lutz and Bujard, 1997], respectively. We were unable to clone *tetA* into a plasmid; we therefore assembled the kanamycin cassette, $\mathrm{P_{LlacO-1}}$ promoter, and *tetA* gene with a *rrnB* terminator *in vitro* using HiFi Assembly Mix (NEB), PCR-amplified the fragment, and integrated it into the *intS* locus. CAT-coding gene was integrated into *galK* locus. Both CERGs were integrated into the chromosome by lambda-red recombineering, selected on kanamycin, which was followed by the resolution of the kanamycin cassette by FLP-resolvase [Datta *et al.*, 2006; Deris *et al.*, 2013; Datsenko and Wanner, 2000; Cherepanov and Wackernagel, 1995]. We verified modified chromosomal segments with PCR and Sanger sequencing. For CERG experiments we dissolved TET and CHL directly in LB, followed by filter-sterilization.

We constructed overexpression strains by transforming HG105 with pCS-λ and plasmids from the ASKA library [Kitagawa *et al.*, 2005] and its derivatives (Fig. B.4). We used ASKA plasmids in which GFP has been excised from the reading frame; we had to repeat the excision of GFP from the *infB*-bearing plasmid by NotI digestion and subsequent ligation as per Ref. [Kitagawa *et al.*, 2005]. All plasmids were Sanger-sequenced. For controls we used (i) plasmid pAA31 (gift from A. Angermayr), in which the open reading frame is cleanly deleted, as transcription-only control, and (ii) the ASKA plasmid bearing *lacZ* as a neutral protein overexpression control. We note that the overexpression of proteins leads to growth inhibition [Scott *et al.*, 2010; Dong *et al.*, 1995]; hence, we actively selected for plasmid maintenance by adding 35 μg mL^{-1} of chloramphenicol into the growth medium.

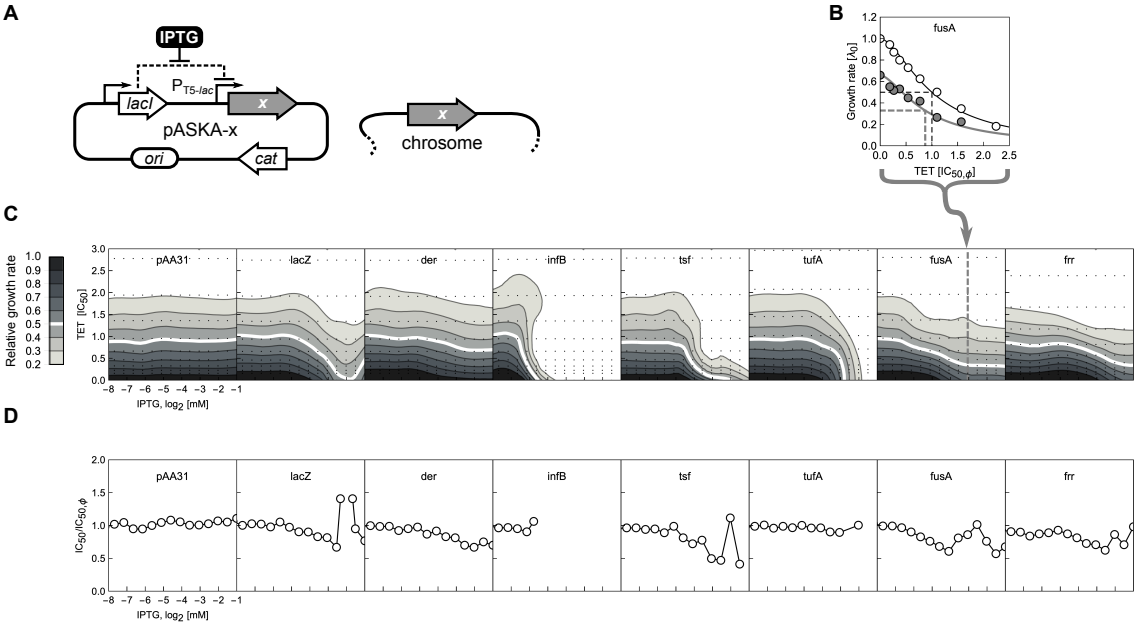

Figure B.4: **Overexpression of translation factors conveys little information about the action of tetracycline. (A)** The overexpression system is based on ASKA library plasmids. High copy plasmid with chloramphenicol resistance (cat) provides a constitutively expressed *lacI* repressor, which controls the expression of P_{T5-lac}-driven gene *x*. The chromosomal copy of the translation factors was left intact. The high copy number of a plasmid enables the overexpression of proteins. **(B)** Example of the tetracycline dose-response curve in the presence or absence of *fusA* overexpression. White and gray circles denote measurements of the dose-response curve in the absence and presence of inducer, respectively. Best-fit Hill functions are shown as solid lines. Dashed lines denote the apparent IC_{50} and corresponding growth rate compared to the no antibiotic at both inducer concentrations. Growth rate is decreased as a consequence of overexpression. Gray dose-response curve is a cross-section of the dose-response surface shown in (C): see arrow. **(C)** Dose-response surfaces for gene-less control (pAA31), protein-overexpression control (*lacZ*) and all six translation factors as indicated. In general, growth rate decreases with overexpression and the action of the antibiotic is not alleviated by overexpressing any of these genes. Cross-section of the dose-response surface shown in (b) for *fusA* is indicated by a dashed gray line. **(D)** Dependencies of the $IC_{50}/IC_{50,\phi}$ ratios ($IC_{50,\phi}$ corresponds to IC_{50} in the absence of inducer) for different overexpression cases as a function of inducer concentration. At each inducer concentration, the apparent IC_{50} is determined from a fit of a Hill function. In general overexpression leads to mild sensitization of bacteria to tetracycline and this trend is largely independent of specific overexpressed gene. The occasional slight increase is mostly due to the poor fits of the dose-response curve or the occurrence of spontaneous mutants.

B.2 Growth rate assay and two-dimensional concentration matrices

Rich lysogeny broth (LB) medium, which at 37°C supports a growth rate of 2.0 ± 0.1 h^{-1}, was used. LB medium was prepared from Sigma Aldrich LB broth powder (L3022), pH-adjusted to 7.0 by adding NaOH or HCl, and autoclaved. Antibiotic stock solutions were prepared from powder stocks (for catalog numbers, see Supplementary Table 1), dissolved either in ethanol (CHL, ERM, and TET), DMSO (LAM and TMP) or water (KAN, CRY, LCY, KSG, FUS, and STR), 0.22 μm filter-sterilized and kept at -20°C in the dark until used. Antibiotics were purchased from Sigma Aldrich or AvaChem. Some of the antibiotics (e.g., ERM, FUS, LCY) are not used in the clinic against certain Gram-negative bacteria due to generally poor efficacy; however, at higher concentrations (yet still well below the solubility limit) inhibition of growth is observed.

A previously established growth-rate assay based on photon counting was used to precisely quantify the absolute growth rates for 5-9 generations [Kishony and Leibler, 2003]. Cultures were grown in 150 μL of media in opaque white 96-well microtiter plates (Nunc 236105), which were tightly sealed by transparent adhesive foils (Perkin-Elmer 6050185 TopSeal-A PLUS) to prevent contamination and evaporation. We prepared glycerol stocks of WT and factor-titration platform strains from saturated overnight cultures. We inoculated the cultures with $\sim 10^2$ cells per well (1:10^6 dilution) from either thawed glycerol stocks (for the drug interaction network) or from liquid cultures in which we first incubated the bacteria containing the factor titration-platform for 1 h in the absence of IPTG (inoculated by 1:2000 dilution of the glycerol stock) to partially dilute out the remaining factor molecules before additional 1:1000 dilution into measurement plates. Between 10-20 plates were cycled through a plate reader using a stacking system (Tecan M1000, controlled by Tecan i-control software, v1.10.4). We built a custom incubator box around the stacker towers to facilitate ventilation and fix the temperature to 37°C (Fig. B.5). This incubator was designed and troubleshot by B.K. and Andreas Angermayr (IST Austria and University of Cologne) and built by IST Miba Machine Shop. Each plate

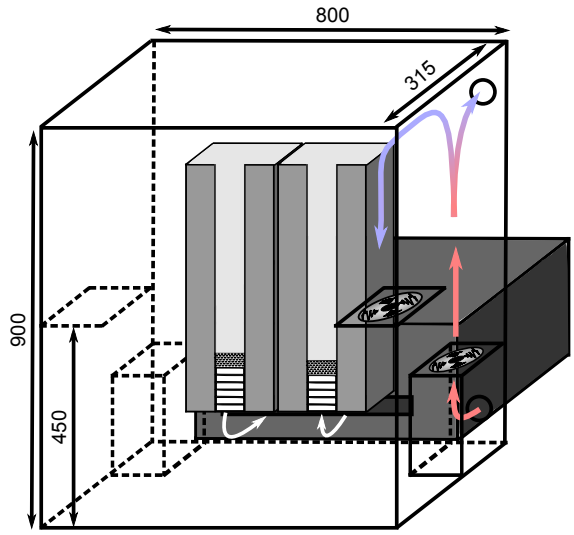

Figure B.5: **Stacker-based setup and incubator box.** Stacker-based setup and incubator box. Microtiter plates are stacked vertically in stacker towers and cycled (white arrows) through the Tecan M1000 plate reader (dark grey box) in which plates are shaken and luminescence is measured. After all plates are stacked in the right tower, the stacking mechanism re-stacks the plates into the left tower to repeat the measurement. Fans circulate the air in the incubator to equilibrate the temperature.

was read every 20-40 min and was shaken (orbital 10 s, 582 rpm) immediately before reading (settle time 10 ms, integration time 1 s). Plates were manually pipetted and concentration gradients of antibiotics and inducers (IPTG, aTc) were prepared by serial dilution (0.70-fold).

Growth rates were determined as a best-fit slope of a linear function fitted to the log-transformed photon counts per second. The fitting procedure and examples of growth curves are shown in Fig. E.3. In rare cases of occurrence of mutants (as evidenced by sudden growth) we manually removed the measurement (only in the case of *tufA* titration). We verified that the luminescence-based technique leads to the same results as a classical optical density-based one (Fig. B.6).

We measured the dose-response surfaces for all 28 drug interactions in duplicate. As the dose-response surface was measured over a 12×16 grid, the duplicates swap the drug axes (12×16→16×12 across two 96-well plates) on different days to check for effects coming from spreading the measurements over different plates. The experimental and analysis procedure led to reproducible measurements of growth rates between days (Fig. E.3D, $\rho \approx 0.86$). For the double factor titration experiment, the inducer gradients were set up across 6 plates to form a 24×24 grid. Each response surface is thus based on multiple measurements and the impact of individual points is assessed by bootstrapping. In total, we measured over 20,000 growth curves. We automatized the collection and analysis of the data to allow for unbiased interpretation of the data.

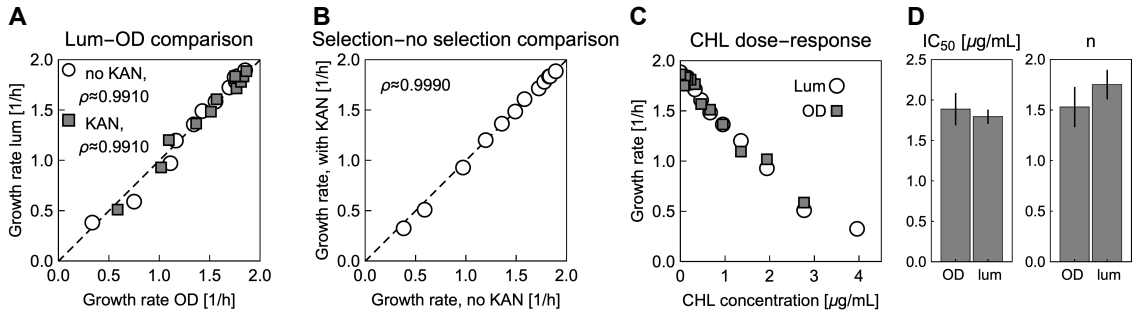

Figure B.6: **Verification of the growth-measurement technique. (A)** Comparison of OD and luminescence-based growth rates for the CHL dose-response curve in the presence or absence of selection. Scatterplot reveals high-correlation between measurements, irrespective of selection. **(B)** Comparison of luminescence-based growth rates in the presence or absence of selection. **(C)** Dose-response curve for CHL, obtained by OD or luminescence assay. Qualitatively, curves match to a high degree. **(D)** Shape parameters of the dose-response curves as obtained from curves in (G). Black lines show standard errors as obtained from fitting.

B.3 Measurement of induction dynamics.

We simultaneously transformed the strain HG105 with both pCS-$\lambda\Delta$*luxA* and pBAD24-*luxA*. After growing the strain in rich SOB medium with antibiotics, we pipetted five 108 μL portions of the exponentially growing culture into a white 96-well plate. After a short incubation, we added either the 5 μL+5 μL of water, or water and cAMP. The cultures were incubated for 10 minutes at 37°C with shaking to enable cAMP to enter the cells. After the incubation, plate was put on the plate reader tray and 10 μL of water, arabinose or arabinose with cAMP was rapidly pipetted into the wells and the measurement of the luminescence time track began. Time tracks are shown in the Fig. B.7.

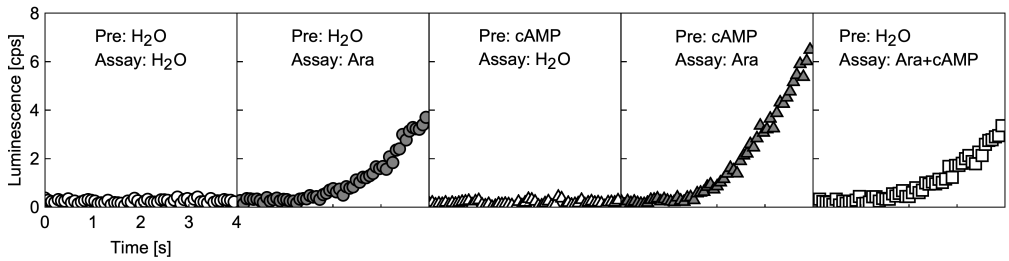

Figure B.7: **Induction is rapid and is made even faster by pretreatment with cAMP.** Panels show different induction protocols, with indicated pretreatment (10 minutes before the induction) and the assayed induction. Tracks indicate that cAMP alone cannot facilitate induction, but if applied before the induction, the expression is more rapid. Applying the cAMP together with arabinose does not accelerate the expression.

C Data analysis methods

C.1 Normalization of dose-response surfaces

All growth rates were normalized relative to the average growth rate in the drug-free medium [for factor-titration strains at the highest inducer concentration (5 mM)]. Small differences between individual dose-response curves were inevitable due to known challenges of preparing identical concentrations gradients on different days. To correct for such day-to-day variability, we rescaled the concentration units to the IC_{50} for each drug. The IC_{50} was obtained from fitting the Hill function $y(x) = 1/\left[1 + (x/IC_{50})^n\right]$ to the individual dose-response curves. The dose-response curve of each drug was measured seven times and averaged. The IC_{50} and corresponding errors reported in Table 3.1 are extracted from such average dose-response curves (Fig. E.1). Induction curves were normalized slightly differently, using a shifted and increasing Hill function in the form $g(b) = [(b + b_0)/IC_{50}]^n / \left\{1 + [(b + b_0)/IC_{50}]^n\right\}$, where b_0 is a concentration offset. The latter parameter was required as the complete cessation of growth was not achievable in some cases even in the absence of inducer as the promoter $P_{LlacO-1}$ is leaky. Inducer concentrations were thus rescaled via $b \rightarrow (b + b_0)/IC_{50}$.

C.2 Smoothing of dose-response surfaces

To reduce noise when plotting response-surfaces, we smoothed the data using a custom Mathematica script that implements locally weighted regression (LOESS) [Cleveland and Devlin, 1988]. This approach only smoothed the contours and did not alter the character of dose-response surfaces. Smoothing was only used for plotting and

not for the analysis in which only linear interpolations between points were used (Mathematica function `Interpolation`).

C.3 Quantification of the drug interaction types and bottleneck dependencies

C.3.1 Loewe interaction score

To quantify the drug interaction between a pair of antibiotics, we defined the Loewe interaction score as

$$LI = \log\left(\frac{\int g(x_1, x_2)\mathrm{d}x_1\mathrm{d}x_2}{\int g_{\mathrm{add}}(x_1, x_2)\mathrm{d}x_1\mathrm{d}x_2}\right), \tag{C.1}$$

where $g(x_1, x_2)$ and $g_{\mathrm{add}}(x_1, x_2)$ are the measured and the predicted additive dose-response surfaces over a 2D concentration field (x_1, x_2), respectively. The LI score is a log-transformed ratio of volumes underneath the dose-response surfaces. It is positive for antagonistic and suppressive interactions, zero for perfectly additive, and negative for synergistic interactions. To avoid imposing arbitrary bounds for classifying a measured interaction as synergistic or antagonistic/suppressive (rather than additive), we performed smooth bootstrapping on a set of ideal additive response surfaces to establish a distribution of interaction indices expected for perfectly additive but noisy surfaces. To achieve this, we generated additive dose-response surfaces for drugs with a Hill steepness parameter n between 1.8 and 6.6 (obtained as 10% and 90% percentiles of the distribution of steepness parameters for measured dose-response curves). We estimated the variabilities of measurements σ_{v} from data from eight replicated dose-response curves with seven replicates per data point and fitting errors σ_{f} from the slope of all growth rate fits. Both error and variability distributions were well described by log-normal distributions. For each point on the generated surfaces, we added Gaussian noise with standard deviation given as $\sqrt{\sigma_{\mathrm{v}}^2 + \sigma_{\mathrm{f}}^2}$, where both σ_{v} and σ_{f} were drawn from respective log-normal distributions. We calculated the LI score for 2,000 response surfaces and obtained the distribution shown in Fig. C.1A. We determined boundaries separating synergistic

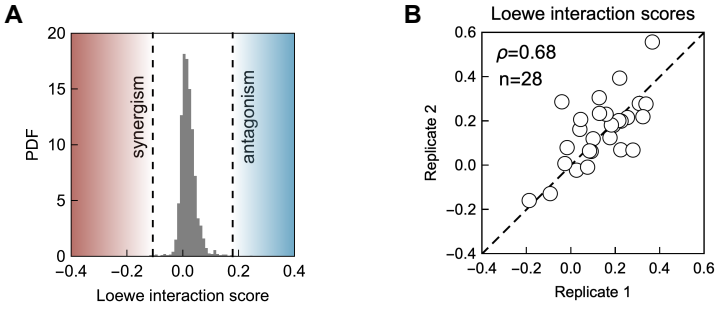

Figure C.1: **Distribution and measurements of LI scores. (A)** Distribution of Loewe interaction scores of noisy additive surfaces for pairs of drugs with different steepnesses, as obtained by bootstrapping. Note, that this reveals a slight bias towards antagonism. Here, LI scores were calculated for 2×10^3 bootstrap surfaces. See section "Loewe interaction score" for details. **(B)** Reproducibility of LI scores between replicates. Each LI score was evaluated for replicated measurements on different days for 28 different antibiotic combinations. The indicated Pearson correlation can be interpreted as an upper bound for the correlation between any predicted and measured LI scores.

and antagonistic LI scores (b_{lower} and b_{upper}, respectively) from additive interval as Bonferroni-corrected percentiles (for $5\%/28 \approx 0.18\%$ and $100\% - (5\%/28) \approx 99.82\%$) of the bootstrapped distribution (Fig. C.1). Mean LI scores for measured response surfaces falling outside of the interval with these boundaries were classified as synergistic or antagonistic; otherwise, the interaction was classified as additive.

C.3.2 Bottleneck dependency score

Similar to LI, the bottleneck dependency score BD is an integrative quantity that concisely reports on the response-averaged deviation from independence. To calculate this score, the antibiotic and inducer concentrations are first converted into corresponding responses using the induction- and antibiotic dose-response curves (Fig. C.2). Mathematically, this means that $r_{\text{x}} = y(c)$ and $r_{\text{y}} = g(b)$ for antibiotic and inducer, respectively. In response space, the null-expectation is independence, *i.e.*, the expected response is a product of individual responses. Thus, we define the BD score as

$$BD = \log\left(\frac{\int r(r_{\text{x}}, r_{\text{y}})\mathrm{d}r_{\text{x}}\mathrm{d}r_{\text{y}}}{\int r_{\text{x}} r_{\text{y}}\mathrm{d}r_{\text{x}}\mathrm{d}r_{\text{y}}}\right). \tag{C.2}$$

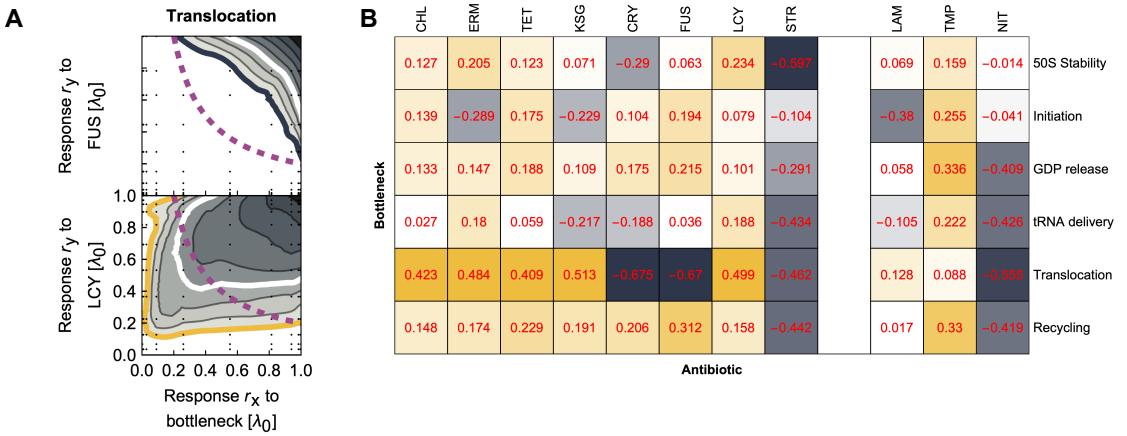

Figure C.2: **Response-response surface and BD score. (A)** Examples of response surfaces over the response-response grid for FUS and LCY in combination with translocation bottleneck. In the response space (r_x,r_y), independence is defined as $r_x r_y$. The logarithm of the ratio of volumes underneath the measured and independent surface yields a bottleneck dependency score. For every antibiotic, six bottleneck dependency scores together yield a bottleneck dependency vector. **(B)** Values of bottleneck dependency scores for all bottleneck-antibiotic pairs.

This score is zero when the two perturbations (bottleneck and antibiotic) are independent; it is positive or negative for alleviation and aggravation, respectively. As for the LI score, we evaluated the independence interval of BD scores by bootstrapping the BD score for independent surfaces at given induction and antibiotic dose-response curves. Evaluating the percentiles of such null-distributions gave the boundaries for evaluation of the type of deviation from independence (alleviation or aggravation).

C.3.3 Clustering of bottleneck-dependency vectors

We performed the clustering of BD vectors projected on a space of lower dimensionality. For dimensionality reduction, we used Principal Component Analysis (PCA). We used the first three principal components which explained $\approx 95.38\%$ of the variance. In this projected three-dimensional space, we performed unsupervised agglomerative clustering (Mathematica function `FindClusters`) with cosine distance as a measure of cluster cohesion.

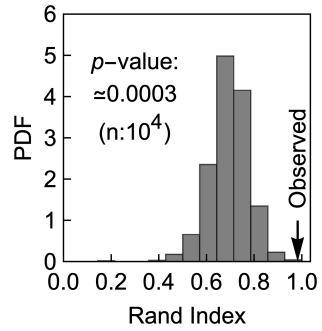

Figure C.3: **Bootstrapped clustering of randomized vectors yields a series of clustering results.** With these clustering results at hand, we calculate the Rand indices $RI(w, w')$ for $n = 10^4$ bootstrap replicates. From the distribution of $RI(w, w')$, we estimate the empirical cumulative distribution function and corresponding empirical p-value for the clustering result

We estimated the p-value of the observed clustering by bootstrapping. We used the Rand index (RI) [Rand, 1971] as a criterion for evaluating the difference between clustering results. For example, if w is the clustering obtained for the reshuffled sample and (consensus) clustering w' is obtained for PCA projection of median bottleneck dependency vectors (shown in Fig. C.2), then the Rand index is

$$RI(w, w') = \frac{\sum_{i<j}^{N} \psi_{ij}}{N(N-1)/2} \in [0, 1]. \tag{C.3}$$

Here, ψ_{ij} is 1 if the i-th and j-th data points are either inside or outside of the same cluster and 0 otherwise; the denominator is the total number of unique pairs between N elements. We generated 10^4 reshuffled datasets, evaluated RI for each clustering of the dataset, and calculated the cumulative distribution function. We evaluated an empirical p-value as

$$p = 1 - \mathrm{CDF}\left(1 - \frac{1}{N(N-1)/2}\right) \approx 3 \times 10^{-4}, \tag{C.4}$$

which is an estimate of the probability for obtaining the observed clustering of median BD vectors by chance. The cluster areas shown in Fig. 3 were obtained by smooth bootstrapping of median BD vectors for a given noise statistics, which were PCA projected, and subsequent calculation of the minimal convex hull (Mathematica function `ConvexHullMesh`). The additional response vectors for LAM, TMP, and NIT were PCA projected (using Mathematica function `DimensionReduction` obtained for the median values of BD vectors).

C.4 Remapping

Our remapping procedure converts inducer concentrations b into the concentrations c of an idealized antibiotic that precisely targets the translation step controlled by the titrated factor. This requires an induction curve and a dose-response curve. The former is described by an increasing Hill function $g(b)$, and the latter by solving Equation (A.4) for y. The conversion between concentrations is formally described as $c = y^{-1}\left(g(b)\right)$ at a given α, which can be arbitrarily chosen for the idealized antibiotic. When $\alpha < \alpha_{\text{crit}}$, the dose-response curve is bistable and has a region in which more than one response will yield the same concentration – in these cases we consider only the concentration corresponding to the highest stable growth rate as the other solutions are either unstable or will be outcompeted. Further, higher inducer concentrations are remapped to lower antibiotic concentrations and an infinite inducer concentration corresponds to zero antibiotic concentration. As this is impractical, we considered all mimicked concentrations (normalized relative to IC_{50}) that are below 0.1 as equivalent to 0.

C.4.1 Regularization of surfaces

Strains containing the factor titration platform have mostly very similar antibiotic dose-response curves to the wild-type at maximal inducer concentrations. However, to correct for small deviations, we rescaled the antibiotic concentrations on the antibiotic-inducer grid. The shape of this transformation is derived from equating the responses of two Hill functions with different steepnesses. Consider two Hill functions with Hill exponents n_{WT} and n_{t}, for WT and factor-titrating strain, respectively. Then, by equating the responses captured by these Hill functions, we calculated the rescaled relative (relative to IC_{50}) antibiotic concentrations as $c_{\text{a,WT}} = c_{\text{a,t}}^{n_{\text{t}}/n_{\text{WT}}}$. We refer to this conversion as the "power-law transform". Such regularized surface was then used in remapping.

C.4.2 Remapping-based equivalence

Factor deprivation is equivalent to the action of a specific antibiotic if both perturbations can be substituted for each other. Upon remapping the inducer concentration, the response surface for an equivalent inducer-antibiotic pair is transformed into an additive response surface. To determine if the deprivation of a specific factor is equivalent to the action of a specific antibiotic, we performed the remapping in tandem with bootstrapping. Bootstrapping assesses the effects of uncertainties in the remapping parameter α (obtained as a response parameter α from a fit of inverted Eq. (A.4) to a drug dose-response curve), artifacts of the response surface over inducer-antibiotic grid and sampling, and inherent noisiness of growth rate determination. We first restricted the dataset to data points with relative growth equal to 0 or above 0.1 with growth rate coefficient of determination $R^2 > 0.8$. In each round of bootstrapping, the following steps are carried out:

1. drawing of a remapping parameter α from a normal distribution, centered at the best-fit-value and with standard deviation estimated from fitting, and remapping,

2. drawing of a random sample from remapped data points that is of random size (between 75% and 100% of the data set),

3. the addition of Gaussian noise to the growth rates (estimated from the growth rate fit),

4. calculation of the ideal additive surface at a given α for comparison, and

5. calculation of LI score.

This procedure was repeated 100 times for each bottleneck-antibiotic pair and yielded a set of distributions. Each LI distribution was then statistically evaluated for being inside the additive interval. We obtained the cumulative distribution function (CDF) for each distribution and we calculated its value on both ends of additive interval (Fig. C.1). If either $1 - \mathrm{CDF}\,(b_{\mathrm{lower}})$ or $\mathrm{CDF}\,\left(b_{\mathrm{upper}}\right)$ is below $p = 0.05$, the pair is considered inequivalent – this is the case in which the remapped surface

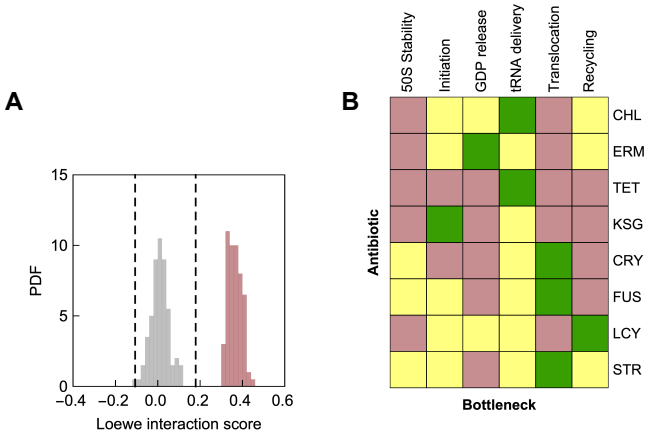

Figure C.4: **Examples of *LI* histograms and tentative modes of action. (A)** Examples of histograms of *LI* for remapped surfaces for CRY in combination with a translocation and recycling bottleneck, respectively. Each histogram is calculated for $n = 100$ bootstrapped *LI* scores. **(B)** Color-coded sequential evaluation of equivalence between bottleneck and translation inhibitor from Fig. E.6. Red and yellow denote that *LI* was outside or inside of the additive interval, respectively. From the cases in which the *LI* is statistically inside the additive interval, the case with highest correlation was chosen as the putative primary mode of action (green). This approach correctly identified the mode of action for all cases in which it is known from the literature (CRY, FUS, STR, KSG, and TET).

is unlikely to be additive. For each antibiotic, more than one of the bottlenecks could be statistically equivalent – we thus deemed the bottleneck-antibiotic pair with the highest correlation between average remapped and ideal additive growth rates to be the primary candidate for equivalence of perturbations.

C.5 Quantitative comparison of predicted and measured response surfaces

Both measured and predicted surfaces match along the individual concentration axes, as these were obtained from the fits of dose-response curves. Thus, points corresponding to such measurements are always a good match and in turn increase the Pearson correlation invariantly of a potential mismatch in surface segments further away from individual axes. The Loewe interaction score is a good measure of interaction strength; however, it is not well suited for comparing the predicted and measured surfaces. Crucially, the same value of *LI* can be obtained for two

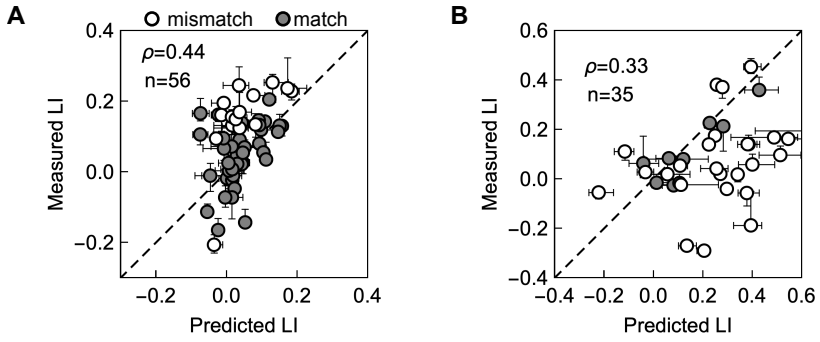

Figure C.5: **Comparison of LI scores for predicted and measured surfaces. A,B** Scatter plots show median values of predicted and measured LI scores for all possible predictions for biophysical model and remapping, respectively. Error bars show 90% bootstrap confidence intervals obtained from 100 bootstrap repetitions. White and gray symbols correspond to match and mismatch cases, respectively, as determined by isobole sliding. In A, the LI score was computed for the best prediction with the binding scheme. Note, that this correlation is not expected to exceed that of replicated LI scores in Fig. C.1.

very different surfaces. For example, if the same suppressive interaction surface is rotated by 90°, the LI score would remain the same, even though the direction of suppression is completely different. We therefore sought an applicable metric that would identify systematic deviations from predicted isoboles.

We developed an "isobole sliding" method in which we determine a mean deviation of points close to some predicted growth rate from measured values. It provides a concise, quantitative description of differences between predicted and measured isoboles and identifies the most discrepant areas of the surfaces. For this, we systematically move along the (ordered) predicted growth values g_i and select $S = 20$ consecutive points and average their deviations from measured values of growth rate h_i. This yields a deviation trajectory $t(\hat{g})$ of a mean deviation as a function of average predicted growth rate

$$t(\hat{g}) = \frac{1}{S}\sum_{i=j}^{j+S-1}\left(h_i - g_i\right), \quad \text{where} \quad g_i < g_{i+1} \text{ and } \hat{g} = \frac{1}{S}\sum_{i=j}^{j+S-1} g_i. \tag{C.5}$$

Keeping the number of points S fixed in the window allows the comparison between different subsets of the data.

To assess the probability of observing such deviation by chance, we created a

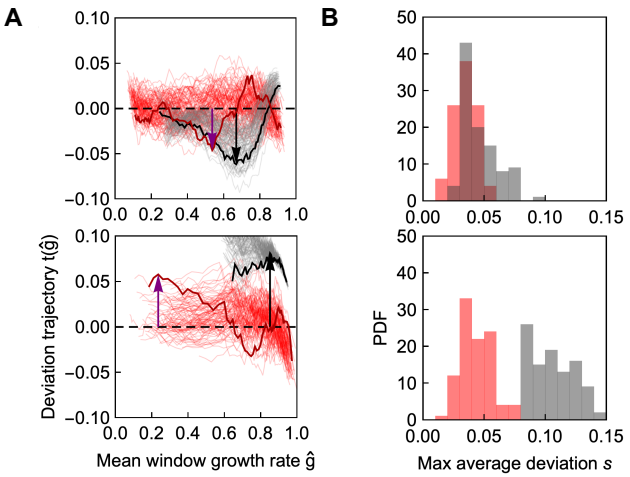

Figure C.6: **Illustration of isobole sliding method. (A)** two examples of deviation trajectories $t(\hat{g})$ for ERM-TET (top) and KSG-STR (bottom). Thin gray and red lines show $n = 100$ bootstrap repetitions of predicted and benchmark trajectories. Two trajectories (thick black and red lines for measured and benchmark, respectively) are highlighted. Black and purple arrows denote the maximal deviation of the trajectory from zero for predicted and benchmark trajectory. The length of the arrow is maximal average deviation s. **(B)** All s values from $n = 100$ bootstrapped repetitions are collected in the histogram. The pair of ERM-TET offers a better match with benchmark distribution compared to KSG-STR.

benchmark dataset by replacing all measured values with predicted ones to which we added Gaussian noise (estimated from bootstrapped dispersion, but of at least 0.05 relative growth units). For each bootstrapped realization (obtained either by remapping or the biophysical model), we randomly drew a subset of random size (between 75% and 100% of the data set) to estimate the robustness of the prediction concerning a low number of outliers. We collapsed each isobole sliding trajectory into a single number s by calculating a maximal deviation, $s = \max_{\hat{g}} |t(\hat{g})|$, thus yielding a distribution of s values for both measured and benchmark trajectory maxima.

Ideally, the distribution of maximal average deviations should either overlap or be below the benchmark distribution. To assess the statistical deviation, we evaluated the CDF of predicted-measured distribution at the 95% percentile of the benchmark distribution. If the value was below 0.05, we rejected the prediction. This method requires that there are no systematic deviations over the whole surface, thus yielding a very stringent criterion for considering a match between two surfaces.

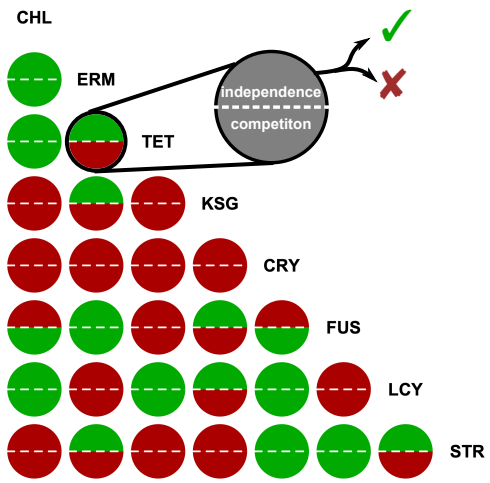

Figure C.7: **Performance of biophysical model against the measurements.** The upper and bottom half of each circle denote independence or competition, respectively, as denoted. Green and red color denote match and mismatch, respectively. Match means that both replicates agree that a certain scheme faithfully predicts observed surface.

Thus, even if two surfaces match qualitatively, isobole sliding might still return a statistically significant mismatch.

To estimate the upper bound of prediction-measurement agreement, we checked for consistency of the measured replicates. For this, we considered one of the replicates as a prediction of the other. In doing so, we observed that twenty-one out of twenty-eight (75%) surfaces act as statistically significant predictions for one another. This serves as an approximate upper bound for how many predictions-measured pairs can be expected to match at the given experimental variability.

C.5.1 Assessment of predictive power

At this point, we can assess the consistency of predictions. Using the method described above, we evaluated both independent and competitive binding schemes for their congruence with measured surfaces. The scheme that led to the distribution with the smallest mean maximal deviation, was considered as a best-match. However, both schemes can yield a good match – by asking how many of the schemes yield a match in both replicates, we obtain an estimate for a fraction of correct predictions (Fig. C.7). By counting cases in which at least one of the schemes yields a match between replicates, we find that sixteen out of twenty-eight interactions can be accounted for by a biophysical model.

Applying isobole sliding to the prediction of remapping shows that even small quantitative deviations will lead to the discarding of the prediction (Figure E.7).

However, counting additionally explained interactions by remapping (TET-CRY, TET-FUS, KSG-CHL, CRY-KSG) increases the total tally of explained interactions to twenty out of twenty-eight (≈71.4%), which is below the estimated self-consistency bound of 75%. As discussed above, qualitative matches are not included in this metric.

D Tagging of chromosomal proteins with GFP

Mapping from the inducer concentration to expression of the gene of interest is not directly accessible, as we discussed in the Chapter 7. We aimed to construct a C-terminal fusions of the integrated factors with fluorescent reporter. We used pKD13 as a vector for construction of the GFP-tagging plasmid. We used a GFPuv4 mutated version of GFP [Ito *et al.*, 1999] and corresponding N-end five amino acid linker (nucleotide sequence GGCCTATGCGGCCGC, *i.e.*, amino-acids GlyLeuCysGlyArg) from ASKA library parent vector pCA24N(+)GFP [Kitagawa *et al.*, 2005]. Used mutated version of GFP can be used at 37°C and has a maturation time of 15.2 minutes [Ito *et al.*, 1999; Iizuka, 2011]. With this template plasmid at hand, we can fuse a GFP with chromosomal genes. Presented strategy is related to a method in Ref. [Watt, 2007].

D.1 GFP-tagging plasmids

We constructed a plasmid pKD13-GFPtag (Fig. D.1), which carries a spacer-flanked GFP upstream of *TrrnB* terminator, followed by a FRT-flanked kanamycin resistance cassette. We amplified GFP and the linker from pCA24N(+)GFP using primers o-ClaI-link-GFP-2-pKD13-F and o-KpnI-link-GFP-2-pKD13-R (Table D.1). We introduced KpnI restriction site by full plasmid PCR using primers o-ClaI-pKD13-full-R and o-KpnI-pKD13-full-F (Fig. D.1, Table D.1); ClaI restriction site is naturally present upstream of *TrrnB* terminator but we introduced specific overhangs in the forward primer. Both PCR amplicons were KpnI, DpnI, and ClaI digested gel purified. After ligation, ligation products were transformed into DH5α-λpir cells and selected on kanamycin and ampicillin.

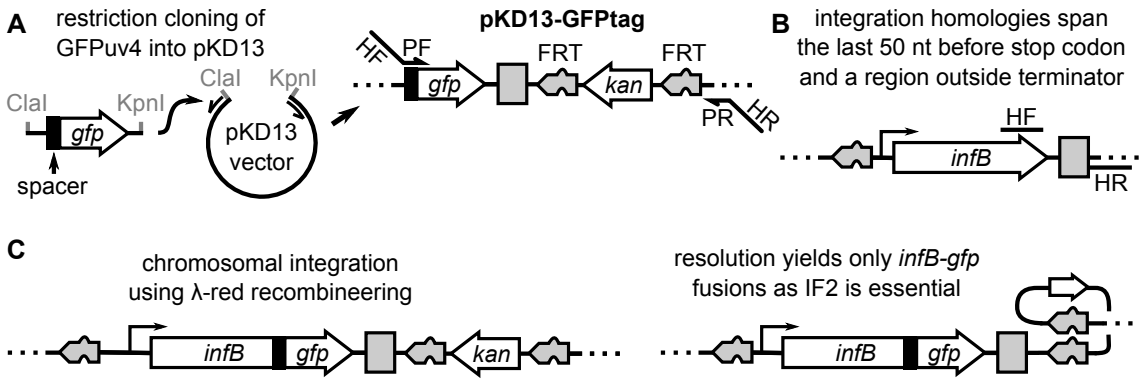

Figure D.1: **Construction of GFP-tagging plasmids and illustration of tagging strategy in the case of *galK*-integrated *infB* gene. (A)** Spacer and GFPuv4 are PCR amplified from ASKA library parent vector and restriction cloned into pKD13 upstream of *rrnB* transcriptional terminator (KpnI site is introduced through full-plasmid PCR), which yields plasmid pKD13-GFPtag. **(B,C)** Chromosomal homologies HF and HR determine the integration site. After integration, gene is in-frame with GFP and has a removable marker downstream.

primer	sequence
o-ClaI-link-GFP-2-pKD13-F	CC **ATCGAT** ACCATCACCATACGGATCCG
o-KpnI-link-GFP-2-pKD13-R	GG **GGTACC** CAGGAGTCCAAGCTCAGCTA
o-ClaI-pKD13-full-R	CC ATCGATGCAGGTGGCACTTT
o-KpnI-pKD13-full-F	GG **GGTACC** GATGGTAGTGTGGGGTCTCC

Table D.1: **Oligonucleotides for construction of GFP-tagging plasmids.** Restriction sites are in bold. Underlined are the annealing regions.

D.1.1 In-frame gene-GFP fusion

The GFP-tagging plasmid enables a general approach for the construction of in-frame GFP-fusions only by redesigning recombination primers. Forward primer has a 20-nt annealing homology (PF: GGCCTATGCGGCCGCAGTAA) that spans over spacer. The overhang is specific to the gene of interest and spans over last 50 nucleotides before stop codon (for tagging *infB*; GCGATGTGATCGAAGTATTCGAAATCATC-GAGATCCAACGTACCATTGCT), which is excluded to open the frame. Figure D.2 shows successful fusion of *infB* integrated into *galK* locus with fluorescent protein. Reverse primer is pKD13-to-galK-R from Table F.4. We successfully tagged the *galK*-

integrated *infB*. However, while tagging resulted in detectable and well resolved fluorescence, it also caused a growth defect of about 10% (1.03 h^{-1} and 0.92 h^{-1} for WT and tagged strain, respectively).

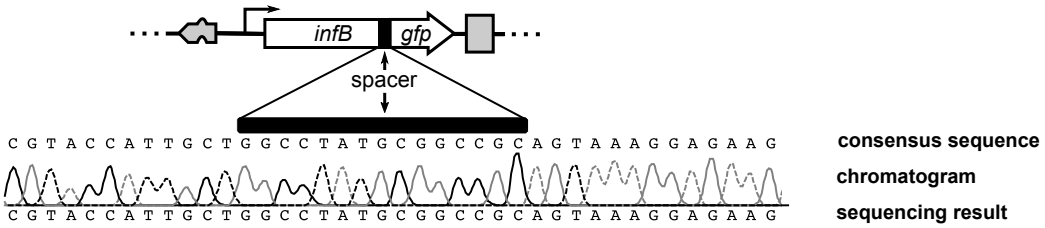

Figure D.2: **Verification of infB-GFP fusion.** Sequencing revealed that *infB* reading frame was correctly opened and extended by the linker and GFPuv4.

D.2 Fluorescence measurements and the induction curve

Tagged proteins become fluorescent only after the GFP chromophore has undergone a maturation process. To correct for this effect we derive a correction factor (following Ref. [Garcia *et al.*, 2011]) that maps the detected of fluorescent proteins f to the concentration of all proteins $p = f + x$, where x is a concentration of proteins with non-matured fluorescent tag. Time derivative of x reads as $\dot{x} = \alpha_p m - \lambda x - \gamma x$, where m, α_p and γ are the steady-state concentration of mRNA transcripts, protein-synthesis rate, and maturation rate, respectively. This yields the steady state solution $x = \alpha_p m/(\lambda + \gamma)$. Concentration of the fluorescent protein f changes in time according to $\dot{f} = -\lambda f + \gamma x$. From this we see that in the steady state $f = x\gamma/\lambda$ and total protein concentration is $p = f(1 + \lambda/\gamma)$. Since fluorescence of the tagged protein F is assumed to be proportional to f, we conclude that $p \propto F(1+\lambda/\gamma)$ or that only a fraction $\gamma/(\lambda + \gamma)$ of tagged proteins is actually fluorescent (which accounts to 80% for $\gamma = 0.25\ h^{-1}$ and $\lambda = 1\ h^{-1}$).

Even in the absence of the fluorescently tagged proteins, bacterial culture exhibits a certain basal level of fluorescence. To correct for this effect, experiments are always conducted in parallel with tagged and non-tagged strain. Autofluorescence changes with the cell density (measured absorbance a being its proxy); it is assumed that

autofluorescence is a continuous function (not necessarily linear) function of cell density. We assume that measured fluorescence F_{m} is given as:

$$F_{\mathrm{m}}(a) = F(f) + F_{\mathrm{bck}} + F_{\mathrm{auto}}(\lambda, a), \tag{D.1}$$

where F_{bck} and $F_{\mathrm{auto}}(\lambda, a)$ are the background fluorescence and autofluorescence, respectively. Background fluorescence can be obtained from the few first initial data points of the given tagged culture, *i.e.*, before the signal from autofluorescence and protein fluorescence is detected. Since translational fusion of a protein and GFP can exhibit decreased enzymatic activity (due to perturbation of folding, active site accessibility, diffusion rate, *etc*), it is not necessarily best to take the non-tagged culture in the same environment as a autofluorescence reference, but it is better to take the non-tagged culture with the same *response*.

In practice this means that for each tagged culture, non-tagged culture with most similar growth rate is found and fluorescence tracks of the latter is used for autofluorescence correction. Once the reference culture is found, data points from an absorbance interval $[a_{\mathrm{min}}, a_{\mathrm{max}}]$ are extracted, binned with $\Delta a = 0.01$, bin-averaged and low-pass filtered (Mathematica function `LowpassFilter`) to reduce noise. Using interpolation with Hermite polynomials, approximative continuous $F_{\mathrm{auto}}(\lambda, a)$ is obtained, which is then subtracted from the measured $F_{\mathrm{M}}(a) - F_{\mathrm{bck}}$ at the given absorbance a. For a steadily growing culture we assume that $F(f) \propto fa$, *i.e.*, the denser the culture more abundant is the protein of interest in the well. Taking $F(f)/a$ and averaging the value should give an estimate for the f, that is average fluorescence per absorbance. However, since such approach involves dividing by absorbance, this can lead to building up of noise effects at low fluorescence signal and low absorbance values. To avoid division, we simply fit a line with zero offset to obtain the value of f. Lastly, obtained estimate is corrected for maturation effect (Sec. D.2) and accompanied by the estimate error and goodnes of fit R^2, which is later used for data selection.

With these corrections at hand, we can adjust the parameters of the model presented in Sec. 7.3. Here, however, adjusted parameters do not have a direct biochemical interpretation. Figure D.3 shows the model; while the data is well

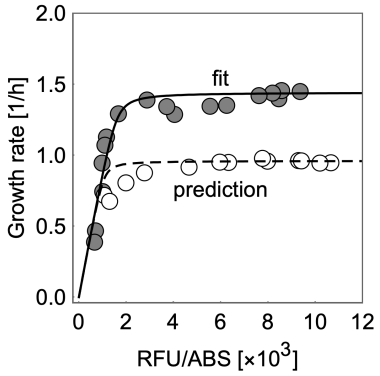

Figure D.3: **Induction curve for GFP-tagged initiation factor.** Gray dots correspond to fluorescent measurements for titratable strain grown in M9 minimal medium with glucose, casamino acids, and nucleotides. Fitted model is used to predict a induction curve for titration curve in M9 minimal medium with glucose and casamino acids that supports lower growth rate.

described by the model, its rate $\zeta_0 = 2.2 \times 10^{-3}$ ABS/(s×RFU), which requires a conversion factor, cannot be interpreted directly. However, with this model at hand, we can predict a dose-response curve in another medium (Fig. D.3).

E Supplementary figures

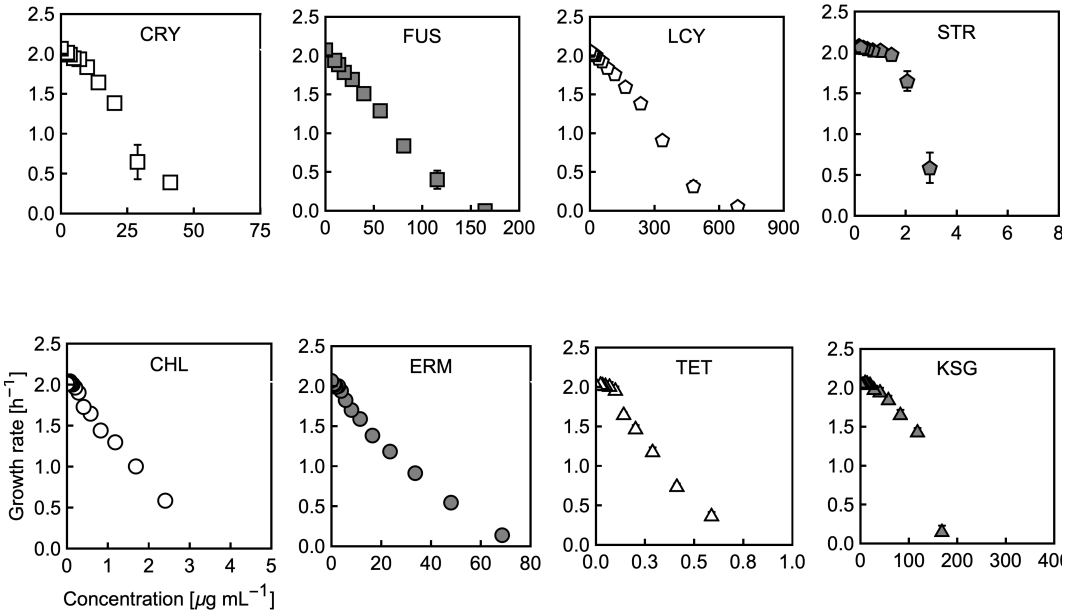

Figure E.1: **Dose-response curves for all antibiotics.** Where error bars are invisible, they are smaller than the symbols. Each dose-response curve was measured $n = 7$ times and non-zero growth rates were used in the calculation of the mean and standard deviation shown in the plot.

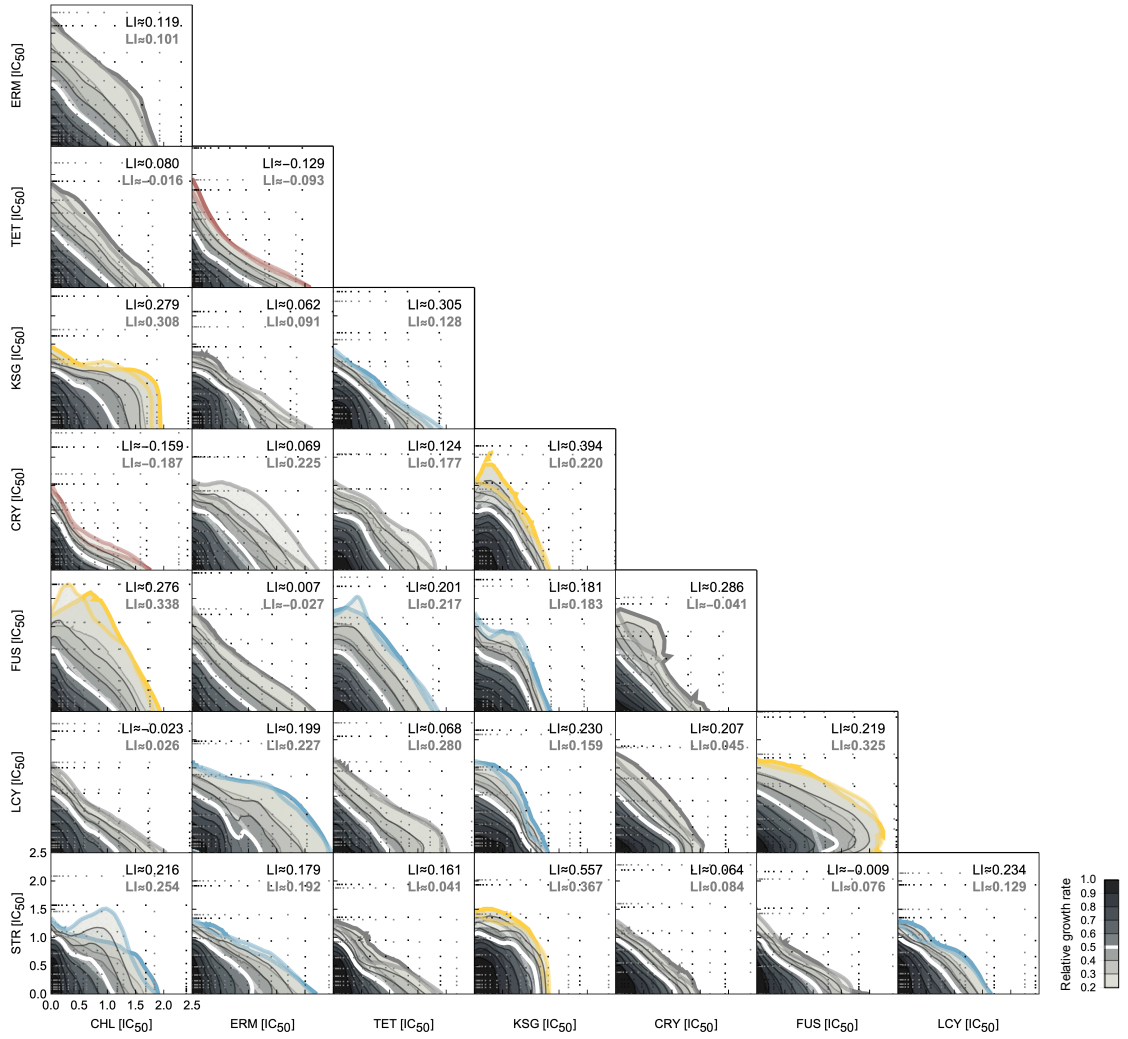

Figure E.2: **All dose-response surfaces.** Duplicates of dose-response surfaces for all 28 antibiotic pairs. Due to small, but systematic variability in concentrations between replicates done on different days, we rescaled concentration axes relative to the IC_{50}. Dose-response surfaces were smoothed using LOESS (Methods). Black and gray dots denote measured points from different experiments. Isoboles from duplicates are in high agreement; small deviations are caused by occasional outliers that skew the isoboles. LI scores are shown for both replicates; gray score corresponds to the slightly transparent surface.

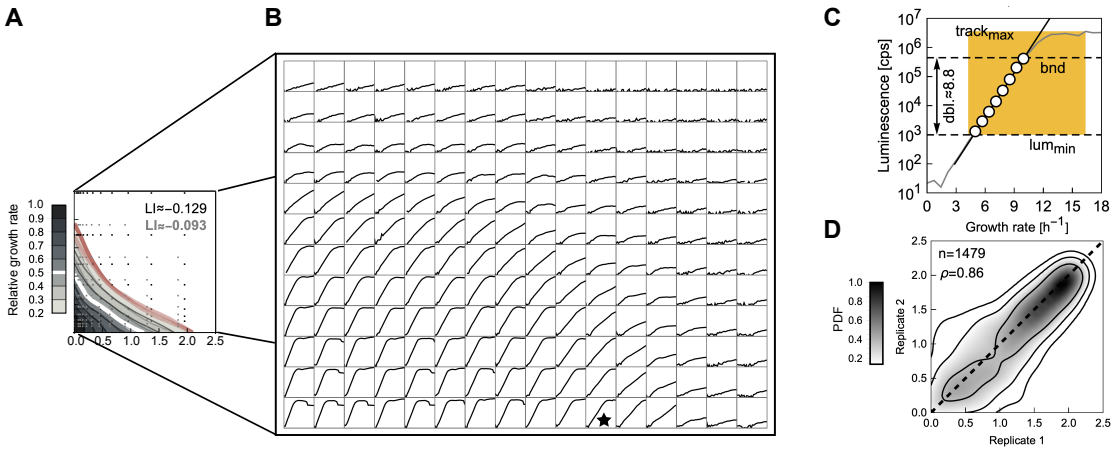

Figure E.3: **Examples of growth curves and fitting procedure. (A)** An example of a dose response surface. **(B)** An example of growth curves over a 12×16 grid. Note, that here the concentrations geometrically change between wells, *i.e.*, the ratio between concentrations in neighboring wells is fixed. Star denotes the curve shown in the next panel. **(C)** Exemplary growth curve from (B) and details of the fitting procedure. The growth rate is determined by fitting a line in the regime of exponential growth. The determination of this regime in the growth curve is carried out automatically; procedure: (i) check if the maximum value of luminescence is above the lower bound of the fitting interval $\text{lum}_{\text{min}} = 10^3$ cps and take points before the maximum, (ii) take points that are the latest to rise over lum_{min}, (iii) determine the upper limit (bnd) of the fitting interval to be either ten-fold above the lum_{min} (guaranteeing $\log_2 10 \approx 3.3$ doublings of a fitting interval) or eight-times less than the track maximum (three doublings away from saturation) and (iv) fit a line to the log-transformed values of the luminescence signal if there are at least three data points. If lum_{min} is not exceeded, the well is counted as having no growth; if any of the other criteria are not fulfilled, growth is characterized as undetermined. For strains with titratable factors, we slightly widened the fitting interval by decreasing the lum_{min} to 500 cps, and the number of doublings from saturation to ≈ 2.6. **(D)** Reproducibility of absolute growth rate measurements between replicates. The smooth kernel representation of replicate measurements (Mathematica function `SmoothKernelDistribution`), performed on different days and different plate arrangements, demonstrates a good agreement overall. Only non-zero growth rates of sufficient quality ($R^2 > 0.5$ and relative error < 0.5) are included, resulting in $n = 1479$ replicated growth rate measurements.

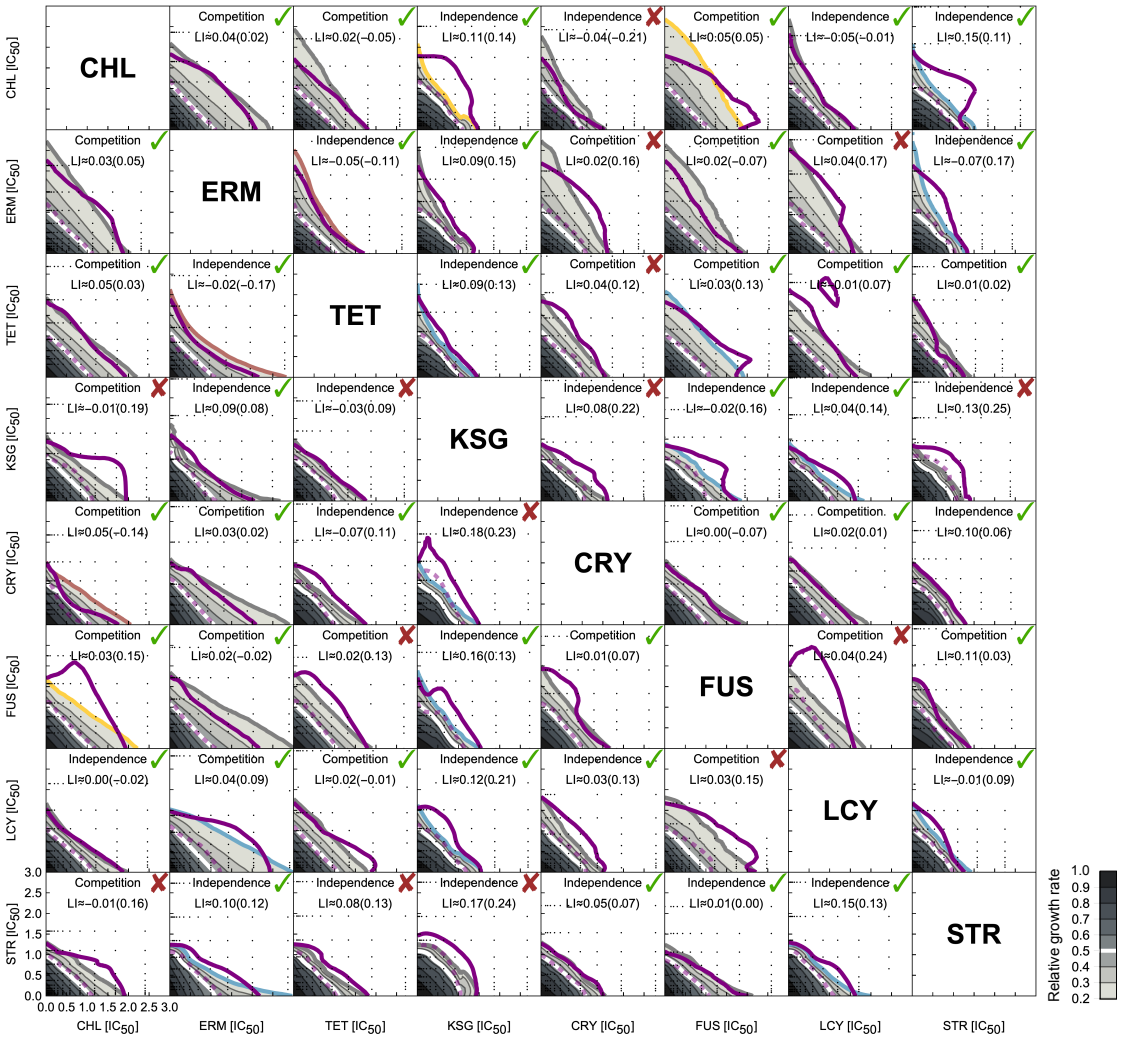

Figure E.4: **All predictions of a biophysical model for replicated measurements.** Predicted surface is shown in full; overlaid thick and dashed purple isobole denote 20% and 50% isobole, respectively, of the measured surface. Each prediction is evaluated for goodness of prediction as described in Methods. Checkmark and cross denote a match and mismatch, respectively. Inset text denotes the best-matching binding scheme. The bootstrapped-LI scores for predicted and measured (in parentheses) surfaces are shown.

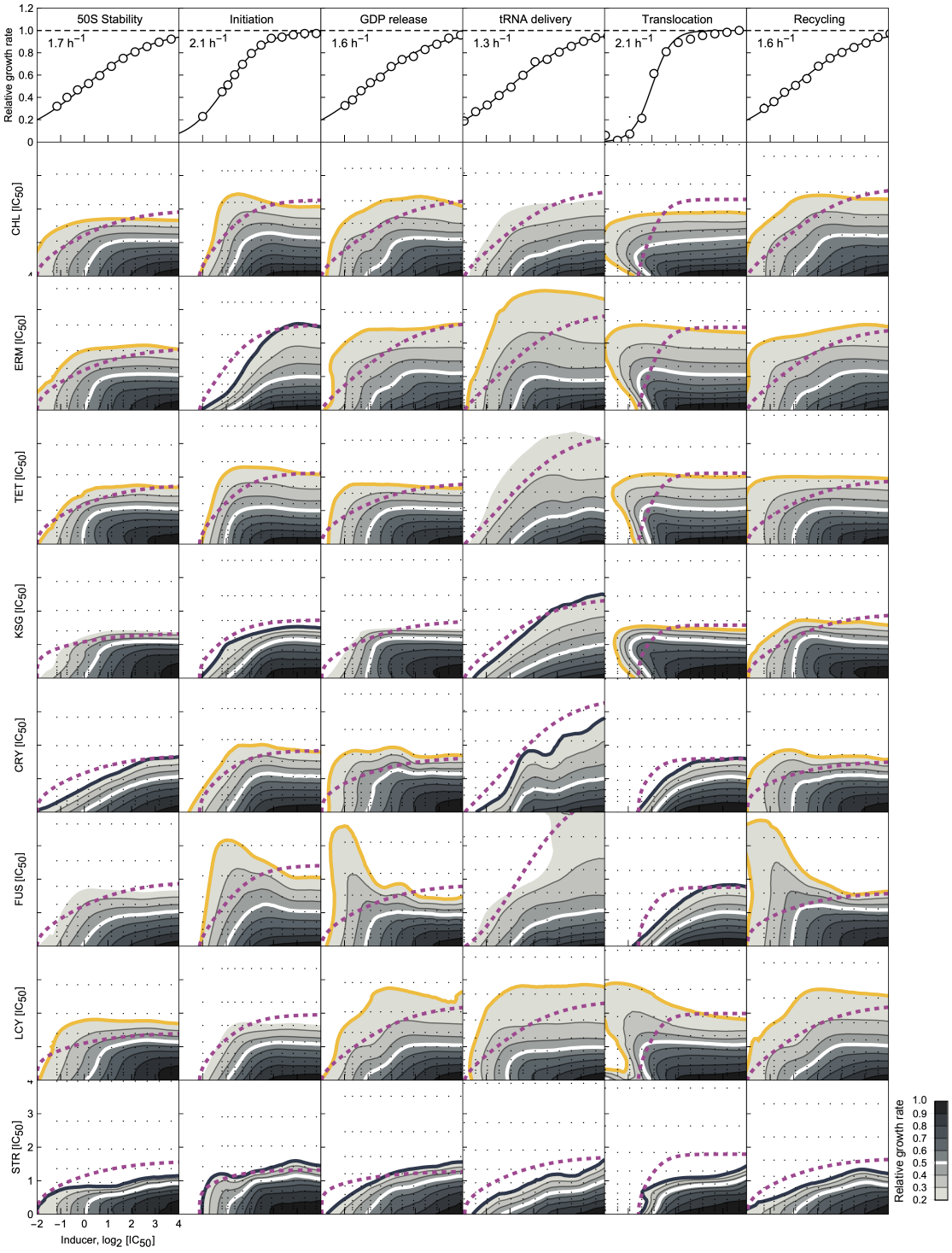

Figure E.5: **Dose-response curves and surfaces for all bottleneck-antibiotic pairs.** Top row: bottleneck dose-response curves. Bottom: Surfaces were smoothed using LOESS (Methods). Note the different characters of deviations from independence.

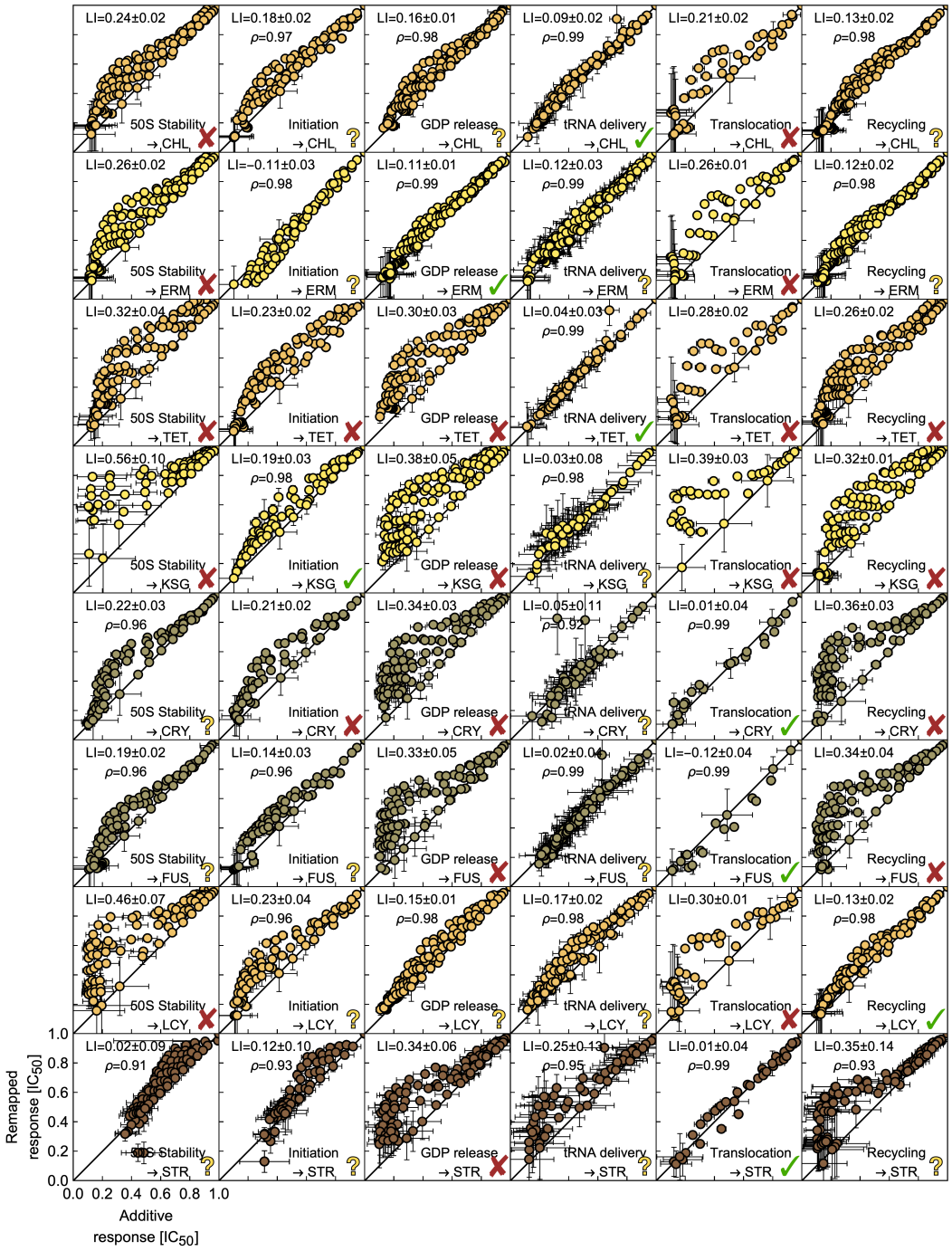

Figure E.6: **Scatter plots of growth rates expected for additivity and obtained by self-remapping.** Error bars correspond to the standard deviation of $n = 100$ bootstrap repetitions. The distribution of LI was compared statistically to the boundaries of the additive interval. Red crosses denote that LI fell outside the additive interval. Green checkmarks and yellow question-marks denote that LI did not fall outside of the additivity interval; in these cases, the rounded correlation ρ is reported. For a given antibiotic, the bottleneck with the highest correlation with the additive expectation is marked with a checkmark and suggests the equivalency of antibiotic and genetic perturbation.

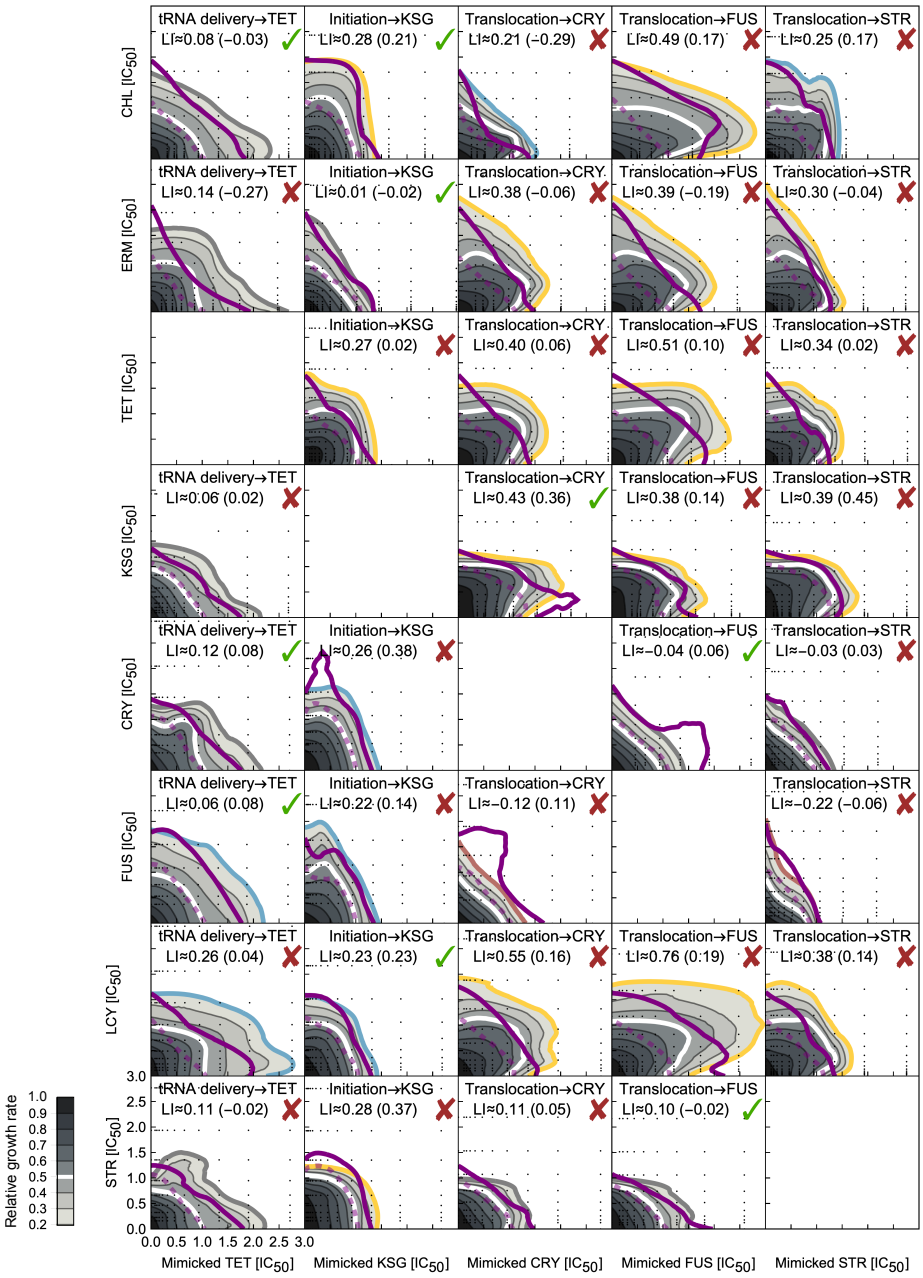

Figure E.7: **All predicted surfaces as obtained by remapping.** The predicted surfaces obtained by remapping are shown in full; overlaid thick and dashed purple contour denote 20% and 50% isobole, respectively, of the measured surface. Each prediction is evaluated for the goodness of prediction as described in Chapter C. Checkmark and cross denote a match and mismatch, respectively.

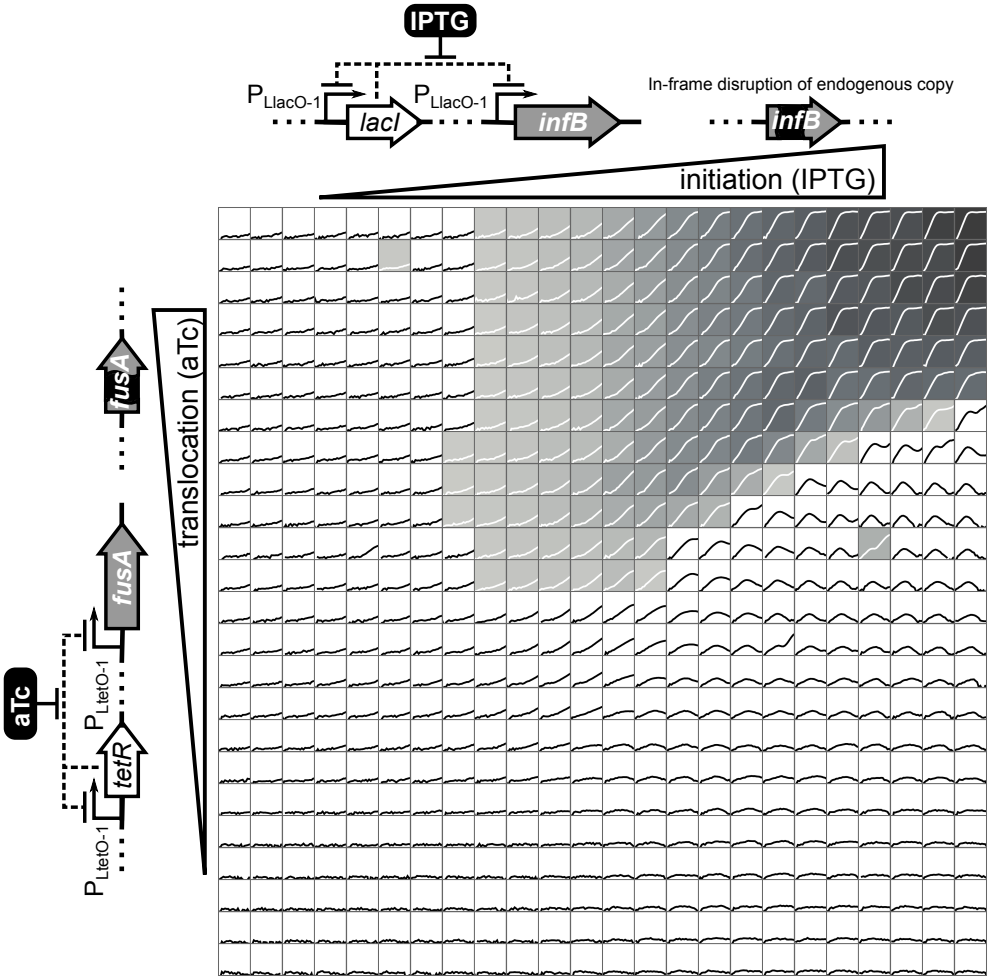

Figure E.8: **Double titration platform and growth curves.** Schematics represent the genetic elements of double titration control: negatively auto-repressed transcription factors *lacI* and *tetR* that control the expression of initiation factor 2 (*infB*) and elongation factor G (*fusA*), respectively; expression is dependent on the shown inducers (IPTG and aTc). The grid shows the growth curves for the response surface in Fig. 6.1. Different shades of gray show the growth rate. Only fits of good quality and with growth rates above 0.199 are included.

F Supplementary tables

Antibiotic	Response parameter α
CHL	1.04 ± 0.04
ERM	1.06 ± 0.14
TET	0.73 ± 0.09
KSG	0.23 ± 0.09
CRY	0.59 ± 0.04
FUS	0.70 ± 0.09
LCY	0.64 ± 0.06
STR	0.46 ± 0.07

Table F.1: **Typical response parameters for used translation inhibitors.** Response parameter values and errors were obtained in fitting to dose-response curves in Fig. E.1.

Type	Chemical name	Catalog numbers	Supplier
Antibiotics	Kanamycin sulfate	K4000-5G	Sigma-Aldrich
	Tetracycline hydrate	268054-25G	Sigma-Aldrich
	Streptomycin sulfate	S6501-25G	Sigma-Aldrich
	Lincomycin hydrocloride	62143-1G/5G	Sigma-Aldrich
	Fusidic acid sodium salt	F0881-1G/5G	Sigma-Aldrich
	Capreomycin sulfate	C4142-1G	Sigma-Aldrich
	Kasugamycin hydrochloride	K4013-10G	Sigma-Aldrich
	Erythromycin hydrate	856193-25G	Sigma-Aldrich
	Chloramphenicol	C0378-25G	Sigma-Aldrich
	Lamotrigine	2652	AvaChem
	Trimethoprim	92131-5G	Sigma-Aldrich
	Spectinomycin sulfate	PHR1441-1H	Fluka
	Ampicillin sodium salt	A9518-5G	Sigma-Aldrich
Inducers	IPTG	2316.4	Roth
	Anhydrotetracycline	631310	Takara
	Anhydrotetracycline hydrochloride	37919-100MG-R	Sigma-Aldrich
Media	LB	L3022	Sigma-Aldrich

Table F.2: **Chemicals used in this study.** Table contains chemical names and purpose categories, catalog codes, and vendor information.

Table F.3: Oligonucleotides used in the construction of tagging plasmids.

Primer name	**Sequence**	**Template**	**Additional comment**
pKD13-HiBit-F	GCTA GCATCCTCACGATAATATCCGGGTAGGCGCAAT CACTTTCG	pKD13	amplifies the backbone
pKD13-HiBit-R	GCTCACAGAACCACCACCAGAACCACCACC CGCGCACATTTCCCCGAAAAGTGCCACCTG	pKD13	amplifies the backbone
UTRgalK-F	AATTCATTAAAGAGGAGAAAGGTACC ATGAGTCTGAAAGAAAAAACACAATCTCTGTTT	genome	amplifies the galK
UTRgalK-R	CCGGATATTATCGTGAGGATGCTAGC TCAGCACTGTCCTGCTCCTTGT	genome	amplifies the galK
HiBit+xhoi-rrnB-F	GGTGGTGGTTCTGGTGGTGGTTCTGTGAGCGGCTGGCGGCTG TTCAAGAAGATTAGCTAACTCGAG GGCCCCCCGATGGTAGTGTGGGGTCTCCCC	pKD13	amplifies the TrrnB terminator and adds flanking restriction sites
HiBit+xhoi-rrnB-R	CGCACGGTGTTAGATATTTATCCTCGAG GGCACTGGCCACGCAAAAAGGCCATCCGTC	pKD13	amplifies the TrrnB terminator and adds flanking restriction sites
Plam+RSs+utr-F	CTCGAGGATAAATATCTAACACCGTGCGTGTTGACTATTTTAC CTCTGGCGGTGATAATGGTTGCATGTACTAAATTCATTAAA-GAGGAGAAAGGTACC	/	introduces the λ-P_R promoter upstream of *galK*

Continued on next page

Table F.3 – continued from previous page

Primer name	Sequence	Template	Additional comment
Plam+RSs+utr-R	GGTACCTTTCTCCTCTTTAATGAATTTAGTACATGCAACCAT TATCACCGCCAGAGGTAAAATAGTCAACACGCACGGTGT- TAGATATTTATCCTC GAG	/	introduces the λ-P_R promoter upstream of *galK*

Table F.4: Oligonucleotides used in the construction of factor-titration strains.

Primer name	**Sequence**	**Template**	**Additional comment**
oEcoRI-infB-F	CCG **GAATTC** ATTAAAGAGGAGAAAGGTACC GGAACAGCATGACAGATGTAACG	genome	for subcloning *infB* into pZA12-GFP (digested with EcoRI and HindIII)
oHindIII-infB-R	CGC **AAGCTT** CCTTAAGCAATGGTACGTTGG	genome	for subcloning infB into pZA12-GFP (digested with EcoRI and HindIII)
fullpKD13-BamHI	CGC **GGATCC** CC GGAATTAATTCTCATGT	pKD13	Used in full-plasmid PCR for effective double digestion of pKD13 with SalI+BamHI
fullpKD13-SalI-R	ACGC **GTCGAC** CTGCAGTTCGAAGT	pKD13	Used in full-plasmid PCR for effective double digestion of pKD13 with SalI+BamHI
oSalI-Plac-F	ACGC **GTCGAC** TCGAGAATTGTGAGCGGATAACA	pZA12-infB	Amplification of Plac-infB-TrrnB fragment for subcloning into pKD13
oBamHI-infB-R	CGC **GGATCC** TCTAGGGCGGCGGATTTG	pZA12-infB	Amplification of Plac-infB-TrrnB fragment for subcloning into pKD13

Continued on next page

Table F.4 – continued from previous page

Primer name	Sequence	Template	Additional comment
del-infB-F	GCTGGTTCGGTGACGAAGCGTAATAAACTGTAGCAGGAA GGAACAGCATG ATTCCGGGGATCCGTCGACC	pKD13	deletion of infB
del-infB-R	GCCTTATCCCGCATGGAACCCTAAAAACCTTAAGCAATGGT ACGTTGGAT TGTAGGCTGGAGCTGCTTCG	pKD13	deletion of infB
infB-locF	ACTGTAGCAGGAAGGAACAGC	genome	verification of infB deletion
infB-locR	TCCCGCATGGAACCCTAAAA	genome	verification of infB deletion
fullpKD13-KpnI	GG **GGTACC** TTTCTCCTCTTTAATGAATT	pKD13-Plac-GFP	Full plasmid PCR to introduce SpeI/KpnI into pKD13-Plac-x
fullpKD13-SpeI	GG **ACTAGT** TTAATTAGCTGAGTCTAGAGGCATCA	pKD13-Plac-GFP	Full plasmid PCR to introduce SpeI/KpnI into pKD13-Plac-x
oKpnI-fusA-F	GG **GGTACC** ATGGCTCGTACAACACCCATC	genome	for subcloning into PCR of pKD13-Plac-GFP with introduced additional SpeI (digested with SpeI and KpnI)
oSpeI-fusA-R	G **ACTAGT** TTATTTACCACGGGCTTCAATTACG	genome	for subcloning into PCR of pKD13-Plac-GFP with introduced additional SpeI (digested with SpeI and KpnI)
del-fusA-F	CTTTGGGCTACTTAAATTGAACGCCTAAAAGATAAACGA GGAAACAAATG ATTCCGGGGATCCGTCGACC	pKD13	deletion of fusA

Continued on next page

Table F.4 – continued from previous page

Primer name	Sequence	Template	Additional comment
del-fusA-R	GCACGGGACTTTGGTATTAACCCTTAGGCTTATTTACCA CGGGCTTCAAT TGTAGGCTGGAGCTGCTTCG	pKD13	deletion of fusA
fusA-locF	GCGCTTCCAGTAAGCAGC	genome	verification of fusA deletion
fusA-locR	TAGTGACGGGTCGGGGTGTC	genome	verification of fusA deletion
Ptet-fusA	TCGAACTGCAGGTCGACTCGAGTCCCTATCAGTGA TAGAGATTGACATCCCTATCAGTGATAGAGATACT GAGCACATCAGCAGGACGCACTGACC	pKD13-Plac-fusA	introduces the PLtetO-1 promoter when combined with intS reverse integration primer.
oKpnI-frr-F	GG **GGTACC** GTGATTAGCGATATCAGAAAAGATGC	genome	for subcloning into pKD13-Plac-GFP (digested with SpeI and KpnI)
oSpeI-frr-R	G **ACTAGT** AAGAAATCAGAACTGCATCAGTTC	genome	for subcloning into pKD13-Plac-GFP (digested with SpeI and KpnI)
del-frr-F	GTGTGACTGTCTGGTCTGACTGAGACAAGTTTTCAAG GATTCGTAACGTG ATTCCGGGGATCCGTCGACC	pKD13	deletion of frr
del-frr-R	ACTGAGCGGCGTTTTTGTCGTTCAAGAAATCAGAACTG CATCAGTTCTGC TGTAGGCTGGAGCTGCTTCG	pKD13	deletion of frr
frr-locF	CTTAGCACACTTCCACTGTGTG	genome	verification of frr deletion
frr-locR	TTGAGACAGAATAAAAAGCAAAACGCC	genome	verification of frr deletion

Continued on next page

Table F.4 – continued from previous page

Primer name	Sequence	Template	Additional comment
oAvrII-der-F	AGTC **CCTAGG** ATGGTACCTGTGGTCGCGCTTG	genome	for subcloning into pKD13-Plac-tufA (digested with SpeI and AvrII)
oSpeI-der-R	G **ACTAGT** TTATTTATTTTTCTTGATGTGCTTCATCAG	genome	for subcloning into pKD13-Plac-tufA (digested with SpeI and AvrII)
del-der-F	AATATAGCGTGCGTTGTCTGATGATTTATAAAAATGAG GCTTTAAACATG ATTCCGGGGATCCGTCGACC	pKD13	deletion of der
del-der-R	GGAATGGCAGATAAAATACTTACGGATAATTATTTATT TTTCTTGATGTG TGTAGGCTGGAGCTGCTTCG	pKD13	deletion of der
der-locF	GCAAAAGACGGAACCGTGTAC	genome	verification of der deletion
der-locR	TCAAGCACATGCTGACATTGTG	genome	verification of der deletion
fullpKD13-AvrII	AGTC **CCTAGG** TTTCTCCTCTTTAATGAATTCGGTCA	pKD13-Plac-fusA	Full plasmid PCR to introduce SpeI/KpnI into pKD13-Plac-x
fullpKD13-SpeI	GG **ACTAGT** TTAATTAGCTGAGTCTAGAGGC	pKD13-Plac-fusA	Full plasmid PCR to introduce SpeI/KpnI into pKD13-Plac-x
oAvrII-tufA-F	AGTC **CCTAGG** ATG TCTAAAGAAAAATTTGAA CGTACAAAACCG	genome	for subcloning into pKD13-Plac-tufA (digested with SpeI and AvrII)

Continued on next page

Table F.4 – continued from previous page

Primer name	Sequence	Template	Additional comment
oSpeI-tufA-R	GG **ACTAGT** TTAGCCCAGAACTTTAGCAACA	genome	for subcloning into pKD13-Plac-tufA (digested with SpeI and AvrII)
tufA-locF	CGTTGCTCAGGCCGTAATTG	genome	verification of tufA deletion
tufA-locR	TTTATTCGTTCTGACAGTACGAATAAG	genome	verification of tufA deletion
tufB-locF	CATTCAACAAGTCGGGCATGTTG	genome	verification of tufB deletion
tufB-locR	GAAAATCACTGATGAGCCAGGTTC	genome	verification of tufB deletion
oKpnI-tsf-F	GG **GGTACC** ATGGCTGAAATTACCGCATCC	genome	for subcloning into pKD13-Plac-fusA (digested with SpeI and KpnI)
oSpeI-tsf-R	G **ACTAGT** TTAAGACTGCTTGGACATCGCA	genome	for subcloning into pKD13-Plac-fusA (digested with SpeI and KpnI)
del-tsf-F	TCTGTGCGGTTTAATGCCGGGCAGATCACATCTCCGAGG ATTTTAGAATG ATTCCGGGGATCCGTCGACC	pKD13	deletion of tsf
del-tsf-R	GCCGCCCTCAGGCGGCTCCTTTTTGATAATTAAGACTG CTTGGACATCGC TGTAGGCTGGAGCTGCTTCG	pKD13	deletion of tsf
tsf-locF	AGACCAGGTAGTACACGTTTGG	genome	verification of tsf deletion
tsf-locR	GACATTGTACGTCGCTTTTCAG	genome	verification of tsf deletion

Continued on next page

Table F.4 – continued from previous page

Primer name	Sequence	Template	Additional comment
oKpnI-fusA-F	GG **GGTACC** ATGAAACCAGTAACGTTATACGATGTCG	genome	for subcloning into pKD13-Plac-fusA (digested with SpeI and KpnI)
oSpeI-fusA-R	G **ACTAGT** TCACTGCCCGCTTTCCAGTC	genome	for subcloning into pKD13-Plac-fusA (digested with SpeI and KpnI)
oKpnI-tetR-F	GG **GGTACC** ATGTCCAGATTAGATA AAAGTAAAGTGATTAAC	pAS014	pAS014 is essentially pZS12-tetR-Boom (boom stands for degradation tag). Unpublished data, Guet group. Used to subclone into pZA21.
oHindIII-tetR-R	CCC **AAGCTT** AGACCCACTTTCACATTTAAGTTG	pAS014	pAS014 is essentially pZS12-tetR-Boom (boom stands for degradation tag). Unpublished data, Guet group. Used to subclone into pZA21.
pKD13-to-galK-F	GTTTGCGCGCAGTCAGCGATATCCATTTTCGCGAATC CGGAGTGTAAGAA GTGTAGGCTGGAGCTGCTTC	pKD13-Py-X	For integration of Py driven gene X together with FRT flanked kanR and TrrnB into galK

Continued on next page

Table F.4 – continued from previous page

Primer name	Sequence	Template	Additional comment
pKD13-to-galK-R	ACCATCGGGTGCCAGTGCGGGAGTTTCGTTCAGCACT GTC-CTGCTCCTTG CTGTCAAACATGAGAATTAA	pKD13-Py-X	For integration of Py driven gene X together with FRT flanked kanR and TrrnB into galK
galK-ver-F	CCTACTCTATGGGCTGGCAC	genome	PCR check and sequencing of galK integration locus
galK-ver-R	GGAAAGTAAAGTCGCACCCC	genome	PCR check and sequencing of galK integration locus
pKD13-to-intS-F	CCGTAGATTTACAGTTCGTCATGGTTCGCTTCAGA TCGTTGACAGCCGCA GTGTAGGCTGGAGCTGCTTC	pKD13-Py-X	For integration of Py driven gene X together with FRT flanked kanR and TrrnB into intS
pKD13-to-intS-R	ATAGTTGTTAAGGTCGCTCACTCCACCTTCTCATC AAGCCAGTCCGCCCA CTGTCAAACATGAGAATTAA	pKD13-Py-X	For integration of Py driven gene X together with FRT flanked kanR and TrrnB into intS
intS-ver-F	GTACTTACCCCGCACTCCAT	genome	PCR check and sequencing of intS integration locus
intS-ver-R	TGTTCAGCACACCAATAGAGG	genome	PCR check and sequencing of intS integration locus
pKD13-to-xylB-F	AGATATATAGATGTGAATTATCCCCCACCCGGTCAGG CAGGGGATAACGT GTGTAGGCTGGAGCTGCTTC	pKD13-Py-X	For integration of Py driven gene X together with FRT flanked kanR and TrrnB into xylB

Continued on next page

Table F.4 – continued from previous page

Primer name	Sequence	Template	Additional comment
pKD13-to-xylB-R	GGCCCGGTTATCGGTAGCGATACCGGGCATTTTT TTAAGGAACGATCGAT CTGTCAAACATGAGAATTAA	pKD13-Py-X	For integration of Py driven gene X together with FRT flanked kanR and TrrnB into xylB
xylB-ver-F	CCATATCTACCAGCGATACATTACG	genome	PCR check and sequencing of xylB integration locus
xylB-ver-R	CAGCAAATCCTGAAAGGCCAAATG	genome	PCR check and sequencing of xylB integration locus
pKD13-to-ycaCD-F	TGGGTGAAAATACGCGATATCCCAGCGGCGGTATTA TCGATTTATATTAC GTGTAGGCTGGAGCTGCTTC	pKD13-Py-X	For integration of Py driven gene X together with FRT flanked kanR and TrrnB into ycaCD
pKD13-to-ycaCD-R	ACGCGATGCATTGCTCTGAAAGCATAGACGGGAA ATATGAGTTTGCTGTG CTGTCAAACATGAGAATTAA	pKD13-Py-X	For integration of Py driven gene X together with FRT flanked kanR and TrrnB into ycaCD
ycaCD-ver-F	GCCAGAGTCAACAAAAGCAGGC	genome	PCR check and sequencing of ycaCD integration locus
ycaCD-ver-R	GCCAGCACGTTATTTTTAAACTTATC	genome	PCR check and sequencing of ycaCD integration locus

Continued on next page

Table F.4 – continued from previous page

Primer name	Sequence	Template	Additional comment
promKan	CAACCTTACCAGAGGGCG	/	binds into the vicinity of kanR promoter and initiates sequencing towards the synthetic promoter and UTR region of pKD13-subcloned genes
TrrnB-rev	AGGATGCGTCATCGCCATTAATTC	/	binds downstream of TrrnB in reverse direction. Sequencing of 3′ region of pKD13-subcloned genes.
ASKA-f	CAACAGTTGCCTAAGAAACCAT	ASKA plasmids	binds upstream of the promoter and allows sequencing into the subcloned gene
ASKA-r	TGAGGTCATTACTGGATCTATCAAC	ASKA plasmids	binds downstream of the gene in reverse direction; allows sequencing of the subcloned genes

Bibliography

[Acinas *et al.*, 2004] S. Acinas *et al.*, "Divergence and Redundancy of 16S rRNA Sequences in Genomes with Multiple *rrn* Operons," *J. Bacteriol.*, 186(9):2629–2635, 2004.

[Allen and Waclaw, 2016] R. Allen and B. Waclaw, "Antibiotic resistance: a physicist's view," *Phys. Biol.*, 13(045001), 2016.

[Aminov, 2010] R. Aminov, "A brief history of the antibiotic era: lessons learned and challenges for the future," *Front. Microbiol.*, 1(134):1–7, 2010.

[Andersen *et al.*, 2006] K. Andersen *et al.*, "Honoring Ole Maaløe," *Microbe*, 1:210, 2006.

[Andrianantoandro *et al.*, 2006] E. Andrianantoandro *et al.*, "Synthetic biology: new engineering rules for an emerging discipline," *Mol. Syst. Biol.*, 2(2006), 2006.

[Arkin and Fletcher, 2006] A. Arkin and D. Fletcher, "Fast, cheap and somewhat in control," *Genome Biology*, 7(114), 2006.

[Arnold and Reilly, 1999] R. Arnold and J. Reilly, "Observation of *Escherichia coli* ribosomal proteins and their posttranslational modifications by mass spectrometry," *Anal. Biochem.*, 269(1):105–112, 1999.

[Artsimovitch *et al.*, 2004] I. Artsimovitch *et al.*, "Structural Basis for Transcription Regulation by Alarmone ppGpp," *Cell*, 117:299–310, 2004.

[Auerbach *et al.*, 2010] T. Auerbach *et al.*, "The structure of ribosome-lankacidin complex reveals ribosomal sites for synergistic antibiotics," *Proc. Nat. Acad. Sci. USA*, 107(5):1983–1988, 2010.

[Avcilar-Kucukgoze *et al.*, 2016] I. Avcilar-Kucukgoze *et al.*, "Discharging tRNAs: a tug of war between translation and detoxification in *Escherichia coli*," *Nucleic Acids Res*, 44(17):8324–8334, 2016.

[Baba *et al.*, 2006] T. Baba, T. Ara, M. Hasegawa, Y. Takai, Y. Okumura, M. Baba, K. Datsenko, M. Tomita, B. Wanner, and H. Mori, "Construction of *Escherichia coli* K-12 in-frame, single-gene knockout mutants: the Keio collection," *Mol. Syst. Biol.*, 2, 2006.

[Bandow *et al.*, 2003] J. Bandow, H. Brätz, L. Leichert, H. Labischinski, and M. Hecker, "Proteomic Approach to Understanding Antibiotic Action," *Antimicrob Agents Chemother*, 47(3), 2003.

[Barry, 2004] J. Barry, *The great influenza : the epic story of the deadliest plague in history*, Penguin books, 2004.

[Bartholomäus *et al.*, 2016] A. Bartholomäus, I. Fedyunin, P. Feist, C. Sin, G. Zhang, A. Valleriani, and Z. Ignatova, "Bacteria differently regulate mRNA abundance to specifically respond to various stresses," *Phil. Trans. R. Soc.*, 374, 2016.

[Baym *et al.*, 2016] M. Baym, L. Stone, and R. Kishony, "Multidrug evolutionary strategies to reverse antibiotic resistance," *Science*, 351, 2016.

[Belousoff *et al.*, 2011] M. Belousoff *et al.*, "Crystal structure of the synergistic antibiotic pair, lankamycin and lankacidin, in complex with the large ribosomal subunit," *Proc. Nat. Acad. Sci. USA*, 107(7), 2011.

[Ben-Bassat *et al.*, 1986] A. Ben-Bassat *et al.*, "Processing of the Initiation Methionine from Proteins: Properties of the *Escherichia coli* Methionine Aminopeptidase and Its Gene Structure," *J. Bacteriol.*, 169(2):751–757, 1986.

[Bennet and Maaløe, 1974] P. Bennet and O. Maaløe, "The Effects of Fusidic Acid on Growth, Ribosome Synthesis and RNA Metabolism in *Escherichia coli*," *J. Mol. Biol.*, 90, 1974.

[Benthin *et al.*, 1991] S. Benthin, J. Nielsen, and J. Villadsen, "A simple and reliable method for the determination of cellular RNA content," *Biotechnol. Tech.*, 5(1):39–42, 1991.

[Bergmiller, 2017] T. Bergmiller, "Biased partitioning of the multidrug efflux pump AcrAB-TolC underlies long-lived phenotypic heterogeneity," *Science*, 356:311–315, 2017.

[Bingel-Erlenmeyer *et al.*, 2008] R. Bingel-Erlenmeyer *et al.*, "A peptide deformylase–ribosome complex reveals mechanism of nascent chain processing," *Nature*, 452:108–111, 2008.

[Bjarnason *et al.*, 2003] J. Bjarnason *et al.*, "Genomic Profiling of Iron-Responsive Genes in *Salmonella enterica* Serovar Typhimurium by High-Throughput Screening of a Random Promoter Library," *J. Bacteriol.*, 185(16):4973–4982, 2003.

[Blanchard *et al.*, 2010] S. Blanchard, B. Cooperman, and D. Wilson, "Probing Translation with Small-Molecule Inhibitors," *Chem. Biol.*, 17(6), 2010.

[Bliss, 1939] C. Bliss, "The toxicity of poisons applied jointly," *Ann. Appl. Biol.*, 26:585, 1939.

[Blount, 2015] Z. Blount, "The Natural History of Model Organisms: The unexhausted potential of *E. coli*," *eLife*, e05826, 2015.

[Blumenthal *et al.*, 1976] R. Blumenthal, P. Lemaux, F. Neidhardt, and P. Dennis, "The Effects of the *relA* Gene on the Synthesis of Aminoacyl-tRNA Synthetases and Other Transcription and Translation Proteins in *Escherichia coli* B," *Molec. gen. Genet.*, 149, 1976.

[Bollenbach, 2015] T. Bollenbach, "Antimicrobial interactions: mechanisms and implications for drug discovery and resistance evolution," *Curr Opin Microbiol*, 27:1, 2015.

[Bollenbach and Kishony, 2011] T. Bollenbach and R. Kishony, "Resolution of Gene

Regulatory Conflicts Caused by Combinations of Antibiotics," *Mol. Cell*, 42:413, 2011.

[Bollenbach *et al.*, 2009] T. Bollenbach, S. Quan, R. Chait, and R. Kishony, "Nonoptimal Microbial Response to Antibiotics Underlies Suppressive Drug Interactions," *Cell*, 139:707, 2009.

[Braun *et al.*, 2001] V. Braun *et al.*, "Outer Membrane Channels and Active Transporters for the Uptake of Antibiotics," *J. Infect.*, 138(Supp. 1):S12–S16, 2001.

[Brauner *et al.*, 2016] A. Brauner *et al.*, "Distinguishing between resistance, tolerance and persistence to antibiotic treatment," *Nat. Rev. Microbiol.*, 14:320–330, 2016.

[Bremer and Churchward, 1977] H. Bremer and G. Churchward, "An Examination of the Cooper-Helmstetter Theory of DNA Replication in Bacteria and its Underlying Assumptions," *J. theor. Biol*, 69:645–654, 1977.

[Bremer and Dennis, 1996] H. Bremer and P. Dennis, "Modulation of Chemical Composition and Other Parameters of the Cell by Growth Rate," In F. Neidhardt, editor, *Escherichia coli and Salmonella*. ASM Press, Washington DC, 1996.

[Brochado *et al.*, 2018] A. Brochado *et al.*, "Species-specific activity of antibacterial drug combinations," *Nature*, 559, 2018.

[Brown, 1962] G. Brown, "The Biosynthesis of Folic Acid," *J. Biol. Chem.*, 237(2):536–540, 1962.

[Brown *et al.*, 1990] M. Brown *et al.*, "Influence of growth rate on susceptibility to antimicrobial agents: modification of the cell envelope and batch and continuous culture studies.," *Antimicrob. Agents Chemother.*, 34:1623–1628, 1990.

[Bunner *et al.*, 2010] A. Bunner *et al.*, "The effect of ribosome assembly cofactors on in vitro 30S subunit reconstitution," *J. Mol. Biol.*, 398:1–7, 2010.

[Cashel and Potrykus, 2001] M. Cashel and K. Potrykus, *Brenner's Encyclopedia of Genetics: Second Edition*, chapter Stringent Response, pages 573–575, Elsevier, 2001.

[Cassels *et al.*, 1995] R. Cassels, B. Oliva, and D. Knowles, "Occurrence of the Regulatory Nucleotides ppGpp and pppGpp following Induction of the Stringent Response in *Staphylococci*," *J. Bacteriol.*, 177:5161–5165, 1995.

[Cayley *et al.*, 1991] S. Cayley *et al.*, "Characterization of the cytoplasm of *Escherichia coli* K-12 as a function of external osmolarity.," *J. Mol. Biol.*, 222:281–300, 1991.

[Chadani *et al.*, 2011] Y. Chadani, K. Ono, K. Kutsukake, and T. Abo, "*Escherichia coli* YaeJ protein mediates a novel ribosome-rescue pathway distinct from SsrA- and ArfA-mediated pathways," *Mol. Microbiol.*, 80, 2011.

[Chait *et al.*, 2007] R. Chait, A. Craney, and R. Kishony, "Antibiotic interactions that select against resistance," *Nature*, 446:668, 2007.

[Chatterji and Ojha, 2001] D. Chatterji and A. Ojha, "Revisiting the stringent response, ppGpp and starvation signaling," *Curr Opin Microbiol*, 4:160–165, 2001.

[Cherepanov and Wackernagel, 1995] P. Cherepanov and W. Wackernagel, "Gene disruption in *Escherichia coli*: Tc^R and Km^R cassettes with the option of Flp-catalyzed excision of the antibiotic-resistance determinant," *Gene*, 158:9, 1995.

[Chevereau and Bollenbach, 2015] G. Chevereau and T. Bollenbach, "Systematic discovery of drug interaction mechanisms," *Mol. Syst. Biol.*, 11:807, 2015.

[Chevereau *et al.*, 2015] G. Chevereau *et al.*, "Quantifying the Determinants of Evolutionary Dynamics Leading to Drug Resistance," *PLoS Biol.*, 13(11), 2015.

[Choi, 2019] J. Choi, "Dynamics of the context-specific translation arrest by chloramphenicol and linezolid," *Nat. Chem. Biol.*, 16, 2019.

[Choi and Lee, 2019] U. Choi and C.-R. Lee, "Distinct Roles of Outer Membrane Porins in Antibiotic Resistance and Membrane Integrity in *Escherichia coli*," *Front. Microbiol.*, 10, 2019.

[Clatworthy *et al.*, 2007] A. Clatworthy *et al.*, "Targeting virulence: a new paradigm for antimicrobial therapy," *Nat. Chem. Biol.*, 3(9):541–548, 2007.

[Cleveland and Devlin, 1988] W. Cleveland and S. Devlin, "Locally Weighted Regression: An Approach to Regression Analysis by Local Fitting," *J Am Stat Assoc.*, 83(403), 1988.

[Cokol, 2014] M. Cokol, "Large-Scale Identification and Analysis of Suppressive Drug Interactions," *Chem. Biol.*, 21:541–55, 2014.

[Cokol *et al.*, 2011] M. Cokol *et al.*, "Systematic exploration of synergistic drug pairs," *Mol. Syst. Biol.*, 7(544), 2011.

[Cole *et al.*, 1987] J. Cole, C. Olsson, J. Hershey, M. Grunberg-Manago, and M. Nomura, "Feedback Regulation of rRNA Synthesis in *Escherichia coli* Requirement for Initiation Factor IF2," *J. Mol. Biol.*, 198:383, 1987.

[Condon *et al.*, 1993] C. Condon, S. French, C. Squires, and C. Squires, "Depletion of functional ribosomal RNA operons in Escherichia coli causes increased expression of the remaining intact copies," *EMBO J.*, 12:4305, 1993.

[Condon *et al.*, 1995] C. Condon *et al.*, "Control of rRNA Transcription in Escherichia coli," *Microbiol. Rev.*, 59(4):623–645, 1995.

[Constanzo *et al.*, 2010] M. Constanzo *et al.*, "The Genetic Landscape of a Cell," *Science*, 327, 2010.

[Cooper and Helmstetter, 1968] S. Cooper and C. Helmstetter, "Chromosome Replication and the Division Cycle or *Escherichia coli* B/r," *J. Mol. Biol.*, 31:519–540, 1968.

[Crick, 1970] F. Crick, "Central dogma of molecular biology," *Nature*, 227:561–563, 1970.

[Dai *et al.*, 2016] X. Dai, M. Zhu, M. Warren, R. Balakrishnan, V. Patsalo, H. Okano, J. Williamson, K. Fredirck, Y. Wang, and T. Hwa, "Reduction of translating ribosomes enables *Escherichia coli* to maintain elongation rates during slow growth," *Nature Microbiology*, 2(16231), 2016.

[Datsenko and Wanner, 2000] K. Datsenko and B. Wanner, "One-step inactivation of chromosomal genes in *Escherichia coli K*-12 using PCR products," *Proc. Nat. Acad. Sci. USA*, 96(12), 2000.

[Datta *et al.*, 2006] S. Datta, N. Constantino, and D. Court, "A set of recombineering plasmids for gram-negative bacteria," *Gene*, 379, 2006.

[Davis, 1987] B. Davis, "Mechanism of Bactericidal Action of Aminoglycosides," *Microbiol Rev*, 51(3), 1987.

[de Evgrafov *et al.*, 2015] M. de Evgrafov *et al.*, "Collateral Resistance and Sensitivity Modulate Evolution of High-Level Resistance to Drug Combination Treatment in *Staphylococcus aureus*," *Mol. Biol. Evol.*, 32:1175–1185, 2015.

[Dennis *et al.*, 2004] P. Dennis, M. Ehrenberg, and H. Bremer, "Control of rRNA Synthesis in *Escherichia coli*: a Systems Biology Approach," *Microbiol. Mol. Biol. Rev.*, 68(4):639–668, 2004.

[Deris *et al.*, 2013] J. Deris, M. Kim, Z. Zhang, H. Okano, R. Hermsen, A. Groisman, and T. Hwa, "The Innate Growth Bistability and Fitness Landscapes of Antibiotic-Resistant Bacteria," *Science*, 342:1237435, 2013.

[Dias *et al.*, 2018] M. B. Dias *et al.*, "Folate biosynthesis pathway: mechanisms and insights into drug design for infectious diseases," *Future Med. Chem.*, 10(8):935–959, 2018.

[Donachie, 1968] W. Donachie, "Relationship between Cell Size and Time of Initiation of DNA replication," *Nature*, 219:1077–1079, 1968.

[Dong *et al.*, 1995] H. Dong, L. Nilsson, and C. Kurland, "Gratuitous Overexpression of Genes in *Escherichia coli* Leads to Growth Inhibition and Ribosome Destruction," *J. Bacteriol.*, 177(6):1497, 1995.

[Dong *et al.*, 1996] H. Dong, L. Nilsson, and C. Kurland, "Co-variation of tRNA Abundance and Codon Usage in Escherichia coli at Different Growth Rates," *J. Mol. Biol.*, 260:649–663, 1996.

[Dunkle *et al.*, 2010] J. Dunkle, L. Xiong, A. Mankin, and J. Cate, "Structures of the *Escherichia coli* ribosome with antibiotics bound near the peptidyl transferase center explain spectra of drug action," *Proc. Nat. Acad. Sci. USA*, 107(40), 2010.

[Durfee *et al.*, 2008] T. Durfee *et al.*, "Transcription Profiling of the Stringent Response in *Escherichia coli*," *J. Bacteriol.*, 190(3):1084–1096, 2008.

[Duval *et al.*, 2015] M. Duval *et al.*, "Multiple ways to regulate translation initiation in bacteria: Mech- anisms, regulatory circuits, dynamics," *Biochemie*, 114:18–29, 2015.

[Elander, 2003] R. Elander, "Industrial production of β-lactam antibiotics," *Appl. Microbiol. Biotechnol.*, 61:385, 2003.

[Elf and Ehrenberg, 2005] J. Elf and M. Ehrenberg, "Near-Critical Behavior of Aminoacyl-tRNA Pools in *E. coli* at Rate-Limiting Supply of Amino Acids," *Biophys. J.*, 88:132–146, 2005.

[Elf *et al.*, 2003] J. Elf, D. Nilsson, T. Tenson, and M. Ehrenberg, "Selective Charging of tRNA Isoacceptors Explains Patterns of Codon Usage," *Science*, 300:1718–1722, 2003.

[Elf *et al.*, 2006] J. Elf, K. Nilsson, T. Tenson, and M. Ehrenberg, "Bistable Bacterial Growth Rate in Response to Antibiotics with Low Membrane Permeability," *Phys. Rev. Lett.*, 97:258104, 2006.

[Elowitz *et al.*, 1997] M. Elowitz *et al.*, "Protein Mobility in the Cytoplasm of *Escherichia coli*," *J. Bacteriol.*, 181:197–203, 1997.

[Falconer *et al.*, 2011] S. Falconer, T. Czarny, and E. Brown, "Antibiotics as probes of biological complexity," *Nat. Chem. Biol.*, 7:415, 2011.

[Fleming, 1929] A. Fleming, "On the Antibacterial Action of Cultures of a Penicillium, with Special Reference to their Use in the Isolation of *B. influenzae*," *Br. J. Exp. Pathol.*, 10(3):226–236, 1929.

[Flensburg and Sköld, 1987] J. Flensburg and O. Sköld, "Massive overproduction of dihydrofolate reductase in bacteria as a response to the use of trimethoprim," *Eur. J. Biochem.*, 162:473–476, 1987.

[Frost *et al.*, 2005] L. Frost *et al.*, "Mobile genetic elements: the agents of open source evolution," *Nat. Rev. Microbiol.*, 3:722–732, 2005.

[Frottin *et al.*, 2006] F. Frottin *et al.*, "The Proteomics of N-terminal Methionine Cleavage," *Mol. Cell. Proteom.*, 5:2336–2349, 2006.

[Furano and Wittel, 1975] A. Furano and F. Wittel, "Syntheses of Elongation Factors Tu and G Are under Stringent Control in *Escherichia coli*," *J. Biol. Chem.*, 251(3), 1975.

[Gaal and Gourse, 1990] T. Gaal and R. Gourse, "Guanosine 3'-diphosphate 5'-diphosphate is not required for growth rate-dependent control of rRNA synthesis in *Escherichia coli*," *Proc. Nat. Acad. Sci. USA*, 87:5533–5537, 1990.

[Gao *et al.*, 2018] Y. Gao *et al.*, "Systematic discovery of uncharacterized transcription factors in Escherichia coli K-12 MG1655," *Nucleic Acids Res.*, 46(20):10682–10696, 2018.

[Garcia *et al.*, 2011] H. Garcia, H. Lee, J. Boedicker, and R. Phillips, "Comparison and Calibration of Different Reporters for Quantitative Analysis of Gene Expression," *Biophys. J.*, 101, 2011.

[Giegé and Springer, 2016] R. Giegé and M. Springer, *Cellular and Molecular Biology of E. coli, Salmonella, and Enterobacteriaceae*, chapter Aminoacyl-tRNA Synthetases in the Bacterial World, American Society for Microbiology, 2016.

[Gilbert *et al.*, 1990] P. Gilbert *et al.*, "Influence of growth-rate on susceptibility to antimicrobial agents-biofilms, cell-cycle, dormancy, and stringent response," *Antimicrob. Agents Chemother.*, 34:1865–1868, 1990.

[Goh *et al.*, 2002] E.-B. Goh *et al.*, "Transcriptional modulation of bacterial gene

expression by subinhibitory concentrations of antibiotics," *Proc. Nat. Acad. Sci. USA*, 99:17025–17030, 2002.

[Goodwin *et al.*, 2016] S. Goodwin *et al.*, "Coming of age: ten years of next-generation sequencing technologies," *Nat. Rev. Genet.*, 17:333–351, 2016.

[Gordon, 1970] J. Gordon, "Regulation of the in vivo synthesis of the polypeptide chain elongation factors in *Escherichia coli*," *Biochemistry*, 9, 1970.

[Gregor *et al.*, 2017] C. Gregor *et al.*, "Strongly enhanced bacterial bioluminescence with the ilux operon for single-cell imaging," *Proc. Nat. Acad. Sci. USA*, 115:962–967, 2017.

[Gregor, 2017] T. Gregor, "Beyond D'Arcy Thompson: Future challenges for quantitative biology," *Mech. Dev.*, 145:10–12, 2017.

[Greulich *et al.*, 2017] P. Greulich, J. Doležal, M. Scott, M. Evans, and R. Allen, "Predicting the dynamics of bacterial growth inhibition by ribosome-targeting antibiotics," *Phys. Biol.*, 14(065005), 2017.

[Greulich *et al.*, 2015] P. Greulich, M. Scott, M. Evans, and R. Allen, "Growth-dependent bacterial susceptibility to ribosome-targeting antibiotics," *Mol. Syst. Biol.*, 11:796–807, 2015.

[Guillon *et al.*, 1992] J. Guillon *et al.*, "Disruption of the gene for Met-tRNA(fMet) formyltransferase severely impairs growth of Escherichia coli," *J. Bacteriol.*, 174(13):4294–301, 1992.

[Guillon *et al.*, 1993] J. Guillon *et al.*, "Importance of formylability and anticodon stem sequence to give a $tRNA^{Met}$ an initiator identity in *Escherichia coli*," *J. Bacteriol.*, 175(14):4507–4514, 1993.

[Guzman *et al.*, 1995] L.-M. Guzman *et al.*, "1995, American Society for Microbiology Tight Regulation, Modulation, and High-Level Expression by Vectors Containing the Arabinose P_{BAD} Promoter," *J. Bacteriol.*, 177(14):4121–4130, 1995.

[Gyorfy *et al.*, 2015] Z. Gyorfy *et al.*, "Engineered ribosomal RNA operon copy-number variants of *E. coli* reveal the evolutionary trade-offs shaping rRNA operon number," *Nucleic Acids Res.*, 1, 2015.

[Harvey and Koch, 1980] R. Harvey and A. Koch, "How partially inhibitory concentrations of chloramphenicol affect the growth of Escherichia coli," *Antimicrob. Agents Chemother.*, 18:323–337, 1980.

[Hausser *et al.*, 2019] J. Hausser *et al.*, "Central dogma rates and the trade-off between precision and economy in gene expression," *Nat. Commun.*, 10(68), 2019.

[Hegreness *et al.*, 2008] M. Hegreness, N. Shoresh, D. Damian, D. Hartl, and R. Kishony, "Accelerated evolution of resistance in multidrug environments," *Proc. Nat. Acad. Sci. USA*, 106(37), 2008.

[Hirel *et al.*, 1989] P. H. Hirel *et al.*, "Extent of N-terminal methionine excision from *Escherichia coli* proteinsisgoverned by the side-chain length of the penultimate amino acid," *Proc. Nat. Acad. Sci. USA*, 86:8247–8251, 1989.

[Hopfield, 1974] J. Hopfield, "Kinetic Proofreading: A New Mechanism for Reducing Errors in Biosynthetic Processes Requiring High Specificity," *Proc. Nat. Acad. Sci. USA*, 71(10):4135–4139, 1974.

[Hughes and Mellows, 1978] J. Hughes and G. Mellows, "Inhibition of Isoleucyl-Transfer Ribonucleic Acid Synthetase in *Escherichia coli* by Pseudomonic Acid," *Biochem. J.*, 176:306–318, 1978.

[Hui *et al.*, 2015] S. Hui, J. Silvermann, S. Chen, D. Erickson, M. Basan, J. Wang, T. Hwa, and J. Williamson, "Quantitative proteomic analysis reveals a simple strategy of global resource allocation in bacteria Quantitative proteomic analysis reveals a simple strategy of global resource allocation in bacteria," *Mol. Syst. Biol.*, 11:784, 2015.

[Hwang and Inouye, 2006] J. Hwang and M. Inouye, "The tandem GTPase, Der, is essential for the biogenesis of 50S ribosomal subunits in *Escherichia coli*," *Mol. Microbiol.*, 61(6):1660–1672, 2006.

[Iizuka, 2011] R. Iizuka, "Kinetic study of de novo chromophore maturation of fluorescent proteins," *Anal. Biochem.*, 414:173–178, 2011.

[Imamovic and Sommer, 2013] L. Imamovic and M. Sommer, "Use of collateral sensitivity networks to design drug cycling protocols that avoid resistance development," *Sci. Transl. Med.*, 5(204), 2013.

[Ito *et al.*, 1999] Y. Ito *et al.*, "A Novel Mutant of Green Fluorescent Protein with Enhanced Sensitivity for Microanalysis at 488 nm Excitation," *Biochem. Biophys. Res. Commun.*, 264:556–560, 1999.

[Izard *et al.*, 2015] J. Izard *et al.*, "A synthetic growth switch based on controlled expression of RNA polymerase," *Mol. Syst. Biol.*, 11(11):840, 2015.

[Janosi *et al.*, 1994] L. Janosi *et al.*, "Ribosome recycling factor (ribosome releasing factor) is essential forbacterialgrowth," *Proc. Nat. Acad. Sci. USA*, 91:4249–4253, 1994.

[Janosi *et al.*, 1998] L. Janosi *et al.*, "Evidence for *in vivo* ribosome recycling, the fourth step in protein biosynthesis," *EMBO J.*, 17(4):1141–1151, 1998.

[Jaynes, 1957] E. Jaynes, "Information theory and statistical mechanics," *Phys. Rev.*, 106(620), 1957.

[Jinks-Robertson *et al.*, 1983] S. Jinks-Robertson, R. Gourse, and M. Nomura, "Expression of rRNA and tRNA Genes in *Escherichia coli*: Evidence for Feedback Regulation by Products of rRNA Operons," *Cell*, 33, 1983.

[Jun *et al.*, 2018] S. Jun, F. Si, R. Pugatch, and M. Scott, "Fundamental principles in bacterial physiology–history, recent progress, and the future with focus on cell size control: a revie," *Rep. Prog. Phys.*, 81(056601), 2018.

[Kaberdina *et al.*, 2009] A. Kaberdina, W. Szaflarski, K. Nierhaus, and I. Moll, "An Unexpected Type of Ribosomes Induced by Kasugamycin: A Look into Ancestral Times of Protein Synthesis?," *Mol. Cell*, 33(2), 2009.

[Kaczanowska and Rydén-Aulin, 2007] M. Kaczanowska and M. Rydén-Aulin, "Ribosome Biogenesis and the Translation Process in *Escherichia coli*," *Microbiol. Mol. Biol. Rev.*, 71:477–494, 2007.

[Kahn *et al.*, 1980] D. Kahn *et al.*, "Methionyl-transfer-RNA transformylase from Escherichia coli. Purification and characterisation," *Eur. J. Biochem.*, 105(3):489–97, 1980.

[Kang and Cantor, 1985] C. Kang and C. Cantor, "Structure of Ribosome-bound Messenger RNA as Revealed by Enzymatic Accessibility Studies," *J. Mol. Biol.*, 181, 1985.

[Kannan *et al.*, 2012] K. Kannan, N. Vazquez-Laslop, and A. Mankin, "Selective Protein Synthesis by Ribosomes with a Drug-Obstructed Exit Tunnel," *Cell*, 151, 2012.

[Katzir *et al.*, 2019] I. Katzir *et al.*, "Prediction of ultra-high-order antibiotic combinations based on pairwise interactions," *PLoS Comput. Biol.*, 15(1):e1006774, 2019.

[Keiler, 2015] K. Keiler, "Mechanisms of ribosome rescue in bacteria," *Nat. Rev. Microbiol.*, 13, 2015.

[Keren *et al.*, 2004] I. Keren *et al.*, "Specialized persister cells and the mechanism of multidrug tolerance in *Escherichia coli*," *J. Bacteriol.*, 186:8172–8180, 2004.

[Kinney *et al.*, 2010] J. Kinney *et al.*, "Using deep sequencing to characterize the biophysical mechanism of a transcriptional regulatory sequence," *Proc. Nat. Acad. Sci. USA*, 107(20):9158–9163, 2010.

[Kishony and Leibler, 2003] R. Kishony and S. Leibler, "Environmental stresses can alleviate the average deleterious effect of mutations," *J. Biol.*, 2:14, 2003.

[Kitagawa *et al.*, 2005] M. Kitagawa, T. Ara, M. Arifuzzaman, T. Ioka-Nakamichi, E. Inamoto, H. Toyonaga, and H. Mori, "Complete set of ORF clones of *Escherichia*

coli ASKA library (A Complete Set of *E. coli* K-12 ORF Archive): Unique Resources for Biological Research," *DNA Research*, 12:291, 2005.

[Klumpp and Hwa, 2008] S. Klumpp and T. Hwa, "Stochasticity and traffic jams in the transcription of ribosomal RNA: Intriguing role of termination and antitermination," *Proc. Nat. Acad. Sci. USA*, 105:18159, 2008.

[Klumpp *et al.*, 2009] S. Klumpp, Z. Zhang, and T. Hwa, "Growth Rate-Dependent Global Effects on Gene Expression in Bacteria," *Cell*, 130:1366, 2009.

[Klumpp *et al.*, 2013] S. Klumpp *et al.*, "Molecular crowding limits translation and cell growth," *Proc. Nat. Acad. Sci. USA*, 110(42):16754–16759, 2013.

[Kochanowski *et al.*, 2017] K. Kochanowski *et al.*, "Few regulatory metabolites coordinate expression of central metabolic genes in *Escherichia coli*," *Mol. Syst. Biol.*, 13:1–14, 2017.

[Kostinski and Reuveni, 2020] S. Kostinski and S. Reuveni, "Ribosome Composition Maximizes Cellular Growth Rates in *E. coli*," *Phys. Rev. Lett.*, 125:028103: 1–6, 2020.

[Kramer and Fussenegger, 2005] B. Kramer and M. Fussenegger, "Hysteresis in a synthetic mammalian gene network," *Proc. Nat. Acad. Sci. USA*, 102:9517–9522, 2005.

[Kubelka *et al.*, 2004] J. Kubelka *et al.*, "The protein folding 'speed limit'," *Curr Opin. Struc. Biol.*, 14:76–88, 2004.

[Kubitschek *et al.*, 1984] H. Kubitschek *et al.*, "Independence of Buoyant Cell Density and Growth Rate in *Escherichia coli*," *J. Bacteriol.*, 158:296–299, 1984.

[Kuwahara and Gao, 2013] H. Kuwahara and X. Gao, "Stochastic effects as a force to increase the complexity of signaling networks," *Sci. Rep.*, 3(2297), 2013.

[Kwok, 2010] R. Kwok, "Five hard truths for synthetic biology," *Nature*, 436:288–290, 2010.

[Lakatos and Chou, 2003] G. Lakatos and T. Chou, "Totally asymmetric exclusion processes with particles of arbitrary size," *J. Phys. A: Math. Gen.*, 36, 2003.

[Lazar *et al.*, 2013] V. Lazar *et al.*, "Bacterial evolution of antibiotic hypersensitivity," *Mol. Syst. Biol.*, 9, 2013.

[Lennox, 1955] E. Lennox, "Transduction of linked genetic characters of the host by bacteriophage P1," *Virology*, 1, 1955.

[Li *et al.*, 2014] G.-W. Li *et al.*, "Quantifying Absolute Protein Synthesis Rates Reveals Principles Underlying Allocation of Cellular Resources," *Cell*, 157:624–635, 2014.

[Liang *et al.*, 1999] S.-T. Liang *et al.*, "Decay of *rplN* and *lacZ* mRNA in *Escherichia coli*," *J. Mol. Biol.*, 288:521–538, 1999.

[Liang *et al.*, 2000] S.-T. Liang *et al.*, "mRNA Composition and Control of Bacterial Gene Expression," *J. Bacteriol.*, 182:3037–3044, 2000.

[Loewe, 1928] S. Loewe, "Die quantitativen Probleme der Pharmakologie," *Ergeb. Physiol.*, 27:47, 1928.

[Loewe and Muischnek, 1926] S. Loewe and H. Muischnek, "Über kombinationswirkungen," *Archiv f. experiment. Pathol. u. Pharmakol.*, 114, 1926.

[Lukačišin and Bollenbach, 2019] M. Lukačišin and T. Bollenbach, "Emergent Gene Expression Responses to Drug Combinations Predict Higher-Order Drug Interactions," *Cell Syst*, 10:1–11, 2019.

[Lukačišinova and Bollenbach, 2019] M. Lukačišinova and T. Bollenbach, "Toward a quantitative understanding of antibiotic resistance evolution," *Curr Opin. Biotechnol.*, 46:90–97, 2019.

[Lukačišinova *et al.*, 2020] M. Lukačišinova, B. Fernando, and T. Bollenbach, "Highly parallel lab evolution reveals that epistasis can curb the evolution of antibiotic resistance," *Nat. Commun.*, 11(3105):1–14, 2020.

[Lutz and Bujard, 1997] R. Lutz and H. Bujard, "Independent and tight regulation of transcriptional units in *Escherichia coli* via the LacR/O, the TetR/O and AraC/I_1-I_2 regulatory elements," *Nucleic Acids Res*, 25(6):1203, 1997.

[Maaløe, 1979] O. Maaløe, *Biological Regulation and Development*, Plenum, 1979.

[MacDonald and Gibbs, 1969] C. MacDonald and J. Gibbs, "Concerning the kinetics of polypeptide synthesis on polyribosomes," *Biopolymers*, 7, 1969.

[MacDonald *et al.*, 1968] C. MacDonald, J. Gibbs, and A. Pipkin, "Kinetics of biopolymerization on nucleic acid templates," *Biopolymers*, 6, 1968.

[Marks *et al.*, 2016] J. Marks *et al.*, "Context-specific inhibition of translation by ribosomal antibiotics targeting the peptidyl transferase center," *Proc. Nat. Acad. Sci. USA*, 113(43), 2016.

[McArthur *et al.*, 2013] A. McArthur *et al.*, "The Comprehensive Antibiotic Resistance Database," *Antimicrob. Agents Chemother.*, 57(7):3348–3357, 2013.

[McCarthy and Holland, 1965] B. McCarthy and J. Holland, "Denatured DNA as a a direct template for *in vitro* protein synthesis," *Biochemistry*, 54:880–6, 1965.

[Milo and Phillips, 2016] R. Milo and R. Phillips, *Cell biology by the numbers*, Garland Science, 2016.

[Milon and Rodnina, 2012] P. Milon and M. Rodnina, "Kinetic control of translation initiation in bacteria," *Crit. Rev. Biochem. Mol. Biol*, 47(4):334–348, 2012.

[Milon *et al.*, 2006] P. Milon *et al.*, "The nucleotide-binding site of bacterial translation initiation factor 2 (IF2) as a metabolic sensor," *Proc. Nat. Acad. Sci. USA*, 103, 2006.

[Milon *et al.*, 2012] P. Milon *et al.*, "Real-time assembly landscape of bacterial 30S translation initiation complex," *Nat. Struct. Mol. Biol.*, 19(6), 2012.

[Mitarai *et al.*, 2008] N. Mitarai, K. Sneppen, and S. Pedersen, "Ribosome Collisions and Translation Efficiency: Optimization by Codon Usage and mRNA Destabilization," *J. Mol. Biol.*, 382, 2008.

[Mitosch and Bollenbach, 2014] K. Mitosch and T. Bollenbach, "Bacterial responses to antibiotics and their combinations," *Environ. Microbiol. Rep.*, 6:545, 2014.

[Mitosch *et al.*, 2017] K. Mitosch, G. Rieckh, and T. Bollenbach, "Noisy Response to Antibiotic Stress Predicts Subsequent Single-Cell Survival in an Acidic Environment," *Cell Syst*, 4, 2017.

[Mitosch *et al.*, 2019] K. Mitosch, G. Rieckh, and T. Bollenbach, "Temporal order and precision of complex stress responses in individual bacteria," *Mol. Syst. Biol.*, 15(e8470):1–15, 2019.

[Młynarski *et al.*, 2019] W. Młynarski *et al.*, "Statistical analysis and optimality of biological systems," *bioRxiv*, page 848374, 2019.

[Mohammad *et al.*, 2019] F. Mohammad, R. Green, and A. Buskirk, "A systematically-revised ribosome profiling method for bacteria reveals pauses at single-codon resolution," *eLife*, 8:e42591, 2019.

[Nakahigashi *et al.*, 2016] K. Nakahigashi *et al.*, "Comprehensive identification of translation start sites by tetracycline-inhibited ribosome profiling," *DNA Research*, 23(3), 2016.

[Neidhardt, 1999] F. Neidhardt, "Bacterial growth: constant obsession with dN/dt," *J. Bacteriol.*, 181:7405–8, 1999.

[Nierhaus and Wilson, 2004] K. Nierhaus and D. Wilson, editors, *Protein Synthesis and Ribosome Structure*, chapter The elongation cycle, Wiley-VCH, 2004.

[Nikolic *et al.*, 2018] N. Nikolic *et al.*, "Autoregulation of *mazEF* expression underlies growth heterogeneity in bacterial populations," *Nucleic Acids Res.*, 46:2918–2931, 2018.

[Noller, 2014] H. Noller, "Evolution of Protein Synthesis from an RNA World," *Cold Spring Harb Perspect Biol.*, 4(4), 2014.

[Nomura *et al.*, 1984] M. Nomura *et al.*, "Regulation of the synthesis of ribosomes and ribosomal components," *Annu. Rev. Biochem.*, 53:75–117, 1984.

[Olofsson *et al.*, 1987] S. Olofsson *et al.*, "Structure and biosynthesis of apolipoprotein B," *Am Heart J.*, 113:446–52, 1987.

[Olsson *et al.*, 1996] C. Olsson, M. Graffe, M. Springer, and J. Hershey, "Physiological effects of translation initiation factor IF3 and ribosomal protein L20 limitation in *Escherichia coli*," *Molec. Gen. Genet.*, 250, 1996.

[Palmer *et al.*, 2018] A. Palmer, R. Chait, and R. Kishony, "Nonoptimal Gene Expression Creates Latent Potential for Antibiotic Resistance," *Mol. Biol. Evol.*, 35(11), 2018.

[Palmer and Kishony, 2014] A. Palmer and R. Kishony, "Opposing effects of target overexpression reveal drug mechanisms," *Nat. Commun*, 5(4296), 2014.

[Palumbi, 2001] S. Palumbi, "Humans as the World's Greatest Evolutionary Force," *Science*, 293:1786–1790, 2001.

[Peil *et al.*, 2013] L. Peil *et al.*, "Distinct XPPX sequence motifs induce ribosome stalling, which is rescued by the translation elongation factor EF-P," *Proc. Nat. Acad. Sci. USA*, 110(38):15265–70, 2013.

[Peske *et al.*, 2004] F. Peske, A. Savelsbergh, V. Katunin, M. Rodnina, and W. Wintermeyer, "Conformational Changes of the Small Ribosomal Subunit During Elongation Factor G-dependent tRNA–mRNA Translocation," *J. Mol. Biol.*, 343, 2004.

[Petrov *et al.*, 2015] A. Petrov *et al.*, "History of the ribosome and the origin of translation," *Proc. Nat. Acad. Sci. USA*, 112(50):15396–15401, 2015.

[Piatkov *et al.*, 2015] K. Piatkov *et al.*, "Formyl-methionine as a degradation signal at the N-termini of bacterial proteins," *Microb. Cell*, 2(13):376–393, 2015.

[Pillai *et al.*, 2005] S. Pillai, R. Moellering, and G. Eliopoulos, *Antibiotics in Laboratory Medicine*, chapter Antimicrobial combinations, Lippincott Williams and Wilkins, 2005.

[Pinheiro *et al.*, 2020] F. Pinheiro *et al.*, "Predicting trajectories and mechanisms of antibiotic resistance evolution," *bioRxiv*, 10.1101/2020.07.02.184622, 2020.

[Pontes *et al.*, 2015] M. Pontes *et al.*, "When Too Much ATP Is Bad forProtein Synthesis," *J. Mol. Biol.*, 427:2586–2594, 2015.

[Potrykus and Cashel, 2008] K. Potrykus and M. Cashel, "(p)ppGpp: Still Magical?," *Annu. Rev. Microbiol.*, 62:35–51, 2008.

[Ramakrishnan, 2018] V. Ramakrishnan, *Gene Machine: The Race to Decipher the Secrets of the Ribosome*, Basic Books, 2018.

[Rand, 1971] W. Rand, "Objective Criteria for the Evaluation of Clustering Methods," *J Am Stat Assoc.*, 66(336), 1971.

[Reuveni *et al.*, 2017] S. Reuveni, M. Ehrenberg, and J. Paulsson, "Ribosomes are optimized for autocatalytic production," *Nature*, 547:293–7, 2017.

[Rode *et al.*, 1989] H. Rode, D. Hanslo, P. Dewet, A. Millar, and S. Cywes, "Efficacy of Mupirocin in Methicillin-Resistant Staphylococcus aureus Burn Wound Infection," *Antimicrob. Agents Chemother.*, 33(8):1358, 1989.

[Rodnina *et al.*, 2011] M. V. Rodnina, W. Wintermeyer, and R. Green, *Ribosomes Structure, Function, and Dynamics*, Springer-Verlag/Wien, 2011.

[Rodnina, 2018] M. Rodnina, "Translation in Prokaryotes," *Cold Spring Harb Perspect Biol.*, 10(9), 2018.

[Rodnina and Wintermeyer, 2011] M. Rodnina and W. Wintermeyer, "The ribosome as a molecular machine: the mechanism of tRNA-mRNA movement in translocation.," *Biochem. Soc. Trans.*, 39:658–662, 2011.

[Rolland *et al.*, 1979] S. Rolland *et al.*, "The characteristics and significance of sulfonamides as substrates for Escherichia coli dihydropteroate synthase.," *J. Biol. Chem.*, 254:10337–10345, 1979.

[Russ and Kishony, 2018] D. Russ and R. Kishony, "Additivity of inhibitory effects in multidrug combinations," *Nat. Microbiol.*, 3, 2018.

[Ruusala *et al.*, 1984] T. Ruusala *et al.*, "Hyper-accurate ribososomes inhibit growth," *EMBO J.*, 3(11):2575–2580, 1984.

[Salis *et al.*, 2009] H. Salis *et al.*, "Automated design of synthetic ribosome binding sites to control protein expression," *Nat. Biotech.*, 27:946–950, 2009.

[Samoilov and Arkin, 2006] M. Samoilov and A. Arkin, "Deviant effects in molecular reaction pathways," *Nat. Biotech.*, 24(10):1235–1240, 2006.

[Santos-Zavaleta *et al.*, 2019] A. Santos-Zavaleta *et al.*, "RegulonDB v 10.5: tackling challenges to unify classic and high throughput knowledge of gene regulation in *E. coli* K-12," *Nucleic Acids Res.*, 47, 2019.

[Sanz-Garcia *et al.*, 2018] F. Sanz-Garcia, S. Hernando-Amado, and J. Martinez, "*Pseudomonas aeruginosa* Resistance to Ribosome-Targeting Antibiotics," *Front. Genet.*, 9, 2018.

[Savageau, 1974] M. Savageau, "Comparison of classical and autogenous systems of regulation in inducible operons," *Nature*, 252:546–549, 1974.

[Savelsbergh *et al.*, 2009] A. Savelsbergh, M. Rodnina, and W. Wintermeyer, "Distinct functions of elongation factor G in translocation and ribosome recycling," *RNA*, 15, 2009.

[Schaechter *et al.*, 1958] M. Schaechter, O. Maaløe, and N. Kjeldgaard, "Dependency on Medium and Temperature of Cell Size and Chemical Composition during Balanced Growth of *Salmonella typhimurium*," *J. Gen. Microbiol.*, 19:592–606, 1958.

[Schleif *et al.*, 1973] R. Schleif *et al.*, "Induction Kinetics of theL-Arabinose Operon of *Escherichia coli*," *J. Bacteriol.*, 115(1):9–14, 1973.

[Schluenzen *et al.*, 2006] F. Schluenzen *et al.*, "The antibiotic kasugamycin mimics mRNA nucleotides to destabilize tRNA binding and inhibit canonical translation initiation," *Nat. Struct. Mol. Biol.*, 13(10), 2006.

[Schmid and Roth, 1987] M. Schmid and J. Roth, "Gene location Affects Expression Level in *Salmonella typhimurium*," *J. Bacteriol.*, 169(6):2872–2875, 1987.

[Schneider and Gourse, 2004] D. Schneider and R. Gourse, "Relationship between growth rate and ATP concentration in *Escherichia coli*: a bioassay for available cellular ATP," *J. Biol. Chem.*, 279(9):8262–8, 2004.

[Scott *et al.*, 2010] M. Scott, C. Gunderson, E. Mateescu, Z. Zhang, and T. Hwa, "Interdependence of Cell Growth and Gene Expression: Origins and Consequences," *Science*, 330:1099, 2010.

[Scott and Hwa, 2011] M. Scott and T. Hwa, "Bacterial growth laws and their applications," *Curr Opin Biotechnol*, 22:559–565, 2011.

[Scott *et al.*, 2014] M. Scott, S. Klumpp, E. Mateescu, and T. Hwa, "Emergence of robust growth laws from optimal regulation of ribosome synthesis," *Mol. Syst. Biol.*, 10:747–761, 2014.

[Segre *et al.*, 2005] D. Segre, A. DeLuna, G. Church, and R. Kishony, "Modular epistasis in yeast metabolism," *Nat. Genet.*, 37(1), 2005.

[Shaw *et al.*, 2003a] K. Shaw *et al.*, "Comparison of the changes in global gene expression of Escherichia coli induced by four bactericidal agents," *J. Mol. Microbiol. Biotechnol.*, 5:105–122, 2003.

[Shaw *et al.*, 2003b] L. Shaw, R. Zia, and K. Lee, "Totally asymmetric exclusion process with extended objects: A model for protein synthesis," *Phys. Rev. E*, 68, 2003.

[Shepheard *et al.*, 1980] N. Shepheard *et al.*, "Synthesis and Activity of Ribonucleic Acid Polymerase in *Escherichia coli*," *J. Bacteriol.*, 141(3):1096–1108, 1980.

[Sievers *et al.*, 2004] A. Sievers *et al.*, "The ribosome as an entropy trap," *Proc. Nat. Acad. Sci. USA*, 101:7897–7901, 2004.

[Simms *et al.*, 2019] C. Simms, L. Yan, J. Qiu, and H. Zaher, "Ribosome Collisions Result in +1 Frameshifting in the Absence of No-Go Decay," *Cell Rep.*, 28, 2019.

[Smith and Chopra, 1984] M. Smith and I. Chopra, "Energetics of Tetracycline Transport into *Escherichia coli*," *Antimicrob. Agents Chemother.*, 25(4):446–449, 1984.

[Sørensen and Pedersen, 1991] M. Sørensen and S. Pedersen, "Absolute *in vivo* Translation Rates of Individual Codons in *Escherichia coli*," *J. Mol. Biol.*, 222:265–280, 1991.

[Stanley *et al.*, 2010] R. Stanley, G. Blaha, R. Grodzicki, M. Strickler, and T. Steitz, "The structures of the anti-tuberculosis antibiotics viomycin and capreomycin bound to the 70S ribosome," *Nat. Struct. Mol. Biol.*, 17(3), 2010.

[Steinrück and Guet, 2017] M. Steinrück and C. Guet, "Complex chromosomal neighborhood effects determine the adaptive potential of a gene under selection," *eLife*, 6:e25100, 2017.

[Stokes *et al.*, 2014] J. Stokes *et al.*, "Discovery of a small molecule that inhibits bacterial ribosome biogenesis," *eLife*, 3:e03574, 2014.

[Sugino *et al.*, 1978] A. Sugino, N. Higgins, P. B. C. Peebles, and N. Cozzarelli, "Energy coupling in DNA gyrase and the mechanism of action of novobiocin," *Proc. Nat. Acad. Sci. USA*, 75, 1978.

[Swaminathan *et al.*, 1997] R. Swaminathan, C. Hoang, and A. VErkman, "Photobleaching Recovery and Anisotropy Decay of Green Fluorescent Protein GFP-S65T in Solution and Cells: Cytoplasmic Viscosity Probed by Green Fluorescent Protein Translational and Rotational Diffusion," *Biophys. J.*, 72:1900–1907, 1997.

[Tan *et al.*, 2009] C. Tan *et al.*, "Emergent bistability by a growth-modulating positive feedback circuit," *Nat. Chem. Biol.*, 5(11):842–847, 2009.

[Tan and Tatsumura, 2015] S. Tan and Y. Tatsumura, "Alexander Fleming (1881–1955): Discoverer of penicillin," *Singapore Med. J.*, 56(7):366–367, 2015.

[Taniguchi *et al.*, 2010] Y. Taniguchi *et al.*, "Quantifying E. coli Proteome and Transcriptome with Single-Molecule Sensitivity in Single Cells," *Science*, 329:533–537, 2010.

[Tomanek *et al.*, 2020] I. Tomanek *et al.*, "Gene amplification as a form of population-level gene expression regulation," *Nat. Ecol. Evol.*, 4:612–625, 2020.

[Tong *et al.*, 2004] A. Tong *et al.*, "Global Mapping of the Yeast Genetic Interaction Network," *Science*, 303, 2004.

[Toprak *et al.*, 2012] E. Toprak *et al.*, "Evolutionary paths to antibiotic resistance under dynamically sustained drug selection," *Nat. Genet.*, 44(1):101–105, 2012.

[Traverse and Ochman, 2016] C. Traverse and H. Ochman, "Conserved rates and patterns of transcription errors across bacterial growth states and lifestyles," *Proc. Nat. Acad. Sci. USA*, 22:3311–6, 2016.

[Tritton, 1977] T. Tritton, "Ribosome-Tetracycline Interactions," *Biochemistry*, 16(18), 1977.

[Ude *et al.*, 2013] S. Ude *et al.*, "Translation elongation factor EF-P alleviates ribosome stalling at polyproline stretches," *Science*, 339(6115):82–5, 2013.

[Uzawa *et al.*, 2002] T. Uzawa, A. Yamagishi, and T. Oshima, "Polypeptide synthesis directed by DNA as a messenger in cell-free poypeptide synthesis by extreme thermophiles, *Thermus thermophilus* HB27 and *Sulfolobus tokodaii* strain 7," *J. Biochem.*, 131:849–853, 2002.

[Vazquez-Laslop and Mankin, 2018] N. Vazquez-Laslop and A. Mankin, "How Macrolide Antibiotics Work," *Trends Biochem Sci*, 43(9), 2018.

[Vogel and Jensen, 1995] U. Vogel and K. Jensen, "Effects of the antiterminator BoxA on transcription elongation kinetics and ppGpp inhibition of transcription elongation in *Escherichia coli*," *J. Biol. Chem.*, 270(31):18335–18340, 1995.

[Walsh, 2003] C. Walsh, *Antibiotics: actions, origins, resistance*, ASM Press, Washington DC, 2003.

[Wang *et al.*, 2010] P. Wang, L. Robert, J. Pelletier, W. Dang, F. Taddel, A. Wright, and S. Jun, "Robust Growth of *Escherichia coli*," *Curr. Biol.*, 20:1099, 2010.

[Wanner *et al.*, 1977] B. Wanner *et al.*, "Physiological Regulation of a Decontrolled *lac* Operon," *J. Bacteriol.*, 130(1):212–222, 1977.

[Warming *et al.*, 2005] S. Warming *et al.*, "Simple and highly efficient BAC recombineering using galK selection," *Nucleic Acids Res.*, 33(4):1–12, 2005.

[Watt, 2007] R. Watt, "Visualizing the proteome of *Escherichia coli*: an efficient and versatile method for labeling chromosomal coding DNA sequences (CDSs) with fluorescent protein genes," *Nucleic Acids Res.*, 35(6):1–11, 2007.

[Weisse *et al.*, 2015] A. Weisse *et al.*, "Mechanistic links between cellular trade-offs, gene expression, and growth," *Proc. Nat. Acad. Sci. USA*, 112(9):1038–47, 2015.

[Wilson, 2014] D. Wilson, "Ribosome-targeting antibiotics and mechanisms of bacterial resistance," *Nature Rev. Microbiol.*, 12:35, 2014.

[Wood *et al.*, 2012] K. Wood, S. Nishida, E. Sontag, and P. Cluzel, "Mechanism-independent method for predicting response to multidrug combinations in bacteria," *Proc. Nat. Acad. Sci. USA*, 109(30):12254, 2012.

[Wood *et al.*, 2014] K. Wood, K. Wood, S. Nishida, and P. Cluzel, "Uncovering Scaling Laws to Infer Multidrug Response of Resistant Microbes and Cancer Cells," *Cell Rep.*, 6:1073–1084, 2014.

[Woolstenhulme *et al.*, 2015] C. Woolstenhulme, N. Guydosh, R. Green, and A. Buskirk, "High-Precision Analysis of Translational Pausing by Ribosome Profiling in Bacteria Lacking EF," *Cell Rep.*, 11, 2015.

[Yaginuma *et al.*, 2014] H. Yaginuma *et al.*, "Diversity in ATP concentrations in a single bacterial cell population revealed by quantitative single-cell imaging," *Sci. Rep.*, 4(6522):1–7, 2014.

[Yamamoto *et al.*, 2006] T. Yamamoto *et al.*, "Mass spectrometry of hydrogen/deuterium exchange in 70S ribosomal proteins from *E. coli*," *FEBS Letters*, 580:3638–3642, 2006.

[Yeh *et al.*, 2006] P. Yeh, A. Tschumi, and R. Kishony, "Functional classification of drugs by properties of their pairwise interactions," *Nat. Genet.*, 38:489, 2006.

[Yeh *et al.*, 2009] P. Yeh, M. Hegreness, A. P. Aiden, and R. Kishony, "Drug interactions and the evolution of antibiotic resistance," *Nat. Rev. Microbiol.*, 7, 2009.

[You *et al.*, 2013] C. You *et al.*, "Coordination of bacterial proteome with metabolism by cyclic AMP signalling," *Nature*, 500, 2013.

[Yu *et al.*, 2009] H. Yu, Y.-L. Chan, and I. Wool, "The Identification of the Determinants of the Cyclic, Sequential Binding of Elongation Factors Tu and G to the Ribosome," *J. Mol. Biol.*, 386, 2009.

[Yu *et al.*, 2006] J. Yu, J. Xiao, X. Ren, K. Lao, and X. Xie, "Probing Gene Expression in Live Cells, One Protein Molecule at a Time," *Science*, 311:1600–1603, 2006.

[Zaman *et al.*, 2007] S. Zaman, M. Fitzpatrick, L. Lindahl, and J. Zengel, "Novel mutations in ribosomal proteins L4 and L22 that confer erythromycin resistance in *Escherichia coli*," *Mol. Microbiol.*, 66, 2007.

[Zaslaver *et al.*, 2006] A. Zaslaver *et al.*, "A comprehensive library of fluorescent transcriptional reporters for Escherichia coli," *Nat. Methods*, 3(8):623–628, 2006.

[Zhang *et al.*, 2006] X. Zhang *et al.*, "Feedback control of ribosome synthesis in *Escherichia coli* is dependent on eight critical amino acids," *Biochemie*, 88(9):1145–1155, 2006.

[Zhu *et al.*, 1997] J. Zhu *et al.*, "Three-dimensional reconstruction with contrast transfer function correction from energy-filtered cryoelectron micrographs: procedure and application to the 70S *Escherichia coli* ribosome.," *J. Struc. Biol.*, 118(3):197–219, 1997.

[Zhu *et al.*, 2016] M. Zhu *et al.*, "Real time determination of bacterial *in vivo* ribosome translation elongation speed based on LacZ complementation system," *Nucleic Acids Res.*, 1, 2016.

[Zia *et al.*, 2011] R. Zia, J. Dong, and B. Schmittmann, "Modeling Translation in Protein Synthesis with TASEP: A Tutorial and Recent Developments," *J Stat Phys*, 144, 2011.

[Zimmer *et al.*, 2016] A. Zimmer, I. Katzir, E. Dekel, A. Mayo, and U. Alon, "Prediction of multidimensional drug dose responses based on measurements of drug pairs," *Proc. Nat. Acad. Sci. USA*, 113, 2016.